Crystal Cartography: Mapping Nanostructure with Scanning Electron Diffraction

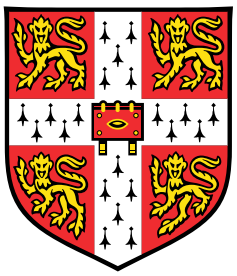

Duncan Neil Johnstone

Department of Materials Science & Metallurgy
University of Cambridge

This dissertation is submitted for the degree of
Doctor of Philosophy

Peterhouse October 2018

Declaration

I hereby declare that except where specific reference is made to the work of others, the contents of this dissertation are original and have not been submitted in whole or in part for consideration for any other degree or qualification in this, or any other university. This dissertation is my own work and contains nothing which is the outcome of work done in collaboration with others, except as specified in the text and Acknowledgements. This dissertation contains fewer than 60,000 words, including summary/abstract, tables, footnotes and appendices, but excluding table of contents, photographs, diagrams, figure captions, list of figures/diagrams, list of abbreviations/acronyms, bibliography and acknowledgements.

Duncan Neil Johnstone
October 2018

Acknowledgements

My PhD supervisor Paul Midgley has given me a unique blend of precise feedback, support and independence that has shaped my approach to doing science, for which I am very grateful. His fingerprints may be found throughout the whole of this thesis. I would also like to thank my colleagues from Department of Materials Science & Metallurgy in Cambridge, both in electron microscopy and beyond, who have played a role in the work done during this PhD. In particular: Alex Eggeman, Jon Barnard, Robert Krakow, Sung-Jin Kang, Rowan Leary, John Meurig Thomas, Sean Collins, Ben Martineau, Phillip Crout, Giorgio Divitini, Rob Tovey, Cate Ducati, and Cathie Rae. Ton van Helvoort from NTNU, Norway, also deserves special mention, both for the supervision that he gave me during the first year of my PhD, during his sabbatical in Cambridge, and for the continued collaboration since. Many others, too numerous to list, have played roles for which I am grateful.

Formal acknowledgements of the work of others presented in this thesis are as follows. The alignment method for precession electron diffraction reported in Chapter 3 was established in collaboration with Jon Barnard who also performed wave optical simulations presented there. Code incorporated into the framework presented in Chapter 4 included significant contributions from Ben Martineau and Phillip Crout. The work presented in Chapter 6 was all performed in collaboration with Robert Krakow and further Ralf Hielscher (TU Chemnitz) gave significant help with the mathematics of orientations including implementation of the code used there. Samples studied in Chapter 7 were provided by Ugo Sassi, Domenico De Fazio and Stephen Hodge working with Andrea Ferrari at the Cambridge Graphene Centre. Samples studied in Chapter 8 were provided by Hiroshi Jinnai and Takeshi Higuchi (Tohoku University), the data presented there was all acquired by Sung-Jin Kang who also played a significant role in analysis and interpretation. A list of work published at the time of writing is provided in Appendix A.

Abstract

Crystal Cartography:
Mapping Nanostructure with Scanning Electron Diffraction
Duncan Neil Johnstone

Nanostructure describes the network of defective and distorted atomic structure existing on the nanoscale within materials. This nanostructure bridges the gap between idealised crystalline structure and real materials, playing a deterministic role in tailoring physico-chemical properties, as well as providing a basis for mechanistic understanding of complex processes such as mechanical deformation and phase transformation. Characterising nanostructure, to develop understanding of materials, requires experimental techniques capable of probing the structure with spatial resolution on the order of nanometres and across regions of interest up to micrometres. Recent developments in electron microscopy, enabling the acquisition of numerous diffraction patterns in a spatially resolved manner, combined with modern computational power, provides a route to meet this need as developed in this work.

Scanning electron diffraction (SED) involves the acquisition of a two-dimensional electron diffraction pattern at each probe position in a two-dimensional scan of a specimen. An information rich 4-dimensional (4D-SED) dataset is obtained that can be analysed extensively *post-facto* using a wide-range of computational methods. The acquisition of such 4D-SED data from the specimen at numerous orientations may also enable the reconstruction of nanostructure in three-dimensions via tomographic methods. In this work, methods for the acquisition and analysis of 4D-SED data are developed and applied to reveal nanostructure in two and three-dimensions. These methods are applied to various prototypical characterisation challenges in materials science, particularly: strain mapping in two and three dimensions, revealing inter-phase crystallographic relationships, mapping grains in two-dimensional materials, and probing nanostructure in polyethylene.

Table of contents

List of figures

List of tables

Nomenclature

The following nomenclature is used throughout this thesis, except where otherwise defined.

Physical Constants

c	Speed of light
e	Elementary charge
h	Planck constant
m_0	Electron rest mass

Symbols

α	Convergence semi-angle
$\chi(\mathbf{k})$	Aberration function
λ	Electron wavelength
$\phi(\mathbf{k}')$	Scattered wave-amplitude
$\Psi(\mathbf{r})$	Electron wavefunction
$A(\mathbf{k})$	Aperture function
d_{hkl}	Interplanar spacing for hkl lattice planes
$F(\mathbf{k}')$	Electron structure factor
$f(\mathbf{k}')$	Electron atomic scattering factor
FT	Fourier transform operator
I_g	Intensity of diffracted beam g

$V(\mathbf{r})$ Coulomb potential

$\mathbf{a}_i$ Real space basis vector

$\mathbf{a}_i^*$ Reciprocal space basis vector

$\mathbf{F}$ Displacement gradient tensor

$\mathbf{g}$ Reciprocal space lattice vector

$\mathbf{g}_i$ Crystal orientation

$\mathbf{k}$ Reciprocal space vector

$\mathbf{k}_0$ Incident wave-vector

$\mathbf{k}$' Scattering vector (reciprocal basis)

$\mathbf{m}_{ij}$ Crystal misorientation

$\mathbf{R}$ Rotation tensor

$\mathbf{r}$ Real space vector

$\mathbf{s}_g$ Excitation error

$\mathbf{U}$ Right stretch tensor

Acronyms/Abbreviations

2D Two-dimensional

3D Three-Dimensional

4D-S(P)ED Four-Dimensional Scanning (Precession) Electron Diffraction

BF Bright-Field

BSS Blind Source Separation

CBED Convergent Beam Electron Diffraction

CCD Charge Coupled Device

CL Condenser Lens

CTEM Conventional Transmission Electron Microscopy

CVD Chemical Vapour Deposition

CVT Centroidal Voronoi Tesselation

DF Dark-Field

DQE Detective Quantum Efficiency

EBSD Electron Backscatter Diffraction

EDX Energy Dispersive X-ray Spectroscopy

EELS Electron Energy Loss Spectroscopy

FEG Field Emission Gun

FFT Fast Fourier Transform

FIB Focused Ion Beam

GND Geometrically Necessary Dislocations

HOLZ Higher Order Laue Zone

ICA Independent Component Analysis

IDL Interactive Data Language

IPF Inverse Pole Figure

LCR Circuit Electrical circuit comprising an inductor, L, a capacitor, C, and a resistor, R.

LRO Long Range Order

LSPR Log Power Spectrum Ratio

MDF Misorientation Distribution Function

MOP Metal-Organic Polyhedral

MRO Medium Range Order

MTF Modulation Transfer Function

NBED Nanobeam Electron Diffraction

NMF Non-negative Matrix Factorization

NNDSVD Non-negative Double Singular Value Decomposition

ODF Orientation Distribution Function

PCA Principal Component Analysis

PDF Pair Distribution Function

PE Polyethylene

PED Precession Electron Diffraction

PG Point Group

PMMA Poly-methyl methacrylate

ROI Region of Interest

SAED Selected Area Electron Diffraction

SED Scanning Electron Diffraction

SEM Scanning Electron Microscopy

SIRT Simultaneous Iterative Reconstruction Technique

SPED Scanning Precession Electron Diffraction

SRO Short Range Order

STEM Scanning Transmission Electron Microscopy

SVD Singular Value Decomposition

SXDM Scanning X-ray Diffraction Microscopy

TCP Topologically Close-Packed

TEM Transmission Electron Microscopy

TKD Transmission Kikuchi Diffraction

UHMWPE Ultra-high Molecular Weight Polyethylene

VBF Virtual Bright-Field

VDF Virtual Dark-Field

XRD X-ray Diffraction

ZOLZ Zero Order Laue Zone

Chapter 1

Material Structure & Characterisation

Understanding materials behaviour involves relating physical properties, processing parameters, and *in-situ* transformations, to structure from the atomic scale (10^{-10} m) to the component scale ($10^{-9} - 10$ m). The structure may then be manipulated in order to obtain properties suitable for technological applications. This requires materials characterisation and modelling across length scales, using numerous techniques, as shown in Figure 1.1. On the nanoscale (1 nm - 1 μm), atomistic modelling is relevant but reaches contemporary limits of scale [29, 30] and there is is no routine, robust and quantitative experimental method for directly determining local atomic structure [31]. Consequently, there is a pressing need to develop nanostructural descriptors and characterisation techniques that may enable nanostructured materials to be engineered [32, 33].

Complete description of material structure would, in principle, require specification of the nature, location, bonding, and dynamics of all atoms comprising it. However, performing that analysis on an atom-by-atom basis is unfeasible due to the sheer number of atoms involved. Instead, parts of the material, with similar *atomic structure*, are identified that may be approximated by relatively simple idealized atomic arrangements either in the limit of complete order or disorder. More complexity is then introduced as deviations away from these ideals using few parameters. Atomistic description may sometimes be necessary for a complete picture but, where possible, more compact representations of essential features are favourable. Descriptors for idealized atomic structures and microstructural deviations are reviewed in Sections 1.1 & 1.2 leading to a more specific definition of the nanostructure problem in Section 1.3. Experimental techniques capable of revealing elements of nanostructure, are then reviewed in Section 1.4 to make the case for developing scanning electron diffraction (SED) microscopy as a direct nanoscale structural probe, which is the aim of this work.

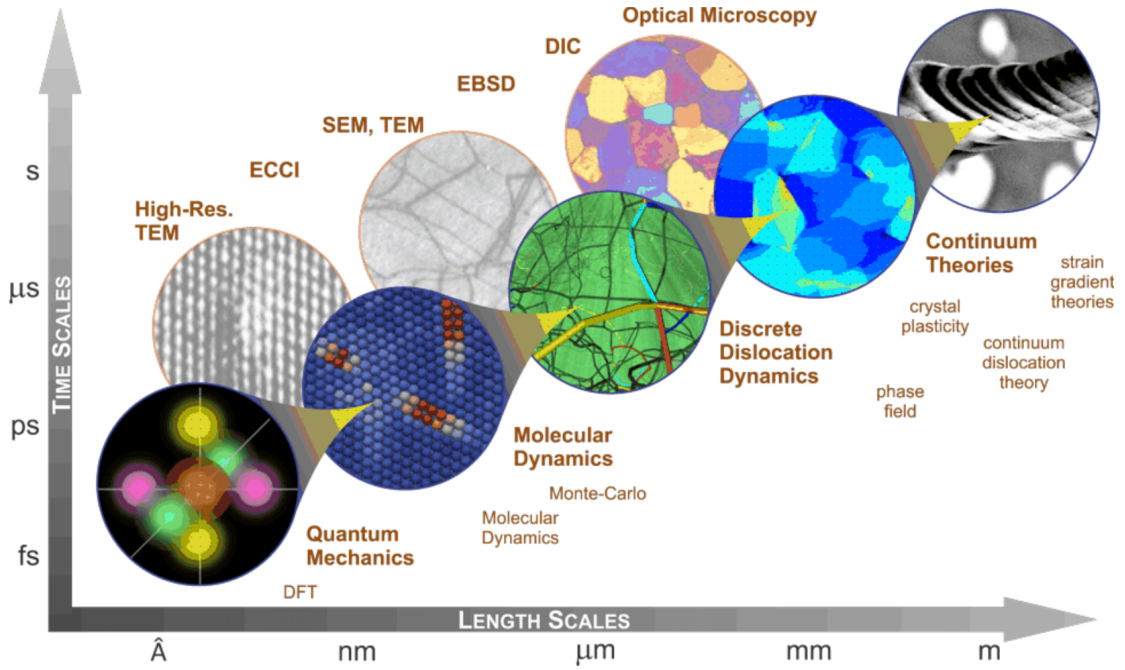

Fig. 1.1 **Multiscale materials modelling and characterisation.** Various techniques applicable across a range of length and time scales. Reproduced from Kochmann [1].

1.1 Atomic Structure

Atoms arrange into energetically stable polyatomic species (e.g. molecules and crystals), subject to kinetic limitations, as a result of interactions defining chemical bonding [34]. This bonding is due to the redistribution of electron density, primarily the most weakly bound (valence) electrons, throughout the structure [35, 36] and is often discussed using an extensive taxonomy of 'bonds' including: 'strong' covalent, ionic and metallic bonds; and 'weak' inter-molecular bonds such as hydrogen bonds, halogen bonds, van der Waals bonds, and $\pi - \pi$ interactions. These bonds, and particularly covalent bonds, may be identified as linkages between structural units [21, 37] although there may also be significant non-directional contributions [38, 35]. The atomic arrangement resulting from these interactions is typically described in terms of atomic coordinates, which is the *atomic structure*.

The atomic structure may be approximated either as a *crystal* possessing long-range atomic order or as a *non-crystal* without long-range atomic order. Crystalline atomic structure can be described by a small atomic unit and a rule for continuing the ordered structure provided by the language of crystallography (see Section 1.1.1), but non-crystalline atomic structure is typically described on a case-by-case basis, without a generalized framework (see Section 1.1.2). In both cases, the identification of linkages between structural groups enables *topological* analysis (see Section 1.1.3) that may reveal structural similarities.

1.1.1 Crystals

Crystals give *essentially sharp* diffraction [39], which is the primary means of probing crystalline structure, such that the diffracted intensity is concentrated in peaks at positions:

$$\mathbf{g} = \sum_{i=1}^{n} h_i \mathbf{a}_i^* (n \geq 3) \tag{1.1}$$

where $\mathbf{a}_i^*$ are reciprocal basis vectors and n is the minimum dimensionality for which all $\mathbf{g}$ can be described with h_i as integer coefficients. Conventional *periodic crystals*, possessing translational symmetry, correspond to $n = 3$, and *aperiodic crystals*, e.g. incommensurately modulated structures and quasicrystals [40, 41], correspond to $n > 3$.

Periodic crystals comprise an atomic *motif* repeated at an infinite periodic array of points connected by *lattice* vectors, $\mathbf{r}_{lat} = u\mathbf{a}_1 + v\mathbf{a}_2 + w\mathbf{a}_3$, where u, v, w are integers and $\mathbf{a}_i$ are direct space basis vectors, which is a set closed under addition and subtraction. The 14 *Bravais lattices* fill three-dimensional space perfectly and this *translational symmetry* implies that the atomic arrangement can be described by repetition of a *unit cell*, within which atoms may be related by symmetry operations that leave at least one point unmoved, i.e. rotation, reflection, and inversion. This *point symmetry* must map the lattice onto itself to be compatible with translational symmetry and must therefore correspond to one of the 32 *crystallographic point groups*, which combined with the Bravais lattices lead to 230 unique *space groups* defining the crystal symmetry. Crystalline atomic structure thus comprises an *asymmetric unit* of atomic structure and appropriate symmetry operators, as illustrated in Figure 1.2.

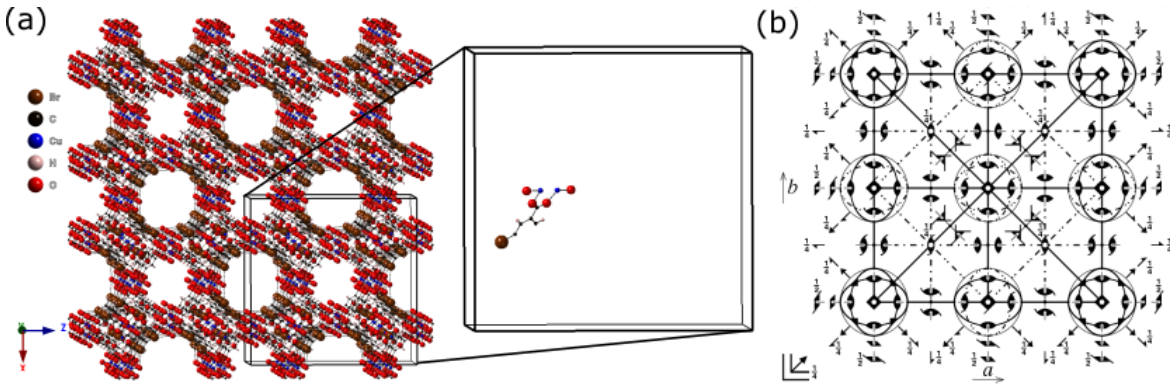

Fig. 1.2 **Symmetry in crystals.** (a) A metal-organic polyhedral (MOP) structure [2], MOP-14, reduced to a unit cell containing 854 atoms by translational symmetry and an asymmetric unit comprising only 15 atoms by point symmetry. (b) Symmetry operators of the $Im\bar{3}m$ space group of MOP-14 as shown in the International Tables for Crystallography [3].

Crystal symmetry is physically significant since Neumann's principle [42] states that the crystal point group must be a subgroup of the symmetry of any physical property. Some physical properties are therefore only possible in non-centrosymmetric crystals, typically those represented by polar tensors of odd rank (piezo/pyro electricity) or axial second rank tensors (optical activity) [42]. Defects in crystals may also be described in terms of the symmetry operations that they break as discussed in Section 1.2.4.

1.1.2 Non-crystals

Non-crystalline atomic structures do not possess the long-range order of crystals, but atoms also do not arrange randomly due to interactions between them, which, at a minimum, prevent very small interatomic separations. Indeed, the taxonomy of crystallography fails on introducing simple local distortions to crystalline structures [4]. But, order in non-crystals has signatures in both the diffraction pattern and the *pair distribution function* (PDF), which is the probability density of interatomic pair separation as a function of distance obtained as the Fourier transform of the total scattering structure factor [43], as in Figure 1.3. These characteristics enable atomic models to be constructed from data, often using reverse Monte Carlo methods [44–46], and *ab initio* using molecular dynamics [46, 47].

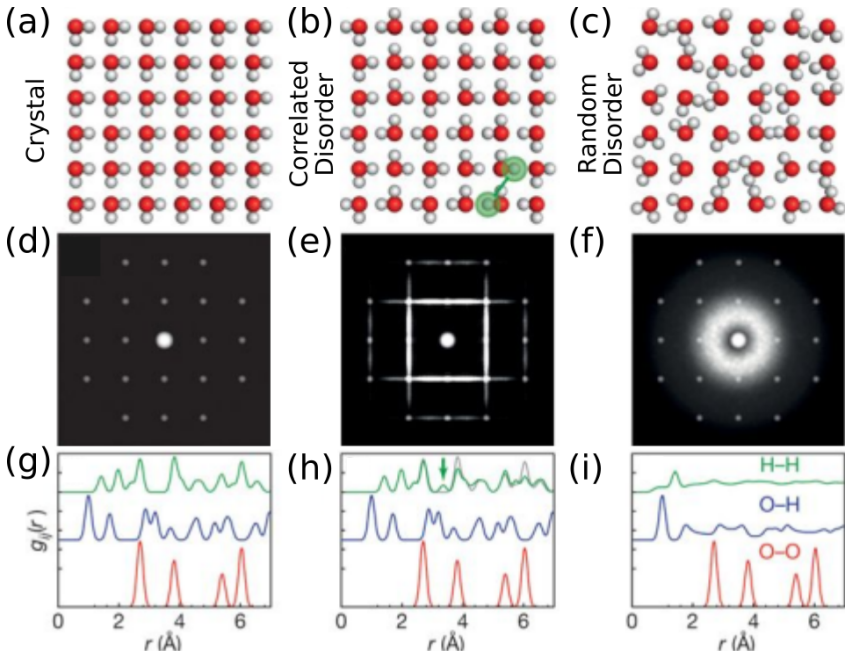

Fig. 1.3 **Atomic order and disorder.** A crystal structure (a) may be made non-crystalline by introducing correlated (b) or random (c) rotations. (d-e) Disorder introduces diffuse scattering, which is structured if the disorder is correlated (e). (g-i) Correlated disorder also leaves signatures in the PDF. Reproduced from reference [4].

Short-range order (SRO) in nearest neighbours occurs due to interactions between atoms and is reflected in the three classical models of amorphous solids [48]: (1) the continuous random network model [49] for covalent network glasses, e.g. a-Si, a-SiO_2 [50] and amorphous metal organic frameworks [51, 52]; (2) the dense random packing model [53] for metallic glasses, which has been modified to introduce local stereochemistry [54] and atomic clusters [55]; and (3) the random coil model [56] for amorphous polymers. Medium-range order (MRO), between approximately third nearest neighbours, is less understood because peaks in the PDF are broad due to the large number of pair correlations at moderate distances [57], but evidence for MRO is growing [58]. Intermediate degrees of order, such as the correlated disorder [4] described above and the various *mesophases* of molecular solids [59], such as *liquid crystals* that possess orientational order but not positional order [60], also exist.

1.1.3 Topology of Chemical Graphs

An atomic structure may be considered as a graph with vertices corresponding to structural groups (e.g. atoms, molecules) and edges to linkages (e.g. chemical bonds) between them [21, 61]. Topological descriptors characterize the set of linkages to assess the connectivity of structural space. For example, a *cycle* is a loop of linkages without crossings and a *ring* is a cycle that is not a sum of two smaller cycles. Important numerical properties include: the *vertex symbol* describing the number of ways a ring may be constructed, and the *transitivity*, which is a measure of complexity described by the number of vertices, linkages, faces and tiles formed when rings are used to construct space filling polyhedra. A topology is invariant to structural distortions provided that linkages are not broken and can be particularly useful in: (1) describing flexible systems [61], (2) identifying structural classes, as in Table 1.1, and similarities between them [21], and (3) identifying the emergence of crystal-like regions in non-crystalline atomistic models e.g. based on persistent homology [62, 63], which accounts for both connectivity and geometry.

Table 1.1 **Classification of crystals based on structural units and bond types.** [1]H-bonds, van der Waals, or specific secondary interactions e.g. S—S, I—I. From Blatov et al [21]

Category	Structural Groups	Intra-bonds	Inter-bonds
Inorganic Ionic Compounds	metal ions, complex ions	covalent	ionic
Intermetallic Compounds	metal ions, metal clusters	metallic	metallic
Porous Structures	cages	covalent	covalent
Coordination Compounds (I)	metal atoms, ligands	covalent	covalent
Coordination Compounds (II)	complex groups	covalent	H-bond
Organic Crystals	organic molecules	covalent	intermolecular

1.2 Microstructure

Real materials, whether bulk materials or nanomaterials, typically possess heterogeneous atomic structure. This heterogeneity defines microstructure and may be manifest in various ways. Many materials are aggregates of *grains* and *precipitates* defining regions within which the atomic arrangement is well approximated by a particular, crystalline or non-crystalline, atomic structure and composition - referred to as a *phase*. Size, morphology and spatial distribution characterize this grain structure (see Section 1.2.1). In polycrystalline materials, grains are crystals with different orientations (see Section 1.2.2) that are sometimes crystallographically related (see Section 1.2.3) and may contain defects (see Section 1.2.4) and/or be distorted continuously (see Section 1.2.5). Bulk amorphous materials may appear more homogeneous but heterogeneity is common in the form of variations in local atomic density or the presence of nanocrystals [64–67]. Here, the focus is on the multiscale network of phases, orientations, defects and distortions, defining microstructure in polycrystalline materials, as illustrated in Figure 1.4.

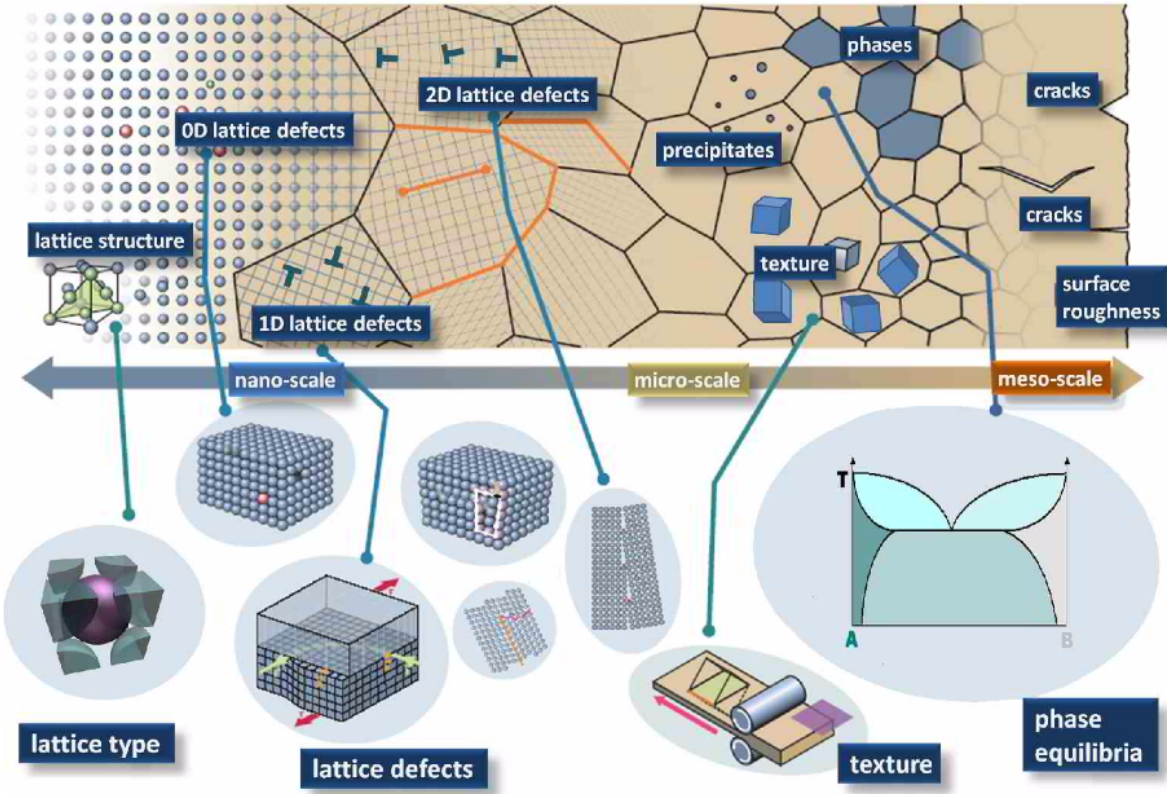

Fig. 1.4 **Microstructure in polycrystalline materials.** Heterogeneities in the atomic structure from the atomic to the macroscopic scale defining microstructure, from [5].

1.2.1 Morphological Parameters

Grain structure is often characterized in terms of grain size and the spatial distribution of phases/precipitates using scalar quantities derived from two-dimensional measurements of cross-sections [68]. Grain sizes may be reported as the equivalent diameter of circles with areas equal to measured grains or spatial distributions in terms of mean distances between points on lines intercepting features of interest [68]. Such characteristic distances may be correlated with physical properties, for example, the Hall-Petch dependence of yield strength [69], but are a simplistic representation of irregular shapes arranged in three-dimensions. A more complete representation could consider grain volume, shape, morphological orientation, number of contiguous nearest neighbour grains, as well as correlations between these parameters [70, 71] but irregular shapes remain a particular challenge [72].

1.2.2 Crystal Orientations & Texture

Crystallographic orientation maps specify the orientation of crystal basis vectors as a function of position, as shown in Figure 1.5a. Coordinate systems are introduced to specify directions in a *specimen reference frame*, r, and *crystal reference frames*, h_i, and the local orientation may then be described as a transformation between coordinate systems. Conventionally, the reference frames introduced are orthonormal, right-handed, and share the same origin. Orientations are defined as passive rotations (i.e. tensor quantities are not rotated) that transfer coordinates with respect to a crystal reference system into coordinates with respect to a specimen reference system. The rotation angle is taken to be positive for a rotation that is counterclockwise when viewed along the corresponding rotation axis towards the origin. An orientation, $\boldsymbol{g}_i$, therefore satisfies

$$r = \boldsymbol{g}_i h_i, \tag{1.2}$$

where $r = (\mathbf{x}, \mathbf{y}, \mathbf{z})$ denotes specimen coordinates, $h_i = (\mathbf{e}_1, \mathbf{e}_2, \mathbf{e}_3)$ crystal coordinates, and the orientation is an element of the rotation group, $\boldsymbol{g}_i \in SO(3)$. These rotations form a non-commutative group [73] implying inverses exist and rotations are combined associatively.

Representations of orientations comprise 3 independent parameters most commonly expressed as Euler angles, an axis and angle of rotation, a quaternion, or a rotation matrix [73]. The distribution of crystal orientations may be quantitatively assessed in terms of the *orientation distribution function* (ODF), which is the continuous probability density function describing the likelihood of observing each orientation within the specimen [74]. There may be a prevalence of some crystal orientations within a material, known as *texture*, which may result in polycrystalline material retaining anisotropy in tensor properties [75].

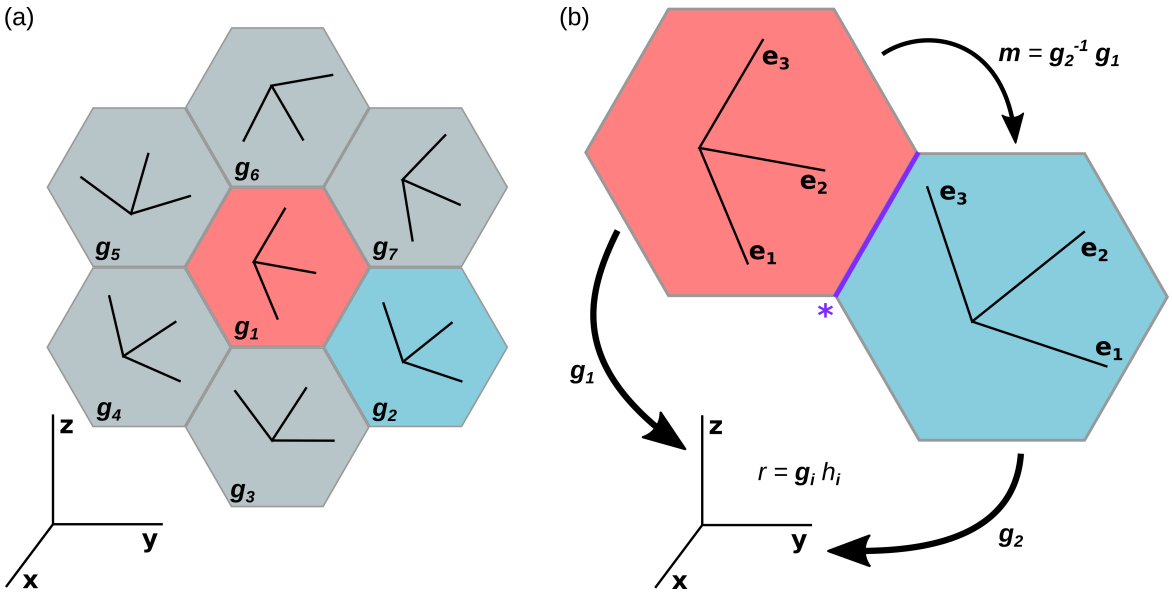

Fig. 1.5 **Crystallographic orientation maps.** (a) Local orientations g_i of crystallographic axes with respect to an external reference frame. (b) Orientations, g_i, as transformations from the crystal reference frames, h_i, into the specimen reference frame, r, and a misorientation, m, describing transformation between crystal reference frames across a boundary element (*).

1.2.3 Interfaces & Crystallographic Relationships

Two crystals (grains or precipitates) may meet at an interface and are related by the nature of the interface and the relative orientation of the crystal lattices. The interface may be coherent, with continuous lattice planes across it, semi-coherent if lattice defects (see Section 1.2.4) are present, or incoherent without any lattice continuity. characterisation of the interface generally requires three-dimensional characterisation and atomistic simulation [76, 77] but may be geometrically classified in terms of five parameters defining the interface plane and the relative lattice orientation [73, 78]. Only the relative lattice orientation, which is accessible from two-dimensional crystallographic orientation maps, is considered below.

Misorientations, $\boldsymbol{m}_{ij}$, describe coordinate transformations between crystal reference frames and, like orientations, are passive rotations described by three-parameters. For two crystals with orientations $\boldsymbol{g}_1$ and $\boldsymbol{g}_2$, as shown in Figure 1.5b, the misorientation $\boldsymbol{m}_{ij}$ between them is defined and transforms crystal coordinates h_1 into crystal coordinates h_2, as follows:

$$\boldsymbol{m}_{12} = \boldsymbol{g}_2^{-1}\boldsymbol{g}_1 \tag{1.3}$$

$$\boldsymbol{m}_{12}h_1 = \boldsymbol{g}_2^{-1}\boldsymbol{g}_1 h_1 = \boldsymbol{g}_2^{-1} r = h_2 \tag{1.4}$$

The *misorientation distribution function* (MDF) is the continuous probability density function for observing misorientations [73] and may indicate special *orientation relationships* if misorientations are more prevalent than a random distribution [79, 80]. Orientation relationships are sometimes well approximated by parallelisms between low-index crystallographic planes and directions [28] or as (near) coincident site lattices in which a fraction of lattice sites associated with each crystal (nearly) coincide if the lattices are interleaved [81] but this does not imply lattice continuity, or the existence of a low energy interface [76]. Shear transformations, i.e. deformation twinning and martensitic transformation, must lead to orientation relationships [82–84]. Those produced by twinning may be described as rotations of 180° about an axis parallel or perpendicular to the plane unaffected by the shear (twin plane) [75], whereas those produced by martensitic transformation may be close to low-index parallelisms but the phase transformation necessitates irrational indices [75].

1.2.4 Defects in Atomic Structure

Defects describe ways in which atoms may be located away from expected positions that are not just a small distortion (see Section 1.2.5) of the ideal structure. For example, an atom (or molecule) may be missing from the structure, leaving a *vacancy*, or replaced by *substitution* with another species. Similarly, additional atoms (or molecules) may be present in *interstitial* positions between ideal atomic sites. Such defects are (0D) point defects and intuitively both (1D) line defects and (2D) surface defects may also exist in three-dimensional materials, as illustrated in Figure 1.4. Surface defects are interfaces, as above, in the special case of like atomic structure and are typically either trivial, with the two materials being structurally separate, or else may be described in terms of multiple line defects, which are the most structurally compelling defects in three-dimensional solids [85].

Line defects may be considered in the theoretical framework of the Volterra process and in terms of topology [6], as shown in Figure 1.6. In the Volterra process, the medium is cut along a surface bound by the line defect and the unbound edges are displaced by a translation $\mathbf{b}$ and a rotation Ω, which, if they are symmetries of the medium, lead to perfect quantized defects [6]. Matter is then removed or added to avoid overlap or voids and the system is relaxed elastically. Topological classification [85, 6] is based on considering an order parameter that varies continuously through the medium, except at defects. For a crystalline solid the order parameter space, V, is the coset space G/H where G is the proper part of the full Euclidean group and H is the proper part of the crystallographic space group [85]. In this case, topologically stable line defects in crystals are characterized by Bravais lattice vectors and proper point group rotations observed on encircling the line, which is consistent with the quantized defects of the Volterra process.

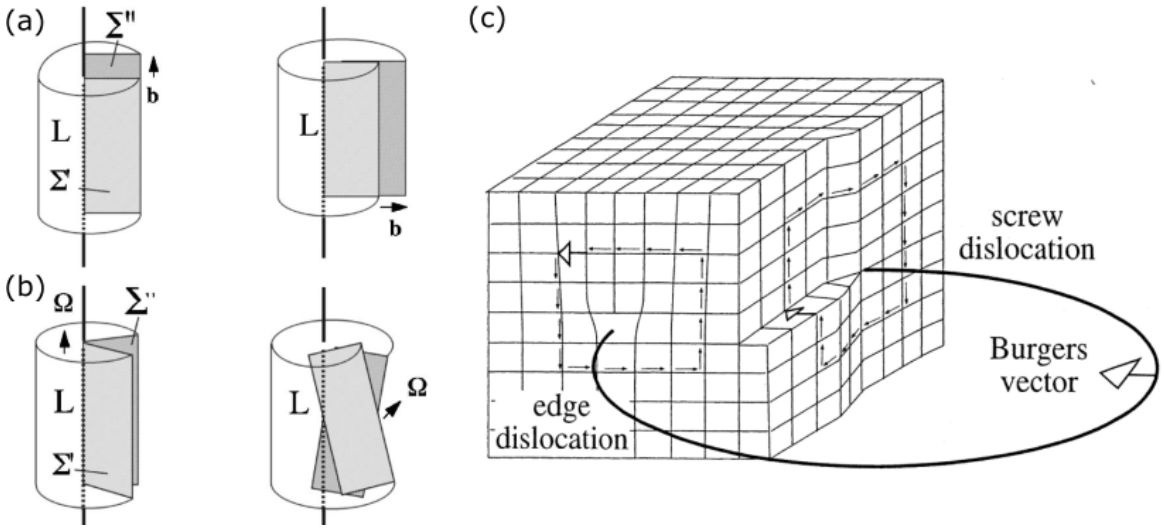

Fig. 1.6 **Line defects in crystals.** (a,b) The Volterra process for: (a) screw and edge dislocations, (b) wedge and twist disclinations. (c) Topological classification of a dislocation with both edge and screw character. Adapted from reference [6].

Classification of line defects as dislocations, disclinations, or dispirations which are associated with translation, rotation, or both, follows from both theories. Dislocations are most significant in three-dimensional crystals [86] and are associated with plastic deformation [87], low-angle grain boundaries [87], and chemical properties [88]. Disclinations are not observed in isolation in three-dimensional crystals due to large stresses, but are important in liquid crystals [6] and two-dimensional materials [89]. Both theories may be applied to any medium with a defined order parameter, which includes non-crystalline solids [6], but the atomic arrangement at the defect line can only be revealed by atomistic simulation.

1.2.5 Continuous Lattice Distortions

Crystal basis vectors may change continuously through a grain due to microstructural strain and rotations associated with defects [69]. This may be formalized by considering the transformation of a vector in an unstrained reference, d$\mathbf{x}$, to a vector in the strained configuration, d$\mathbf{x}$ = d$\mathbf{X}$ + d$\mathbf{u}$, where d$\mathbf{u}$ is the differential total displacement vector. These vectors are then related, as illustrated in Figure 1.7, by the *deformation gradient tensor*, $\mathbf{F}$:

$$d\mathbf{x} = \mathbf{F}d\mathbf{X} = \frac{\partial \mathbf{x}}{\partial \mathbf{X}} d\mathbf{X} = (\mathbf{I} + \nabla \mathbf{u}) d\mathbf{X} \tag{1.5}$$

where $\mathbf{I}$ is the second rank identity and $\nabla \mathbf{u}$ is the displacement gradient tensor, which describes both local distortion and rotation of the material.

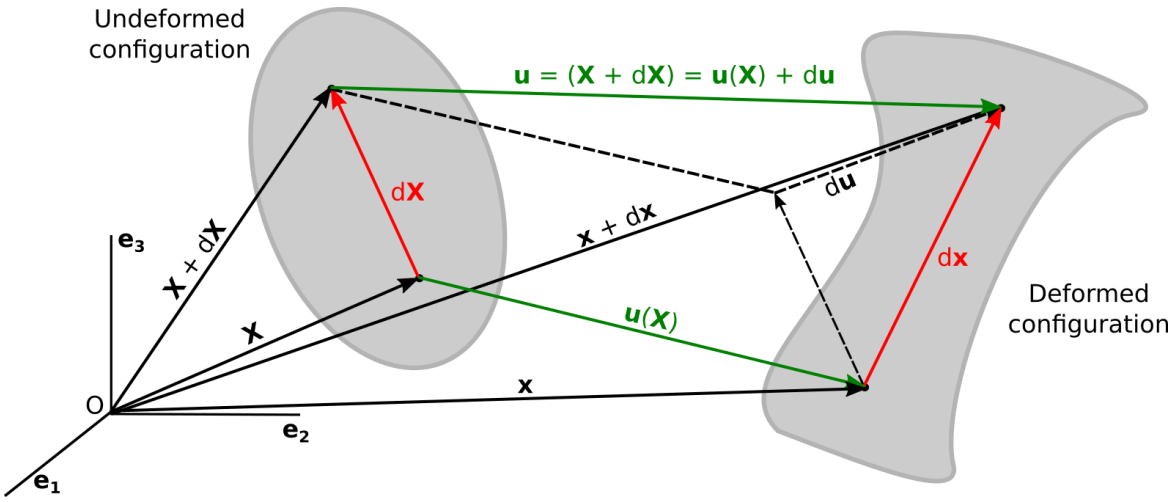

Fig. 1.7 **Deformation of a solid.** The transformation that maps an undeformed configuration onto a deformed configuration is and inhomogeneous displacement field that may be described by the deformation gradient tensor, defined as in Equation 1.5.

The deformation gradient tensor can be decomposed, $\mathbf{F} = \mathbf{RU} = \mathbf{VR}$, using polar decomposition, into the product of an orthogonal rotation tensor, $\mathbf{R}$, and a positive definite symmetric (right or left) stretch tensor, $\mathbf{U}$ or $\mathbf{V}$. In the Lagrangian convention, i.e. in material coordinates, the strain, ε, is defined,

$$\varepsilon = \frac{1}{2}(\mathbf{F}^T\mathbf{F} - \mathbf{I}) \approx \frac{1}{2}(\mathbf{F} + \mathbf{F}^T) - \mathbf{I} = \frac{1}{2}(\nabla\mathbf{u} + \nabla\mathbf{u}^T) \approx \mathbf{U} - \mathbf{I} \tag{1.6}$$

where the small strain approximation was used for approximate equalities. *Deviatoric strain* changes the shape of an object whilst preserving volume and *hydrostatic stain* changes volume. The strain field is related to physical properties such as charge carrier mobility [90] and rotation fields may be interpreted in terms of a distribution of unpaired dislocations known as geometrically necessary dislocations (GND) or Nye's tensor [91].

1.3 Nanoscale Structure & Characterisation

Nanoscale structural heterogeneity may include all microstructure as well as the smallest regions of order in non-crystals and nanomaterials. Characterizing this nanostructure is challenging in two regards. Firstly, there is no obvious general framework for structural description that improves upon an atomistic description, although there are many useful descriptors for specific cases, as set out above. Secondly, the numerous possible structures make the construction of models from bulk experimental data inherently ambiguous, although statistical measures such as X-ray pole figures [74] and pair distribution function analysis

[43] have been fruitful. This ambiguity in structure determination, as compared with the perceived certainty of crystallography, is the nanostructure problem [31]. One route to address this problem may be to consider nanostructure solution based on spatially resolved measurements rather than the long-range averages that are helpful for crystallography.

Structural investigation with nanoscale (<100 nm) spatial resolution is typically achieved using X-rays or electrons, which are penetrating, produce a plethora of physical signals and may form nanoscale probes [92, 7, 93]. Imaging techniques may be applied to characterize structure with the necessary spatial resolution and there have been important recent advances in: diffraction contrast imaging and tomography for grain reconstruction in polycrystalline specimens using both X-rays [94, 95] and electrons [96]; X-ray coherent diffractive imaging [97], particularly for three-dimensional strain reconstruction in single crystals smaller than the coherence length [98–100]; and atomic resolution electron microscopy [101] and tomography of robust nanocrystals [102–105]. However, these techniques are only appropriate for limited specimens and each reveal rather particular aspects of nanostructure. A more versatile approach may be to obtain spatial resolution through the use of a nanoscale probe, allowing various analytical signals to be recorded from each volume addressed [92, 7, 93]. The acquisition of numerous local signals then enables nanoscale analytical mapping, which may provide a route to solve the nanostructure problem on a more routine basis.

1.4 Nanoscale Analytical Mapping

Analytical mapping techniques involve the acquisition of numerous analytical (spectroscopic or diffraction) signals in a spatially resolved manner, typically by moving the probe across the specimen, or the specimen through the probe [92, 7, 93]. Two-dimensional maps are then obtained that may be used to perform three-dimensional reconstructions with an analytical signal associated with every pixel or voxel, leading to multi-dimensional data, as illustrated in Figure 1.8. Spectroscopic mapping, based on the absorption and emission of radiation by matter as a function of energy, provides powerful means to investigate local composition and bonding. X-ray absorption spectroscopy, X-ray fluorescence spectroscopy, electron energy loss spectroscopy and energy dispersive X-ray spectroscopy are all important in this regard. Diffraction mapping typically involves the acquisition of two-dimensional diffraction patterns which may be analysed to reveal local atomic structure as is the focus here. In both cases, *post-facto* computational analysis enables structural heterogeneity to be elucidated in various ways. Most current analyses assume homogeneity within the sampling or reconstruction volume, which is reasonable only if that size is significantly smaller than the characteristic size of nanostructure present.

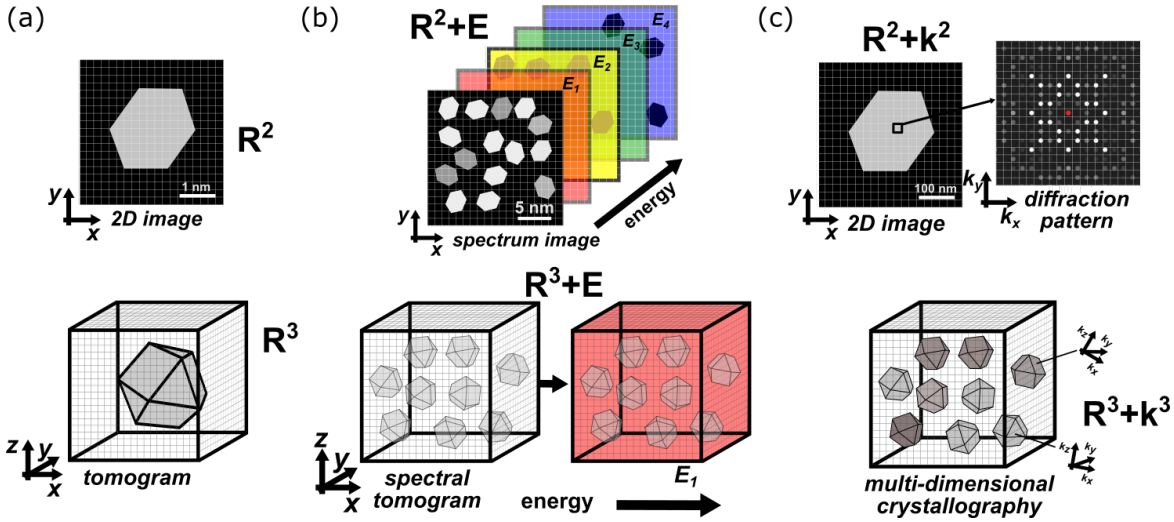

Fig. 1.8 **Multi-dimensional analytical mapping.** (a) 2D and 3D imaging with a single value associated with each pixel or voxel; (b) spectroscopic mapping, in which at each pixel/voxel is associated with a spectrum in the energy domain; (c) diffraction mapping, in which at each pixel/voxel is associated with a 2D or 3D diffraction pattern. Adapted from [7].

Diffraction mapping may be applied to local changes in non-crystalline structure, via calculation of the PDF at each probe position [106], but diffraction mapping to reveal local crystal phase, orientation and strain is much more developed using X-ray diffraction (see Section 1.4.1), electron backscatter diffraction (see Section 1.4.2), transmission Kikuchi diffraction (see Section 1.4.3) and transmission electron diffraction (see Section 1.4.4). These scanning diffraction microscopy techniques are all provide insights in both real and reciprocal space and are in this sense hybrid diffraction/microscopy techniques with many common features although interestingly different aspects have been developed in each case.

1.4.1 Scanning X-ray Diffraction Microscopy

Scanning X-ray diffraction microsocpy (SXDM) involves scanning the specimen through a collimated, monochromatic or polychromatic, X-ray probe and recording an XRD pattern, on an area detector, at each probe position [107–109]. SXDM performed with monochromatic X-rays typically records a single Bragg reflection per scan and can map strain averaged along the beam path, in approximately single lattice specimens, for a particular set of lattice planes with very high ($\sim 10^{-5}$) precision [110]. Larger detectors may enable more reflections to be recorded simultaneously and the use of monochromatic X-rays is advantageous for simultaneous spectroscopic mapping. However, structural mapping is more generally developed using polychromatic X-rays to record Laue patterns.

Laue microdiffraction is capable of mapping both strain ($\sim 10^{-4}$ precision [23]) and orientation ($\sim 0.01^{\circ}$ precision [23]) in polycrystalline and highly deformed samples in two and three dimensions. Achromatic focusing optics, typically Kirkpatrick–Baez mirrors, are used to focus the polychromatic beam to a lateral size $20-200$ nm [23] and the superposition of Laue patterns from along the beam path, at the detector, can be avoided by using a differential aperture geometry [22], as shown in Figure 1.9. X-ray Laue patterns contain numerous non-coplanar reflections and four such reflections are sufficient to determine the unit cell shape: $a/c, b/c; \alpha, \beta, \gamma$ and its orientation, without knowledge of the X-ray wavelength [23]. These parameters are sufficient to determine the deviatoric components of the strain tensor but to determine all components of the strain tensor the unit cell parameters are required, which is possible if the the wavelength associated with one reflection is found by inserting a monochromator into the beam path and performing an additional scan.

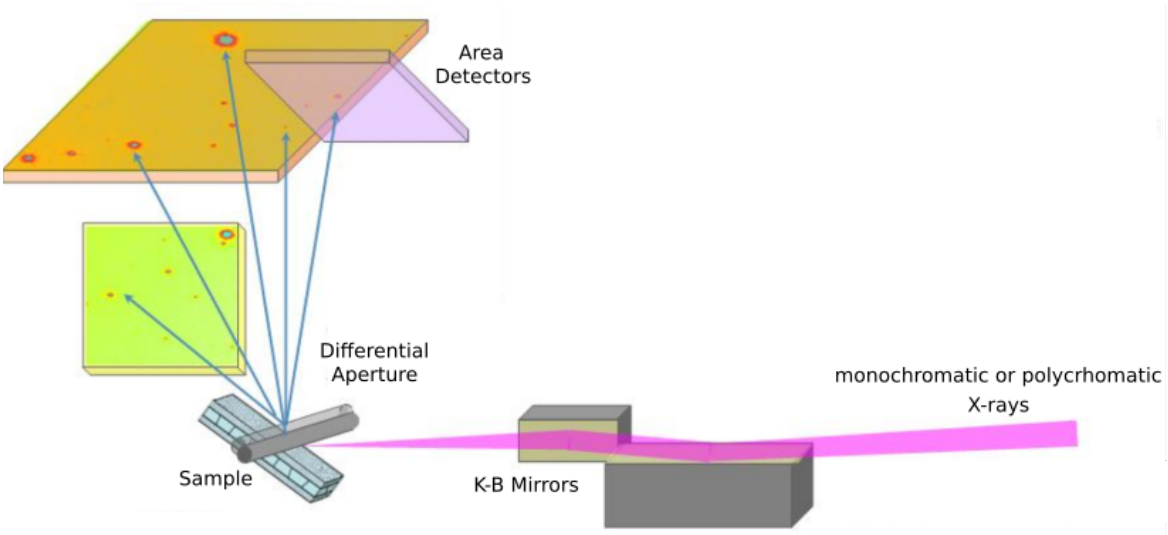

Fig. 1.9 **Scanning X-ray Diffraction Microscopy**. Laue microdiffraction geometry with detectors positioned near to 90° scattering angles and differential aperture microscopy performed using a wire near to the specimen surface to separate scattering from along the beam path. A monochromator may be moved in and out of the beam path, from [8].

1.4.2 Electron Backscatter Diffraction

Electron backscatter diffraction (EBSD), performed in a scanning electron microscope (SEM), involves recording, at each probe position, the Kikuchi pattern formed by incoherent quasi-elastic scattering of incident electrons followed by coherent elastic scattering of those electrons as they exit the specimen surface [111]. Spatial resolution in EBSD is dictated by the interaction volume of the electron beam with the sample, which has dimensions

in the range 20-80 nm [112], defining both lateral and depth resolution. Kikuchi patterns comprise numerous bands that are direct projections of the crystal lattice planes onto the detector. Orientation analysis is based on relating the macroscopic sample axes to three crystallographic axes identified in the pattern, at Kikuchi band intersections, typically using the Hough transform [113–115]. Indexation is then achieved by comparing measured inter-zonal/inter-planar angles to a table of known structures and the angular resolution of such analysis is $\sim 0.5 - 1\,^{\circ}$. Pattern matching approaches, based on comparing measured patterns to a library of pre-calculated simulations, have been recently reported [116–120] offering similar angular resolution. Incorporating dynamical simulation of intensities [121] into the matching has also enabled polar domain structures to be mapped [122].

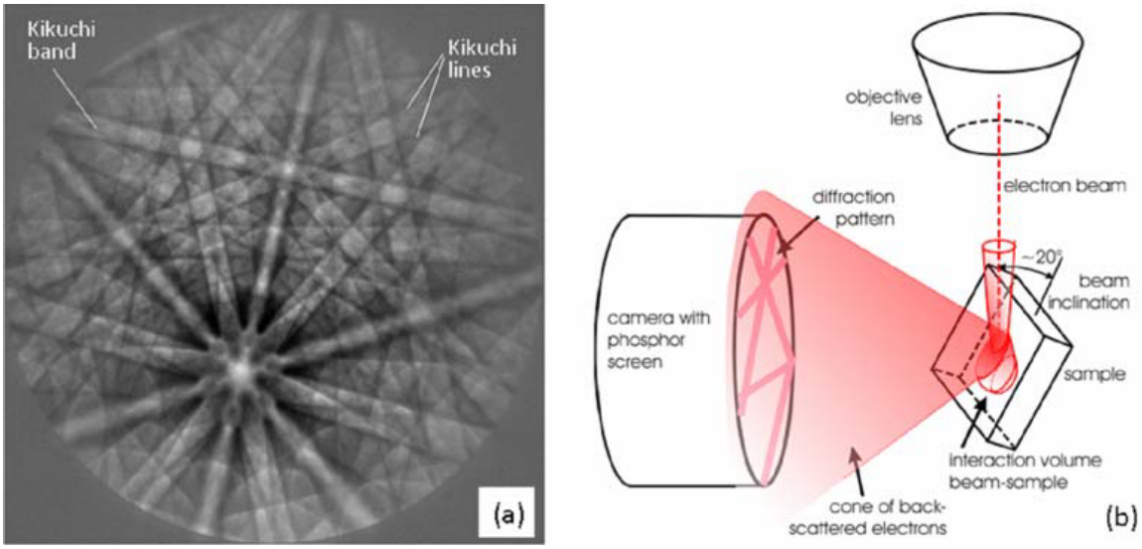

Fig. 1.10 **Electron Backscatter Diffraction.**(a) A typical Kikuchi pattern recorded in EBSD and (b) schematic drawing of a typical experimental set up. (c) Indexation of a Kikuchi pattern based on band intersection. Reproduced from Zaefferer [9].

High-sensitivity ($\sim 10^{-4}$ precision) EBSD is based on measuring small band shifts in multiple regions of the Kikuchi patterns using cross-correlation [123, 124] to determine shifts of ~ 0.05 pixels [123]. This may be enhanced by pattern binning and averaging, suggesting a resolution limit of 4×10^{-7} [125]. Shifts in 4 non-coplanar regions of the Kikuchi pattern are required to determine 8 components of the deformation gradient tensor [123], although more regions are typically used [126]. The remaining degree of freedom is pure hydrostatic strain, which may be determined by assuming that the local stress state must satisfy equilibrium conditions with no stress normal to the free. Three-dimensional reconstruction may be achieved using a dual-beam focused ion beam (FIB) SEM, in which slices of the material are sequentially mapped as successive layers are removed via FIB milling [127].

1.4.3 Transmission Kikuchi Diffraction

Transmission Kikuchi Diffraction (TKD) uses the Kikuchi pattern formed by electrons passing through a thin film specimen, and may be performed in a scanning transmission electron microscope (STEM) [128–131] and an SEM modified with a transmission detector [25, 26]. In STEM-TKD an accelerating voltage of 60-300 keV and a collection angle of $\sim 10^{\circ}$ is typical, as compared with 5-30 keV and $\sim 50^{\circ}$ for SEM-TKD. These differences impact the appropriate specimen thickness (5-100 nm vs. 50-250 nm), spatial resolution (1 nm vs. 10 nm) and analysis. SEM-TKD data may be analysed in the same way as EBSD data using Hough transform based indexation to achieve $\sim 0.5 - 1^{\circ}$) angular precision [25, 26]. STEM-TKD data is not usually suitable for such analysis since 3 zone axes are not typically recorded. This leads to ambiguity in some indexations, but tracking shifts in band positions has enabled small rotations to be mapped with $\sim 0.01^{\circ}$ angular resolution [132, 133]. TKD is typically limited by pattern clarity, which requires a specimen thickness in a range where there is sufficient incoherent scattering to form a Kikuchi pattern but not so much as to create excessive background. Further, the Kikuchi pattern is degraded by the presence of lattice defects and distortions that are common in regions of interesting deformation.

1.4.4 Scanning Electron Diffraction Microscopy

Scanning electron diffraction (SED) microscopy involves recording a two-dimensional electron diffraction pattern at every probe position as a focused electron probe is scanned across the specimen in an STEM. The probe typically has a convergence angle in the range 0.5-5 mrad usch that the recorded diffraction patterns comprise separated small discs where the Bragg condition is satisfied, as shown in Figure 1.11. This is in contrast to related 4D-STEM experiments in which large convergence angles are used to obtain overlapping discs suitable for analyses such as ptychographic reconstruction [134, 135]. SED data analysis varies considerably depending on whether the contrast within diffraction discs is considered, i.e. the patterns are analysed as convergent beam electron diffraction (CBED) patterns, or else the pattern of discs is considered, i.e. the patterns are analysed as spot patterns. CBED analysis enables higher order Laue zone (HOLZ) lines to be tracked [136–144] to map small strains and rotations at high precision ($\sim 10^{-4}$), with sensitivity to all 9 components of the deformation gradient tensor [145]. Dynamical contrast within discs may also be used to map polar domain structures [146, 147]. Such analysis is however limited to rather perfect specimens by the high sensitivity of CBED contrast. For example, HOLZ lines are often only visible away from major zone axes, in moderately thick specimens, with little lattice distortion [148]. More general progress has been made based on spot pattern analysis.

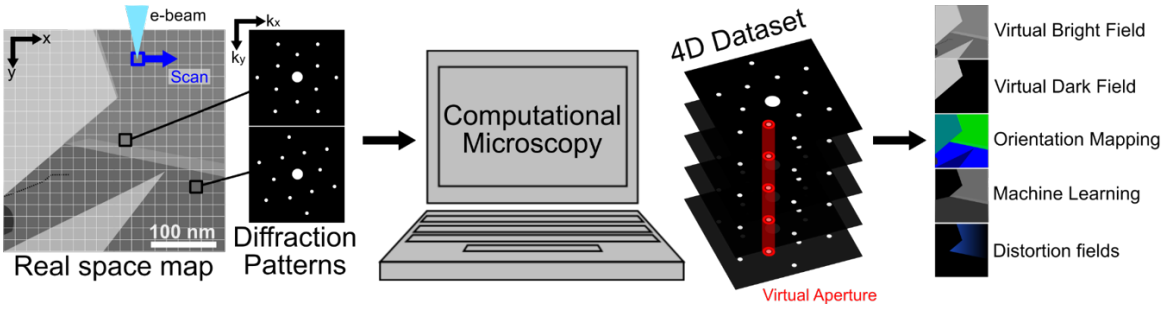

Fig. 1.11 **Scanning Electron Diffraction.** Two-dimensional electron diffraction patterns are recorded at each probe position in a two-dimensional scan to obtain a four-dimensional (4D-SED) dataset that may be analysed computationally in various ways.

Analysis of SED data as a series of spot diffraction patterns is based on associating diffraction disc positions with reciprocal lattice vectors to determine lattice orientation [149, 150] and strain [27]. SED data for such analysis is typically recorded with a convergence angle in the range 0.5-1.5 mrad leading to diffraction limited probe sizes in the range $1.5 - 5$ nm. Orientation mapping based on such data has been achieved by indexation of individual scattering vectors [149] as well as by pattern matching based on comparing each measured diffraction pattern with a library of pre-calculated templates [150]. Both of these methods are based primarily on the diffraction geometry, i.e. they do not consider the diffracted intensity fully, giving an angular precision of $\sim 1^\circ$ [151]. The method also struggles near to zone axes where data is recorded from a single Laue zone and, for example, patterns rotated 180° about the beam direction are geometrically identical. Strain mapping has been achieved by mapping variation in the scattering (reciprocal lattice) vectors to obtain 3 components of strain perpendicular to the beam direction and 1 component of rotation about the beam direction [152–159]. This approach has been enhanced by the use of dynamical double-conical-rocking illumination to achieve a precision of $\sim 10^{-4}$ and with a spatial resolution of 2 nm [27, 160–163]. Three-dimensional reconstruction, based on SED microscopy, has been performed only for grain-wise orientation mapping based essentially on diffraction contrast tomography [164, 165]. These spot pattern methods are the basis of work presented in this thesis and are explained and developed in greater detail in Chapters 4 & 5.

1.5 Summary & Motivation

Nanostructure characterisation is limited both by the lack of a pragmatic general framework for structure description and the need to develop versatile structurally sensitive characterisation techniques that achieve nanoscale spatial resolution. Perhaps the most tractable challenge

is to map crystal phase, orientation and strain fields and a number of scanning diffraction microscopy techniques have been developed using X-rays and electrons to achieve these goals. These techniques differ in terms of the sensitivity and resolution that they achieve, as well as the means by which three-dimensional reconstruction is achieved, as summarized in Table 1.2. SED microscopy offers the highest spatial resolution of these techniques but the least sensitive measurements, although the sensitivity is sufficient to be useful. Three-dimensional reconstruction differs significantly between scanning microscopies owing to instrumental constraints and SED tomography seems set to be based on tomographic reconstruction [166] from numerous two-dimensional measurements made in projection as has been the case for annular dark-field STEM imaging [167] and analytical electron spectroscopies [168, 169]. SED tomography has only been achieved grain-wise based essentially on diffraction contrast tomography [164, 165] and developing the method to reconstruct continuous changes is a particular challenge (see Chapter 5). Further development of two-dimensional SED microscopy, particularly as regards establishing robust analysis routines and workflows is also required in order to establish it as an applicable technique in materials science.

Table 1.2 **Comparison of diffraction mapping techniques.** Comparison of XRD [22, 23], EBSD [24], TKD [25, 26] and SPED [27] based on spatial resolution, d, strain precision, $\Delta\varepsilon$, number of strain and orientation components measured, **#F**, orientation precision, $\Delta\omega$, typical region of interest size, ROI, and method for three-dimensional reconstruction.

	d (nm)	$\Delta\varepsilon$	**#F**	$\Delta\omega$ (°)	ROI (μm)	3D
XRD	20-500	10^{-4} - 10^{-5}	9	0.01	2000×2000	differential aperture
EBSD	20-100	10^{-4}	8	0.01 - 1	10×10	slice & view
TKD	10-50	-	-	1	2×2	-
SED	1-10	10^{-3} - 10^{-4}	4	1	2×2	diffraction contrast

Research presented in this thesis develops and applies SED microscopy for practical elucidation of nanostructure. The technique has been progressed by: establishing a method for aligning a double-conical-rocking electron probe that enables routine scanning precession electron diffraction with nanometre resolution (Chapter 3); developing a robust code framework for reproducible analysis of SED data (Chapter 4); and taking steps towards nanoscale strain tomography (Chapter 5). SED microscopy was also applied to prototypical materials characterisation challenges, namely: identification of orientation relationships in a nickel based super alloy (Chapter 6); grain and multi-layer mapping in graphene (Chapter 7), and characterisation of semi-crystalline polyethylene nanostructure (Chapter 8). This work establishes the broad applicability of SED microscopy across materials science as well as looking towards less ordered and more sensitive systems than previously addressed.

Chapter 2

Scanning Electron Diffraction Theory

Scanning (precession) electron diffraction (S(P)ED) microscopy involves the acquisition of a two-dimensional electron diffraction pattern at every probe position, as a focused electron probe is scanned across the specimen, as shown in Figure 2.1. To glean insight from such 4D-S(P)ED data, both via analysis of the diffraction patterns and through *post-facto* image formation, it is necessary to develop a theoretical understanding of electron diffraction (see Section 2.1), the focused probe conditions used to obtain electron diffraction from nanoscale volumes (see Section 2.2), and diffraction contrast imaging (see Section 2.3). This treatment shows how 4D-S(P)ED data can be interpreted, at least to a reasonable first approximation, by analogy to more conventional electron microscopy.

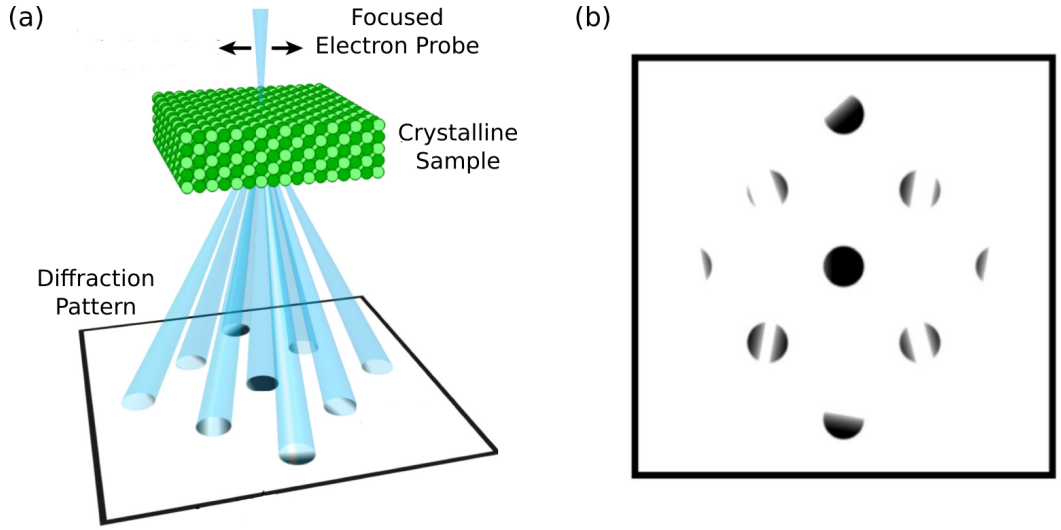

Fig. 2.1 **Electron diffraction of a focused electron probe.** (a) Diffraction of a focused electron probe, which may be scanned across the specimen. (b) Illustrative example of a focused probe electron diffraction pattern. Adapted from [10].

Electrons may be scattered elastically, without energy transfer or inelastically with energy transfer. There may be coherent contributions to the total wave function, preserving the phase relationship between scattered and unscattered waves, as well as incoherent contributions where the phase relationship is lost. Electron diffraction is modelled as coherent elastic scattering in Sections 2.1.1-2.1.5 and inelastic scattering is considered only briefly in Section 2.1.6. Numerous texts [11, 170–172, 13, 173, 12, 174, 15, 175] provide more comprehensive coverage and the treatment presented follows particularly those by Zuo [11], Kirkland [170], and Humphreys [176].

2.1 Electron Diffraction Theory

Coherent elastic scattering of fast electrons, may be treated as the scattering of electrons by the static crystal Coulomb potential, $V(\mathbf{r})$, and relativistic effects may be adequately accounted for by correction to the electron mass, i.e. $m = m_0(1-\frac{v^2}{c^2})^{1/2}$, where v is the electron velocity, m_0 is the rest mass, and c is the speed of light [176]. The electron wavefunction, $\psi(\mathbf{r})$, is then the the solution of the time-independent Schrödinger equation:

$$\nabla^2\psi(\mathbf{r}) + 4\pi[k^2 + U(\mathbf{r})]\psi(\mathbf{r}) = 0 \tag{2.1}$$

where $k^2 = \frac{2mE}{h^2}$, $U(\mathbf{r}) = \frac{2meV(\mathbf{r})}{h^2}$, E is the electron accelerating potential, $e = |e|$, and $V(\mathbf{r})$ is the electrostatic scattering potential. Rigorous solutions only exist for well defined specimen geometries (see Section 2.1.5) and various approximate solutions are thus essential to interpret electron diffraction from general three-dimensional potentials [11].

2.1.1 First-Order Born Approximation

The Schrödinger equation (Equation 2.1) may be transformed [11, 12], for scattering of an incident plane wave, $\psi_0 = \exp(2\pi i\mathbf{k}_0 \cdot \mathbf{r})$, into the integral form:

$$\psi(\mathbf{r}) = \exp(2\pi i\mathbf{k}_0 \cdot \mathbf{r}) + \pi \int \frac{\exp(2\pi ik|\mathbf{r}-\mathbf{r}'|)}{|\mathbf{r}-\mathbf{r}'|} U(\mathbf{r}')\psi(\mathbf{r}')d^3\mathbf{r}' \tag{2.2}$$

where the first term represents the incident plane wave and the integral represents the scattering of the wave by the potential $U(\mathbf{r}')$. In the first-order Born approximation, the scattering is assumed to be weak so that the wave function inside the integral is approximately equal to the incident wave, i.e. $\psi(\mathbf{r}') = \exp(2\pi i\mathbf{k}_0 \cdot \mathbf{r})$. This implies that only direct scattering from the incident wave contributes to the scattered wave, which is the kinematical, or single scattering, approximation.

Within the first-order Born approximation and assuming (see Figure 2.2) the point of observation, $\mathbf{r}$, is distant with respect to the dimensions of the scattering potential, i.e. $|r| \gg |r'|$, the total wave function is the sum of the incident wave and the scattered wave:

$$\psi(\mathbf{r}) \approx \exp(2\pi i \mathbf{k}_0 \cdot \mathbf{r}) + \phi(\mathbf{k}') \frac{\exp(2\pi i \mathbf{k} \cdot \mathbf{r})}{|\mathbf{r}|} \tag{2.3}$$

where $\mathbf{k}' = \mathbf{k} - \mathbf{k}_0$, and;

$$\phi(\mathbf{k}') = \frac{2\pi me}{h^2} \int_{-\infty}^{\infty} V(\mathbf{r}') \exp(2\pi i \mathbf{k} \cdot \mathbf{r}') d^3\mathbf{r}' \tag{2.4}$$

where $\phi(\mathbf{k}')$ is the probability amplitude for electron scattering from the potential, $V(\mathbf{r}')$. The integral in Equation 2.4 is the Fourier transform of the Coulomb potential, $V(\mathbf{r}')$, which is thus proportional to the scattered wave amplitude. Similar equations may be obtained for X-ray and neutron diffraction, making the Fourier transform the unifying concept in diffraction theory [174]. The intensity measured in diffraction experiments, $I(\mathbf{k}') = |\phi(\mathbf{k}')|^2$.

2.1.2 Electron Atomic Scattering Factor

The scattering amplitude from an atom, within the first-order Born approximation, i.e. the *atomic scattering factor*, $f(\mathbf{k}')$, can be found by substituting the electrostatic potential of the atom, $\mathbf{V}^a(\mathbf{r}')$, into Equation 2.4. This potential may be related to the charge density of the atom through Poisson's equation [176] to obtain the Mott-Bethe formula relating the electron atomic scattering factor, $f(\mathbf{k}')$, to the X-ray atomic scattering factor, $f^X(\mathbf{k}')$, as:

$$\begin{aligned} f(\mathbf{k}') &= \frac{2\pi me^2}{h^2 k'^2} \int_{-\infty}^{\infty} \left[Z\delta(\mathbf{r}') - \rho_e(\mathbf{r}') \right] \exp(2\pi i \mathbf{k}' \cdot \mathbf{r}') d^3\mathbf{r}' \\ &= \frac{2\pi me^2}{h^2 k'^2} \left[Z - f^X(\mathbf{k}') \right] \end{aligned} \tag{2.5}$$

where $\rho_n(\mathbf{r}') = Z\delta(\mathbf{r})$ is the nuclear charge density, $\rho_e(\mathbf{r}')$ is the electron charge density, Z is the atomic number, and the X-ray atomic scattering factor, $f^X(\mathbf{k}')$, has been identified as the Fourier transform of the electron charge density.

The atomic scattering factor is parameterized, e.g. due to Doyle and Turner [177]. Typical values for electrons are 1-10 Å as compared with equivalent quantities of $\sim 10^{-4}$ Å for neutrons and X-rays [176], i.e. electron scattering is much stronger. The electron and X-ray atomic scattering factors decrease with angle due to phase differences between waves scattered from different parts of the atom, as shown in Figure 2.2.

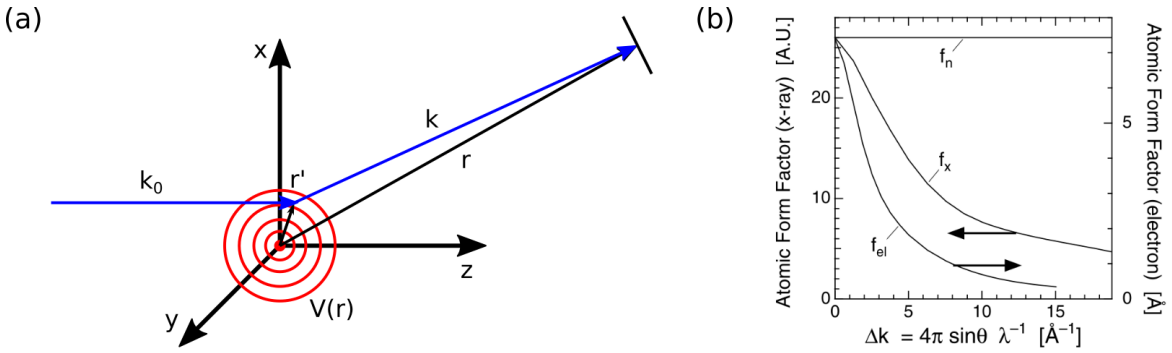

Fig. 2.2 **Electron scattering from a potential** (a) Electron scattering geometry and coordinate system. Adapted from [11]. (b) Comparison of atomic scattering amplitudes for X-rays, neutrons and electrons. Reproduced from [12].

2.1.3 Kinematical Electron Diffraction

Kinematical electron diffraction can be developed in terms of Fourier transforms, following Equation 2.4 and the treatment presented by Zuo [11]. The potential, $V(\mathbf{r})$, of an arbitrary arrangement of atoms may be written, dropping primes on position vectors, as a convolution between atomic potentials, $V^a(\mathbf{r})$, and delta functions describing their positions:

$$V(\mathbf{r}) = \sum_i V_i^a(\mathbf{r}) * \sum_j \delta(\mathbf{r} - \mathbf{R}_{i,j}) \tag{2.6}$$

where $\mathbf{R}_{i,j}$ is the atomic position, and the subscripts i and j denote atomic species and all positions of a given species, respectively.

The scattered wave amplitude for scattering vector $\mathbf{k'} = \mathbf{k} - \mathbf{k}_0$ is found by taking the Fourier transform of this potential, as:

$$\phi(\mathbf{k}') = \sum_i f_i(\mathbf{k}') \sum_j \exp(-2\pi i \mathbf{k}' \cdot \mathbf{R}_{i,j}) \tag{2.7}$$

which is the sum of atomic scattering factors, $f_i(\mathbf{k}')$, with a phase factor due to position.

Diffraction from perfect crystals

Atoms in crystalline materials are located at positions that may be expressed in terms of a lattice vector, $\mathbf{r}_{lat}$, and a position vector, $\mathbf{r}_{i,j}$, within the unit cell:

$$\mathbf{R}_{i,j} = u\mathbf{a} + v\mathbf{b} + w\mathbf{c} + \mathbf{r}_{i,j} = \mathbf{r}_{lat} + \mathbf{r}_{i,j} \tag{2.8}$$

where $\mathbf{a}$, $\mathbf{b}$ and $\mathbf{c}$ are lattice basis vectors in direct space.

The potential of a crystal, $V^c(\mathbf{r})$ may then be expressed:

$$V^c(\mathbf{r}) = \sum_i V_i^a(\mathbf{r}) * \sum_j \delta(\mathbf{r} - \mathbf{r}_{i,j}) * \sum_{u,v,w} \delta(\mathbf{r} - u\mathbf{a} - v\mathbf{b} - w\mathbf{c}) \tag{2.9}$$

where the first convolution defines the potential within the unit cell and the second convolution describes the periodic repetition of the unit cell over a lattice.

The scattered wave amplitude from a perfect crystal, $\phi^c(\mathbf{k}')$, is then given by:

$$\phi^c(\mathbf{k}') = \left[\sum_i f_i(\mathbf{k}') \sum_j \exp(-2\pi i \mathbf{k}' \cdot \mathbf{r}_{i,j})\right] \cdot \left[\sum_{h,k,l} \delta(\mathbf{k}' - h\mathbf{a}^* - k\mathbf{b}^* - l\mathbf{c}^*)\right] \tag{2.10}$$

which could have been obtained by substituting Equation 1.8 into Equation 1.7. The first term is a summation of atomic scattering over the unit cell, which is the *structure factor*,

$$F(\mathbf{k}') = \sum_i f_i(\mathbf{k}') \sum_j \exp(-2\pi i \mathbf{k}' \cdot \mathbf{r}_{i,j}) \tag{2.11}$$

that determines the kinematical intensity of the diffracted beam. The second term is the Fourier transform of the lattice, which is the reciprocal lattice, and defines the geometry of diffraction according to the Laue diffraction condition:

$$\mathbf{k}' = \mathbf{g} = h\mathbf{a}^* + k\mathbf{b}^* + l\mathbf{c}^* \tag{2.12}$$

where $\mathbf{a}^*$, $\mathbf{b}^*$ and $\mathbf{c}^*$ are lattice basis vectors in reciprocal space.

Diffraction from nanocrystals

The potential of a nanocrystal may be expressed as the product of the potential of an infinite crystal, $V^c(\mathbf{r})$ and a shape function, $s(\mathbf{r})$, i.e. $V(\mathbf{r}) = s(\mathbf{r}) \cdot V^c(\mathbf{r})$. The total scattered wave amplitude from the truncated nanocrystal, $\phi^{nc}(\mathbf{k}')$, is therefore the convolution of the Fourier transformed shape function and the scattered wave amplitude of the perfect crystal, i.e. $\phi^{nc}(\mathbf{k}') = FT[s(\mathbf{r})] * \phi^c(\mathbf{k}')$. The implication is that the scattered wave amplitude is peaked near to the Laue condition but there is appreciable scattered amplitude away from the exact Laue condition. To explore this, it can be convenient to express $\mathbf{k}'$ as,

$$\mathbf{k}' = \mathbf{g} + \mathbf{s}_g \tag{2.13}$$

where $\mathbf{g}$ is a reciprocal lattice vector and $\mathbf{s}_g$ is the excitation error describing the deviation of the scattering vector from the Laue condition.

The scattered wave amplitude from a finite nanocrystal, near to a particular Laue condition, $\phi_g^{nc}(\mathbf{k}')$, can then be written similarly to Equation 2.10 but with a finite sum, as:

$$\begin{aligned}\phi_g^{nc}(\mathbf{k}') &= F(\mathbf{k}') \cdot FT\left[\sum_{u,v,w}^{N} \delta(\mathbf{r}-\mathbf{r}_{lat})\right] \\ &= \sum_i f_i(\mathbf{g}+\mathbf{s}_g)\sum_j \exp(-2\pi i(\mathbf{g}+\mathbf{s}_g)\cdot\mathbf{r}_{i,j})\sum_{u,v,w}^{N}\exp(-2\pi i(\mathbf{g}+\mathbf{s}_g)\cdot\mathbf{r}_{lat})\end{aligned} \tag{2.14}$$

which can be simplified by noting that $|\mathbf{s}_g| \ll |\mathbf{g}|$ such that the $\mathbf{s}_g \cdot \mathbf{r}_{i,j}$ term may be neglected, and that $\mathbf{g}\cdot\mathbf{r}_{lat} = integer$, to give:

$$\phi_g^{nc}(\mathbf{k}') = \sum_i f_i(\mathbf{g})\sum_j \exp(-2\pi i\mathbf{g}\cdot\mathbf{r}_{i,j})\sum_{u,v,w}^{N}\exp(-2\pi i\mathbf{s}_g\cdot\mathbf{r}_{lat}) \tag{2.15}$$

i.e. $\phi_g^{nc} = F(\mathbf{g})\cdot S(\mathbf{s}_g)$, where $F(\mathbf{g})$ is the structure factor at the Laue condition and $S(\mathbf{s}_g)$ is the shape factor, which depends only on s_g and is related to the Fourier transform of the nanocrystal shape function.

Diffraction from distorted crystals

Atoms in distorted crystals are displaced from their ideal atomic sites by a vector, $\mathbf{u}(\mathbf{r}_{lat})$, that depends on which unit cell the atom is located within, i.e.,

$$\mathbf{R}_{i,j} = \mathbf{r}_{lat} + \mathbf{r}_{i,j} + \mathbf{u}(\mathbf{r}_{lat}) \tag{2.16}$$

The scattered wave amplitude from a distorted crystal of finite dimensions, near to a particular Laue condition, $\phi_g(\mathbf{k}')$, may be expressed, following similar manipulations as in Equations 1.14 an 1.15 and neglecting the $\mathbf{s}_g\cdot\mathbf{u}(\mathbf{r}_{lat})$ term, as:

$$\begin{aligned}\phi_g(\mathbf{k}') &= F(\mathbf{k}')\cdot FT\left[\sum_{u,v,w}^{N}\delta(\mathbf{r}-\mathbf{r}_{lat}-\mathbf{u}(\mathbf{r}_{lat}))\right] \\ &= F(\mathbf{g})\sum_{u,v,w}^{N}\exp(-2\pi i\mathbf{s}_g\cdot\mathbf{r}_{lat})\exp(-2\pi i\mathbf{g}\cdot\mathbf{u}(\mathbf{r}_{lat}))\end{aligned} \tag{2.17}$$

Atomic displacements thus introduce an additional *geometric phase* term, $\alpha = -2\pi\mathbf{g}\cdot\mathbf{u}$, to the scattered wave amplitude if $\mathbf{g}\cdot\mathbf{u} \neq 0$, i.e. if the displacement is not parallel to $\mathbf{g}$. This also implies the displacement field leads to diffuse scattering away from the Laue condition.

2.1.4 Diffraction Geometry

Diffraction from a crystal is geometrically described by the Laue condition (Equation 2.12), which may be visualized in the Ewald sphere construction, as shown in Figure 2.3. The Ewald sphere construction is made in reciprocal space with the incident wavevector, $\mathbf{k}_0$, drawn towards the origin of a reciprocal lattice representing the crystal. The start point of the incident wavevector defines the centre of the sphere, which has a radius equal to $|\mathbf{k}_0|$, so that the surface of the sphere represents all possible elastically scattered wavevectors, $\mathbf{k}$. When the surface of the sphere intercepts a reciprocal lattice point, the Laue condition is met.

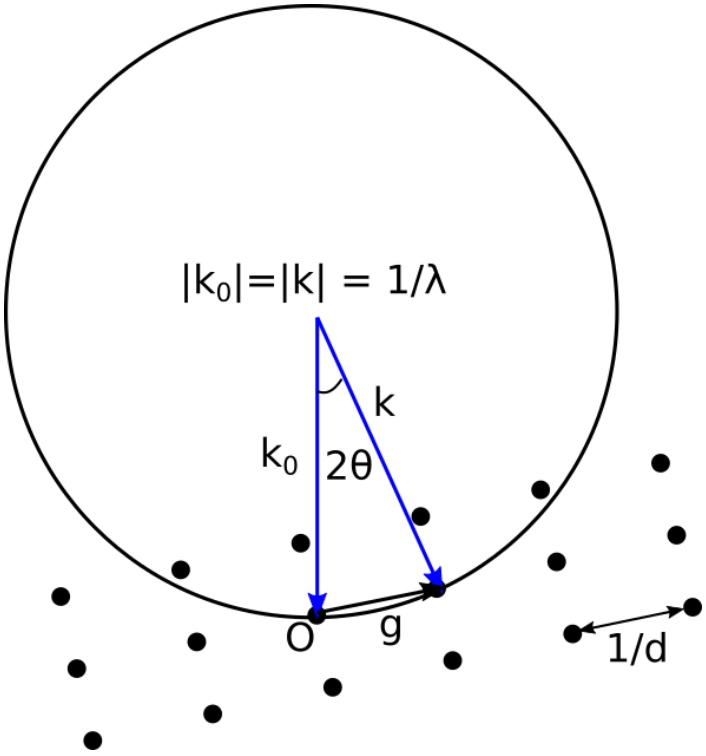

Fig. 2.3 **The Ewald sphere construction.** Geometric construction of diffraction from a perfect crystal, showing the equivalence of the Laue condition and Bragg's law.

Noting that $|\mathbf{k}_0| = \frac{1}{\lambda}$ and $|\mathbf{g}_{hkl}| = \frac{1}{d_{hkl}}$, where d_{hkl} is the interplanar spacing in real space, trigonometry yields the equivalence between the Laue condition and Bragg's law:

$$\lambda = 2d_{hkl}\sin(\theta) \tag{2.18}$$

where θ is the scattering angle. The essential physical insight of Bragg's approach is that a scattered wave corresponds to scattering from particular atomic planes the normal of which is represented by the $\mathbf{g}$ vector in reciprocal space.

In electron diffraction, $|\mathbf{k}_0| \gg |\mathbf{g}|$ and the intersection between the Ewald sphere and the reciprocal lattice approaches a plane for paraxial scattering. Further, thin (< 200 nm) specimens required for electron transmission, allow significant deviation parameters, $\mathbf{s}_g$, as shown in Figure 2.4. A zone-axis diffraction pattern is obtained with the incident wave vector normal to a dense plane of reciprocal lattice points. The central part of the zone-axis pattern samples diffraction conditions perpendicular to the incident beam direction, known as the zero-order Laue zone (ZOLZ), and diffraction conditions related by passing through the origin, i.e. $\pm\mathbf{g}$, have equal deviation parameters. At higher scattering angles, the Ewald sphere intercepts the layer of diffraction conditions in the reciprocal lattice planes above the ZOLZ, which leads to rings of reflections associated with each higher-order Laue zone (HOLZ). When the incident wavevector is not in a zone-axis direction, the intersection between the Ewald sphere and the lattice leads to Laue circles with a point on the circumference of the zeroth order circle passing through the origin.

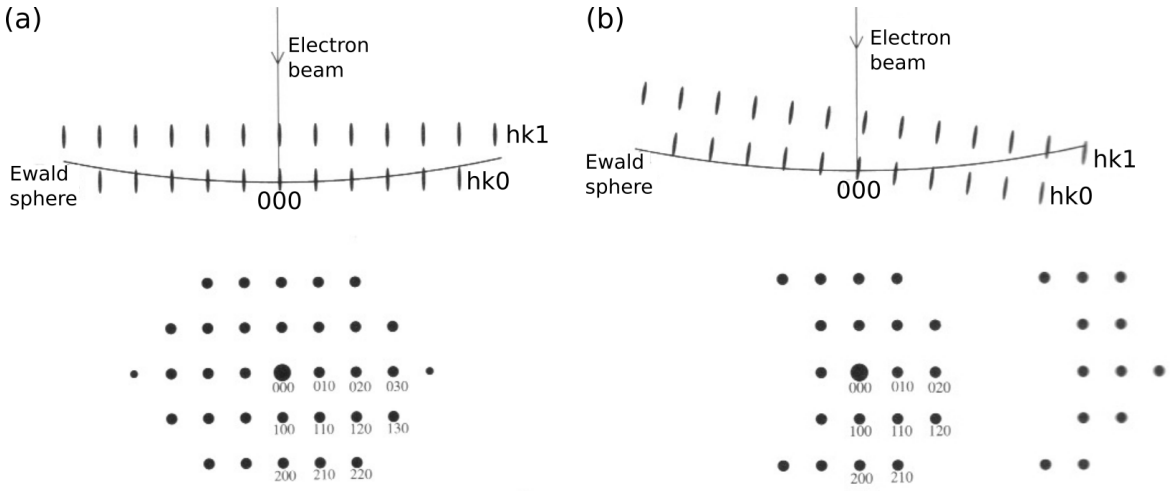

Fig. 2.4 **Ewald sphere construction for electron diffraction.** (a) In zone-axis geometry with $\pm\mathbf{g}$ equally excited. (b) Away from zone-axis with strong diffraction on Laue circles.

Planar detectors are typically used to record electron diffraction patterns and the measured scattering vector coordinates on the detector should be related back to three-dimensional coordinates, accounting for the Ewald sphere geometry as,

$$\mathbf{k}' = \left(k_{dx}, k_{dy}, \frac{1}{2|\mathbf{k}_0|}(k_{dx}^2 + k_{dy}^2) \right) \tag{2.19}$$

where k_{dx} and k_{dy} are coordinates in the detector plane, perpendicular to $\mathbf{k}_0$. Since $|\mathbf{k}_0| \gg |\mathbf{k}'|$ in the paraxial geometry typical of electron diffraction, this correction is small.

2.1.5 Dynamical Electron Diffraction

Electrons typically undergo multiple scattering due to the strength of the Coulomb interaction between incident electrons and the electrostatic potential of the specimen [176]. An approach beyond the first-order Born approximation is thus needed to develop a dynamical electron diffraction theory incorporating multiple scattering [170]. Analytical and numerical solutions may be obtained using the wave mechanical Bloch wave method, which is rigorous and the expressions obtained provide valuable insight into the scattering process [11]. However, this approach is limited to quite ideal systems. More general numerical solutions are possible using the multislice method to obtain a finite difference solution.

The Schrödinger equation (Equation 2.1) may be rewritten (see Kirkland [170]), for fast electrons, by assuming the wave function may be represented as a modulated plane wave,

$$\psi(\mathbf{r}) = \varphi(\mathbf{r})\exp(2\pi i\mathbf{k}\cdot\mathbf{r}) \tag{2.20}$$

travelling predominantly in the z direction such that $\frac{\partial^2\psi(\mathbf{r})}{\partial z^2} \ll k\frac{\partial\psi(\mathbf{r})}{\partial z}$ and the second derivative with respect to z may be neglected to give:

$$\nabla^2_{x,y}\varphi(\mathbf{r}) + 4\pi\left[ik\frac{\partial}{\partial z} + U(\mathbf{r})\right]\varphi(\mathbf{r}) = 0 \tag{2.21}$$

This forward scattering approximation is also known as the paraxial approximation or the high-energy approximation and will be the starting point for solutions developed here.

The Bloch Wave Method

The Bloch wave method [178] solves the Schrödinger equation (i.e. Equation 2.1 or 2.21) in a periodic potential, such as a crystal with translational symmetry. A periodic potential may be expanded as a Fourier series,

$$U(\mathbf{r}) = \sum_g U_g \exp(2\pi i\mathbf{g}\cdot\mathbf{r}) \tag{2.22}$$

where the spatial frequencies, $\mathbf{g}$, correspond to reciprocal lattice vectors of the crystal. Bloch wave solutions are then sought with the same periodicity,

$$\varphi(\mathbf{r}) = \sum_g \varphi_g(z)\exp(2\pi i\mathbf{g}\cdot\mathbf{r}) \tag{2.23}$$

where the Fourier coefficients, φ_g, vary in z because the scattered amplitude changes as the electrons propagate through the specimen.

Substituting Equations 2.22 and 2.23 into Equation 2.1 or 2.21 and equating coefficients yields Bloch wave solutions in the general case or the forward scattering approximation respectively. Here, the latter case (see Kirkland [170]) is considered, which yields:

$$\frac{\partial \varphi_g(z)}{\partial z} = 2\pi i \mathbf{s}_g \varphi_g(z) + i\pi \sum_{g'} U_{g'} \varphi_{g'}(z) \tag{2.24}$$

which is a set of coupled first order linear differential equations known as the Howie-Whelan equations. The number of Bloch wave solutions is equal to the number of Fourier coefficients included in the expansion of the potential and the wave function inside the potential is the linear superposition of these Bloch waves. Coefficients in this superposition are determined by boundary conditions and this is typically only possible for simple geometries, for example a parallel sided specimen with electrons incident normal to the surface [11]. Analytical solutions may be obtained for a small number of coefficients (i.e. 2 or 3) whereas many beam solutions require computational methods.

Distorted crystals may be considered similarly, by expressing the potential of the distorted crystal in the deformable ion approximation:

$$U(\mathbf{r}) = \sum_g U_g \exp(2\pi i \mathbf{g}\cdot\mathbf{r}) \exp(2\pi i \mathbf{g}\cdot\mathbf{u}) \tag{2.25}$$

where U_g are Fourier coefficients of the crystal potential. Substituting Equations 2.25 and 2.23 into Equation 2.21, within the forward scattering approximation, yields the Howie-Basinski equations (see Zuo [11]), which become Howie-Whelan equations for a defective crystal if the displacement field varies only in z and the column approximation (see Section 2.3.1) holds.

$$\frac{\partial \varphi_g(z)}{\partial z} = 2\pi i \mathbf{s}_g^u \varphi_g(z) + \frac{i\pi}{(\mathbf{g}+\mathbf{s}_g)_z} \sum_{g'} U_{g'} \varphi_{g'}(z) \tag{2.26}$$

where,

$$\mathbf{s}_g^u = \mathbf{s}_g + \mathbf{g}\cdot\frac{\partial \mathbf{u}(\mathbf{r})}{\partial z} \tag{2.27}$$

and thus it is the derivative of the displacement field not parallel to $\mathbf{g}$ that produces contrast. This is similar to the insight obtained within the kinematical framework via Equation 2.17.

The Multislice Method

The multislice method is to solve the Schrödinger equation by numerical integration and was first developed from a physical optics perspective by Cowley and Moodie [179]. Here, the multislice method is framed, following Kirkland [170], as a finite difference solution to Equation 2.21, which may be written as a first order differential equation in z:

$$\frac{\partial \psi(\mathbf{r})}{\partial z} = \left[\frac{i}{4\pi k}\nabla_{x,y}^2 + iU(\mathbf{r})\right]\psi(\mathbf{r}) \tag{2.28}$$

Numerical solution of such a differential equation, given an initial value, is typically based on Taylor expansion of the dependent variable in powers of Δz, i.e.,

$$\psi(x,y,z+\Delta z) = \psi(\mathbf{r}) + \Delta z\frac{\partial \psi(\mathbf{r})}{\partial z} + \mathscr{O}(\Delta z^2) \tag{2.29}$$

Substituting Equation 2.28 into Equation 2.29 and identifying the lowest order terms of the Taylor expansion of an exponential within the resulting expression yields,

$$\begin{aligned}\psi(x,y,z+\Delta z) &= \left[1+\Delta z\left[\frac{i}{4\pi k}\nabla_{x,y}^2 + iU(\mathbf{r})\right]\right]\psi(\mathbf{r}) + \mathscr{O}(\Delta z^2)\\ &= \exp\left[\frac{i\Delta z}{4\pi k}\nabla_{x,y}^2 + i\Delta z U(\mathbf{r})\right]\psi(\mathbf{r}) + \mathscr{O}(\Delta z^2)\\ &= \exp\left(\frac{i\Delta z}{4\pi k}\nabla_{x,y}^2\right)\exp\left(i\Delta z U(\mathbf{r})\right)\psi(\mathbf{r}) + \mathscr{O}(\Delta z^2)\end{aligned} \tag{2.30}$$

With some manipulations (see Kirkland [170]), and dropping terms of order Δz^2, this equation may be rewritten as a product between a transmission function, $t(x,y,z)$, and the wave function convolved with a propagator function, $p(x,y,\Delta z)$, as:

$$\psi(x,y,z+\Delta z) = p(x,y,\Delta z) * [t(x,y,z)\psi(x,y,z)] \tag{2.31}$$

where the propagator function, $p(x,y,\Delta z) = \exp\left(\frac{i\Delta z}{4\pi k}\nabla_{x,y}^2\right)$, may be identified as describing Fresnel propagation over a distance Δz and the transmission function may be interpreted as the phase grating due to the projected potential in the interval between z and $z+\Delta z$,

$$t(x,y,z) = \exp\left[i\int_z^{z+\Delta z} U(\mathbf{r})dz'\right] \tag{2.32}$$

which approximates the object as a quasi-two-dimensional phase object that introduces a position dependent phase change in the electron wave function exiting the object. The application of this transmission function to an incident electron wave function can be seen

as a near-field kinematical scattering solution, which can be propagated to the far-field diffraction pattern and in the paraxial approximation this is equivalent to the first-order Born approximation [11]. The separation of near-field and far-field solutions is very helpful for image simulation [173] and it is the near field solution that is needed at intermediate steps in the finite difference solution for multiple scattering.

The electron wave function at depth z inside the specimen may be calculated by repeated evaluation of Equation 2.31 beginning with an incident wave function. This requires dividing the specimen into thin slices of thickness Δz, each with a transmission function and a propagation function. Efficient computation is achieved by making much use of the fast Fourier transform (FFT) so that transmission and propagation may be achieved as multiplications in real and reciprocal space with FFT and inverse FFT transformations between, i.e.:

$$\psi_{n+1}(x,y) = FT^{-1}\{P_n(k_x,k_y,\Delta z_n)FT[t_n(x,y)\psi_n(x,y)]\} \tag{2.33}$$

where $P_n = FT[p(x,y,\Delta z)]$. This multislice solution is formally equivalent to solution of the Howie-Whelan equations in the limit where Δz goes to zero [170]. Since each slice is independent, the transmission function may vary from one slice to the next and simulations may thus be performed for non-periodic potentials.

2.1.6 Inelastic Electron Scattering

Inelastic scattering involves transfer of energy between the incident electrons and the specimen. Contributions to inelastic scattering are predominantly due to core electron excitation, plasmons and phonons. These inelastic effects may be introduced into the theory developed above through an imaginary contribution to the interaction potential [11],

$$U(\mathbf{r}) = U^c(\mathbf{r}) + iU'(\mathbf{r}) \tag{2.34}$$

where $U(\mathbf{r})$ is the total optical potential, $U^c(\mathbf{r})$ is the real crystal potential, and $U'(\mathbf{r})$ is a potential accounting for the depletion of the elastic wave due to inelastic scattering. This depletion is often referred to as "absorption". Calculation of the appropriate absorption coefficients including all scattering contributions is challenging and often, as here, inelastic contributions are neglected. Experimentally, it may be possible to reduce inelastic contributions by energy filtering [180]. Further, energy transfer during inelastic scattering enables electron energy loss spectroscopy [181] and plays a significant role in beam damage under electron irradiation [182–185].

2.2 Electron Diffraction of Focused Probes

S(P)ED experiments are typically performed using a focused probe to obtain spatial resolution by illuminating a small volume at each probe position. In the "critical illumination" condition [13], shown in Figure 2.5a, the electron source is imaged onto the specimen plane by the probe forming lenses and the illumination aperture, which is usually circular, subtends an angle, α, at the specimen. The convergence semi-angle, α, defines a range of incidence angles for each of which an Ewald sphere may be drawn representing the section of scattering power distribution sampled, as shown in Figure 2.5b. The illumination aperture is imaged onto the diffraction plane as a circular disc within which the intensity distribution is a two-dimensional rocking curve over the range of incidence angles, as in Figure 2.5c.

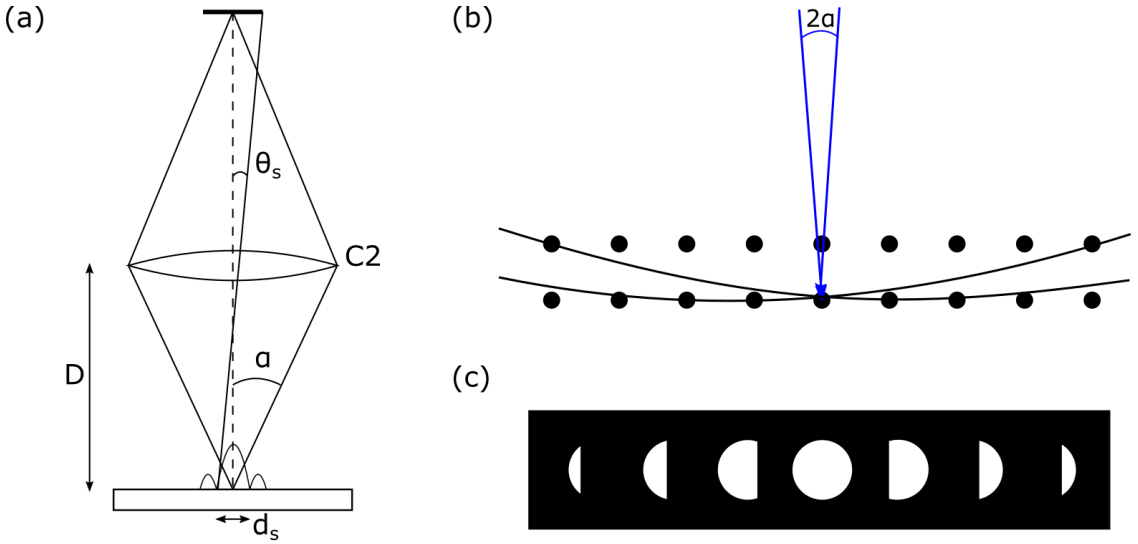

Fig. 2.5 **Convergent beam electron diffraction.** (a) *Critical illumination* the source is imaged in the specimen plane and the illumination aperture subtends an angle, α to the optic axis. Adapted from [13]. (b) Ewald sphere geometry for convergent beam illumination with a range of incidence angles. (c) Schematic CBED pattern for condition in (b).

S(P)ED experiments are typically performed with convergence angles of 1-3 mrad such that the diffraction discs of different orders do not overlap. This is in contrast to so-called 4D-STEM experiments in which the different orders must overlap to enable phase contrast atomic resolution imaging [173]. If SED is performed with a convergence angle of 2-3 mrad the intensity distribution within diffraction discs may be analysed e.g. using HOLZ lines to map strain [140], or using the symmetry of dynamical intensity distribution to map polar domains [146, 147]. In this work, the analysis is primarily based on the geometry of diffraction patterns and imaging using diffracted intensities using data acquired in nanobeam (see Section 2.2.1) and precession (see Section 2.2.2) electron diffraction modes.

2.2.1 Nanobeam Electron Diffraction

Nanobeam electron diffraction (NBED) is typically performed with a ~ 1 mrad convergence angle, using a small diameter (e.g. $d_a = 10\ \mu$m) illumination aperture. Coherent illumination is obtained [13] if the *transverse coherence length* of the electron beam, $X_a = \frac{D\lambda}{\pi d_s}$, see Figure 2.5a, is larger than the diameter of the aperture, i.e. $X_a > d_a$. This is typically the case when a field-emission gun and a small illumination aperture are used. Under coherent conditions and assuming a point source, the probe wave function may be written [175]:

$$\begin{aligned}\psi_p(\mathbf{r}) &= \int_{-\infty}^{\infty} A(\mathbf{k}_t)\exp(i\chi(\mathbf{k}_t))\exp(2\pi i\mathbf{k}_t\cdot\mathbf{r})d\mathbf{k}_t \\ &= FT\Big[A(\mathbf{k}_t)\exp(i\chi(\mathbf{k}_t))\Big]\end{aligned} \tag{2.35}$$

where $A(\mathbf{k}_t)$ describes the illumination aperture as a Heaviside function $\Theta(|\mathbf{k}_t| - \alpha|\mathbf{k}_0|)$, which is 1 for $|\mathbf{k}_t| < \alpha|\mathbf{k}_0|$ and 0 for $|\mathbf{k}_t| > \alpha|\mathbf{k}_0|$; $\chi(\mathbf{k}_t)$ is the wave aberration function of the probe forming lenses (see Chapter 3) and $\mathbf{k}_t$ is the component of $\mathbf{k}_0$ perpendicular to the optic axis. In NBED the use of a small illumination aperture gives $\chi(\mathbf{k}_t) \sim 0$ and the probe function is the Fourier transform of the Heaviside function, which is the Airy function [175].

The electron wave function exiting the specimen may be written in the weak phase object approximation (see Equations 2.28-2.30), for a probe focused at position, $\mathbf{r}_p$, as:

$$\begin{aligned}\psi_e(\mathbf{r}) &= \psi_p(\mathbf{r}-\mathbf{r}_p)\exp(i\overline{U}(\mathbf{r})) \\ &\approx \psi_p(\mathbf{r}-\mathbf{r}_p)\Big[1+i\overline{U}(\mathbf{r})\Big]\end{aligned} \tag{2.36}$$

where $\overline{U}(\mathbf{r})$ is the projected potential in the beam direction. The diffracted wave amplitude is the Fourier transform of the exit wave and the diffracted intensity is therefore:

$$I(\mathbf{k}',\mathbf{r}_p) = \left|FT\Big[\psi_p(\mathbf{r}-\mathbf{r}_p)\exp(2\pi i\mathbf{k}'\cdot\mathbf{r}_p)\Big] * FT\Big[1+i\overline{U}(\mathbf{r})\Big]\right|^2 \tag{2.37}$$

which is a convolution between the Fourier transform of the projected potential, which describes kinematical scattering (including the shape factor and elastic diffuse scattering) and the aperture function. To incorporate the effects of multiple scattering Equation 2.35 may be used as the initial value for a multislice simulation (see Section 2.1.5) or incorporated into the Bloch wave formalism [186]. If the crystal is perfect, all points within the diffraction disc are independent but elastic diffuse scattering from nearby source wave vectors will interfere coherently within the diffraction disc.

2.2.2 Precession Electron Diffraction

Precession electron diffraction (PED) patterns are recorded using a double conical beam rocking geometry in which the electron probe is rocked through a hollow cone at an angle, ρ, to the optic axis above the specimen and de-rocked below the specimen to obtain a static diffraction pattern, as shown in Figure 2.6. The PED patterns obtained by rocking a convergent probe comprise diffraction discs of integrated intensity, which have proven more amenable to structure solution and refinement using both kinematical and dynamical models [187]. More reflections are typically recorded in PED patterns than the corresponding static beam diffraction patterns due to the large range of reciprocal space integration, which may yield more patterns that contain sufficient data to be indexed in automated orientation mapping [188]. Further, the homogeneous intensity distribution within diffraction discs may facilitate disc position determination and improve the precision of strain mapping [162, 189].

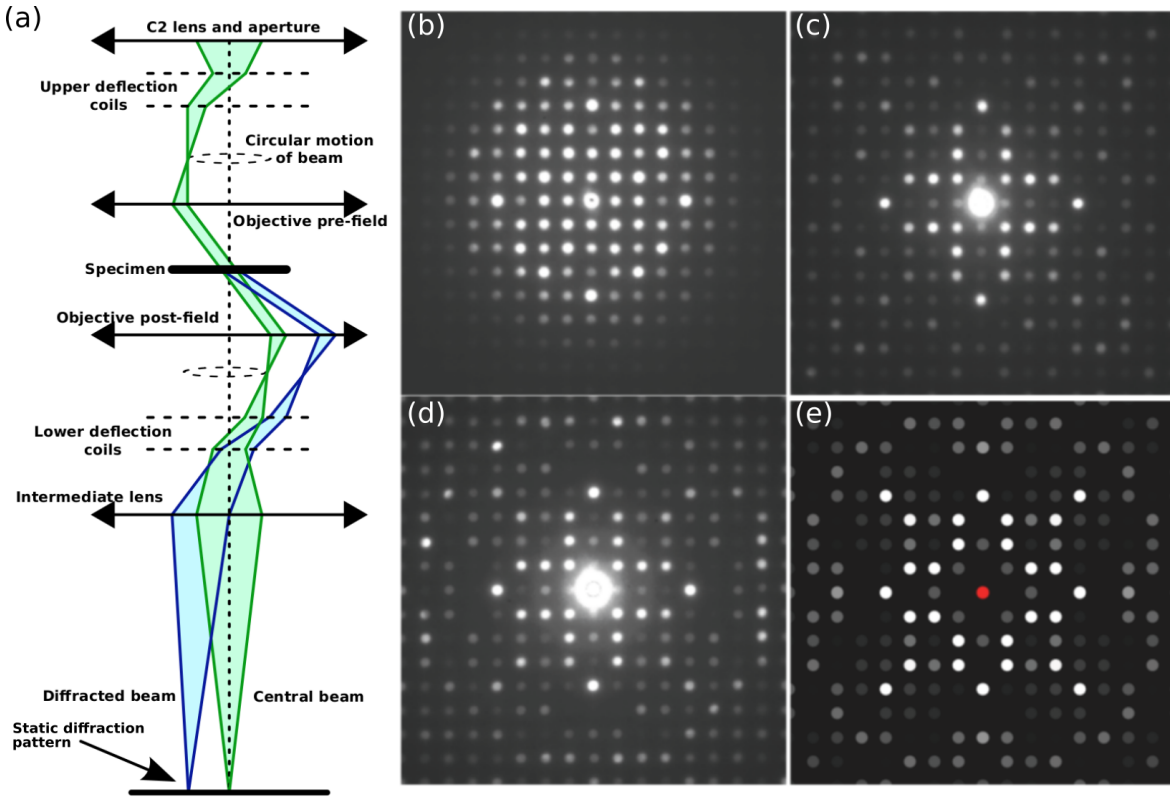

Fig. 2.6 **Precession electron diffraction (PED).** (a) Schematic ray diagram for PED illustrating rocking and de-rocking of the electron beam before and after the specimen. (b-e) Representative diffraction patterns from the [001] zone-axis of $Er_2Ge_2O_7$ (b) without precession, (c) with 20 mrad precession, (d) with 47 mrad precession, (e) simulated in the kinematical framework. Reproduced from [14].

Integration of intensity, $I^p(\mathbf{k}')$ in PED occurs on the detector and is therefore, for plane wave illumination, an incoherent azimuthal integration at the precession angle, ρ, i.e.

$$I^p(\mathbf{k}') \propto \int_0^{2\pi} I(\mathbf{k}')d\rho \tag{2.38}$$

where $I(\mathbf{k}')$ is an expression for the diffracted intensity obtained within one of the theoretical frameworks described in Section 2.1.

PED may yield diffraction patterns with zone-axis geometry but with the beam having been rocked around that zone-axis to record many diffraction discs integrated twice through the Bragg condition [18], as shown in Figure 2.6 for example. In this zone-axis geometry, the integration of Equation 2.37 may be written as an integration over the deviation parameter, s_g, for convergent probe [190], as:

$$\int_0^{2\pi} I_g(s_g)ds_g \propto \left[1 - \left(\frac{g}{2R_0}\right)^2\right] I_g^{prec.} \tag{2.39}$$

where g is the magnitude of the reciprocal lattice vector and R_0 is the radius of the zero-order Laue circle (see Section 2.1.4). The integration over deviation parameters makes the zone axis PED pattern less sensitive to small orientation changes and non-systematic dynamical effects are reduced because the beam is never parallel to the zone axis [18]. PED patterns are "more-kinematical" insofar as the integrated intensities are less sensitive to the phase terms in structure factors [191] and the relative ranking of intensities remains fairly constant and consistent with the kinematic ranking [192, 193]. This leads to visual similarity between PED patterns and kinematical simulations, as in Figure 2.6. However, individual intensities deviate significantly from kinematical values [193] and dynamical simulations are required to obtain a good fit, for example in structure refinement [187, 194]. Nevertheless, PED patterns are considered practically advantageous for structure refinement because the intensities are less sensitive to thickness variations and small misorientations [187].

In crystallographic mapping, zone-axis PED patterns are typically recorded for strain mapping [27, 162] whereas mapping polycrystalline materials typically yields many off-axis diffraction patterns [195]. In strain mapping, precession may improve the precision of measurements by yielding patterns that appear closer to zone axis and with homogeneously filled diffraction discs that are more amenable to automated tracking [162, 189]. In orientation mapping, typically based on template matching with kinematical simulations [150], precession may improve the correlation between simulations and measurements because recording more reflections are typically recorded which reduces the impact of some indexation ambiguities [196]. Precession may therefore improve the accuracy of orientation mapping experiments but the integration through orientations places a limit on precision.

2.3 Diffraction Contrast Imaging Theory

Imaging based on S(P)ED data is most simply performed by plotting the integrated intensity within a subset of pixels in the detector, positioned in the back focal plane, as a function of probe position. This is similar to STEM imaging [175, 173] except that the whole two-dimensional pattern is recorded and the integration window is selected *post-facto*. The image intensity in the pixel corresponding to the probe at position, $\mathbf{r}_p$, may be written:

$$I(\mathbf{r}_p) = \int D(\mathbf{k}')I(\mathbf{k}', \mathbf{r}_p)d\mathbf{k}' \tag{2.40}$$

where $D(\mathbf{k}')$ is a function describing the integration window in the diffraction plane and detector sensitivity, and $I(\mathbf{k}', \mathbf{r}_p)$ is the diffracted intensity as a function of scattering vector, $\mathbf{k}'$ for the probe positioned at $\mathbf{r}_p$, which is given by Equation 2.37 & 2.38 for SED and SPED experiments, respectively, within the kinematical approximation.

Simulating S(P)ED diffraction contrast microscopy images by evaluating Equation 2.40, does not generally yield convenient analytical forms, and it is often necessary to simulate a two-dimensional electron diffraction pattern for every probe position followed by numerical integration over $D(\mathbf{k}')$. However, if the integration is complete over a particular Bragg diffraction disc, and the convergence angle is small (i.e. ~ 1 mrad), an analogy can be made with diffraction contrast imaging in conventional TEM (CTEM), as illustrated in Figure 2.7. In this case, contrast may be interpreted, to a reasonable first approximation, based on modulation of the intensity of the diffracted beam, I_g, evaluated under plane wave illumination conditions. When SPED is performed, the integration over illumination conditions must be considered, which generally reduces the contrast due to structural distortions [197].

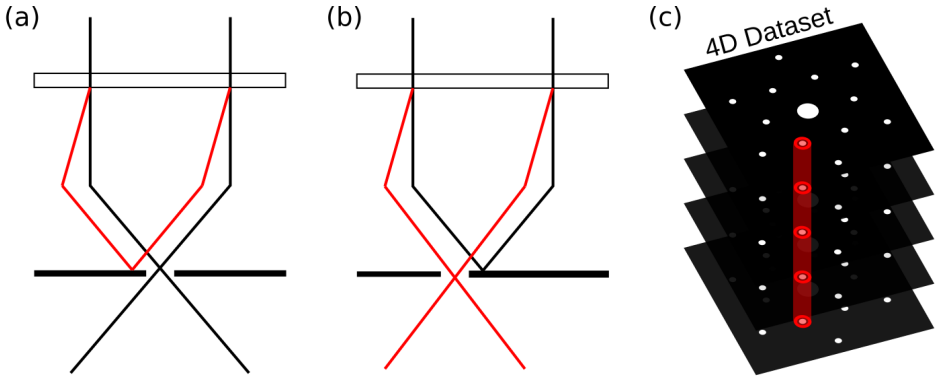

Fig. 2.7 **Diffraction contrast imaging in CTEM and SED.** (a,b) In CTEM (a) the direct beam or (b) a diffracted beam is selected using an aperture to form a bright-field or dark-field image. (c) In SED, diffraction contrast images are formed by integrating *post-facto* within a window (virtual aperture) in the diffraction pattern as a function of probe position.

2.3.1 The Column Approximation

An extensive theory for diffraction contrast imaging of defects has been established [15] for conventional TEM imaging based on the *column approximation* in which the specimen is considered as comprising numerous narrow columns, with their length parallel to the diffracting planes, such that any displacement field varies only along the column length, i.e. $\mathbf{u}(z)$. The column approximation is reasonable if columns may be chosen to be sufficiently narrow that any change in displacement across the column is negligible but also sufficiently wide so that an electron entering the column is not scattered out of the column whilst passing through the specimen. Considering the geometry of a column along a diffracted beam shown in Figure 2.8 with a specimen of thickness $t = 200$ nm, an electron wavelength $\lambda = 2$ pm and an interplanar spacing $d = 2$Å the width of a column is ~ 2 nm. This is similar to, or smaller than, the step size used in typical S(P)ED experiments and in this context it may be assumed that each pixel in the S(P)ED microscopy image corresponds to a probe positioned in a separate column.

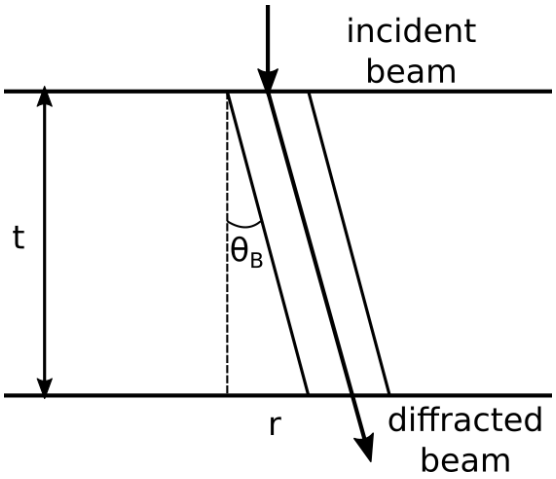

Fig. 2.8 **The column approximation.** Geometrical parameters for a column along a diffracted beam. Adapted from [15].

Within the column approximation and in the kinematical framework the amplitude of a diffracted beam ϕ_g can be related to a displacement field $\mathbf{u}(\mathbf{r})$, by:

$$\phi_g = \frac{i\pi}{\xi_g} \int_0^t e^{-2\pi i \mathbf{g}\cdot\mathbf{u}} e^{-2\pi i s_g z} dz \tag{2.41}$$

where $\mathbf{g}$ is the diffracted beam used for imaging, ξ_g is the extinction length, s_g is the component of the excitation error in the z-direction, and z is the position along the incident beam direction. This equation may be considered as an integral form of Equation 2.17 or as the single scattering form of Equation 2.26.

2.4 Modelling S(P)ED Data

Theory of electron diffraction has been set out here in the context of understanding S(P)ED experiments and as a platform for interpreting S(P)ED data. S(P)ED is modelled as the coherent elastic scattering of a focused probe (Section 2.2) located at numerous positions, which may be simulated within the single-scattering kinematical framework (Section 2.1.3) or in the multiple-scattering dynamical framework (Section 2.1.5). Key features of electron diffraction patterns were highlighted by this theoretical treatment, primarily within the kinematical framework, and include: (1) diffraction from (defective) crystals is strong near to Laue conditions defined by the average reciprocal lattice, (2) the shape of reflections is determined by the shape of the object, atomic displacements and the illumination condition, and (3) the intensity scattered to a given wave vector is modulated by displacement fields and further by multiple scattering effects.

Various elements of the theory presented here are drawn upon in subsequent chapters. In Chapter 4, dynamical multislice simulations (Section 2.1.5) of SPED experiments, with precession modelled by integrating simulations for numerous tilted illuminations, are used to validate the application of unsupervised machine learning approaches to S(P)ED data. Further, simple kinematical simulations and the geometry of electron diffraction are used as a basis for orientation and strain mapping. In Chapter 5, the theoretical considerations set out here form the basis of a discussion regarding possible strain tomography. Finally, in Chapters 7 and 8 kinematical simulations and the column approximation are used to interpret SED microscopy images.

Chapter 3

Scanning (Precession) Electron Diffraction

The modern (scanning) transmission electron microscope ((S)TEM) is a versatile instrument capable of acquiring numerous signals spanning dimensions of real space, reciprocal space, energy, and time [93, 7]. Acquisition of data across these dimensions, as illustrated in Figure 3.1a, defines a paradigm of multi-dimensional electron microscopy of which scanning (precession) electron diffraction (S(P)ED) is a part [93, 7]. S(P)ED involves scanning a convergent, nanobeam or double-rocking probe across the specimen and acquiring a two-dimensional electron diffraction pattern at each position. Here, the focus is on optimizing S(P)ED experiments based on an understanding of the hardware involved.

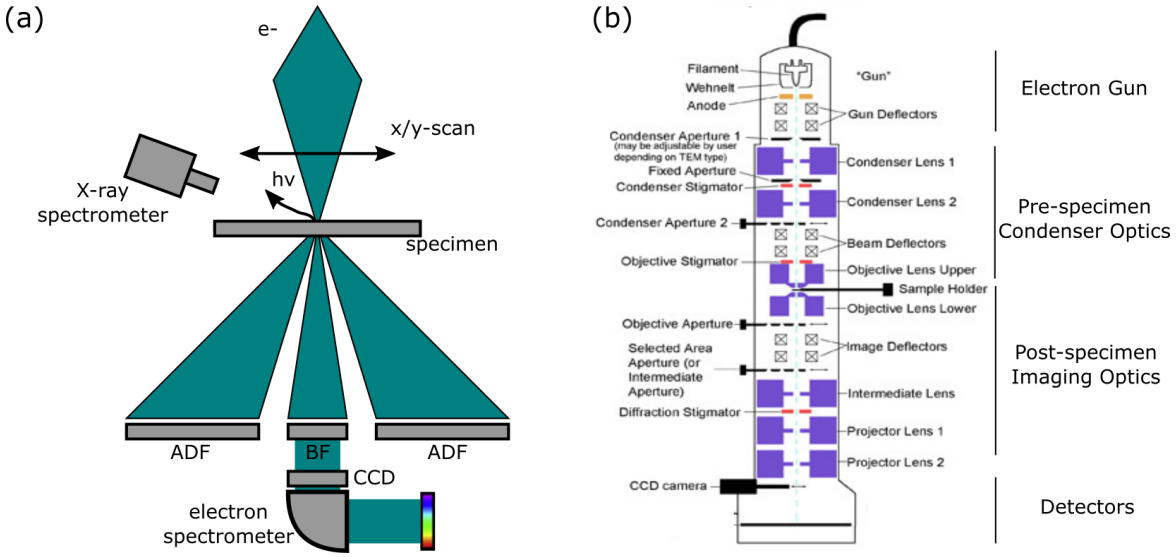

Fig. 3.1 **The (scanning) transmission electron microscope.** (a) A tool for acquiring numerous analytical signals. (b) Outlined as an electron optical system. Adapted from [16]

A typical (S)TEM comprises various lenses, apertures, deflectors and detectors in a complex electron optical arrangement that is typically considered in the following parts: the gun, the pre-specimen condenser lens system, the post-specimen image lens system and the detectors, as illustrated in Figure 3.1b. The gun controls the extraction of electrons from a source and determines brightness and coherence of the probe [11, 198]. Most modern (S)TEMs are fitted with a field emission gun (FEG) comprising a sharp W tip acting as a cathode above two metal plates acting as anodes [11]. The first anode extracts electrons from the tip and the second accelerates the electrons to the desired energy. The electric field of the anodes acts as an electrostatic lens, producing the first cross-over of the optical system. The condenser lens system is responsible for probe formation and controls the range of electron incidence angles (i.e. the convergence angle) and the probe size in the specimen plane. The deflectors responsible for scanning the electron probe across the specimen and rocking the beam away from the optic axis are also located within the condenser system, between the condenser lenses and the specimen. Aligning the probe-forming lens system optimally is the most important practical element of performing S(P)ED experiments and is considered in detail in Sections 3.2 & 3.3. Post-specimen optics collect the scattered electrons and, when configured for a S(P)ED acquisition, focus the diffraction pattern on to the electron detector. Deflectors are also situated in the post-specimen optics to direct the diffraction pattern onto the detector. Alignment of the post-specimen optics is important to avoid distortions to the recorded diffraction pattern and the performance of the electron detector affects the analysis that can be achieved, as discussed in Section 3.4. The particular system used in this work is described in Section 3.5 and prospects for further improvement of the S(P)ED method are set out in Section 3.6.

3.1 Electron Optics

Electrons are lensed and deflected in the (S)TEM using magnetic fields produced using electromagnets [171]. A charged electron moving with velocity, $\mathbf{v}$, in a magnetic field, $\mathbf{B}$, experiences a Lorentz force, $\mathbf{F} = -e\mathbf{v} \times \mathbf{B}$, and the strength of the magnetic field produced by an electromagnet depends on the current flow through the electromagnetic coil [171]. This electrical control of the electron optics is central to the operation of modern digitally controlled electron microscopes, enabling numerous optical alignments to be obtained [171]. In such instruments the electromagnetic coils are typically actuated via reference voltages fed to pre-amplifiers and current amplifiers [171]. Key properties are discussed below.

3.1.1 Electron Deflection

Electrons are deflected in the (S)TEM using electromagnetic dipoles [17, 11]. These deflector coils are extended over a large arc (saddle yoke configuration) [11] producing a homogeneous magnetic field between them, as illustrated in Figure 3.2a. A pair of such deflector coils can be used both to shift the electron beam along an axis in the specimen plane and to tilt the beam with respect to the optic axis, as shown in Figure 3.2b,c. The component of tilt/shift imparted by a pair of deflector coils depends on the ratio of currents through the coils, which controls the pivot point. These ratios are adjusted in standard alignment procedures to achieve pure tilt or shift as required. Introducing a second pair of deflector coils, typically orthogonal to the first pair, enables arbitrary beam tilt and shift in two dimensions.

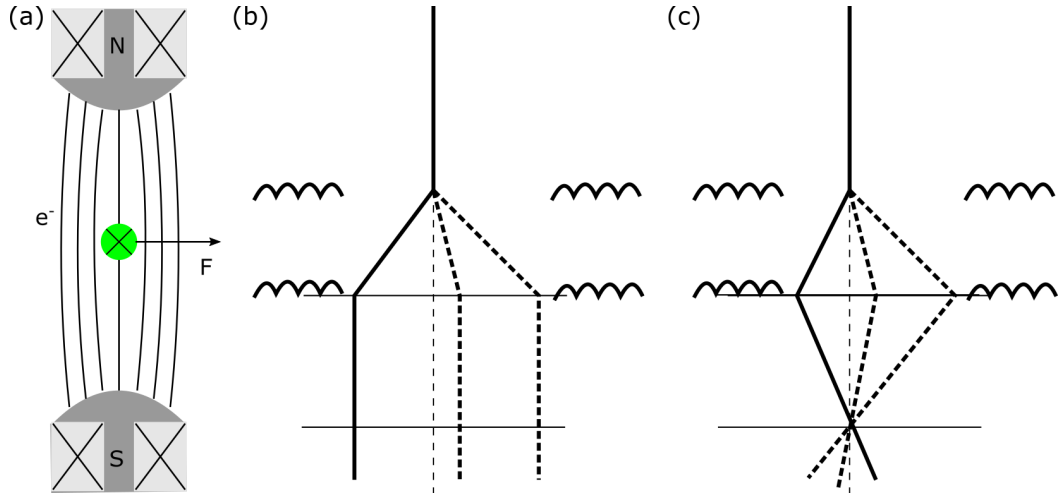

Fig. 3.2 **Electron deflection by a dipole.** (a) Electromagnetic dipole and corresponding field lines resulting in a force on an electron beam travelling into the page. Adapted from [17]. (b, c) Ray diagrams showing the action of a pair of deflector coils used to produce (b) shift and (c) tilt of the beam depending on the ratio of deflection magnitudes in the dipole pair.

S(P)ED experiments involve scanning the electron beam across the specimen and, when a dynamic double-rocking probe geometry is used in SPED, rocking the beam around a cone. This is achieved by driving the deflector coils with a scan generator, as shown in Figure 3.3. The scan of the beam across the specimen is achieved using two saw-tooth signals for the x/y-scan respectively [11]. Double-rocking is achieved by driving the pre- and post-specimen deflector coils synchronously using an oscillating sine wave [11, 18, 199]. Ensuring that accurate shift and tilt is achieved is therefore very important for these experiments. Both scanning and dynamic rocking of the electron beam require the deflector coils to be driven at high-frequency so that data may be acquired in a reasonable time. This directs attention towards the high-frequency performance of the deflector coils.

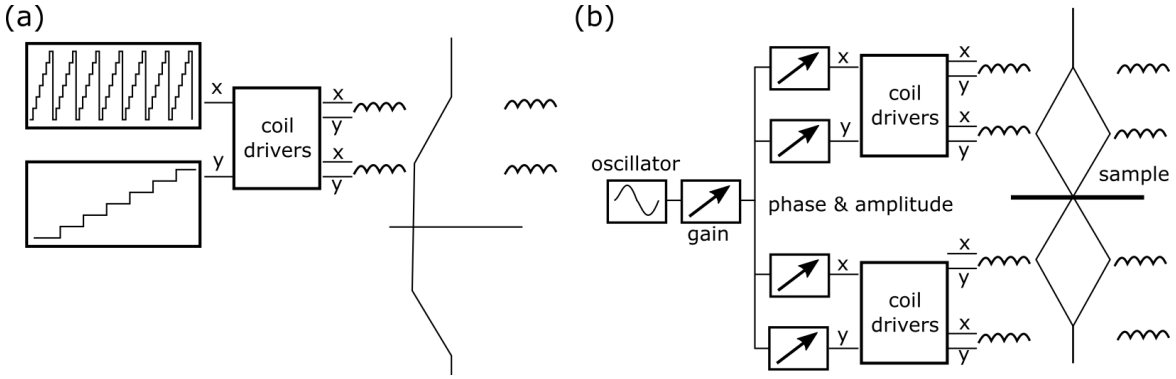

Fig. 3.3 **Block diagram of deflector coil electronics.** (a) A single frame raster scan using a digital saw-tooth waveform to drive the x (fast) and y (slow) scan. The flyback time corresponds to the drop time. Adapted from [11]. (b) The conical double-rocking system for coils above and below the specimen. Adapted from [18].

Deflector Response Frequency

The most demanding high-frequency electron deflection arises in SPED experiments when the probe is setup in a dynamic double-rocking geometry as well as being scanned across the specimen. In early implementations of the double-rocking optical alignment, the frequency was capped at 30-35 Hz [18] due to deflector bandwidth limitations. Frequencies of ~ 100 Hz are now typical and contemporary hardware is capable of reaching 1 kHz [200]. At such high frequencies there is a phase lag between the voltage applied to actuate the deflector and the current flowing, which controls the deflection. This is because each deflector coil acts as an inductor, L_{coil}, with internal resistance, R_{coil}, connected in series with a foot resistor, R_{foot}, and therefore acts as an LCR circuit, with a phase lag of:

$$\arctan\left(\frac{\omega L_{coil}}{(R_{coil}+R_{foot})}\right) \tag{3.1}$$

This assumes that there is negligible stray capacitance and for very high double-rocking and scan speeds, e.g. kHz, the stray capacitance would need to be accounted for. Practically this phase lag has two effects. Firstly, the double-rocking angle becomes frequency dependent so alignment must be performed at the same frequency as the experiment. Secondly, the deflector coils are all independent and their phase lags cause discrepancies that must be corrected during alignment. Accounting for these factors are significant advantages of the double-rocking probe alignment procedures set out in Section 3.3.

3.1.2 Electron Lenses

Electron lenses are round (cylindrically symmetrical) magnetic lenses, which act to cause electrons at an angle to the optic axis to spiral around the optic axis, as shown in Figure 3.4a. This focusing effect arises due to variation of the radial component of the magnetic field, **B**, which rises and falls in the direction parallel to the optic axis. The spiral trajectory further means that the electron lens will invert and rotate the object in addition to magnifying it. An ideal round lens would cause a ray passing through it to be deviated by an angle proportional to its distance to the optic axis (Figure 3.4b). However, in a round magnetic lens high-angle rays are focused too strongly [17] and the requirement for Laplace's equation to be obeyed means that aberrations will be significant [17].

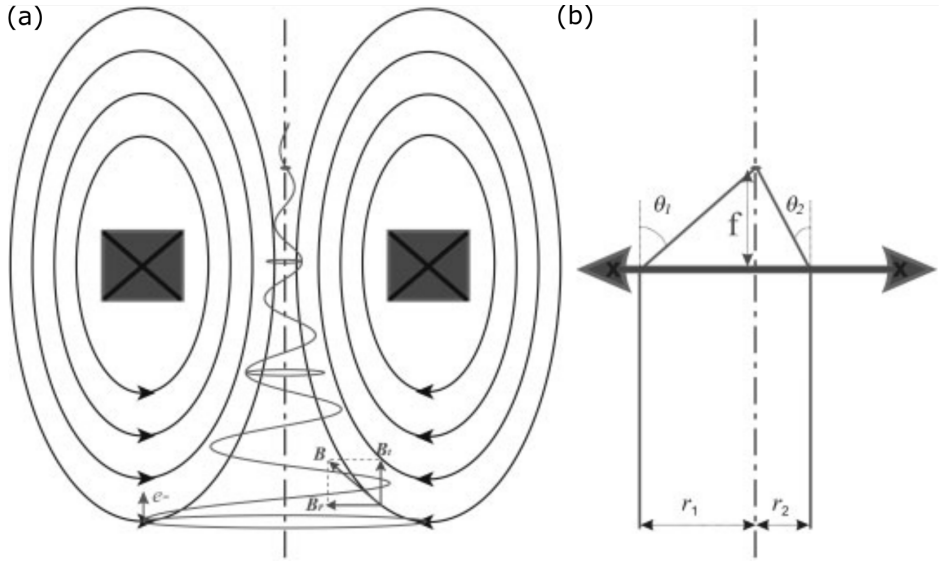

Fig. 3.4 **Electron lensing.** (a) Trajectory through a round magnetic lens and corresponding **B**-field lines. Variation of the radial component, $\mathbf{B}_r$, causes focusing. (b) Geometric ray diagram for an ideal electromagnetic lens that deviates rays by an angle θ_i proportional to their distance to the optic axis r_i. Reproduced from Brydson *et al.* [17].

Correction of lens aberrations up to angles of ~ 50 mrad from the optic axis [201, 202], has now been achieved by incorporating non-round (e.g. quadrapoles, hexapoles) magnetic lens elements [203, 204]. However, such aberration correction is often not implemented in instruments with which S(P)ED currently performed. SED is a STEM experiment performed with a small convergence angle where the effects of aberrations are least significant but when SPED is performed with an electron probe rocked to high angles, the effects of lens aberrations are significant. Although aberration corrected PED has been discussed and demonstrated [199, 205] this has not yet been translated into practical solutions for high-resolution SPED. Detailed consideration of lens aberrations therefore remains important.

Lens Aberrations

An ideal lens would take a plane wave of wavevector, **k**, and produce a spherical wave coming to a point focus in the Gaussian image plane of the lens. Geometric aberrations distort the wavefront but retain coherence and are considered here, neglecting chromatic aberrations [17, 11]. The wave aberration function, $\chi(\mathbf{k}) = \frac{2\pi}{\lambda} W(\mathbf{k})$, is defined as the phase difference between the ideal spherical wavefront and the actual wavefront. This phase difference is the error in the wavefront measured as a distance, $W(\mathbf{k})$, multiplied by $\frac{2\pi}{\lambda}$, where λ is the electron wavelength. It is useful to note that a ray passing through a point in the lens, **k**, passes through a point in the conjugate Gaussian imaging plane, **r**, according to:

$$\mathbf{r} \propto \nabla W(\mathbf{k}) \tag{3.2}$$

That is to say that the Gaussian image plane coordinates are gradient mappings, with respect to k, of the aberration function [17], as shown in Figure 3.5.

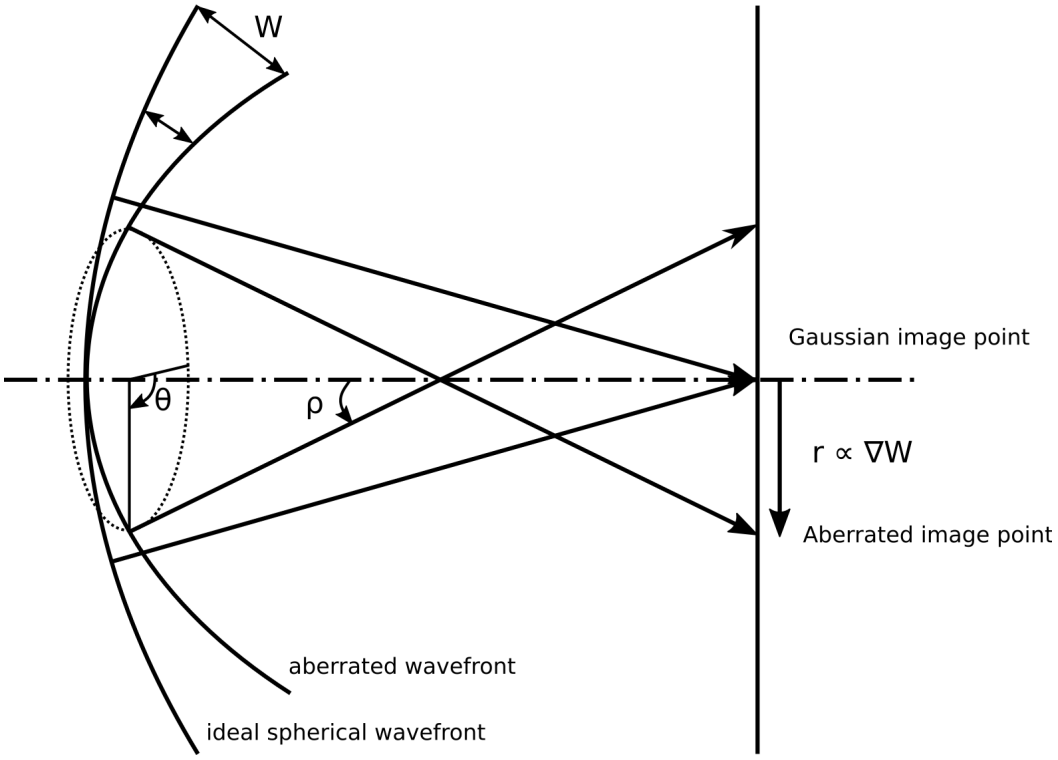

Fig. 3.5 **Wave aberration and ray aberration.** The wave aberration W measures the distance by which an aberrated wavefront deviates from the ideal spherical case. The corresponding phase difference is called the aberration function, χ. The shift of the Gaussian image point due to the aberrations is called the ray aberration. The ray aberration r is proportional to the gradient of the wave aberration W. Reproduced from Brydson *et al.* [17].

The two-dimensional surface describing the aberration function is typically expressed as a function of angle to the optic axis, ρ, and the azimuthal angle around the optic axis, θ, and may be expanded to third order as[1]:

$$\begin{aligned}\chi(\rho,\theta) = const. &+ \rho(C_{01a}\cos(\theta) + C_{01b}\sin(\theta)) \\ &+ \frac{\rho^2}{2}(C_{10} + C_{12a}\cos(2\theta) + C_{12b}\sin(2\theta)) \\ &+ \frac{\rho^3}{3}(C_{23a}\cos(3\theta) + C_{23b}\sin(3\theta) + C_{21a}\cos(\theta) + C_{21b}\sin(\theta)) \\ &+ \frac{\rho^4}{4}(C_{30} + C_{34a}\cos(4\theta) + C_{34b}\sin(4\theta) + C_{32a}\cos(2\theta) + C_{32b}\sin(2\theta))\end{aligned} \tag{3.3}$$

where the numerical coefficients, C_{ij} are the aberration coeeficients in the Krivanek convention [204]. The index, i, denotes the radial, ρ, dependence of the induced phase shift and is referred to as the order of the aberration. The index, j, denotes the symmetry of the azimuthal, θ, dependence. The effect of each contribution to the aberration function is perhaps most easily visualized by considering the distortions they introduce to an ideal spherical wavefront, as shown in Figure 3.6. It is also convenient to name the aberrations for discussion, as set out in Table 3.1.

Table 3.1 **Naming of the most important aberration coefficients.**

	Name
C_{10}	Defocus
C_{12}	Two-fold Astigmatism
C_{21}	Coma
C_{23}	Three-fold Astigmatism
C_{30}	Spherical Aberration

Routine alignment of a "non-corrected" (S)TEM includes correction of two-fold astigmatism, using a weak quadrupole magnetic field, and minimization of coma by aligning the beam tilt through the lens. The aberration function is then dominated by defocus and spherical aberration and may be approximated as:

$$\chi(\rho,\theta) = \frac{\rho^2}{2}C_{10} + \frac{\rho^4}{4}C_{30} \tag{3.4}$$

which implies only radial variation to this first approximation. The effect of rocking the beam in a lens with such an aberration function is now considered.

[1]This angular description is related to the plane wave vector, $\mathbf{k} = \frac{1}{\lambda}(\rho\cos(\theta) + \rho\sin(\theta))$

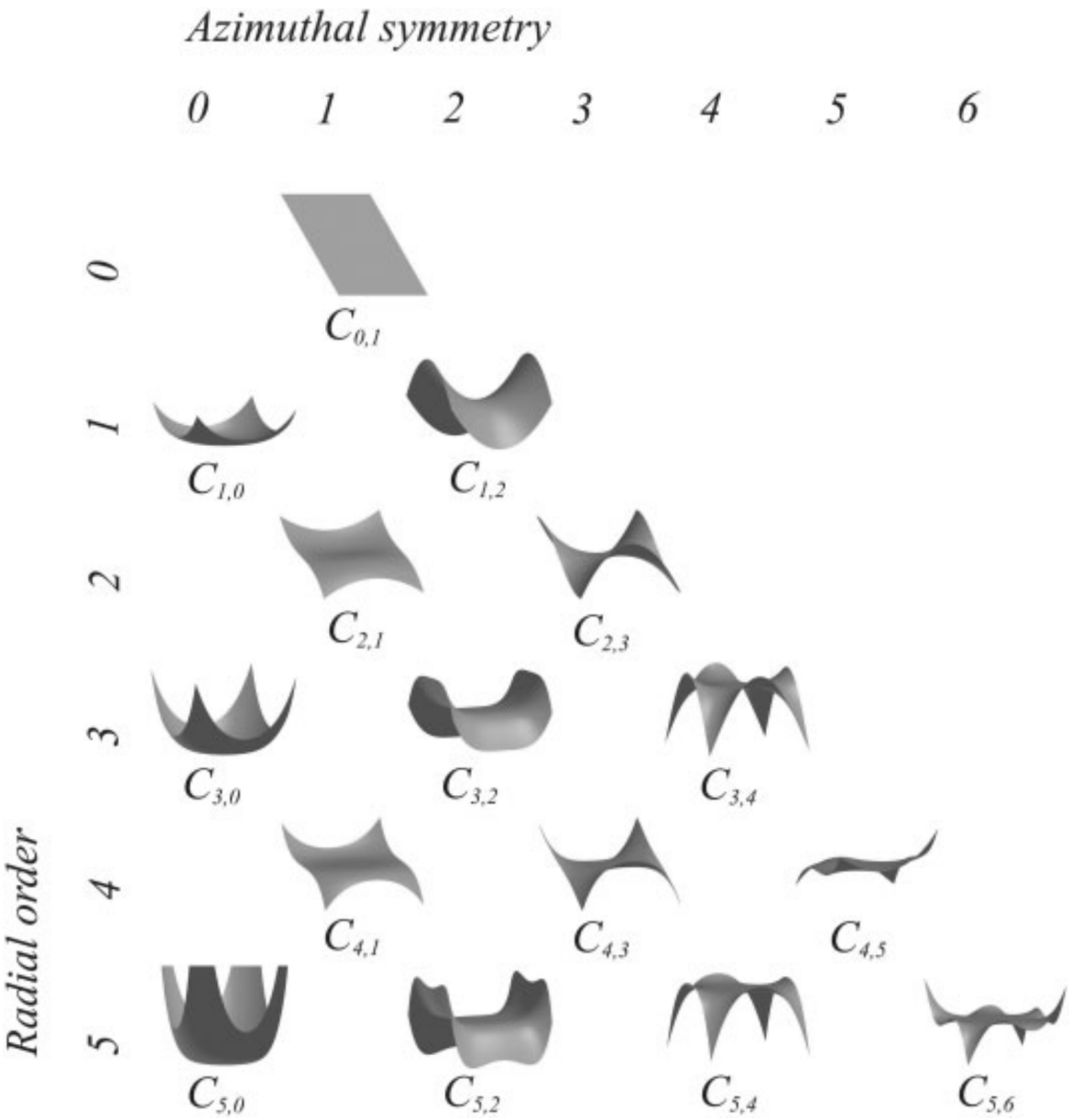

Fig. 3.6 **Graphical glossary of aberration coefficients.** Three-dimensional rendering of the distortions introduced in a spherical wavefront by all aberrations up to fifth order. Note the similarity between aberrations with the same azimuthal symmetry. Reproduced from [17].

Beam Rocking & Lens Aberrations

In S(P)ED the electron probe is formed with a small convergence angle (i.e. 1-3 mrad). Tilting this electron beam away from the optic axis of an aberrated lens has a number of effects on the probe. Firstly, the center of the probe is displaced by a vector proportional to the gradient of the aberration function, evaluated at the value of **k** corresponding to the tilt, according to Equation 3.2. Secondly, the curvature of the aberration function results in second order effects being induced [17], which affect the probe shape and convergence. These second order effects are found by evaluating the eigenvalues of the curvature tensor of the aberration function, which is written:

$$\nabla^2_{\mathbf{k}}\chi = \begin{pmatrix} \frac{\partial^2\chi}{\partial k_x^2} & \frac{\partial^2\chi}{\partial k_x \partial k_y} \\ \frac{\partial^2\chi}{\partial k_x \partial k_y} & \frac{\partial^2\chi}{\partial k_y^2} \end{pmatrix} \tag{3.5}$$

and, to first order, has the eigenvalues [206]:

$$\frac{1}{2}(C_{10}(\rho,\theta) \pm |C_{12}(\rho,\theta)|) \tag{3.6}$$

That is to say that the tilt of the probe away from the optic axis induces defocus away from the Gaussian imaging plane and two-fold astigmatism extending the shape of the probe. Minimising the probe displacement and the influence of second order effects, when the probe is rocked, is therefore essential in order to perform SPED experiments with a double-rocking probe and nanometre spatial resolution, as set out in Section 3.3.

The Ronchigram

The Ronchigram is a projection image of a specimen formed on the diffraction plane with a convergent incident electron beam focused near the specimen plane [207]. It is an in-line hologram of the specimen [208] and the sensitivity to phase distribution as well as the simultaneous access to real space and reciprocal space information has made it one of the most important signals for STEM alignment both with and without aberration correction [207, 209]. Since the deviation of a ray at the Gaussian focal plane is proportional to the gradient of the aberration function (Equation 3.2) the Ronchigram is a map of the gradient of the aberration function [17]. For example, defocus gives a linear ray deviation uniformly magnifying the image in the Ronchigram. The Ronchigram is therefore an ideal way to visualize the movement of the probe on the specimen as a result of tilt and therefore to correct it, as utilized in Section 3.3.

3.2 Nanobeam Electron Probes

Electron probes for SED experiments are typically nanometre sized and formed with a small convergence angle (i.e. 1-3 mrad). Alignment of such a nanobeam electron probe typically involves the use of a small illumination aperture and the adjustment of a pair of condenser lenses. The particular optical arrangement depends on the condenser lens system, which can vary significantly between instruments, as shown in Figure 3.7. The most important factor is whether or not there are three or more condenser lenses. When only two condenser lenses (CLs) are present, the first lens (CL1) controls the demagnification of the source and the second lens (CL2) controls the focusing of the probe onto the specimen [11, 198]. The only means by which to control the convergence angle is via the CL2 aperture. When three or more condenser lenses are present the convergence angle may also be affected by adjusting the excitation of any pair of lenses below CL1 (e.g. CL2 & CL3) that have a cross-over between them [11]. If an aberration corrector is incorporated in the condenser system then its optics should also be considered to avoid inducing parasitic aberrations.

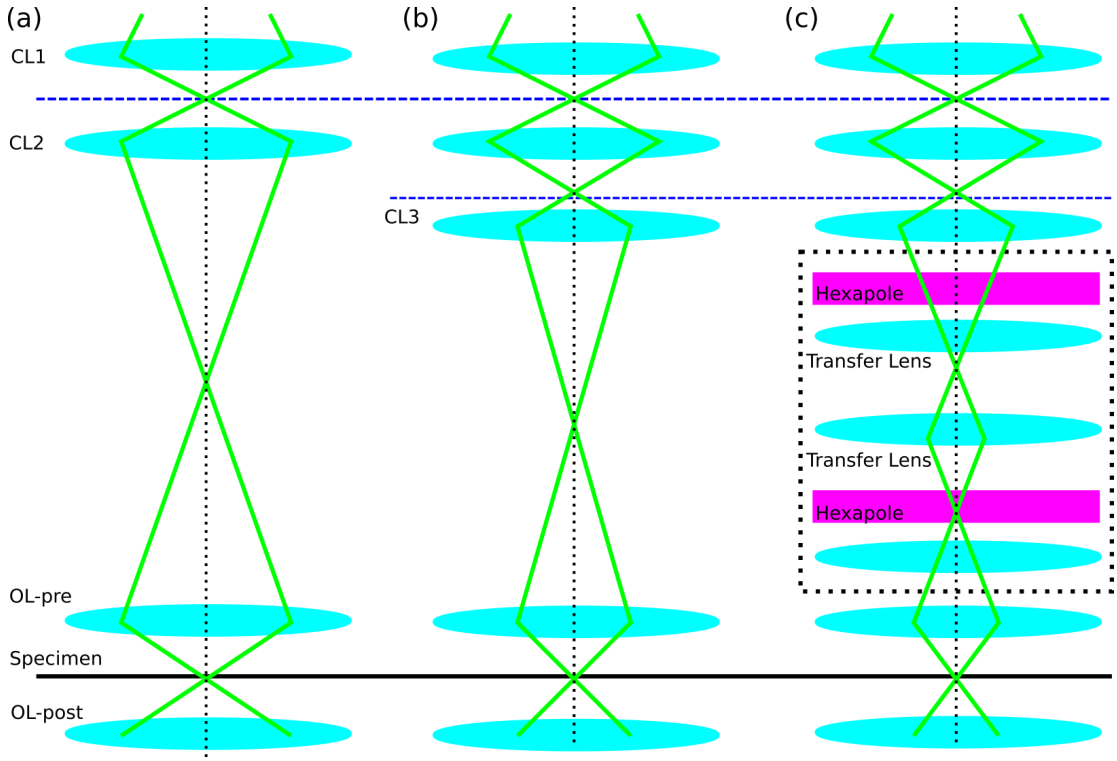

Fig. 3.7 **Probe forming optics**. (a) Two condenser lens (CL) system. CL1 controls demagnification of the source. CL2 controls the focusing of the probe onto the specimen. (b) Three condenser lens system. CL2 and CL3 can be adjusted as a pair to affect the convergence angle whilst maintaining focus. (c) A condenser lens system containing an aberration corrector which in this (CEOS) case contains additional transfer lenses and hexapoles.

3.2.1 Alignment of a Nanobeam Probe

Alignment of a nanobeam probe should begin with the microscope well aligned in STEM mode following standard alignment procedures. The specimen should be positioned at eucentric height and particular attention should be paid to the alignment of the pivot points (tilt/shift purity), rotation center, and astigmatism. Regardless of the complexity of the condenser lens system, the nanobeam configuration involves the use of a small condenser aperture of $\sim 5-10$ μm, which is typically the smallest available. When this aperture is inserted it must be centered carefully on the optic axis by expanding the illumination in imaging mode and re-centering the illumination by adjusting the aperture. If the condenser lens system comprises only two condenser lenses then, having aligned the smallest CL2 aperture and converged the probe on the specimen, nanobeam alignment is complete.

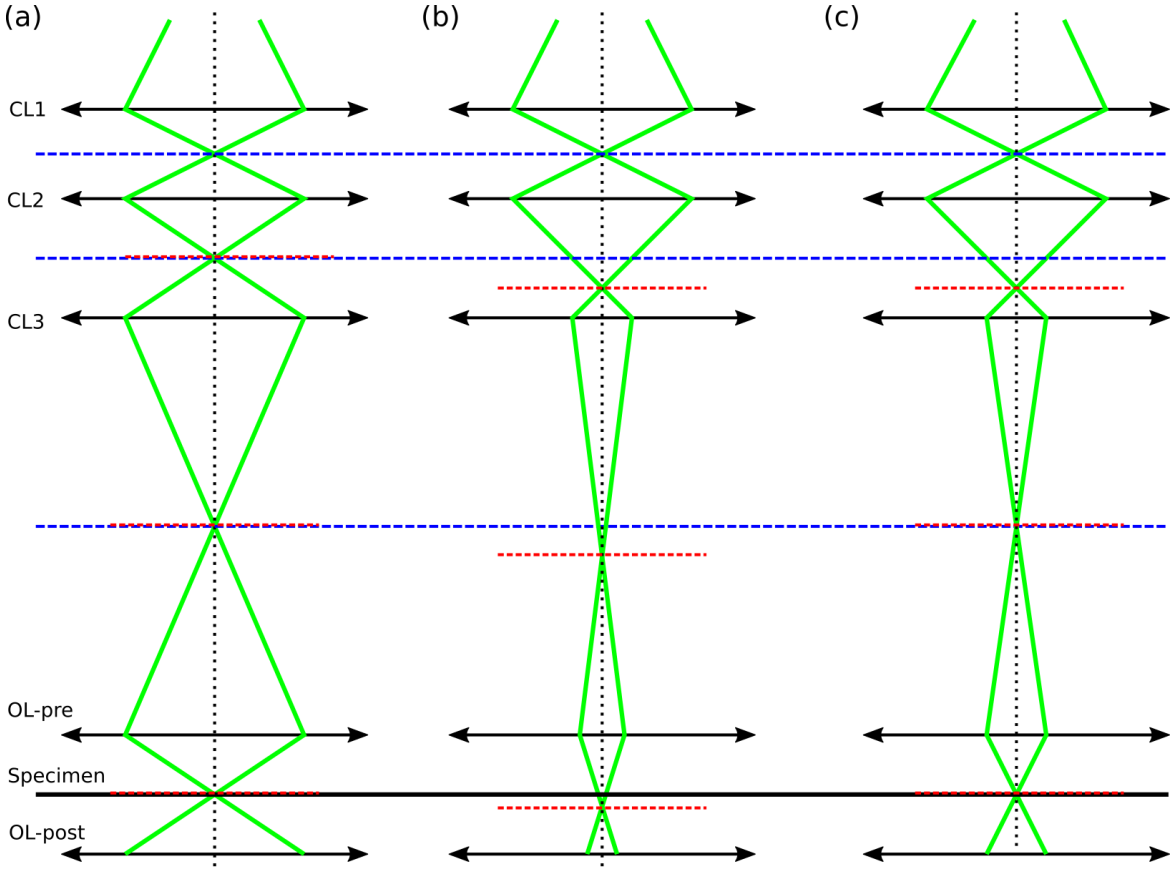

Fig. 3.8 **Ray diagrams showing the reduction of the convergence angle with three condenser lenses.** (a) Typical alignment of a convergent beam with a large condenser aperture. (b) Reducing the excitation of CL2 moves the subsequent cross overs towards CL3 and below the specimen plane. (c) Increasing the excitation of CL3 re-focuses the probe in the specimen plane. A small condenser aperture is also required for a small convergence angle.

Condenser lens systems comprising three or more lenses offer greater optical flexibility and the ability to adjust the convergence semi-angle continuously [210] using a pair of lenses below CL1 with a cross-over between them. To reduce the convergence angle, the excitation of the first lens (e.g. CL2) is reduced to move cross over towards the second lens (e.g. CL3). Increasing the excitation of the second lens (CL3) refocuses the probe in the specimen plane so that both a small convergence angle and a small probe can be obtained simultaneously, as illustrated in Figure 3.8. The smallest convergence angle that can be obtained is dictated by the allowed range of lens excitations, the physical arrangement of lenses and the condenser aperture. Typically a small condenser aperture (i.e. $\sim 5-10$ μm) will still be required to obtain a convergence angle of 1-3 mrad. These adjustments can induce aberrations, particularly coma and two-fold astigmatism, that are corrected as usual.

Probe corrected instruments typically have at least three condenser lenses prior to the corrector [210]. A nanobeam alignment is best obtained using these lenses, via the method described above, as this would have the least effect on aberrations. However, since some aberration corrected STEM instruments are optimized for large convergence angles, which improve spatial resolution in high-resolution STEM, the excitation range available with these lenses may be insufficient to reduce the convergence angle to the 1-3 mrad regime of SED. In this case a pair of transfer lenses within the corrector can be used to reduce the convergence angle further. This requires that the corrector hexapoles are manually turned off, the quadrupoles are used to correct two-fold astigmatism and coma is corrected using beam tilt. The hexapoles can then be used to correct three-fold astigmatism. Reduction of the convergence angle then follows a similar procedure to the three-condenser lens case.

3.2.2 Probe Size

Alignment of the microscope following the procedure described above is intended to minimize the effects of the lowest order lens aberrations (i.e. defocus, two-fold astigmatism and coma). Assuming that the alignment is performed well, the probe size will be limited by spherical aberration balanced with the Rayleigh diffraction limit. The probe size, d, is is typically [17, 11, 171] expressed as:

$$d = C_{3,0}\alpha^3 + \frac{0.61\lambda}{\alpha} \tag{3.7}$$

where $C_{3,0}$ is the spherical aberration coefficient, α is the convergence semi-angle and λ is the electron wavelength.

3.3 Double-Rocking Electron Probes

Rocking the electron probe to multiple tilts away from the optic axis in order to sample numerous diffracting conditions has been implemented in numerous contexts including: hollow cone dark-field imaging [197, 211], large angle rocking beam electron diffraction [212, 213], and precession electron diffraction (PED) [18]. Only PED involves double rocking of the electron beam back to the optic axis below the specimen in order to measure integrated diffraction intensities [18], as illustrated in Figure 3.9. The key optical requirements of the setup are: (1) rock the beam around a circular cone, (2) de-rock the diffracted beams back to uniform disks in the diffraction plane, and (3) align the conical rocking fulcrum to intersect the specimen precisely. Various configurations have been implemented and a detailed design approach was reported by Own *et al.* [200] incorporating geometric distortion corrections.

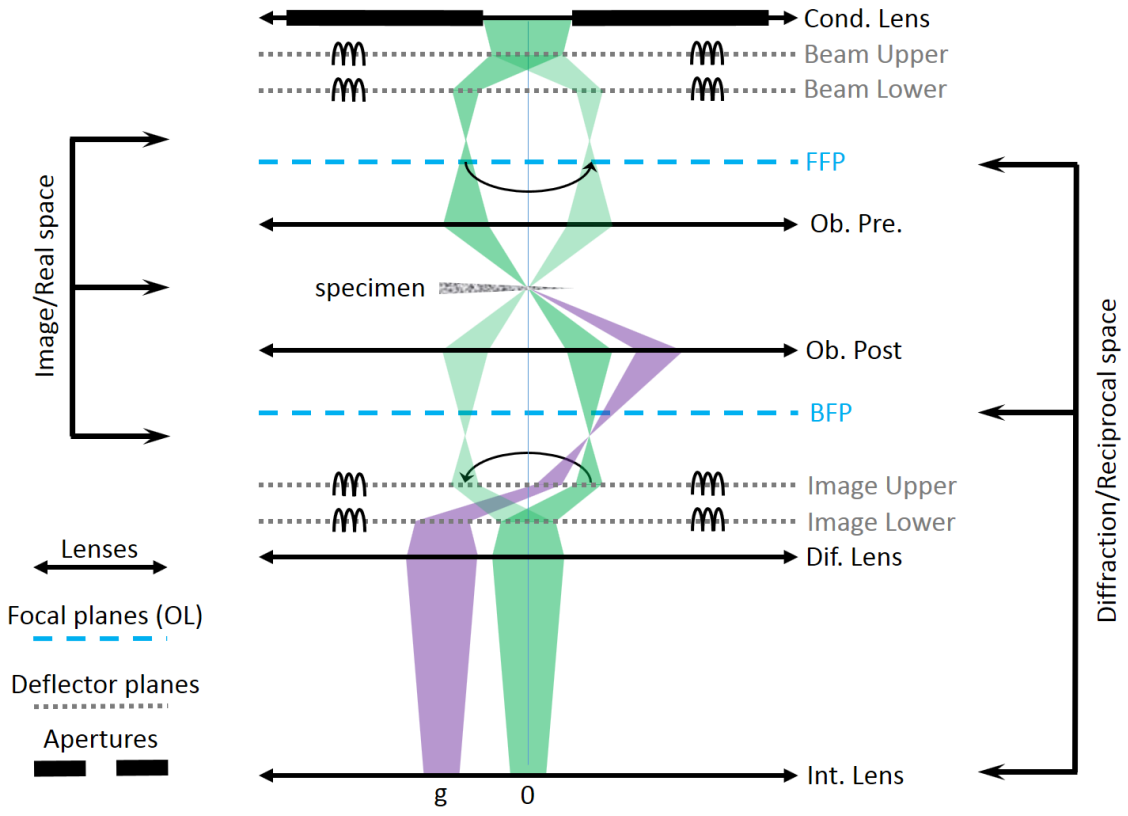

Fig. 3.9 **Schematic of the focused double-rocking probe geometry.** Two points on the azimuth are depicted for the direct beam, 0, with one diffracted beam, g, illustrating the diffraction condition being met at a particular azimuth. The pre and post specimen deflector coils that rock and de-rock the electron beams are depicted along with key lenses.

SPED is performed in an (S)TEM fitted with signal generators on the pre and post specimen deflector coils to produce the necessary double-rocking (tilt and rotation) and scanning of the beam [18, 200]. The set-up used in this work comprises a scan generator (Digistar P1000) produced by NanoMEGAS retro-fitted to a Philips CM300-FEG microscope, which has a two condenser lens system. The precession frequency used in this work was nominally 100 Hz although the hardware can achieve frequencies in the range 1-1000 Hz.

3.3.1 Alignment of a Double-Rocking Probe

Double-rocking probe alignment must bring the beam pivot point into the specimen plane to minimize displacement with tilt. Minimization of probe wander on the viewing screen, with the sample in focus, is only sufficient to achieve this if the instrument is fitted with an image lens aberration corrector so that the image of the probe is an accurate representation of the probe at the sample [27, 162, 163]. For non-image-corrected instruments, spherical aberration in the imaging lens and small misalignments between the pre-field and post-field objective lens pole pieces lead to a misrepresentation of the probe position and shape on the viewing screen [214]. Aligning the pivot point in imaging mode can be successful if the probe movement relative to the sample is minimized [212]. However, the shadow image in the bright-field (BF) CBED disk, is a more appropriate representation for aligning the pivot point accurately [212] and a method based on this is developed here[2].

Alignment of a double-rocking probe should begin with the microscope well aligned for convergent or nanobeam experiments as described in Section 3.2. The principles of aligning a double-rocking probe using the shadow image are illustrated in Figure 3.10. The most general condition occurs when the probe focal plane, C, pivot point plane, P, and the specimen plane, S, are at different heights, as shown in Figure 3.10(a). As the probe moves around the sample, during double-rocking, the shadow image of the specimen describes a circular path within the BF-CBED disk. As the double-rocking pivot point alignment is improved, the pivot point, P, moves closer to the specimen plane, S, and the circular movement of the shadow image within the BF-CBED disk is reduced at the same angular magnification (Figure 3.10(b)). Only when the pivot point plane, P, coincides with the specimen plane, S, does the shadow image of the specimen no longer move within the bright-field disk (Figure 3.10(c)). The incident angle continues to change so, if the sample diffracts, the static image will twinkle. Finally, when the probe focal plane, C, is moved into coincidence with the pivot point, P, and the specimen plane, S, the bright-field disk becomes featureless and any change in intensity is due to the diffraction condition alone (Figure 3.10(d)).

[2]This method was developed together with Jon Barnard and was reported in Barnard *et al.* [215]

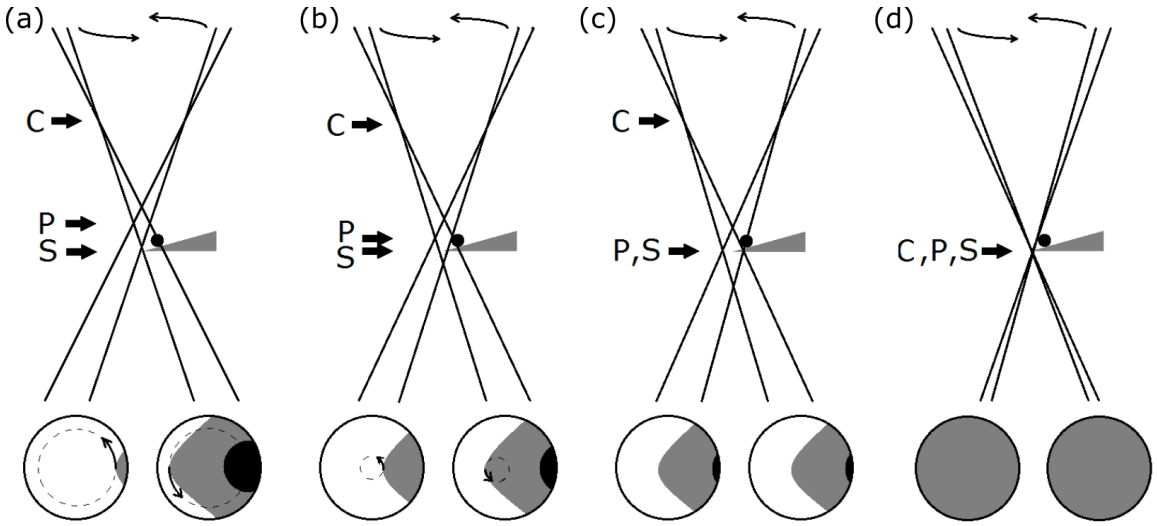

Fig. 3.10 **Ray diagrams and schematic shadow images within the bright-field disk at two points on the double-rocking cone at different stages of alignment.** The probe crossover (C), pivot point (P) and specimen (S), planes must be brought into coincidence. (a, b) The shadow image follows a circular path, when S and P are not coincident. (c) Alignment of P and S results in a static shadow image magnified depending on the distance between C and S. (d) The bright-field disk appears featureless when C, S and P are aligned.

In practice, alignment (see Figure 3.11) involves defocusing the condenser lens to obtain a high contrast shadow image, over a sufficiently wide field of view, within the BF disk (step 1). Successful pivot-point alignment of the double-rocking probe (step 2) requires that the de-rocking, below the specimen, is also aligned to keep the BF disk stationary. Since the de-rocking is contingent on the position of the pivot point plane, iterative refinement of the pivot-point and de-rocking is necessary (steps 3 and 4). The spatial accuracy of the pivot point alignment is only as good as the angular resolution and the angular magnification within the BF disk. Therefore, the defocus is reduced, typically by a factor of two (step 5), several times, to increase the angular magnification and reduce the pivot point error. When no further improvement in the pivot point can be accomplished by the pivot point adjustment alone, dynamic compensation is applied (step 6). Dynamic compensation modulates the beam deflector coils, over the double-rocking cycle, to null probe shifts caused by non-round aberrations in the probe forming lens [200]. Like the pivot point adjustment, the dynamic compensation is refined by reducing motion of the shadow image within the BF disk during precession. The non-precessed shadow image is depicted for comparison in Figure 3.11 and any blur must be related to residual pivot point error or electronic noise in the scan coils. The alignment is terminated when no further sharpening is seen. The probe is then refocused using the condenser lens and a smaller illumination aperture is inserted (step 7).

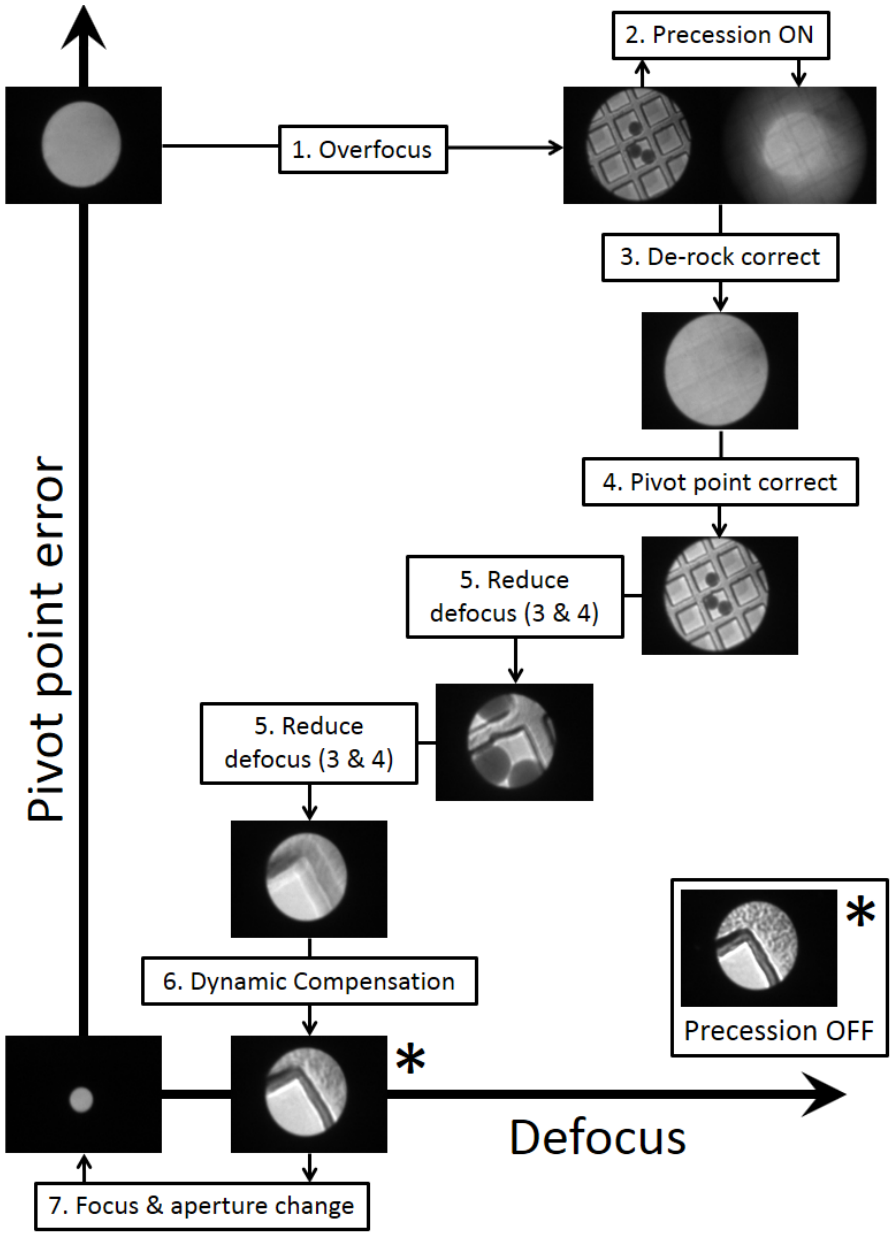

Fig. 3.11 **Steps involved in aligning a double-rocking probe**. Illustrated through time averaged images of the BF-CBED disk, with an integration time longer than one precession cycle, such that motion of the BF disk or of the shadow image within the BF disk appears as a blurring. The alignment begins by focusing the probe onto the sample and switching to diffraction mode. Overfocusing the probe with the condenser lens widens the BF CBED disk to give a large field of view (step 1). With precession on (step 2), de-rocking is adjusted first (Image Upper and Image Lower deflectors, Fig. 1) to sharpen the BF disk (step 3). Next, the pivot point is adjusted (Beam Upper and Beam Lower deflectors, Fig. 1) to give a sharp sample image within the BF-disk (step 4). As the overfocus is reduced (step 5), the de-rocking and pivot points are refined (steps 3 & 4, repeated). When no further improvement can be achieved by pivot-point adjustment, the dynamic compensation is adjusted (step 6). The alignment terminates by refocusing and reducing the illumination aperture (step 7). The inset (*) shows the non-precessed shadow image at step 6 for comparison.

In summary, the alignment (Figure 3.11) is described by the following steps:

1. Insert a large illumination aperture and over-focus the electron probe.
2. Find a region with highly visible features and activate precession at both the precession angle, ϕ, and precession frequency to be used.
3. Obtain a static BF-CBED disk by adjusting the phase and amplitude of the signals applied to the post-specimen deflector coils.
4. Minimize motion of the shadow image within the BF disk by adjusting the phase and amplitude of signals applied to the pre-specimen deflector coils.
5. Reduce the defocus by a factor of two and repeat steps 3 and 4 until no further improvement is seen.
6. Apply dynamic compensation to further reduce motion of the shadow image within the BF-CBED disk.
7. Refocus the probe using the condenser lens and insert a smaller illumination aperture.

Three further points are worth making. First, the initial gross errors in both the pivot point and de-rocking for precession angles beyond ca. 20 mrad ($> 1°$), make correction with steps 2, 3 and 4 difficult. By starting with a lower precession angle and finding the correct pivot point and de-rocking settings there and then increasing , in a stepwise fashion, the correct pivot point and de-rocking settings can be found, i.e. steps 2, 3 and 4, can be iteratively refined with an increasing precession angle. Second, when moving the sample from the alignment region to the region of interest (ROI), the height of the new region has to be set carefully, as a height deviation of Δz from the pivot point plane will resultant in conic blur of approximately $\phi\Delta z$. To achieve this, having set the pivot point plane at the alignment region, precession can be switched off and the probe focused to Gaussian focus, the specimen is then moved to the ROI and the height adjusted to give the same Gaussian focus conditions as before. Precession can be turned back on and the condenser lens underfocused by $2C_{30}\phi^2$, where C_{30} is the spherical aberration coefficient of the probe forming lens, (see Discussion & Figure 6) before starting the SPED scan over the ROI. Finally, it is noteworthy that the specimen height is typically not changed significantly in this procedure allowing a position close to eucentric height to be maintained, which is advantageous for scanning precession electron tomography [164] experiments.

Why align with positive defocus (overfocus)?

The Gaussian image plane coordinates are gradient mappings of the aberration function in Fraunhofer diffraction, as given by Equation 3.2. For an aberration free probe-forming lens, only the defocus term, $\chi(\mathbf{k}) = \pi C_{10}\lambda k^2$, contributes to the aberration function. When the probe is underfocused ($C_{10} < 0$) or overfocused ($C_{10} > 0$) there is a linear, one-to-one correspondence between a point in the diffraction disk and a point on the sample within the illuminated area of the probe. Either condition works for aligning a precessing probe.

For a microscope with positive spherical aberration (C_{30}) in the probe forming lens, the one-to-one relationship is maintained only with a positive defocus (overfocus). If underfocus is used, the one-to-one correspondence is lost over a range of defocus, resulting in strong warping within the shadow image due to natural focusing as the curvature of the aberration function disappears at certain regions within the illuminated cone [216, 175]. This makes pivot point correction difficult. An additional, practical, benefit of using the overfocus condition is the slight widening of the illumination aperture, rendering a wider field of view.

Why change to a smaller illumination aperture?

Together with the lattice parameter of the material under examination, the illumination aperture determines the extent of reflection overlap in the PED pattern. Automated reflection identification generally requires non-overlapping CBED disks, i.e. smaller illumination apertures. The size of the precessing probe is also determined by the aperture size (see Section 3.3.3) and smaller apertures generally improve spatial resolution of SPED data sets. In practical terms, the illumination aperture is typically changed in imaging mode. However, it is advantageous to operate only in diffraction mode to avoid any effects of hysteresis in the intermediate lenses. To maintain this advantage, the illumination aperture can be changed in diffraction mode and positioned with reasonable accuracy by marking the position of the BF-CBED disk center with the larger illumination aperture aligned and then inserting the smaller aperture and adjusting its position to return the BF-CBED disk to the same position.

3.3.2 Limitations of the Proposed Alignment Method

Aligning the double-rocking probe using the shadow image offers significant advantages in terms of visualizing the effects of misalignment with high fidelity. However, the approach is not without limitations. First, a large illumination aperture is necessary for the alignment, which has to be changed to a smaller aperture for the experiment. This has two consequences: (1) If one, or both apertures are dirty, the rocking probe acquires an additional aberration that stays constant throughout the precession cycle. As with regular STEM, this can be corrected

by adjusting the condenser stigmators; (2) If the small aperture is not centered precisely on the rocking cone, the probe acquires a sinusoidal probe displacement and aberration. This is perhaps the biggest weakness of the proposed method. Secondly, a prominent feature is required for alignment, especially with the relatively large (ca. 100 μm) defocus used at the start of the alignment process. Small (ca. 10 nm) features work well for modest precession angles, up to about 20 mrad (ca. 1°) with larger (ca. 100 nm) features necessary for precession angles above this. Corners of specimens work well too – two sharp edges provide reliable information about the probe wander in the orthogonal directions – especially for the dynamic compensation at the end of the alignment procedure. However, the need to find appropriate features for alignment is a common part of much electron microscopy and typically a suitable feature can be found or contrived. Thirdly, shadow image contrast in the CBED disk is low for microscopes with W-filament and LaB_6 thermionic emitters, because the overall shadow image is an incoherent superposition of individual shadow images from points within the (extended) crossover sitting above the sample. Visibility is improved by reducing the spot size, but at the expense of probe current. In contrast small, coherent sources such as a Schottky thermionic emitter or cold field emitter afford significantly greater probe currents (> 1 pA). Users of SPED systems fitted to older microscopes may, therefore, find the shadow image alignment challenging.

3.3.3 Probe Size & Spatial Resolution

The probe size in double-conical-rocking beam experiments and the was initially estimated by Vincent & Midgley [18] based on the disk of least confusion in the specimen plane, as:

$$d = 4C_{3,0}\phi^2\alpha \tag{3.8}$$

which shows that the probe size increases as the square of the precession angle and proportional to the convergence angle. This simple estimate is however slightly pessimistic as can be seen using a more complete wave-optical assessment. The full wave-optical structure of the inclined probe at one instantaneous azimuth in the precession cycle, for two different illumination aperture sizes, is shown in Figure 3.12. For the $\alpha = 3$ mrad aperture, the probe is an ellipse at the Gaussian imaging plane (z = 0) with a small amount of coma (magnitude, $C_{2,1}^{eff} = 6C_{3,0}\phi$), which makes the probe slightly brighter on one side. Above the Gaussian imaging plane, i.e. the overfocusing condition, two line foci are seen and separated in height by a distance equal to the tilt-induced two-fold stigmatism, $C_{1,2}^{eff} = 2C_{3,0}\phi^2$ (this is the definition of 2-fold stigmatism). Detail of the probe at height, $z = 2C_{3,0}\phi^2$, i.e. midway between the line foci, shows that the 3 mrad probe is composed of four fold caustics

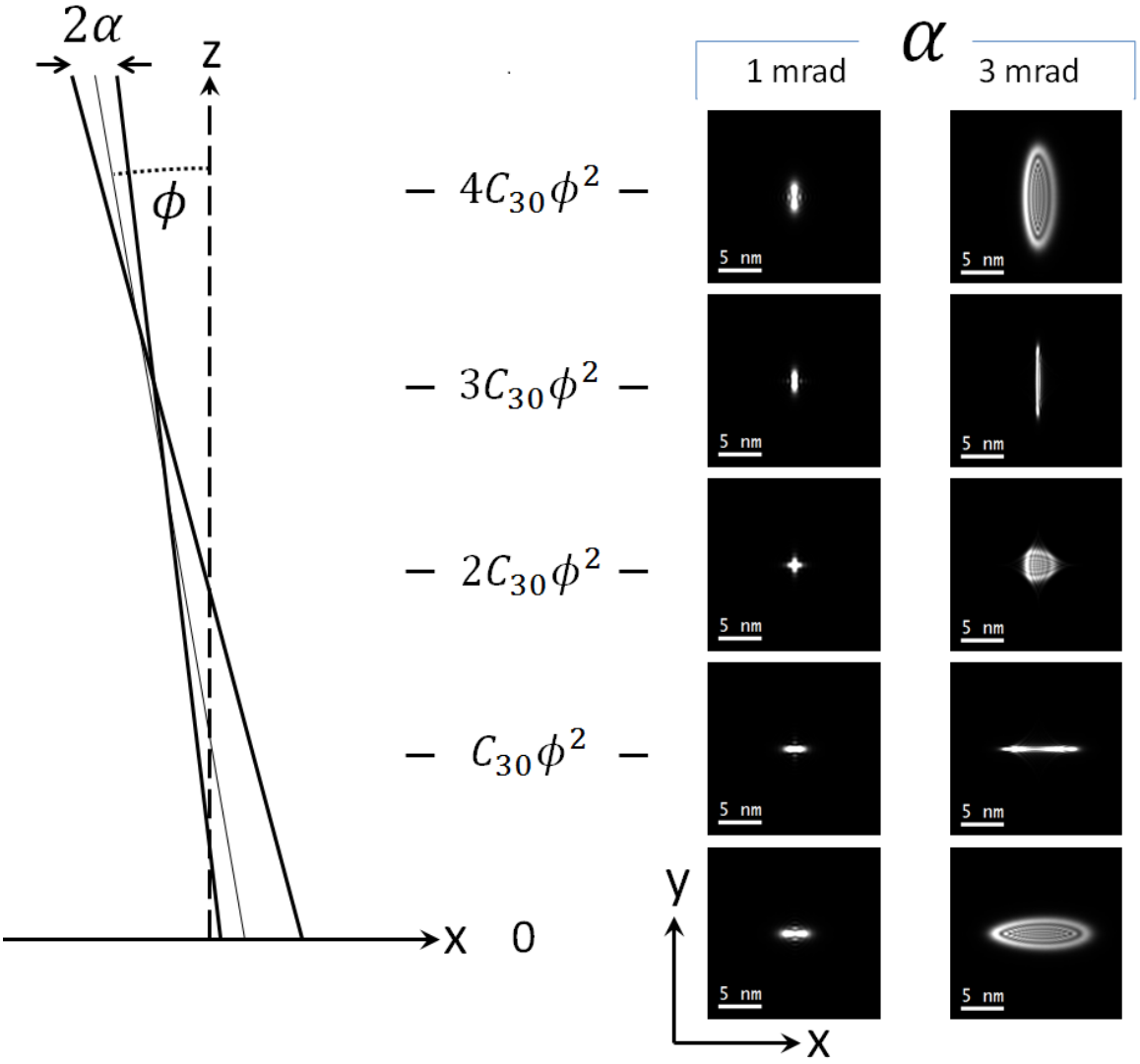

Fig. 3.12 **Geometric rays and wave-optical simulations of the electron probe**. For a convergent probe, tilted by a precession angle of ϕ = 35 mrad, in the presence of spherical aberration coefficient ($C_{3,0} = 1.2$ mm) relative to the optic axis (—). The principal (central) ray crosses the optic axis at $C_{3,0}\phi^2$ and rays about this ($\phi \pm \alpha$) in the radial direction cross at $C_{3,0}(\phi \pm \alpha)^2$, creating two caustic folds in the probe – a radial caustic (line focus, X-direction) at $C_{3,0}\phi^2$ and an azimuthal caustic (Y-direction) at $3C_{3,0}\phi^2$ (Note: Lateral displacements between the wave-optical probe simulations have been removed for convenience). Halfway between these two folds, at a height of $C_{3,0}\phi^2$, the probe is most compact. The Vincent-Midgley disk-of least-confusion diameters are 5.9 and 17.6 nm for α = 1 and α = 3 mrad respectively.

decorated with Airy fringes. The top-bottom pair are azimuthal fold caustics that coalesce at height,$z = C_{3,0}\phi^2$, to form one line-focus. The left-right pair are radial fold caustics that coalesce at height, $z = 3C_{3,0}\phi^2$, to form the other (orthogonal) line focus. Between the two, the probe is underfocused in one direction (azimuthally) and overfocused in the other (radially). The probe is also at its most compact size, having a size $2C_{3,0}\phi^2\alpha$ according to the geometric ray model, i.e. half that of the Vincent-Midgley expression.

Considering the intensity distribution in the full wave-optical assessment shows that the probe is slightly smaller still, $r_{80} = 0.89C_{3,0}\phi^2\alpha$ (80% probe intensity). This value was obtained by evaluating the probe size midway between line foci was measured using simulated wave-optical calculations calculated in IDL using a fast Fourier transform (FFT) [46]. The defocused probe was calculated using a defocus term equal to $C_{1,0} = -2C_{3,0}\phi^2$ (the precession angle, ϕ, was fixed at 35 mrad) in the aberration function and various circular illumination apertures applied to low-pass the spatial frequencies, $0.1 \leq \alpha \leq 4.1$ mrad, in the probe wave-function, $\psi_{probe}(\mathbf{k})$, prior to the FFT. The results of the probe intensity $|\psi_{probe}(\mathbf{r})^2$ are depicted in Fig. 3.13(a) for one instantaneous precession azimuth. Because the probe rotates around the optic axis (assuming the probe is centred on the optic axis) the radially averaged probe is pertinent to the spatial resolution of the SPED experiment. The integrated radial probe profile is depicted in Fig. A1(b) with two lines, corresponding to the 50% (red) and 80% (green) probe intensity thresholds.

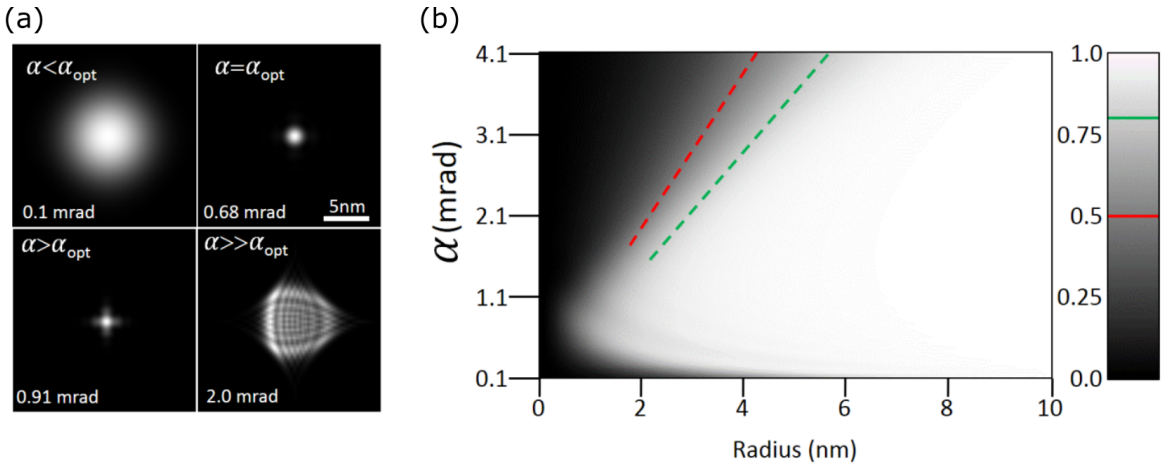

Fig. 3.13 **Simulated probe sizes.** (a) Four simulated probes for one (instantaneous) azimuth with a precession angle of 35 mrad with illumination angles below, at, above and many times greater than the optimum illumination angle. (b) The cumulative radially averaged electron probe as a function of shows the linear increase in probe size with illumination angle with 50% (red) and 80% (green) asymptotes illustrated.

The optimal convergence semi-angle can be evaluated [205] by balancing the tilt-induced two-fold astigmatism against the difraction limit to give:

$$\alpha_{opt}(\phi) = 0.55\sqrt{\frac{\lambda}{C_{3,0}}\phi^2} \tag{3.9}$$

For a given precession angle and wavelength this yields an optimum probe size of:

$$d_{opt}(\phi) = 2.19\sqrt{\lambda C_{3,0}\phi^2} \tag{3.10}$$

This means that there is an optimized illumination aperture for each precession angle, which could be selected to minimize precession-induced blur.

Measuring SPED spatial resolution

STEM probe sizes are typically measured using a grating or nanostructure with a well-defined lateral size [217]. In SPED, the same approach is desirable, but the need to maintain non-overlapping disks in the SPED diffraction patterns means lattice fringes will not be visible. Instead, virtual bright-field images (VBFs) (see Chapter 4) were formed using an integration disk slightly larger (1.2 mrad) than the convergence semi-angle, as shown in Figure 3.14 along with corresponding power spectra. The SPED data for this assessment of spatial resolution were acquired from an Agar Scientific combined test specimen, comprising a holey carbon film (thickness, $t = 20$ nm) decorated with a uniform distribution of gold particles approximately 10 nm in diameter. Diffraction patterns were recorded with 144×144 pixels and 8 bits per pixel over 256×256 probe positions with a spatial sampling of 1.9 nm/pixel. Precession angles between 1.4 mrad and 41 mrad (calibrated in-situ using polycrystalline gold ring patterns) were used at a precession frequency of 100 Hz. Other important parameters include: illumination semi-angle,$\alpha = 0.9$ mrad; probe current = 0.5 pA; camera length = 850 mm; exposure time = 10 ms, such that recorded diffraction patterns were not saturated.

The sharpest images were obtained without precession ("$\phi = 0$ mrad") and the gold particles were easy to discern. Darker-than-average contrast amongst some particles suggested they were diffracting strongly. Indeed, their corresponding diffraction patterns showed several CBED disks excited. As the precession angle was increased, the blur in the VBF was modest, e.g. 3.4 and 13.5 mrad, and faint blurring could be seen at the edge of the gold islands. No stretching of the islands was apparent, suggesting that contrast transfer by the SPED probe was isotropic. Increasing the precession angle beyond approximately 20 mrad led to a rapid increase in the VBF blur. During the alignment it was more difficult to keep the islands sharp within the shadow image and significantly larger features, such as holes in the

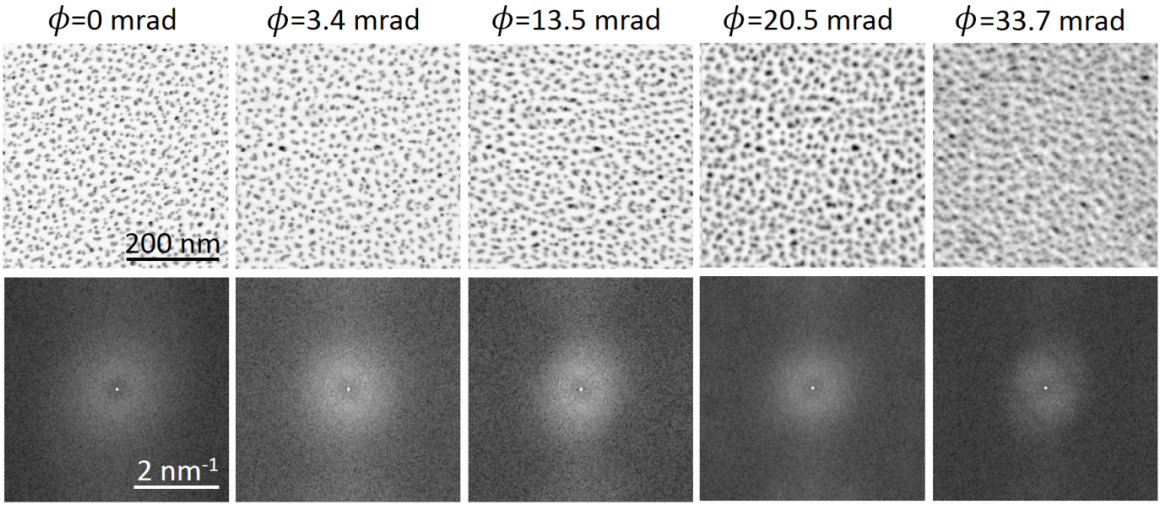

Fig. 3.14 **Virtual bright-field images of the gold-on-carbon test sample.** The virtual collection angle was $\beta = 1.2$ mrad and their log-power spectra, $\rho(k|\phi)$. Each VBF has 256^2 pixels, with width 1.9 nm. Nyquist frequency is 0.26 nm^{-1}.

carbon film and clusters of gold particles, were needed to find the correct pivot point. Above 30 mrad precession angle the VBF images demonstrated some streakiness, which could be discerned in the power spectra as lines of zero-visibility (Figure 3.14); this suggested some anisotropy in the transfer of contrast.

Precession-induced blur, i.e. spatial resolution loss, was determined by measuring the effective damping envelope, in the Fourier domain, of the *rotationally averaged* VBF power spectra at low spatial frequencies ($k < 0.2$ nm^{-1}). If the effect of precession-induced blur can be modelled as a Gaussian blur (width, d) of an unprecessed VBF image, then, in the Fourier domain, the power spectrum of the precessed VBF, $\rho(k|\phi)$, is equal to the unprecessed VBF power spectrum, $\rho(k|0)$, multiplied by a Gaussian damping envelope, $\exp(-4\pi^2 d^2 k^2)$. Therefore, taking the logarithm of the ratio of the power spectra, $\rho(k|\phi)/\rho(k|0)$, should yield a parabolic variation in the low-k domain[3]. A least-squares fitting algorithm was used to find the parabolae that matched the log-power-spectra-ratio (LPSR),

$$L(k) = \log_{10}\left(\frac{\rho(k|\phi)}{\rho(k|0)}\right) \tag{3.11}$$

in the low-k domain, using one or two parameter fits. In the one-parameter fit, $L(k) = 4\pi^2 d^2 k^2 \log_{10} e$, i.e. proportional to the square of the Gaussian blur, d. The single-parameter fit implicitly assumed that the total intensity in precessed and unprecessed VBFs were the

[3]This argument holds even if the precessed and unprecessed images are not of the same area. The only requirement is that the statistical properties of the gold-on-carbon films are the same, i.e. island size, spatial homogeneity. All indications were that this was indeed the case.

same. In the two-parameter fit, i.e. $L(k) = A - 4\pi^2 d^2 k^2 \log_{10} e$, where A is a (fitting) constant, considers the possibility that total VBF intensity is different. The blur coefficients, d, were used as a proxy for precession probe size.

Figure 3.15 (a) shows the LPSRs for low, medium and high precession angles, with their respective parabolic fits to the low domain. The domain over which the parabolic fit was appropriate became narrower with increasing precession angle. The prominent rise in the LPSR for the 13.5 (33.7) mrad curves in the domains $k > 0.15$ ($k > 0.10$) nm^{-1}, was due to algebraic nature of the LPSR. Rewriting the LPSR,

$$L(k) = \log_{10} \rho(k|\phi) - \log_{10} \rho(k|0) \tag{3.12}$$

shows that the high-k domain of $L(k)$ is dominated by the large (negative) values of the unprecessed VBF image, i.e. there is more high-k structure in the unprecessed VBF power spectrum. This creates a strong negative dip in the LPSR. However, as $k \to \infty$, the power spectra of both VBFs tends to the same frequency-independent noise floor, so that their ratio, the LPSR, tends to $\log_{10} 1 = 0$. Simply interpreted, the rise is due to the precessed VBF power spectrum hitting the frequency-independent noise floor before the unprecessed VBF power spectrum. Thus, the spatial-frequency domain over which the parabolic approximation is valid continues to shrink for increasing precession angle.

Figure 3.15 (b) shows the Gaussian blur measured for each precession angle LPSR function, against the measured precession angle, for both the 1-parameter and 2-parameter parabolic fitting functions. Both 1-parameter and 2-parameter models show the same slow increase in the blur, which, with a least squares fit, scales as for precession angles below 15 mrad. Above 15 mrad (ca. 1°), the resolution worsens faster, scaling as $\phi^{1.7}$ and $\phi^{1.6}$ for the 1-parameter and 2-parameter fits respectively. Asymptotically, both curves appear to approach the Vincent-Midgley expression (Equation 1.8), which is shown for comparison, in the high-ϕ limit. Both the 1-parameter and 2-parameter blur curves show that the VBF images for a precessed electron probe can be equated to an unprecessed VBF with Gaussian blur of ~ 2 nm for precession angles less than about 15 mrad (ca. 1°).

Measurement of the probe size by estimating the damping envelope of the power spectra associated with VBF images appears to give reasonable results. The precession angle dependence of resolution degradation can be explained as follows. At low precession angles, the $\phi^{0.4}$ dependence is close to $\sqrt{\phi}$, which suggests resolution is limited by noise in the scan electronics rather than aberrations. This argument is predicated on two suppositions. First the angular displacement of the electron beam by a deflector coil is proportional to the current flowing through it. Second, noise in the deflector coil is primarily shot noise, which increases in proportion to the square root of total current flowing through it [218]. Therefore,

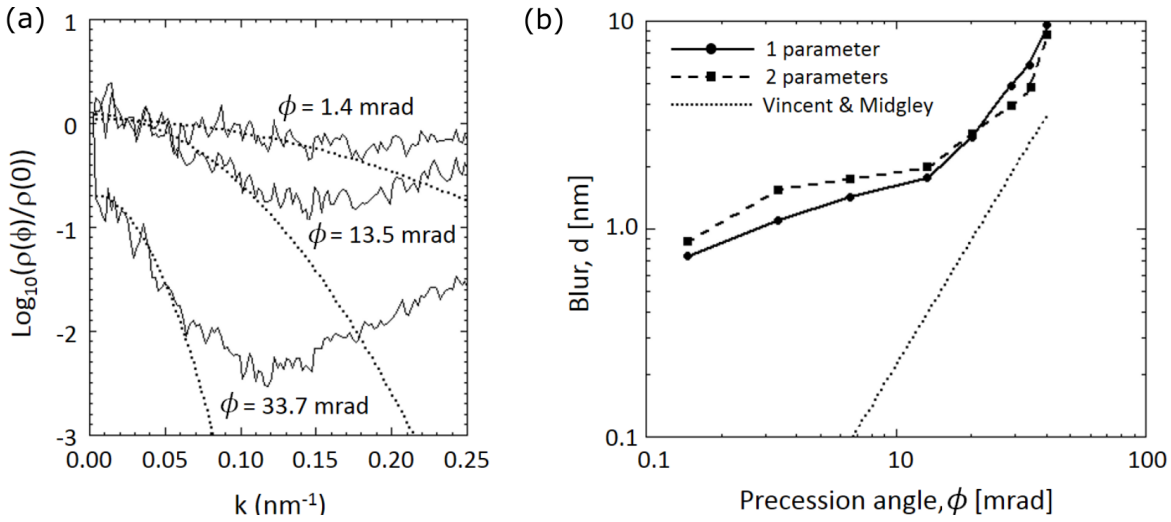

Fig. 3.15 **Log-power-spectrum-ratios for small, medium and large precession angles.** (a) The dotted lines are the 2-parameter fits to the low-k domain assuming a parabolic variation. The rises in the LSPRs for $k > 0.1$ nm^{-1} (ϕ = 33.7 mrad), $k > 0.15$ nm^{-1} (ϕ = 13.5 mrad) and $k > 0.2$ nm^{-1} (ϕ = 1.4 mrad) correspond to the differeng extents of the frequency-independent noise floors in each case. The precession-induced blur is shown in (b). The low-ϕ domain shows a $\phi^{0.4}$ variation for both 1- and 2-parameter fits; the high-ϕ domain shows $\phi^{1.6}$ (2-parameter) and $\phi^{1.7}$ (1-parameter) variation. The probe size predicted by Vincent & Midgley [18] is shown as a dotted line. $\alpha = 0.9$ mrad.

the (shot) noise in each deflector coil, even when the probe is stationary at a pixel point, is related to the total current, $I_{tilt}(t) + I_{shift}$, not just the shift signal. Effectively, the probe shift signal is superposed on the same noisy electronic channel that the (double-rocking) tilt signal passes. One possible method to mitigate this would be to have separate deflector coils for the (probe) shift and (double-rocking) tilt actions. It has to be noted that, since the CM series of instruments used in this work, considerable improvement in the electronic noise in the scan system of subsequent microscope platforms has been achieved.

At high precession angles the $\phi^{1.7}$ dependence seen (Fig. 3.15) is close to the ϕ^2 dependence expected theoretically. If we had pushed the precession angle higher, then the curve in Fig. 3.15(b) would almost certainly have steepened. Thus, by using the shadow image alignment method, we appear to be reaching the limit in spatial resolution dictated by spherical aberration of the probe forming lens ($C_{3,0} = 1.2$ mm) and the tilt-induced two-fold astigmatism, $C_{1,2}^{eff} 2C_{3,0}\phi^2$, of the precessing probe.

3.4 Electron Detection

Accurate measurement of an electron diffraction pattern, in terms of incident electron intensity and geometry, depends on the detector characteristics and the optics that project the diffraction pattern onto the detector. Detectors for S(P)ED experiments must be able to acquire frames with an exposure times in the range 1-100 ms, so that scans of a useful size (e.g. 256×256) pixels may be acquired in a reasonable time considering microscope stability. This precludes the use of traditional recording media such as photographic film, imaging plates, electron diffractometers and slow scan charge coupled devices (CCDs) and has been the dominant constraint on detector systems installed for S(P)ED experiments. This speed requirement led to the most common commercial implementation of S(P)ED using a fast optical camera to image the phosphor viewing screen [219, 150] although this does not address the speed of the phosphor properly. Fast high-efficiency detectors have also been required for recent developments in low-dose imaging particularly in the field of cryo electron microscopy and this has driven the development of numerous new *direct electron detectors* [220, 221]. These new detectors operate with the electrons incident directly on the imaging electronics i.e. there is no intermediate scintillator as in traditional CCDs used in electron imaging [220, 221].

3.4.1 Detector Characteristics

Detector characteristics are measurable quantities describing the relationship between the incident electron intensity on the detector and the recorded intensity [222, 172]. The most important detector characteristics are the modulation transfer function (MTF) and the detective quantum efficiency (DQE). The MTF is the ratio of output to input modulation as a function of spatial frequency and describes how the detection system attenuates the amplitudes of a sinusoidal series. The DQE is the ratio of the square of the output to the square of the input signal-to-noise-ratio measured as a function of spatial frequency and measures combined effects of the signal and noise performance of the imaging system [222]. These quantities are however a direct result of the detector design and configuration and are essentially fixed at the point when the experiment is performed. From the perspective of experimental data acquisition and analysis it is more immediately important to consider the gain of the detector and the response linearity. The gain, $\overline{g}$, is defined:

$$\overline{g} = \frac{\overline{I} - \overline{b}}{\overline{N}_e} \tag{3.13}$$

where $\bar{I}$ is the average counts measured, $\bar{b}$ is the background and $\overline{N}_e$ is the average electron dose per pixel. Practically, the gain is measured and then corrected by exposing the detector with a uniform illumination and averaging over pixels and the background is measured by recording an image without electron illumination using the same exposure time for recording the image. The response linearity describes the increase in measured intensity for equal increments of electron dose. Often it is sufficient to assume linearity over the range of incident electron intensities encountered but this can fall down for very intense diffraction disks. Linearity is assessed by increasing the dose by known increments and measuring the response this is often achieved by increasing exposure times. If the response is non-linear a curve is obtained, which may be fitted and used to correct measured intensities [222].

3.4.2 Projection Distortions

Recorded electron diffraction patterns may be distorted due to the projector optics [223] or due to the use of an off-axis camera [150, 188]. Distortions due to the projection lens system are a result of lens aberrations and can be minimized by good alignment of the microscope, particularly considering coma and optimization of an image side aberration corrector if present. Off-axis cameras lead to an approximately rectangular distortion of the diffraction pattern, which can be calibrated using a reference specimen and corrected by affine transformation of the data, as discussed in Chapter 4.

3.5 Experimental Setup

S(P)ED data presented throughout this work was acquired using a Phillips CM300 FEG-TEM retrofitted with a Nanomegas Digistar scan system and a Schottky FEG providing a small, bright and reasonably coherent electron source. The condenser lens system comprises two lenses meaning that a nanoprobe alignment only involves inserting and aligning the smallest condenser aperture available, which is 5μm on this instrument. The Nanomegas Digistar system comprises a scan generator that drives the scan deflector coils to achieve simultaneous double-rocking and spatial scanning of the electron beam, as required for SPED experiments. The Nanomegas system also enables the acquisition of an electron diffraction pattern at each probe position using an external optical CCD coupled to the small phosphor viewing screen of the microscope, which suffers from the rectangular distortion described in Section 3.4.2.

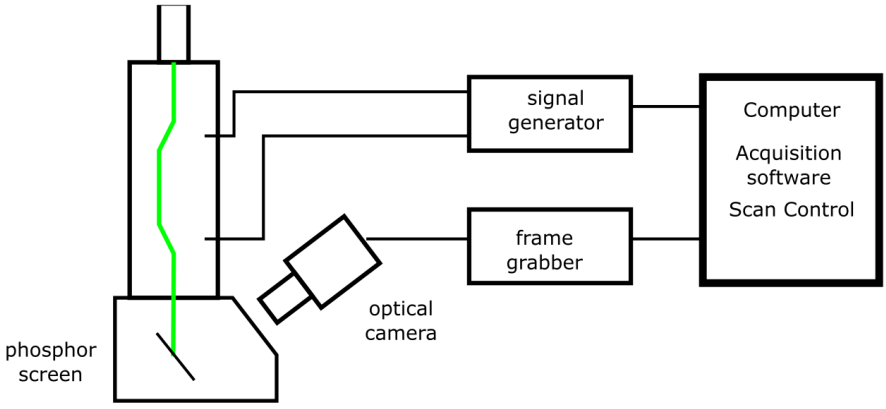

Fig. 3.16 **Experimental setup.** Schematic representation of the retrofitted Nanomegas system that enables S(P)ED to be performed under computer control. The system comprises a signal generator that drives the deflector coils and an external optical camera to record the diffraction pattern on the phosphor viewing screen.

3.6 Summary & Prospects

Experimental aspects of S(P)ED have been set out in detail, providing a comprehensive guide to performing such experiments. Particular attention has been paid to the electron optical arrangement and practical methods for alignment, which were essential for obtaining high quality S(P)ED data with nanoscale spatial resolution. Most notably, the use of the Ronchigram to align a double-rocking probe at the experimental rocking frequency was suggested and demonstrated for the first time. Without this approach it had not been possible to obtain SPED data at high-resolution in a routine and reliable manner. Further improvements in the electron optical configuration for SPED are likely to be possible with the incorporation of aberration correction. Although there has been some exploration of aberration correction in the context of single point PED [199, 206] experiments and SPED has been performed on aberration corrected instruments [27, 163], it remains the case that little has been done to optimize the corrector setup for hollow cone illumination. The Ronchigram method set out here for pivot point alignment will remain applicable in aberration corrected SPED.

Electron detection systems have developed significantly in the past 5 years since direct electron detectors have become available in various guises. Many of these detectors have been optimized in the context of fast imaging experiments and it remains the case that further exploration of their performance and optimization for fast and quantitative diffraction experiments is required. Preliminary results using such detectors have been reported in the literature and here in Chapter 8 and appear promising but demonstration of quantitative use of diffracted intensities will be the ultimate goal. Finally, in the context of using diffracted intensities quantitatively in S(P)ED experiments it is likely that energy filtering will prove

beneficial [206]. This is because electron diffraction theory, as discussed in Chapter 2, typically only describes elastic scattering of electrons and therefore removing inelastic contributions to the measured intensity improves quantification. The benefits of such filtering are most significant when the elastic/inelastic scattering ratio is low, which is typically the case in light element materials. Finally, it would be interesting to combine S(P)ED with the acquisition of spectroscopic signals (e.g. energy dispersive X-ray spectra (EDX) [224] and electron energy loss spectra (EELS) [225]) to provide complementary physico-chemical insights. Overall, a general framework for S(P)ED experiments is now established and there remains a number of avenues for further improvement of the experimental method particularly towards quantitative use of diffracted intensities.

Chapter 4

pyXem - Pythonic Crystallographic Electron Microscopy

Analysis of 4D-S(P)ED datasets, comprising many thousands of electron diffraction patterns, requires robust and reproducible data-analysis workflows. To facilitate this analysis a Python package was developed as a library of functions for common 4D-S(P)ED data analysis tasks and defining classes for important objects arising through the analysis[1]. The package was named *pyxem* as a library for *Pythonic Crys(X-)tallographic Electron Microscopy* [226]. This code development underpins a philosophy of data-analysis in which the methods applied to each dataset are written as a script, describing a workflow that may be modified and repeated, yielding reproducible results from an analysis perspective. To ensure the necessary robustness, hard coded unit tests were written for every function [227].

A python framework was chosen because it is increasingly recognized as the *lingua franca* of open-source scientific computing [228–230]. This wide usage and open-source philosophy has made many libraries available that can be built on. *Pyxem* depends primarily on: hyperspy for multi-dimensional data structures [231], diffpy for manipulation of atomic structures [232], scikit-learn for machine learning methods [233], scikit-image for image processing tools [234], numpy for array manipulations [235], scipy for common scientific operations such as fitting algorithms [236], and matplotlib for plotting [237]. Further, python is an object-oriented programming language [228–230], meaning that the code is organized around objects and methods that may be applied to those objects. This is conducive to developing adaptable analysis workflows in which objects are defined at various stages of processing and different paths may be followed from acquired data to final result.

[1]The code development was undertaken with Phillip Crout & Ben Martineau and all contributors to the project, can be viewed at: www.github.com/pyxem/pyxem/graphs/contributions. The overall architecture of the package as a framework for 4D-S(P)ED analysis and much of the code was due to the author.

Pyxem is a specialized extension of the hyperspy library [231] for multi-dimensional hyperspectral data analysis [231]. The pythonic object central to hyperspy is the *Signal* class, which provides a convenient way to address entries in a data array. If the data array is imagined as a tensor, D, of rank n then entries are addressed by n subscripts, $D_{i,j,\ldots,n}$. Addressing entries using subscripts is central to array based manipulations, which is the function of the numpy library [235]. If the data array is made a hyperspy *Signal* then instead of all indices being equivalent we can designate two kinds of subscript or equivalently two kinds of axis, which we refer to as either *navigation axes* or *signal axes*. In the context of a 4D-S(P)ED experiment the two axes corresponding to the real-space scan dimensions (i, j) are set as navigation axes and the two axes corresponding to the diffraction pattern plane (α, β) are set as signal axes, which can be written:

$$< i, j | \alpha, \beta > \tag{4.1}$$

The separation of axes in hyperspy enables functions to be written to apply to the signal axes and for these functions to then be iterated over the navigation axes efficiently. This iteration is achieved using the hyperspy *map()* function, which has the special features that: (1) navigation axes are preserved, (2) signal axes to be iterated may have arbitrary shape (including unequal lengths), (3) iteration may be performed in parallel. This function is used extensively within *pyxem* methods. Further, hyperspy offers access to unsupervised machine learning algorithms [233] and advanced model fitting routines [238].

4.1 Code Architecture

Specialized classes are implemented in *pyxem* for analysis of 4D-S(P)ED data and correspond to four kinds of object:

1. **Signals** contain raw or processed experimental data and define methods that may be applied to these data directly.

2. **Generators** establish conditions for performing simulations, comparing simulations with experimental data, or combining the results of two different analyses.

3. **Components** are computed objects that are fit in models to experimental data.

4. **Libraries** contain simulation results for later comparison with experimental data.

Objects in these classes can be combined to construct a wide range of 4D-S(P)ED data analysis workflows, as illustrated in Figure 4.1, creating a versatile analysis framework.

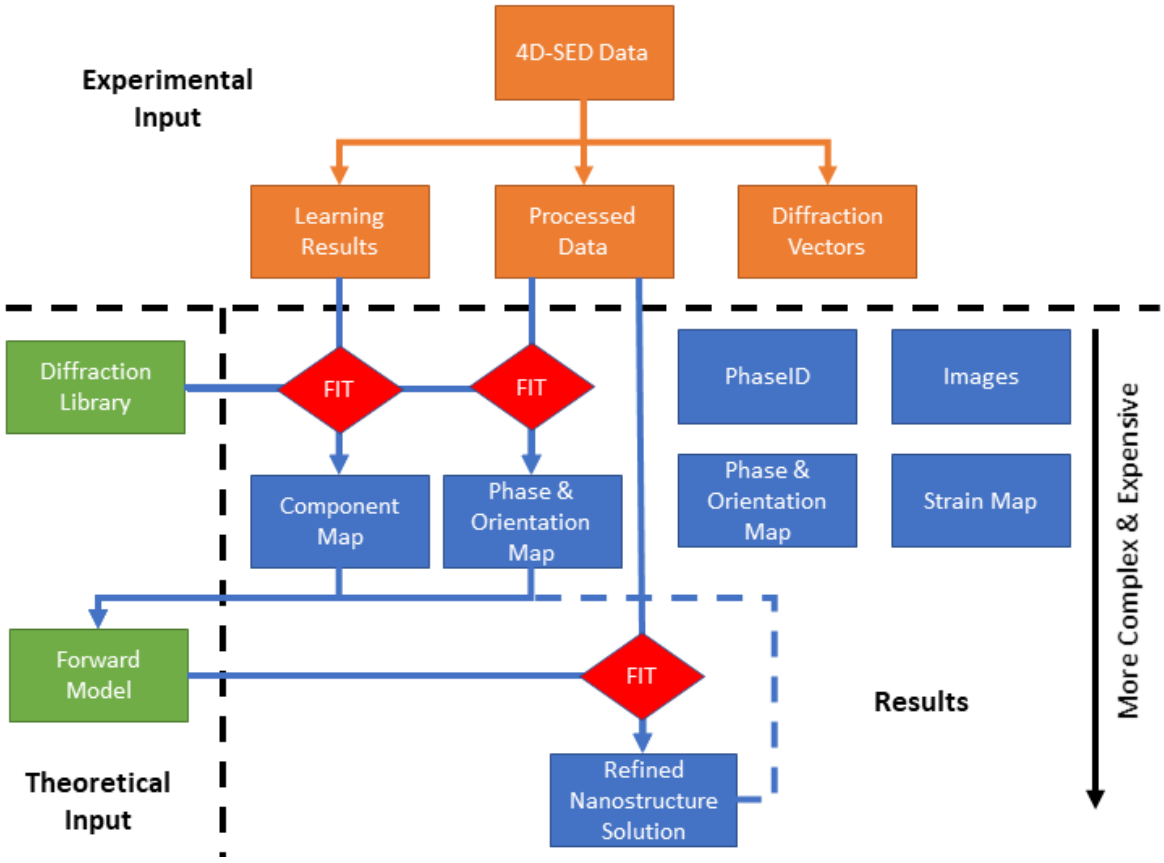

Fig. 4.1 **Analysis workflows in *pyxem*.** Flow diagram illustrating the architecture of *pyxem* and key steps involved in analysing 4D-S(P)ED data to extract physical insight.

Processing experimental data to glean physical insight is the primary objective when using *pyxem*. Many important data pre-processing steps are therefore defined as methods within the data containing *Signal* classes, which are the *ElectronDiffraction* class (see Section 4.2) and the *DiffractionVectors* class (see Section 4.3) for two-dimensional electron diffraction data. Physical insight is then obtained by incorporating *Generators, Components* and *Libraries* into workflows, which are described in detail for: *post-facto* diffraction contrast imaging (see Section 4.4), unsupervised machine learning (see Section 4.5), phase and orientation mapping (see Section 4.6), and strain mapping (see Section 4.7). The aim here is to illustrate the most important workflows, enabled by *pyxem*, that are used throughout this work.

4.1.1 Illustrative Data

Data analysis with *pyxem* is illustrated with data from a GaAs nanowire[2] grown by molecular beam epitaxy [239] and containing type I twin boundaries, as shown in Figure 4.2. Such twins can be described as a rotation of 180° about an axis normal to the $\{111\}$ twin plane [75], which is a $\langle 111 \rangle$ direction parallel to the long axis of the nanowire in this system. The twin boundaries provide a sharp interface when projected along a $\langle 110 \rangle$ direction, enabling analyses to be demonstrated clearly. The nanowire is several micrometres long and the cross-section is approximately hexagonal with a vertex-to-vertex distance of $\sim$ 150 nm.

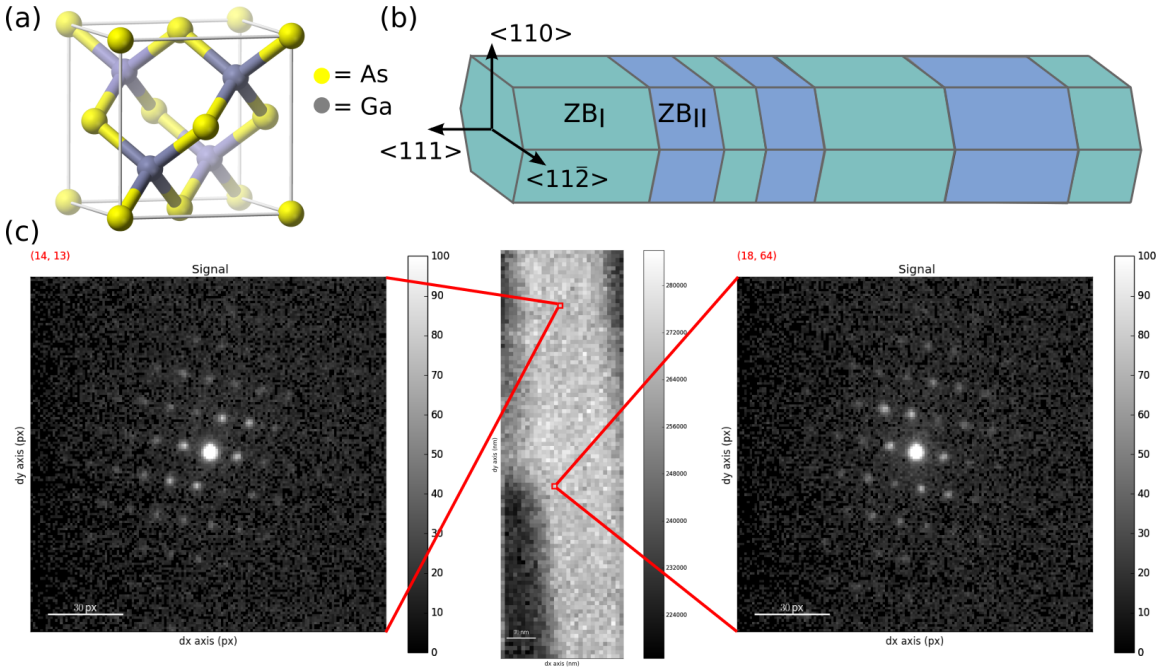

Fig. 4.2 **4D-SPED data from a GaAs nanowire.** (a) GaAs crystal structure. (b) Twinned nanowire geometry. (c) 4D-SPED data (35 mrad precession) navigated in *pyxem* by dragging the position marker. Diffraction patterns from two twinned crystals are shown with an image formed by integrating the intensity in each diffraction pattern.

4D-S(P)ED data were acquired using a Philips CM300 FEGTEM fitted with Nanomegas hardware and operated at 300 kV with a step size of $\sim$ 10 nm and an exposure time of 60 ms. The illumination convergence angle was $\sim$ 0.5 mrad and data were acquired with precession angles of 0 mrad, 9 mrad and 35 mrad so that the effect of precession on analysis could be explored. The scan was performed with 30×100 probe positions and electron diffraction patterns were recorded with 144×144 pixels. Noise and geometric distortion due to the off-axis camera geometry were significant, as shown in Figure 4.2c.

[2]Nanowire specimens were provided by Prof. Ton van Helvoort, NTNU, Norway.

4.2 *ElectronDiffraction* Signal Class

The *ElectronDiffraction* class defines an object for numerous two-dimensional electron diffraction patterns. Methods are defined to apply various processing steps prior to other analyses and to directly reveal structure, e.g. by *post-facto* imaging or unsupervised machine learning. The *ElectronDiffraction* class inherits from the hyperspy *Signal2D* class and typically has one or two navigation axes (real space) and two signal (reciprocal space) axes.

4.2.1 Data Corrections & Calibration

Common artifacts in 4D-S(P)ED data include: recorded intensities that depend on detector characteristics, geometric distortions due to non-ideal projector optics, and shifts in the direct beam position. Intensities may be most simply corrected by gain normalization using the *apply_gain_normalization()* method and geometric distortions may be corrected using the *apply_affine_transformation()* method, provided calibration data has been recorded. Alignment and centring of the diffraction patterns is essential for many subsequent analyses. The *center_direct_beam()* method achieves this by performing cross-correlations with circular elements of multiple sizes to determine the direct beam position, which is the maximum in the cross-correlation, with sub-pixel (~ 0.5 pixel) accuracy and shifting this position to the centre of the data array. The region within which the maximum cross-correlation is sought may be restricted to mitigate the effect of very strong Bragg reflections. In some cases the shift in the direct beam position is physically significant and the *get_direct_beam_position()* method returns these shifts for further analysis. The effects of geometric distortion correction and pattern centring are shown in Figure 4.3.

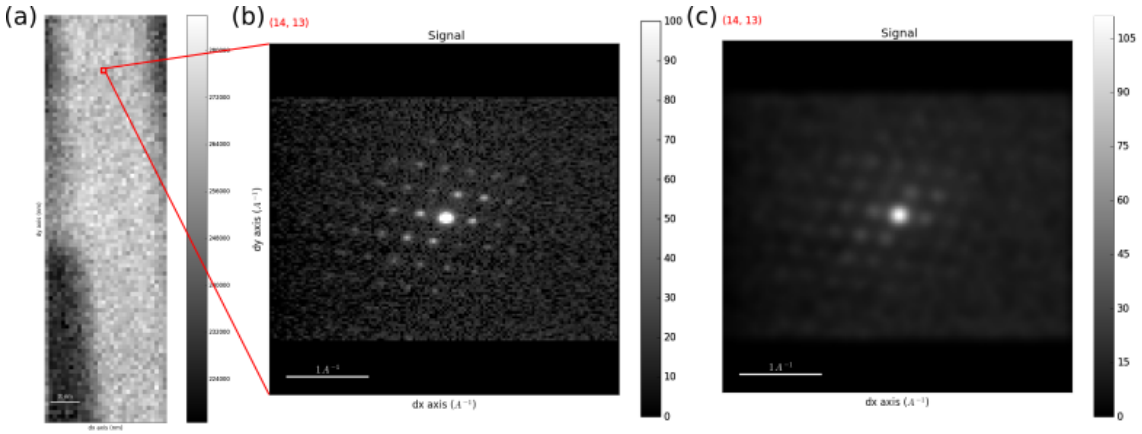

Fig. 4.3 **4D-S(P)ED data corrections & calibration**. (a) Navigation window showing diffraction pattern location. (b) Distortion corrected and centred diffraction pattern. (c) Cross-correlation with a disc element used for centring.

Axis calibration, following alignment and correction of the data, can be performed using the *set_scan_calibration()* and *set_diffraction_calibration()* methods enabling further operations to be performed in calibrated units. Values must first be determined using a reference sample and the reciprocal space calibration should be set in $Å^{-1}$/pixel to match simulations. Further, experimental metadata may be set using the *set_experimental_parameters()* method.

4.2.2 *ElectronDiffractionProfile* Analysis

Azimuthal integration of a two-dimensional electron diffraction pattern about its centre yields a one-dimensional *ElectronDiffractionProfile* signal of diffracted intensity as a function of scattering vector magnitude, as shown in Figure 4.4. This integration is performed using the *get_radial_profile()* method of an *ElectronDiffraction* object and significantly reduces the size of the data, sometimes without loss of information (e.g. polycrystalline ring patterns). Peaks may be found in the diffraction profile using the *find_peaks_ohaver()* method inherited from hyperspy, which is often useful for calibrating the diffraction plane or for performing phase identification by indexation of the scattering magnitudes, as shown in Figure 4.4b. Further possible analysis of radial profiles includes total scattering and powder diffraction methods, e.g. calculation of the one-dimensional pair distribution function [43].

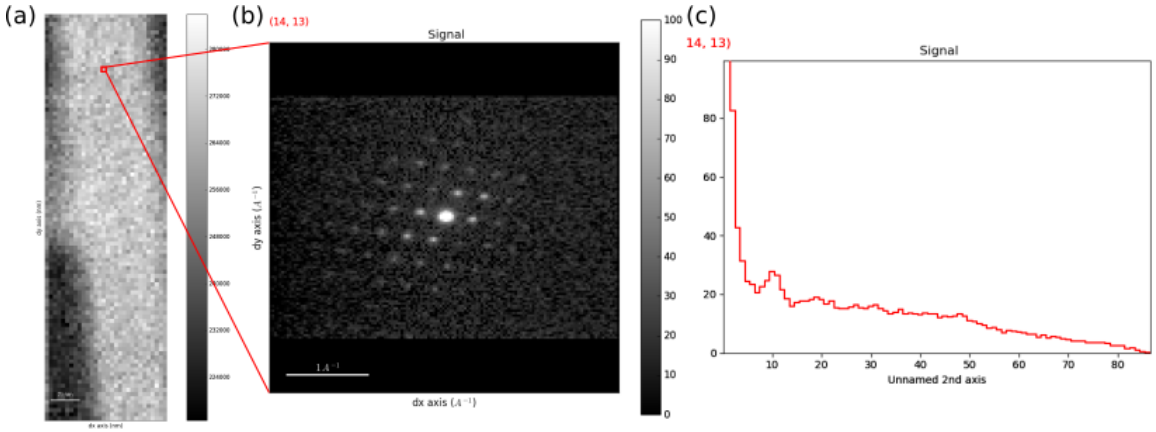

Fig. 4.4 ***ElectronDiffractionProfile* map**. (a) Navigation window showing diffraction pattern location. (b) Distortion corrected and centred diffraction pattern. (c) Radial profile obtained by azimuthal integration.

4.2.3 Background Subtraction

Background subtraction is typically applied to enable accurate diffracted intensities to be extracted or to achieve more reliable peak finding and pattern matching. If the aim is to extract intensities then the fidelity of the background subtracted intensities is critical, but applied as a pre-processing step for determination of pattern geometry, as is the case for most analysis presented here, factors such as computational efficiency and applicability to a wide range of data may be more important. A number of background subtraction methods, illustrated in Figure 4.5, are therefore made available through the *remove_background()* method, as follows:

- **h-dome**: A 'seed' image is formed by subtracting a constant offset from the raw image, which is then morphologically dilated to replace high values with nearby low values and this image is then subtracted from the raw diffraction pattern.
- **gaussian_difference**: Takes the difference between two Gaussian convolutions to determine peak positions and sets all other pixel values to zero.
- **median_filter**: Blurs each diffraction pattern with a median filter of manually specified size, which should be larger than the diameter of diffraction discs, and subtracts this from the raw pattern.
- **reference_pattern**: Subtracts a specified reference pattern, for example the average pattern from a region in the scan containing to specimen, from all recorded patterns.

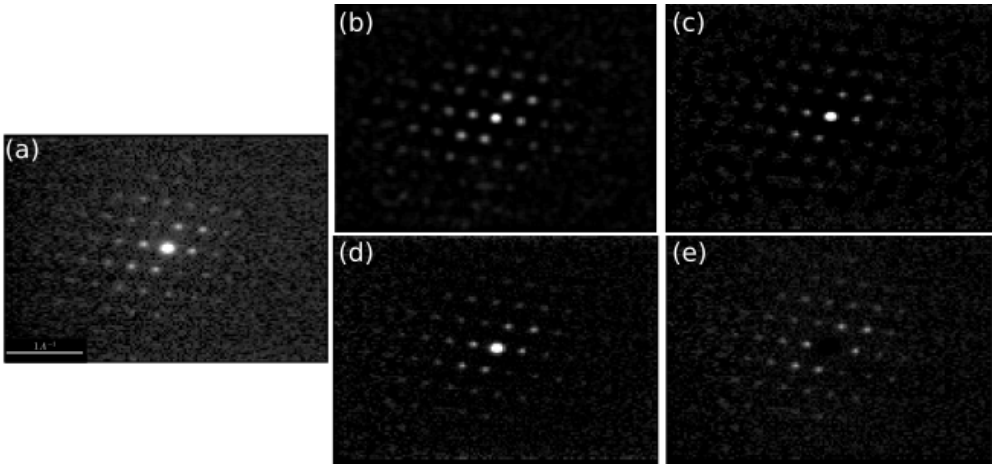

Fig. 4.5 **Background subtraction methods**. Background subtraction from (a) raw diffraction pattern shown in Figure 4.3b using various methods: (b) h-dome, (c) gaussian_difference, (d) median_filter, (e) reference_pattern. All shown on the same 0-100 scale.

4.2.4 Peak Finding

Determining the position of Bragg diffraction peaks in measured diffraction patterns enables scattering vectors to be associated with reciprocal lattice vectors of crystals and is the basis for much crystallographic analysis as defined for the *DiffractionVectors* class described in Section 4.3. Peak (or disc) positions can be found using various approaches, e.g. Figure 4.6, implemented in the *find_peaks()* method, as follows:

- **zaeferrer**: Uses a gradient threshold followed by a local maximum search within a square window, which is moved until it is centred on the brightest point and accepted as a peak if it is within a certain distance of the starting point [149].
- **stat**: Finds points with a statistically higher values than surrounding areas and iterates between smoothing and binarising until the number of peaks has converged [240].
- **laplacian_of_gaussians**: Computes the Laplacian of Gaussian images with successively increasing standard deviation and stacks them in a cube in which maxima are the peaks sought. This is a wrapper for scikit-image [234] functionality.
- **difference_of_gaussians**: The image is blurred with increasing standard deviations and the difference between two successively blurred images are stacked up in a cube in which maxima are the peaks. This is a wrapper for scikit-image [234] functionality.

These methods require parameters to be set manually, which may be done interactively using the utility function *find_peaks_interactive()*. The number of parameters and speed of these methods varies considerably. The 'stat' method requires the fewest parameters and but requires slow iterations and the Zaeferrer method is simple but not very robust. The matrix based, Laplacian of Gaussian and difference of Gaussian, methods are much faster and, although they have many manually determined parameters, the results are often relatively insensitive to changing parameters for data containing sharp diffraction peaks.

4.3 *DiffractionVectors* Signal Class

The *DiffractionVectors* class is a signal class for experimentally measured diffraction vectors in two-dimensions, as obtained by finding peaks in an *ElectronDiffraction* signal. These vectors are two-dimensional position vectors in calibrated units and may be manipulated in various ways prior to use for orientation or strain mapping (see Sections 4.6 & 4.7). The *DiffractionVectors* class inherits from the hyperspy *BaseSignal* class and typically has one or two navigation axes (real space) and ragged (varying number of peaks) signal axes.

A *DiffractionVectors* object can be reduced to contain each measured vector only once using the *get_unique_vectors()* method, based on a distance threshold with respect to vectors already included. The unique *DiffractionVectors* are useful for: phase identification, assessing the sampling of reciprocal space, and forming diffraction contrast images with all relevant conditions (see Section 4.4). The measured diffraction vectors may also be summarized by plotting a histogram of their magnitudes, as shown in Figure 4.6b, using the *get_magnitude_histogram()* method. The magnitude histogram may be indexed to assess crystal phases present, similar to peak finding in an *ElectronDiffractionProfile* with the advantage of an improved signal-to-noise ratio as compared with azimuthal integration. Further, the pixels in which diffraction vectors were recorded can be mapped, as shown in Figure 4.6c, using the *get_diffracting_pixels_map()* method, which may return the number of vectors per pixel or a binary map that reveals the location of crystals within a scanned region.

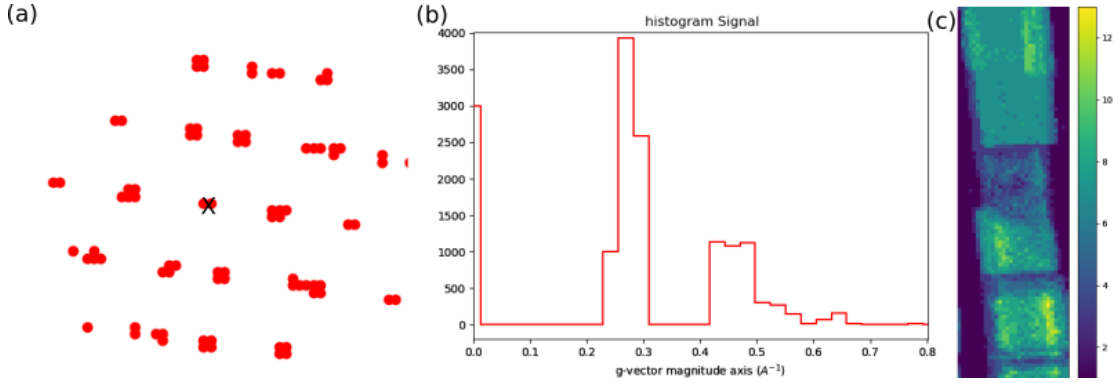

Fig. 4.6 **Diffraction vector analysis.** (a) Peaks found in the diffraction pattern averaged over the scan region. (b) Histogram of diffraction vector magnitudes indexed with respect to the GaAs structure. (c) Map of the number of diffraction vectors at each probe position.

4.4 Virtual Diffraction Contrast Imaging

Diffraction contrast images can be formed from 4D-S(P)ED data by plotting the intensity within a subset of pixels in the diffraction pattern as a function of probe position. Such images are referred to as "virtual dark-field" (VDF) images (see Chapter 2). Typically, integration windows are specified as discs around particular diffracting conditions or as annuli covering a particular scattering range, as shown in Figure 4.7. VDF images may be obtained interactively using the *plot_interactive_virtual_image()* method of an *ElectronDiffraction* signal or using a *VDFGenerator* class to form the VDF image associated with all vectors in a *DiffractionVectors* object for a particular *ElectronDiffraction* signal. In both cases, a *VDFImage* object is returned.

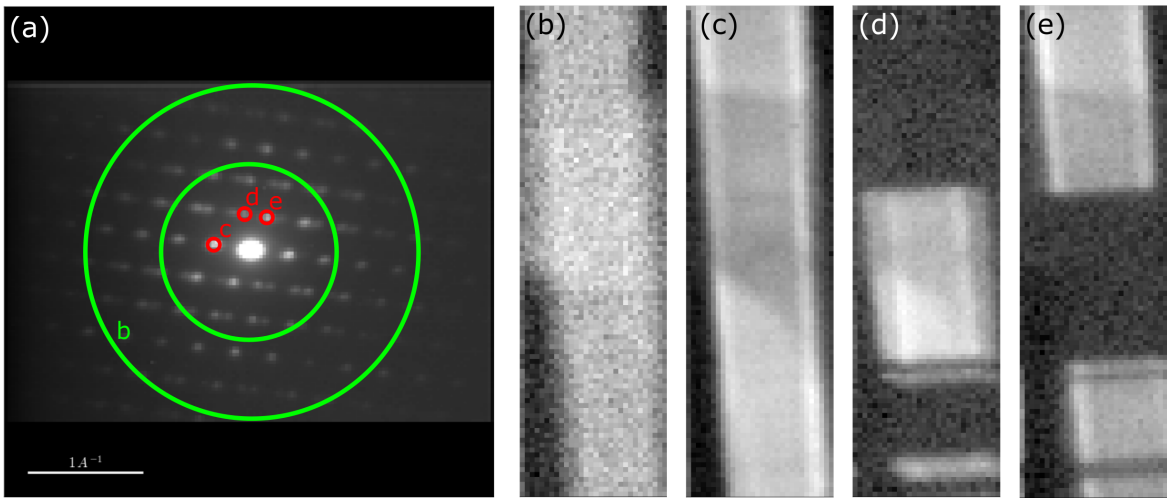

Fig. 4.7 **Virtual diffraction contrast imaging.** (a) Average diffraction pattern from the scan region with integration windows for image formation. (b) Annular VDF image showing the nanowire and carbon support film. (c) VDF image using reflection common to both twins. (d,e) VDF images using reflections unique to each twin.

Contrast in VDF images may be interpreted by analogy to diffraction contrast imaging in conventional TEM and to STEM performed with annular detectors, which have received extensive consideration in literature, as discussed in Chapter 2. Indeed VDF imaging is a form of 4D-STEM imaging with the primary difference being that the camera length is selected to maximise the visible diffraction pattern, which typically restricts the annular integration range to ~ 30 mrad. This range falls within the medium angle annular dark-field regime in which diffraction contrast dominates. The analogy with diffraction contrast imaging performed in a conventional TEM for VDF images formed with discs around diffracted beams is perhaps less obvious since the illumination is a focused probe in SED as compared with parallel illumination in conventional TEM. However, typically the convergence angle in SED is sufficiently small (i.e. ~ 1 mrad) that the range of incidence angles is similar to conventional TEM. The theory of diffraction contrast imaging based on the column approximation (see Chapter 2) is developed fully in terms of the intensity of diffracted beams (i.e. with phase information already lost), which means that the theory should apply exactly to SED data provided that the column size is considered as the volume sampled at each probe position. If a SPED experiment is performed, with double-conical-rocking illumination, then the situation is analogous to conical dark-field imaging.

4.5 Unsupervised Machine Learning

Unsupervised learning is a descriptive form of machine learning, which aims to find patterns in data given only the data and minimal constraints [241]. 4D-S(P)ED data typically comprises many more diffraction patterns than significantly distinct microstructural elements (e.g. crystal phases or orientations) in the region sampled. A dimensionality reduction, ideally to one representative diffraction pattern per microstructural element, may then be possible. Further, some diffraction patterns will contain contributions from multiple microstructural elements sampled along the beam path. Unmixing these *mixed* diffraction patterns is important (e.g. for crystallographic tomography [164, 165]) and may be possible due to the experimental oversampling. Unsupervised learning may enable both dimensionality reduction and signal unmixing by learning *component patterns* that make up the data, together with their associated *loadings* at each scan pixel, as illustrated in Figure 4.8.

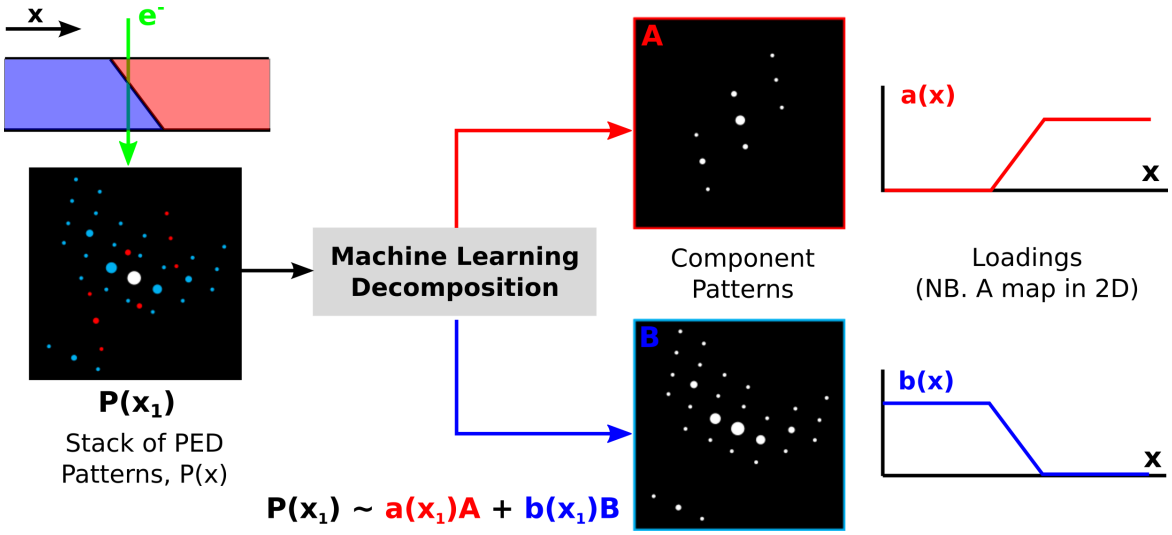

Fig. 4.8 **Unsupervised learning principle for 4D-S(P)ED data.** Electron diffraction patterns are acquired from many positions in each distinct microstructural element, enabling component patterns and spatial loadings to be learned even in overlapping regions.

In analytical electron microscopy, the oversampling and signal mixing described above are common and unsupervised learning techniques [242, 243] have been applied to electron energy loss [244] and energy dispersive X-ray [245] spectral data as well as 4D-S(P)ED data [164]. The methods applied so far, in electron microscopy, have been *latent linear models* and important such methods are made available through *pyxem*. As linear models, there is an implicit assumption that signal mixing is linear, which does not, in general, reflect the physics of electron scattering. Therefore a validation and assessment of the limitations of these methods, as applied to 4D-S(P)ED data, is presented.

4.5.1 Learning with Linear Latent Variable Models

Latent linear models describe data by linear combination of *latent variables* (or basis vectors) that are learned from the data rather than measured. If the data lie close to a manifold of lower dimensionality than the original data space, then the data can be well approximated using a smaller number of variables, revealing *intrinsic dimensionality* in the data. With appropriate constraints, learned basis vectors may also be physically interpretable.

A linear model of a data matrix, $\mathbf{X}$, can be expressed as a matrix of linear basis vectors, $\mathbf{W}$, and corresponding loadings, $\mathbf{Z}$. The reconstruction error may be expressed as an objective function to be minimized in a least squares scheme:

$$||\mathbf{X} - \mathbf{WZ}||_F^2 \tag{4.2}$$

where $||\mathbf{A}||_F$ is the Frobenius norm[3] of matrix $\mathbf{A}$. Alternative objective functions may be defined, for example incorporating sparsity promoting weighting factors [241], but only objectives of the form in Equation 4.2 were used here. The decomposition is not necessarily performed by error minimization but this expression is useful for comparison.

4D-S(P)ED data is manipulated into a data matrix, $\mathbf{X}$, by transforming each $m \times m$ diffraction pattern into a one dimensional vector and flattening the $p \times q$ scan dimensions to produce a $m^2 \times pq$ data matrix. The data matrix is then decomposed, as in Figure 4.9, into an $m^2 \times j$ factor matrix, $\mathbf{W}$ and a $j \times pq$ loading matrix, $\mathbf{Z}$. Constraining the decomposition may lead to rows of $\mathbf{Z}$ that are interpretable as the spatial distribution of component diffraction patterns, which are the columns of $\mathbf{W}$. Choosing the number of latent dimensions, j in which to describe the data is challenging because as a decomposition, rather than a generative model of the data, any metric based on accurate representation of the data will always improve if more latent dimensions are included. This problem is typically addressed by plotting the reconstruction error for increasing latent dimensions, i.e. a "scree plot" as Figure 4.10, and identifying a transition from relatively large errors to relatively small errors [241, 246].

Three linear decompositions were explored, namely: principal component analysis (PCA) [241], independent component analysis (ICA) [247], and non-negative matrix factorisation (NMF) [248, 249]. The implementations used were those available through HyperSpy [231], which draws on scikit-learn [233]. PCA corresponds to $\mathbf{W}$ being orthonormal. The optimal solution to rank L is then obtained when $\mathbf{W}$ is estimated by eigenvectors corresponding to the L largest eigenvalues of the empirical covariance matrix[4]. These eigenvectors are known as *principal components*. The optimal low-dimensional encoding of the data is given by

[3]The Frobenius norm is defined as; $||\mathbf{A}||_F = \sqrt{\sum_{i=1}^{m}\sum_{j=1}^{n} a_{ij}^2} = \sqrt{tr(\mathbf{A}^T\mathbf{A})}$

[4]The empirical covariance matrix, $\Sigma = \frac{1}{N}\sum_{i=1}^{N} \mathbf{x}_i\mathbf{x}_i^T$

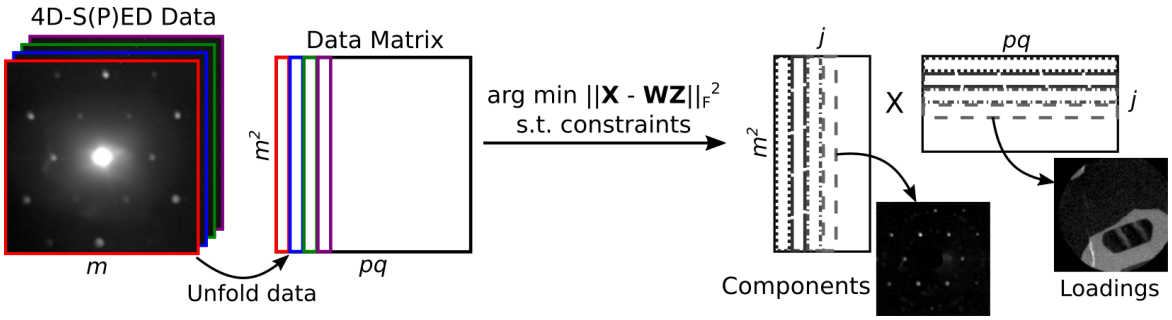

Fig. 4.9 **Learning by linear decomposition.** Visual representation of the linear decomposition of data matrix, $\mathbf{X}$, into a component matrix, $\mathbf{W}$, and a loading matrix, $\mathbf{Z}$, to obtain a rank-L approximation to the data.

$\mathbf{z}_i = \mathbf{W}^T\mathbf{x}_i$, which is an orthogonal projection of the data on to the corresponding principal subspace and maximises the statistical variance of the projected data. Further, this optimal reconstruction may be obtained via truncated singular value decomposition (SVD) of the data matrix [241], which enables efficient computation. PCA is therefore a statistical and well posed decomposition that can be computed efficiently to determine intrinsic dimensionality but, as will become clear, it is not ideal for learning physical signals.

Determining source signals from mixed measurements, without knowledge of the sources, is known as blind source separation (BSS) [241]. PCA is not effective for BSS, i.e. principal components do not typically correspond well with the original sources, because the constraints discussed above correspond to the assumption that each source has a Gaussian distribution. The symmetry of this provides no way to determine the appropriate rotation in the principal subspace to uniquely recover source signals. ICA identifies this rotation by allowing non-Gaussian distributions and maximizing non-Gaussianity, which is equivalent to maximising mutual independence or information entropy [250]. Data previously projected using PCA can be treated with ICA using the widespread FastICA algorithm [247].

NMF [248, 249] imposes $\mathbf{W} \geq 0, \mathbf{Z} \geq 0$ and is typically achieved by numerical minimisation of Equation 4.2. As a minimisation, there is no guarantee of convergence to a global minimum and the results may be sensitive to initialization. The implementation used here initializes the optimization using a non-negative double singular value decomposition (NNDSVD), which is based on two SVD processes, one approximating the data matrix, the other approximating positive sections of the resulting partial SVD factors. This algorithm gives a well defined non-negative starting point suitable for obtaining a sparse factorization by subsequent coordinate descent minimisation. It should be noted that the product $\mathbf{WZ}$ is invariant under the transformation $\mathbf{W} \to \mathbf{W}\Lambda$, $\mathbf{Z} \to \Lambda^{-1}\mathbf{Z}$, where Λ is a diagonal matrix, so components and loads may linearly be rescaled.

4.5.2 Unsupervised Learning of 4D-S(P)ED Data

Linear decomposition was applied to 4D-S(P)ED data acquired from the GaAs nanowire [5], with and without precession, as shown in Figure 4.10. Bending of the nanowire is evident in the data acquired without precession since at position iii the it is near zone axis, whereas at position i a Laue circle is visible. The radius of the Laue circle estimates the bending angle as ∼24 mrad. When a precession angle of 35 mrad (i.e. larger than the bending angle) was used all measured patterns appear close to zone axis due to the reciprocal space integration achieved by precession. This integration also affects VDF image contrast, which shows bend contours without precession and more homogeneous intensity with precession. Precession therefore leads to the data better approximating one diffraction pattern per microstructural element, i.e. two twinned crystals and vacuum surrounding the sample. The region of interest also contains a small portion of carbon support film, which is just visible in the virtual dark-field images as a subtle change in image intensity.

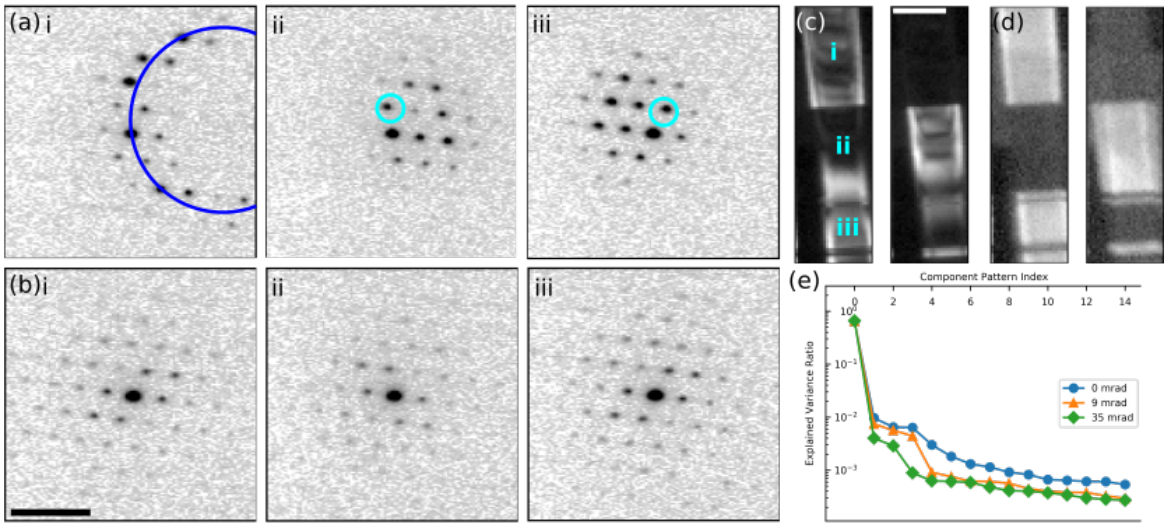

Fig. 4.10 **4D-S(P)ED data for unsupervised learning.** (a) Without and (b) with 35 mrad precession leading to (c,d) smoother 111 VDF images (3 pixel integration) and (e) a fewer significant principal components.

Scree plots showing the fraction of total variance in the data explained by each principal component pattern, obtained following SVD, are shown in Figure 4.10e. A regime change, from relatively high variance components to relatively low variance components, may be identified [241, 246] after 3 components for the data acquired with 35 mrad precession, after 4 components with 9 mrad precession, and cannot clearly be identified without precession. The use of precession therefore reduces the the number of components required to describe the

[5] This work was reported in collaboration with Ben Martineau in [251]

data, consistent with the intuitive understanding of the effect of reciprocal space integration on SPED data. The 4th component, in the 9 mrad data, arises because the top and bottom of the nanowire are sufficiently misoriented to be distinguished by the decomposition. Further analysis was therefore focused data acquired with larger precession angles.

Component patterns and corresponding loading maps obtained by SVD, ICA and NMF of 35 mrad SPED data are shown in Figure 4.11. In all these analyses the first component pattern corresponds to the vacuum surrounding the nanowire. The second and third component patterns correspond to the two twinned crystal orientations of the nanowire. However, in results obtained by SVD and ICA the learned component patterns contain significant negative intensities and so do not correspond well with the source diffraction signals. The description of the data is mathematically sensible and physical insight can be obtained from the differences between diffraction patterns that are highlighted by negative values in the SVD and ICA component patterns. NMF performed with 3 components, guided by the intrinsic dimensionality indicated by the SVD analysis, yielded learned component patterns that more closely resemble physical diffraction patterns. In the NMF component patterns, white spots are visible, representing intensity lower than background level. We describe these as a pseudo-subtractive contribution of intensity from those locations.

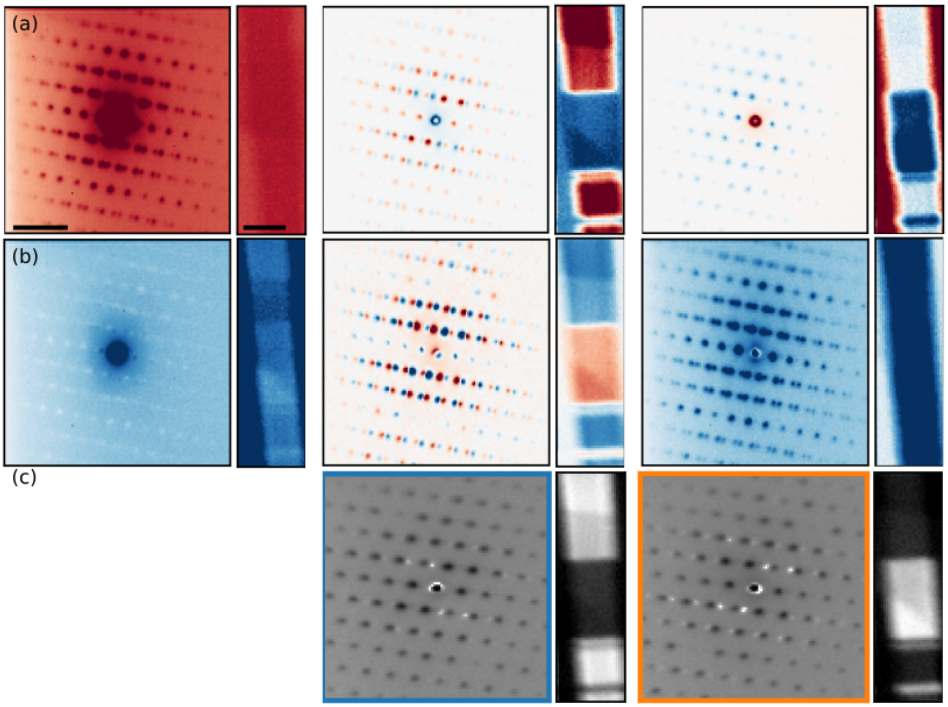

Fig. 4.11 **SVD, ICA and NMF analysis of SPED data.** First 3 (a) SVD components, (b) ICA components and (c) NMF components. Red indicates positive values and blue indicates negative values. Scale bars measure 1 Å^{-1} and 150 nm.

The unmixing of diffraction signals from overlapping crystals was investigated. SPED data with a precession angle of 18 mrad was acquired from a nanowire tilted away from the $[1\bar{1}0]$ zone axis by $\sim$30°, such that two twins overlapped in projection. The overlap of the two crystals was assessed using VDF imaging and NMF loading maps, as shown in Figure 4.12, which give good agreement. The VDF result can be considered a reference and is obtained with minimal processing but requires manual specification of appropriate diffracting conditions for image formation. The NMF loading corresponding to the background component decreases along the profile, which may be related to the underlying carbon film and the direct beam intensity is much lower in the NMF component patterns than in the true source signals. NMF therefore achieves a successful decomposition of the SPED data, but some unintuitive and potentially misleading features are present in the learning results, which directs attention towards potential limitations.

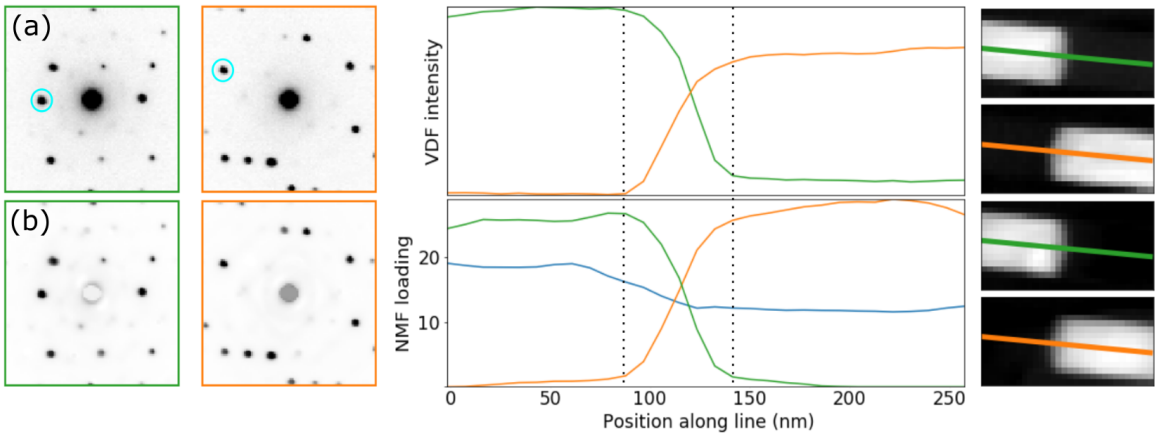

Fig. 4.12 **SPED data overlapping twins in a GaAs nanowire.** (a) Virtual dark-field images formed, using a virtual aperture 4 pixels in diameter, from the circled diffraction spots. (b) NMF decomposition results. In (b) the profile is taken from the line scans indicated, and the blue profile represents the intensity of the background component.

4.5.3 Limitations of Machine Learning 4D-S(P)ED Data

NMF was demonstrated above to yield a small number of component patterns that resemble physical electron diffraction patterns. Artifacts in the learning results were however identified, particularly when applied to achieve signal unmixing, and these are explored further. To illustrate potential artifacts, model SPED datasets were constructed based on line scans across inclined boundaries in hypothetical bicrystals, as shown in Figure 4.13. These models were intended to reflect features of two-dimensional diffraction-like signals rather than the physics

of diffraction and were constructed with the strength of the signal directly proportional to thickness of the hypothetical crystal at each point, with no noise, and Gaussian peak profiles.

Two model SPED datasets are shown in Figure 4.13. The first comprises the linear summation of two square arrays of Gaussian peaks with no overlap between the two patterns. NMF decomposition exactly recovers the signal profile in this simple case. The second is composed of two source signals that contain coincident peaks from distinct microstructural elements. This is similar to the physical case where a crystallographic orientation relationship exists between crystals. In this case, the NMF decomposition yields a factor containing all of the common reflections and a factor containing the reflections unique to only one end member. Whilst this is interpretable, it is not physical, although it should be noted that this is an extreme example where there is no unique information in one of the source patterns. Nevertheless, it should be expected that the intensity of shared peaks is likely to be unreliable in the learned factors and this was the case for the direct beam in learned component patterns shown in Figure 4.12. As a result, components learned through NMF should not be analysed quantitatively. This problem may be mitigated by enforcing a sum-to-one constraint on the loadings learned through NMF during optimization. See for example [252].

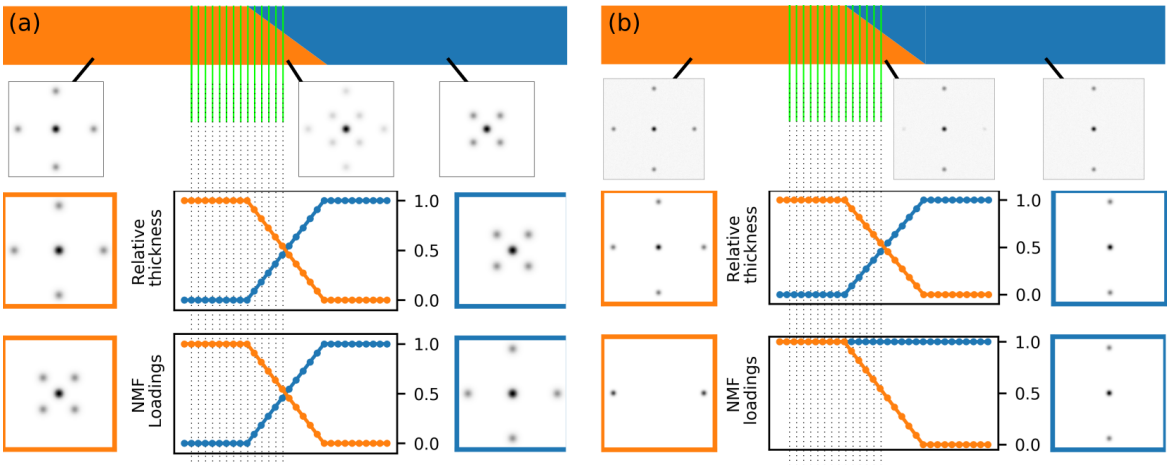

Fig. 4.13 **Non-independent components.** (a) Expected result for an artificial dataset with two ‘phases’ with overlapping peaks. (b) NMF decomposition.

Precession was found empirically to improve machine learning decomposition and this was attributed primarily to integration through bending of the nanowire. Precession may also result in a more monotonic variation of diffracted intensity with thickness [253] as a result of integration through the Bragg condition. It was therefore suggested that precession may improve the approximation that signals from two overlapping crystals may be considered to be combined linearly. To explore this a multislice simulation was performed[6] for a twinned

[6]This simulation was performed by Dr. Alex Eggeman.

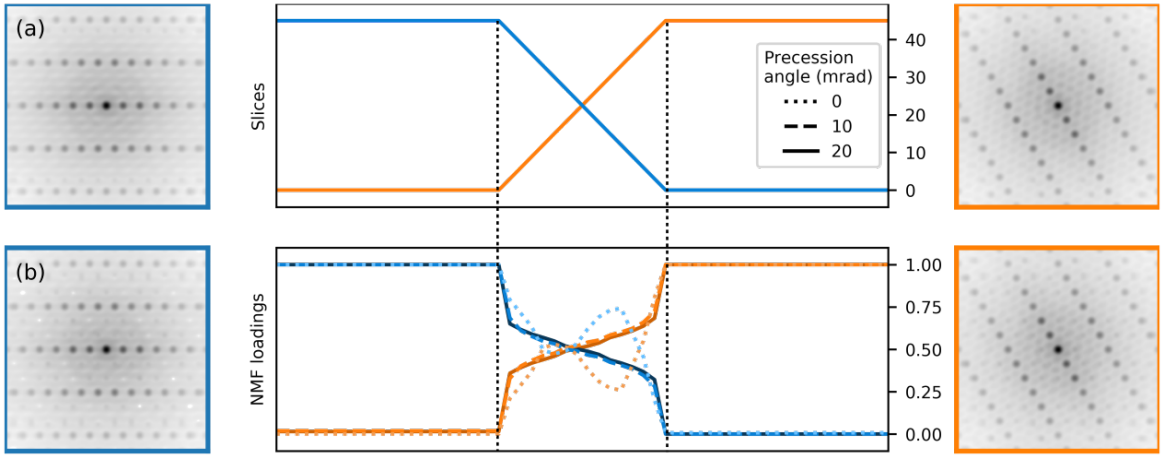

Fig. 4.14 **Unsupervised learning applied to dynamically simulated data.** (a) Original data with a 20 mrad precession angle. (b) NMF decomposition, in which the loadings have been re-scaled as in Figure 4.13. Without precession, NMF cannot reproduce the original data structure.

bi-crystal model constructed with the normal to the $[111]$ twin boundary inclined at an angle of 55° to the incident beam direction so that the two crystals overlapped in projection. In this geometry both crystals are oriented close to $\langle 511 \rangle$ zone axes with coherent matching of the $\{0\bar{6}\bar{6}\}$ and $\{2\bar{8}\bar{2}\}$ planes in these zones. Three precession angles were simulated using the TurboSlice package [205]: 0, 10 and 20 mrad, with 200 distinct azimuthal positions about the optic axis to ensure appropriate integration in the resultant simulated patterns [187]. The crystal model used in the simulation comprised 9 unique layers each 0.404 nm thick. 15 layers were used leading to a total thickness of 54.6 nm. These 512×512-pixel patterns with 16-bit dynamic range were convolved with a 4-pixel Gaussian kernel.

Decomposition of the dynamically simulated SPED data showed that without precession NMF loadings do not increase monotonically with thickness but rather vary significantly in a manner reminiscent of diffracted intensity modulation with thickness due to dynamical scattering. A subsidiary minimum is reached when the corresponding component is just thicker than half the thickness of the simulation, which corresponds to a thickness of approximately 100 nm. This is similar to the $2\bar{2}0$ extinction length for GaAs of 114 nm, which is the dominant scattering vector. With 10 or 20 mrad precession this intensity modulation is suppressed and the loading maps obtained show a monotonic increase across the inclined boundary. Precession is therefore beneficial for the application of unsupervised learning algorithms both in reducing the impact of bending, which is a common artifact of specimen preparation, and of dynamical signal mixing.

Noise and background are both significant in determining the performance of unsupervised learning algorithms. Extensive exploration of these parameters is beyond the scope of this work but it is noted that the various direct electron detectors that have recently been developed and that are likely to play a significant role in future SPED studies have very different noise properties and understanding the optimal noise performance for unsupervised learning may become an important consideration. The pseudo-subtractive features of NMF decomposition may become more significant with a higher background level.

4.5.4 Prospects for Machine Learning SPED Data

Unsupervised machine learning methods, particularly NMF, have been demonstrated to be capable of learning the significant microstructural features within SPED data in cases where the region of interest comprises a finite number of significantly different microstructrual elements, i.e. crystals of particular phase and/or orientation. SVD and ICA provide effective dimensionality reduction but the components are not readily interpreted using analogous methods to conventional electron diffraction analysis, owing to the presence of many negative values. The SVD and ICA results do nevertheless tend to highlight physically important differences in the diffraction signal across the region of interest. The massive data reduction is very useful, as is the unmixing achieved. None of these approaches are well suited to mapping continuous changes in crystal structure and in this case it is more appropriate to use phase, orientation and strain mapping methods described in Sections 4.6 and 4.7.

4.6 Phase & Orientation Mapping

Phase and orientation mapping based on spot diffraction pattern analysis is typically achieved in two ways: (1) by automated indexation of measured diffraction vectors [9], based on comparing vector magnitudes and inter vector angles with given structures (see Section 4.6.1); and (2) by pattern matching [150], based on comparing each measured diffraction pattern against a library of simulated templates (see Section 4.6.2). Both approaches are implemented in *pyxem* and have complementary features, as discussed in Section 4.6.3. Both methods involve two primary steps: (1) generation of a *DiffractionLibrary* or *VectorLibrary* for all expected crystal structures, which must be specified at least in terms of unit cell parameters, in a *StructureLibrary*[7] and (2) comparison between the theoretical and experimental data.

[7]Restricting the *StructureLibrary* to the minimal number of phases and orientations required to describe the microstructure, based on prior characterisation, can increase the speed of the matching step significantly.

4.6.1 Vector Indexation

Vector based indexation for phase and orientation determination has been implemented by a number of authors, in the context of crystallographic mapping [149, 165]. The *Diffraction-Library* constructed for such indexation comprises a lookup table of all reciprocal lattice vector magnitudes up to a specified threshold and a lookup table of all pairs of reciprocal lattice vectors and the corresponding inter-vector angles, which is thus purely based on lattice geometry. These theoretical vector magnitudes and inter-vector angles are then compared, within given tolerances, with the corresponding quantities for the measured *DifractionVectors* in the data. Possible indexations for each pair of measured vectors are thus obtained and corresponding orientations may be calculated [149] by solving:

$$\begin{aligned} \mathbf{g}^o_{(hkl),1} \cdot \mathbf{r}^o_{[uvw]} &= d_{hkl,1}\cos(\alpha_1) \\ \mathbf{g}^o_{(hkl),2} \cdot \mathbf{r}^o_{[uvw]} &= d_{hkl,2}\cos(\alpha_2) \\ |\mathbf{r}^o_{[uvw]}| &= 1 \end{aligned} \tag{4.3}$$

where; $\mathbf{g}^o$ is a reciprocal lattice vector in the orthonormalized crystal coordinate system, $\mathbf{r}_{[uvw]}$ is the beam direction or the goniometer axis to be found and α is the angle between the indexed diffraction vector and the direction sought as measured from the experiment [149]. Having calculated the crystal orientation corresponding to each possible indexation a self-consistent explanation, up to a defined tolerance is sought for all vectors in each recorded diffraction pattern [149]. If necessary, some vectors may be excluded to obtain a match.

4.6.2 Pattern Matching

Pattern matching for phase and orientation mapping was introduced by Rauch & Dupuy[8] [150] and is illustrated in Figure 4.15. Both library generation and data comparison steps are more involved than for vector indexation, but also offer more opportunity for development. Library generation for pattern matching requires specification of the full crystal structure, in order to correctly simulate diffracted intensities, and the expected orientations of the crystal structure for which to perform the simulation. Orientations may be uniformly sampled from the symmetry reduced region of orientation space[9] or may be restricted to an angular range away from a reference, as appropriate for the specimen. The generation of a *DiffractionLi-*

[8]The Rauch & Dupuy implementation formed the basis of a commercial phase and orientation mapping package, called ASTAR, which was used for much of the work presented in Chapter 6.

[9]The ASTAR package uses an equal number of steps between the vertices of the symmetry reduced pole figure segment, which is a somewhat inhomogeneous sampling of orientation space.

brary then requires an electron diffraction simulation to be performed for each structure and orientation. So far, only the simplest kinematical simulations are used to generate point like geometric templates with associated intensities both using the *DiffractionLibraryGenerator()* of *pyxem* and in commercial solutions.

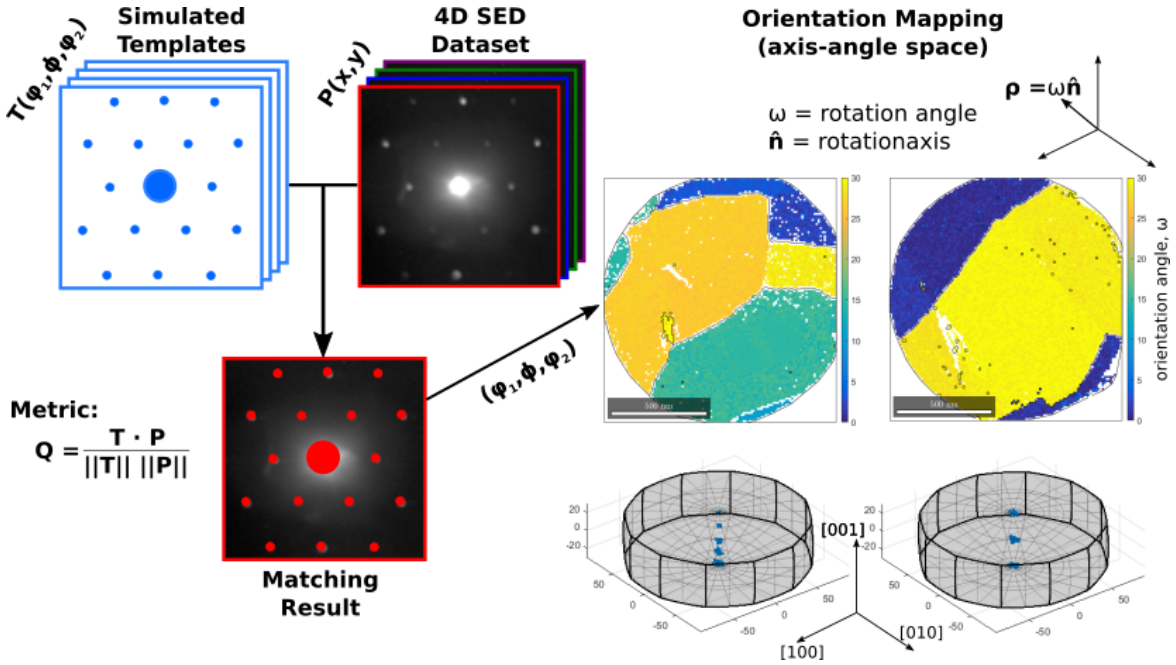

Fig. 4.15 **Phase and orientation mapping by template matching.** Each experimental diffraction pattern in the 4D-SED dataset is compared against a library of simulated templates by evaluating a matching metric. The phase and orientation mapping results obtained may be analysed in numerous ways e.g. Chapter 6.

Comparison between theoretical templates and experimental S(P)ED data is achieved using an *IndexationGenerator*, which is initialized with an *ElectronDiffraction* object containing experimental data and a *DiffractionLibrary* containing simulated templates, to perform comparison between theoretical templates and experimental data by maximizing a normalized correlation index, Q_i, which Rauch & Dupuy [150] defined as:

$$Q_i = \frac{\sum_{x,y} P(x,y) T_i(x,y)}{\sqrt{\sum_{x,y} P^2(x,y)} \sqrt{\sum_{x,y} T_i^2(x,y)}} \tag{4.4}$$

where $P(x,y)$ is the intensity of the pixel with coordinates (x,y) in the experimental diffraction pattern and $T_i(x,y)$ is the intensity of template i at (x,y). Efficient evaluation of Equation 4.4 is achieved by only considering pixels corresponding to non-zero values in the geometric templates. In *pyxem*, Q_i is normalized only by T to avoid the computationally costly product over the experimental pattern.

This metric has two primary limitations: (1) the range of values is not normalized between different phases meaning that some phases will typically give higher scores than others, and (2) the presence of additional diffraction peaks in the experimental diffraction pattern with respect to the template is not penalized but the opposite is. It should also be noted that this matching is typically performed after various preprocessing steps have been applied to the electron diffraction data to mitigate issues with matching diffuse background.

4.6.3 Vector Indexation vs. Pattern Matching

Pattern matching is computationally attractive, achieving both indexation and orientation determination in a single step. It has yielded sensible results in a number of cases and has become widely adopted in comparison with vector based approaches owing to both speed and commercialization. However, as implemented, pattern matching may produce apparently reasonable results from specimens where it is unclear that a single phase and orientation can sensibly be assigned to each pixel in two-dimensions [254] due to multiple crystals being sampled along the beam path. Care must therefore be taken. Vector indexation highlights such issues and the identification of nonassignable vectors may be helpful, but will never go beyond geometry. Pattern matching may become a route to more physical insight if simulations and matching metrics are developed further.

4.7 Strain Mapping

A crystal oriented near to a major zone axis will produce an electron diffraction pattern that can be approximated as a two-dimensional lattice of *DiffractionVectors* with two basis g-vectors. When the crystal is strained, with components perpendicular to the beam direction, the basis g-vectors recorded are transformed by a two-dimensional affine transformation, **H**, associated with the distortion, as illustrated in Figure 4.16.

The affine transformation, **H**, obtained from diffraction data is in the reciprocal basis but can be readily related to an affine transformation in direct space, $\mathbf{F} = \mathbf{H}^T$ [145]. This direct space affine transformation can then be separated into a rotation matrix, **R**, and a distortion matrix, **U**, by polar decomposition and related to strain, ε, as:

$$\begin{aligned} \mathbf{F} &= \mathbf{RU} \\ \varepsilon &= \mathbf{U} - \mathbf{I} \end{aligned} \tag{4.5}$$

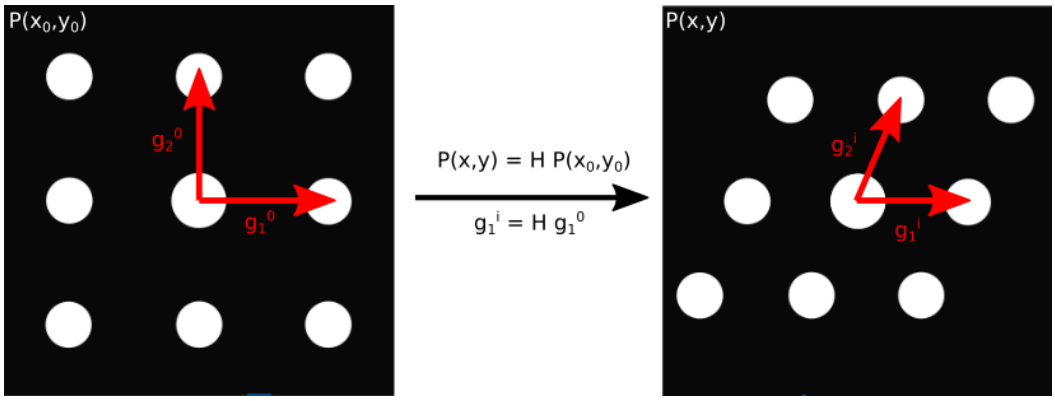

Fig. 4.16 **Strain mapping as a two-dimensional affine transformation.** Near to a major zone axis the diffraction pattern is approximately a two-dimensional lattice that is distorted by lattice strain, which it is the aim to map.

Mapping the two-dimensional transformation of basis vectors to determine local strain and rotation has become an important application of 4D-S(P)ED [163]. Typically vectors are assigned to peaks/discs found in the data and compared with a reference region (see Section 4.7.1). A novel method was implemented in this work, based on selecting a reference diffraction pattern within the data and calculating the image affine transform between it and all others (see Section 4.7.2). The relative merits of these methods are discussed in Section 4.7.3 and only the image affine transform approach is used throughout this work.

4.7.1 Vector Transformation

Determining two basis g-vectors, $\mathbf{g}_1$ and $\mathbf{g}_2$, enables a local "diffraction matrix" $\mathbf{G}$ to be constructed [255, 157] for each probe position as:

$$\mathbf{G} = \begin{pmatrix} g_{x1} & g_{x2} \\ g_{y1} & g_{y2} \end{pmatrix} \tag{4.6}$$

If G_0 is the reference diffraction matrix then a distortion matrix can be defined:

$$\mathbf{F} = (\mathbf{G}_0\mathbf{G}^{-1})^T \tag{4.7}$$

which is easily related to strain by Equation 4.5. The sensitivity of this approach depends primarily on how precisely g-vectors can be measured, which has been found to be easier when larger, but not overlapping, discs are recorded [10] and when precession is used [189]. Often only two diffraction discs are used to determine basis vectors [27], but more recent work has sought to refine the whole lattice [157, 160, 256].

4.7.2 Image Transformation

The image affine transformation approach implemented in *pyxem* casts the strain mapping problem as a model fitting problem. A model is constructed comprising *ScalableReferencePattern* component, which is a pattern, $P(x_0, y_0)$, identified as an unstrained reference within the data[10], transformed by a two-dimensional affine transformation, $\mathbf{H}$ using the transformation implemented in scikit-image [234], to model the other diffraction patterns:

$$P(x, y) = \mathbf{H}P(x_0, y_0) \tag{4.8}$$

This two-dimensional affine transformation has 3 independent parameters that are refined by model fitting, typically using a least squares cost function. Model fitting involves two major steps: (1) initialization of the problem with a starting model, and (2) fitting the model by refining parameters to minimize an appropriate cost function. These problems are coupled when fitting numerous signals from material that is connected, because having successfully fitted one signal it is a good guess to attempt to fit signals from neighbouring probe positions using the result of the first fitting as initialization. This strategy is adopted in the "Smart and Adaptive Model Fitting" (SAMFire) capability of hyperspy [238] and numerous initial fits may be made at the outset if there is known heterogeneity e.g. grain structure. It was found to be essential to use this approach, or else initialize every fit from the identity matrix, which is much slower, to avoid local minima or divergence. A demonstration of this image transformation approach is reported in Chapter 5 along with a practical estimation of errors. In practice (see Chapters 5 & 7) it was necessary to apply image pre-processing steps in order to obtain reasonable maps.

4.7.3 Vector Transformation vs. Image Transformation

Vector transformation is perhaps the most obvious way to assess changes in the crystal lattice. The method has appealing features in being able to provide measures of precision with which a particular g-vectors are determined from a pattern, by considering the fit to the whole lattice (although this metric does not appear to have been reported in literature). The image transformation approach is rather a computationally attractive way to use all of the data and obtains the transformation in one step that automatically obtains sub-pixel accuracy through the implementation of the image transformation. Pre-processing can be required if the signal is weak, but this is comparable to steps involved in peak finding. A more esoteric advantage

[10]The reference pattern may be averaged over an unstrained region to reduce noise in the pattern.

of the image transformation approach is that casting the problem as a model fitting problem may be a platform for further development, as discussed in Chapter 5.

4.8 Summary & Prospects

A framework for crystallographic electron microscopy has been established in a flexible python code structure named *pyxem*. The code is modular, comprising four types of pythonic object (signals, generators, components, and libraries) for which specialized classes are implemented and that may be used together to define a wide range of workflows for 4D-S(P)ED data analysis. These workflows have been illustrated here in application to a GaAs nanowire. The application of unsupervised machine learning algorithms, most notably non-negative matrix factorization (NMF) to 4D-S(P)ED data has been explored. It has been demonstrated that NMF can be successfully applied to reveal the location and characteristic diffraction associated with different crystals including cases where crystals are overlapping in projection but that there are some limitations when information is shared between two constituent diffraction patterns. It was also found that the use of precession can facilitate the successful application of linear decomposition methods.

Model fitting was used as a novel approach to strain mapping using 4D-S(P)ED data, which is perhaps most significant in establishing a code framework for model fitting that could be extended to compare full physical simulations with experimental observations. A simple *ElectronDiffractionForwardModel*, based on kinematical simulation, was implemented as a step in this direction and had some utility, but to realize the full potential it will be necessary to implement more physical, but fast, simulators and to develop a fuller characterisation of the noise properties of detectors used for 4D-S(P)ED. Other areas for development include extending the analysis of one-dimensional *ElectronDiffractionProfile* signals for example towards spatially resolved total-scattering measurements. Overall, the establishment of this robust, modular and extensible code framework paves the way for a broad range of technique developments base on 4D-S(P)ED as well as potentially the various other forms of scanning diffraction microscopy (see Chapter 1).

Chapter 5

Towards Tensor Tomography

Nanoscale strain fields have become increasingly important in materials science as microstructural strain engineering has been developed as a means to tailor physical properties in areas from microelectronic devices [257] to engineering alloys [258]. This microstructural strain is often the result of lattice continuity between dissimilar phases on the nanoscale. High spatial resolution strain measurements are therefore required, which has motivated the development of (scanning) transmission electron microscopy (S)TEM techniques [148]. It should be noted that the need for electron transparent specimens presents the challenge of stress relaxation on producing thin films from the bulk [259–262], which will alter the strain distribution. However, such thinning is not required when considering strain in nanomaterials and may be overcome by refining a finite element model, for example [262]. Strain is frequently measured in the (S)TEM by assessing the *geometric phase*, $\alpha_g = -2\pi\mathbf{g}\cdot\mathbf{u}$, imparted in a scattered beam, $\mathbf{g}$, by atomic displacements, $\mathbf{u}$, (see Chapter 2) using either electron holography [263, 162] or Fourier analysis of atomic resolution images [264, 265]. Atomic resolution images may also be analysed in terms of peak positions to assess changes in the local inter-atomic separation [266] due to strain. Recently, scanning (precession) electron diffraction (S(P)ED) has proved advantageous for mapping strain over regions on the order of microns with nanometre resolution [27, 163].

Strain mapping based on S(P)ED typically produces two-dimensional strain maps of 3 strain components, perpendicular to the incident beam direction, and 1 rotation parameter, about the beam direction. Four (of nine) components of the deformation gradient tensor are therefore obtained, based on affine transformation of the reciprocal lattice, as described in Chapter 4. Two-dimensional strain maps obtained in this way reveal the distortion of the projected lattice compared to a selected reference, which includes changes in the lattice due to composition variations. There are two major limitations: (1) only 4 of the 9 components of the displacement gradient tensor are measured, and (2) strain measurements

in projection depend on the strain distribution along the beam path. The latter *projection problem* is important when the strain field varies significantly within the sampling volume, as illustrated in Figure 5.1, and is compounded by the intricacies of dynamical electron diffraction discussed in Chapter 2. The "grand challenges" of nanoscale strain mapping with electrons are therefore to measure all components of the displacement gradient tensor and reconstruct the three-dimensional distribution of these components. Here, the focus is on reconstruction of the strain distribution in three-dimensions and the steps required to move towards three-dimensional reconstruction of the full strain tensor.

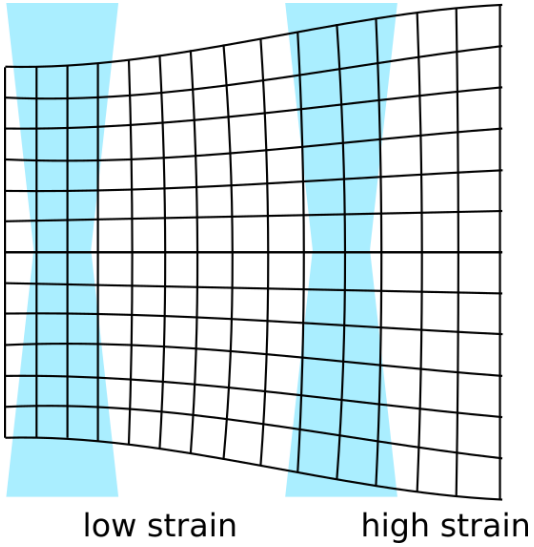

Fig. 5.1 **Schematic beam paths through a strained specimen**. In low strain regions the lattice is strained homogeneously within the sampling volume. In high strain regions the lattice is strained inhomogeneously within the sampling volume and the strain varies along the beam path. The aim is to reconstruct this variation along the beam path.

Three-dimensional strain reconstruction has been achieved using X-ray coherent Bragg diffractive imaging for strain reconstruction within single crystals smaller than the X-ray probe [98–100], micro-Laue mapping experiments using a differential aperture [22], and tomographic back-projection methods applied to transmission X-ray diffraction data acquired from polycrystalline specimens [267, 268]. Achieving three-dimensional strain reconstruction based on S(P)ED experiments could enable reconstruction of strain in a wider range of specimens and/or at higher spatial resolution than any of these X-ray methods alone. Since S(P)ED data is acquired in projection, three-dimensional reconstruction based on tomographic back-projection is the natural starting point and the work presented here builds on the X-ray work by Korsunsky *et al.* [267, 268] and recent mathematical treatments of the tensor tomography problem [269, 270] suggest a route forward. To illustrate the strain mapping performed here an axially heterostructured III-V nanowire was considered.

5.1 Materials & Methods

5.1.1 Material Background

An axially heterostructured GaAs nanowire containing a $GaAs_{1-x}Sb_x$ insert was taken as a test specimen. This nanowire was grown[1] by molecular beam epitaxy involving a vapour-liquid-solid mechanism catalysed by gold as described by Kauko *et al.* [271]. The growth process produces a gradual compositional variation at the insert interfaces [271]. Such axial heterostructures are often produced in optoelectronic III-V semiconductor nanowires in order to tune the electronic bandstructure for particular wavelengths [272–274] but there have been relatively few attempts to measure strain in such samples [275, 276]. Crystallographically, the GaAs grows in both the zinc blende (ZB) and wurtzite (WZ) polymorphs in a $\langle 111 \rangle_{ZB}$ direction and with an hexagonal cross-sectional geometry. Specimens were prepared for transmission electron microscopy by scraping them from the silicon substrate on which they were grown onto holey carbon coated copper grids.

5.1.2 SED Acquisition

S(P)ED was performed using a Philips CM300 FEGTEM operated at 300 kV and controlled using a Nanomegas Digistar system, as described in Chapter 3. The diffraction patterns were recorded with 144×144 pixels per pattern, an exposure time of 60 ms and a nominal camera length of 21 cm. The step size in the scan was $\sim$ 10 nm and the convergence semi-angle was $\sim$1.5 mrad. Data was acquired without precession and with precession angles of 18 mrad or 27 mrad, as indicated below. Tilt series were performed using a combination of a Fischione tilt-rotate holder and an FEI double tilt holder, as described in Section 5.3.1.

5.1.3 Data Processing

Analysis of the 4D-SED data was performed using methods described in Chapter 4. A distortion correction corresponding to a vertical compression by a factor of 0.69 was applied to correct for the off-axis camera geometry and the data was aligned with respect to translation of the direct beam. Pre-processing using the h-dome (h=0.5) method (see Chapter 4) was performed to improve the performance of the image affine transform strain mapping algorithm. Optimization of the image affine transformation was achieved using the smart adaptive model fitting procedures [238] implemented through the HyperSpy python library [231] and this was found to be very important in avoiding divergence of the fitting procedure.

[1] The nanowire sample was provided by Prof. Ton van Helvoort, NTNU, Norway.

5.1.4 Electron Tomography

Electron tomography [277, 19] uses tomographic reconstruction methods [278] to reconstruct a three-dimensional object from a series of two-dimensional projection images. The specimen is tilted in the microscope, typically about a single axis, and a projection image is recorded at each tilt. Usually the tilt axis does not pass exactly through the centre of the specimen and the projections must be aligned to a common tilt axis. The three-dimensional object is then reconstructed in consecutive two-dimensional slices, typically using a back-projection algorithm. Raw back-projection results often require further processing prior to visualization and analysis of the reconstruction. These general steps in electron tomography are summarized in Figure 5.2. Iterative reconstruction techniques, based on the premise that reprojecting the reconstruction ought to reproduce the experimental projection images, such as the algebraic reconstruction technique (ART) [279] and the simultaneous iterative reconstruction technique (SIRT) [280] are commonly used in electron tomography to improve reconstructions from undersampled data [277] and there have also been significant recent advances in the use of compressive sensing [281] and model based reconstruction techniques [169, 282]. Here, alignment was achieved using the phase correlation method implemented in the HyperSpy python library [231] and tomographic reconstruction was achieved using SIRT (with 20 iterations) as implemented in the TomoPy python library [283].

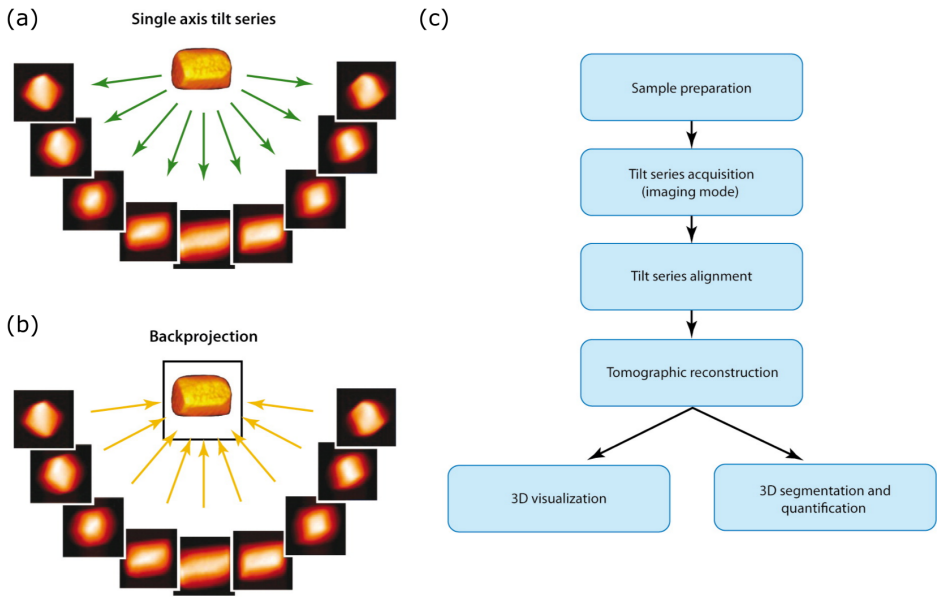

Fig. 5.2 **Steps involved in electron tomography**. (a) A tilt series comprising 2D projection images of a 3D object recorded as a function of tilt is (b) back-projected to reconstruct the 3D volume. (c) Steps involved in an electron tomography experiment from sample preparation to 3D visualization and quantification. Reproduced from [19].

5.2 Strain Mapping in 2 Dimensions

4D-S(P)ED data acquired from a nanowire oriented near to a $[1\bar{1}0]_{ZB}$ zone axis both without precession and with a precession angle of 27 mrad, as shown in Figure 5.3. The nanowire initially forms with GaAs in the zinc blende polymorph and retains this structure within the antimony doped insert. Within the insert, the atomic structure is expanded because antimony is larger than arsenic, which can be seen as a contraction of the reciprocal lattice. When the antimony is removed during growth, GaAs continues to grow in the wurtzite structure. The gold droplet that catalyzed growth remains at the tip and is non-crystalline. Comparing data acquired with and without precession in Figure 5.3, PED patterns appear closer to zone axis and contain more intense higher order reflections.

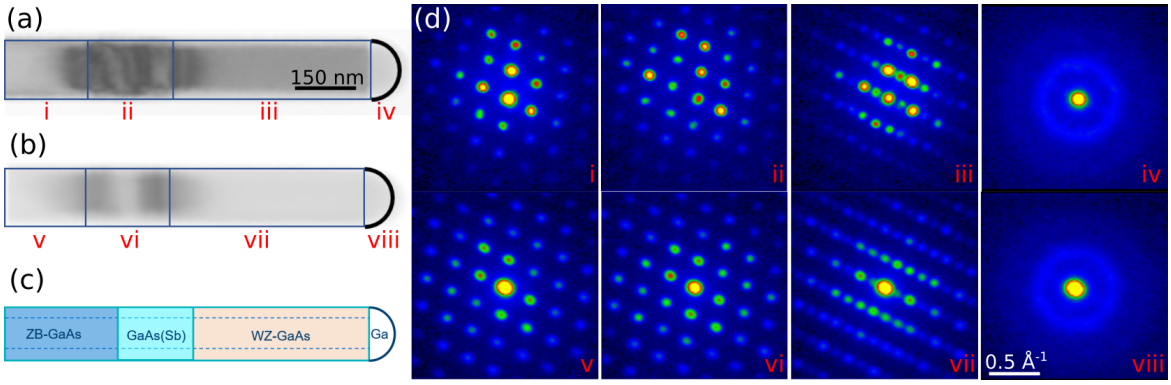

Fig. 5.3 **4D-S(P)ED data from a GaAs nanowire axial heterostructure.** (a,b) Virtual bright-field images (a) without precession (b) with 27 mrad precession. (c) Structurally distinct regions of the nanowire. (d) Diffraction patterns from each region of the nanowire as indicated in (a/b).

Qualitative insight into the nanowire strain state may be obtained from virtual dark-field (VDF) images formed using SED data acquired without precession, as shown in Figure 5.4, based on interpretation within the column approximation, as discussed in Chapter 2. VDF images associated with reflections corresponding to atomic planes perpendicular (i.e $\{111\}$) and parallel (i.e $\{22\bar{4}\}$) to the long axis of the nanowire both show significant changes in intensity in ~ 75 nm regions adjacent to the interfaces with the $GaAs_{1-x}Sb_x$ insert. This contrast is dominated by the bending of atomic planes near the interfaces to produce a stress free surface [259, 260] and a schematic model of plane bending may be constructed, as shown in Figure 5.4e. VDF images may also be formed with the integration window positioned between Bragg reflections to form an image based on diffuse scattering, which is increased in the regions where the atomic structure deviates most from an ideal crystal (see Chapter 2), which is in the strained region and the non-crystalline gold tip, as shown in Figure 5.4d.

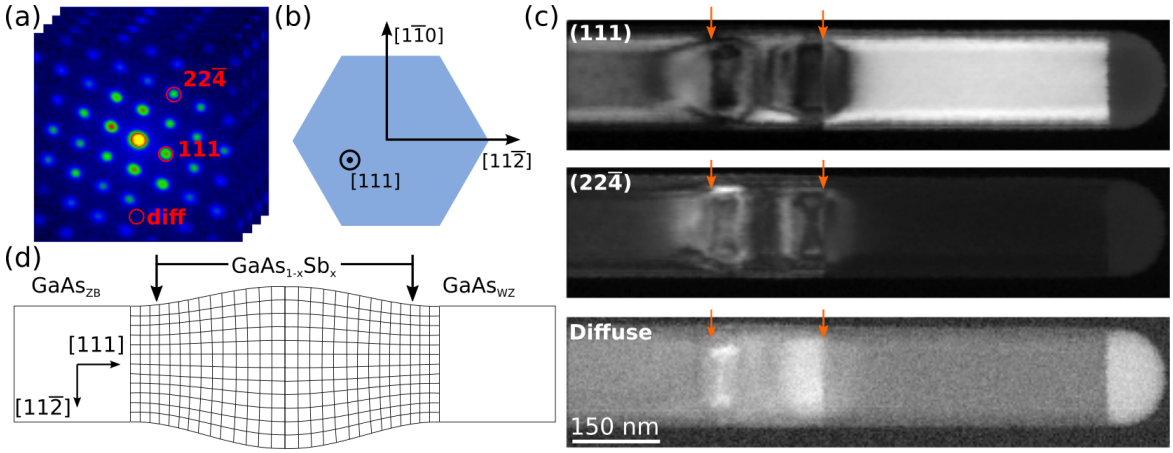

Fig. 5.4 **Virtual dark-field imaging of strain**. (a) Diffraction pattern, integration windows marked. (b) Nanowire cross section and crystallography. (c) VDF images corresponding to 111, 22$\bar{4}$ and diffuse scattering conditions. (d) Schematic of atomic plane bending.

5.2.1 Two-dimensional Strain Maps

Two-dimensional strain maps are shown in Figure 5.5 for both the zinc blende and wurtzite phases. SPED data acquired with 27 mrad precession were used to obtain these maps using reference patterns at either end of the scan region, far from the insert and in the appropriate phase. The projected zinc blende lattice is approximately homogeneously expanded in the insert as a result of antimony incorporation. Measurement error can be approximated from the spread of values in unstrained regions, which is on the order of ± 5 millistrain. As an estimate of precision this is about an order of magnitude larger than some literature reports [162], which is partly because the estimation here is based on the absolute spread in values rather than a root mean square value. It is also likely that the raw diffraction patterns being smaller and noisier than those typically reported has contributed to this relatively poor precision.

The maximum lattice expansion measured is $+2.5 \pm 0.5\%$ which corresponds [284] to an antimony concentration of $\sim 35 \pm 5\%$, consistent with expectations based on the growth conditions. Interestingly, the ε_{xx} strain component in the wurtzite phase, i.e. the normal strain component along the short axis of the nanowire, is small immediately adjacent to the interface with the antimony doped insert. This is consistent with previous reports [285] that showed that the wurtzite GaAs is expanded $\sim 1\%$ in the close packed $\{0001\}$ plane compared to the close-packed $\{111\}$ plane of zinc blende GaAs. The wurtzite phase may thus have improved epitaxy with an expanded zinc blende structure and this may explain why the wurtzite polymorph forms after the antimony doped insert has been grown. The rotation maps highlight the plane bending is localized near the interfaces, consistent with the model inferred from VDF image contrast.

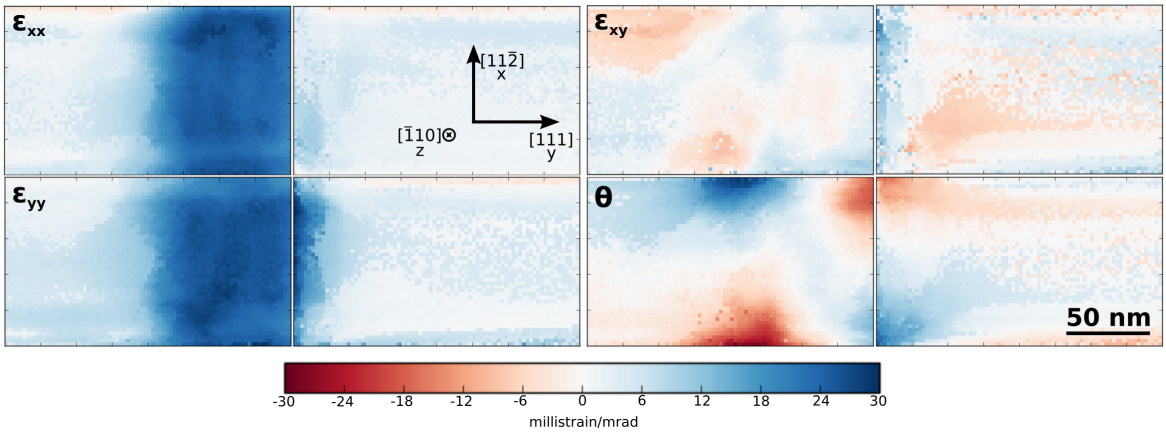

Fig. 5.5 **Nanowire strain mapped in two-dimensions**. Column averaged strain components in zinc blende (left) and wurtzite (right) GaAs. Positive rotations are anticlockwise about z.

5.3 Single Component Strain Tomography

Tomographic reconstruction of a single normal strain component may be reduced to a scalar tomography problem for a component of strain parallel to an axis about which a tilt series is performed [267, 268]. Reconstruction may then be achieved by standard tomographic methods based on back-projection, as described in Section 5.1.4. A proof-of-principle demonstration of such a reconstruction using 4D-SPED data is described here, highlighting important practical aspects of experimental design and data analysis that must be considered to move towards tensor tomography. In practice, the primary challenges are to determine most appropriate data acquisition scheme and reconstruction method.

5.3.1 Data Acquisition Design & Implementation

Reconstruction of the normal strain parallel to the tilt axis requires the projected strain parallel to that axis to be measurable throughout a tilt series. This condition is easily met for polycrystalline specimens illuminated with a probe larger than the grain size [267, 268] because a ring pattern is recorded in all orientations and the component of elliptical distortion parallel to the tilt axis can be measured. However, when a single crystal is probed, projected strain can only be measured in directions where the diffraction condition is met. It is therefore necessary to satisfy a particular diffraction condition throughout the tilt series, which requires the tilt series to be performed about an axis parallel to the corresponding reciprocal lattice vector. This requires the selected reciprocal lattice vector to be aligned parallel to the tilt axis of the microscope. Here, such a tilt series was performed about the long axis of the nanowire, i.e. the $[111]^*$ axis, so that the 111 systematic row of reflections was recorded at every tilt.

A tilt series was performed over $\pm 30^\circ$ from the $[1\bar{1}0]$ zone axis in steps of $\sim 5^\circ$, i.e. 12 projections and the data was replicated 6 times, based on assumed 6-fold symmetry about the wire axis (neglecting polarity), to obtain a more complete dataset. In order to perform this tilt series about the $[111]$ crystallographic axis two different holders were used to align the long axis of a nanowire with the tilt axis. First a tilt-rotate holder was used to identify a nanowire lying near to the $[1\bar{1}0]$ zone axis and rotate it so that the long axis was approximately parallel to the goniometer (α-tilt) axis. The specimen was then transferred to a double-tilt holder, maintaining the in-plane rotation found, and the tilt series was performed manually using primarily the α-tilt with the β-tilt adjusted to maintain excitation of the 111 systematic row. 4D-S(P)ED data was acquired at each tilt with a precession angle of 18 mrad.

5.3.2 Analysis & Reconstruction Method

Two-dimensional strain maps were obtained from the 4D-SPED data recorded at each tilt, as described in Section 5.2.1. Components of strain in these two-dimensional maps were assumed to be column averaged strain, $\overline{\varepsilon}$, components. In every map in the tilt series the $\overline{\varepsilon_{yy}}$ component was the component of strain along the nanowire axis, $\overline{\varepsilon_{yy}} = \overline{\varepsilon_{111}}$, which can be written explicitly as a column average,

$$\overline{\varepsilon_{111}} = \frac{\int_s \varepsilon_{111} ds}{\int_s ds} \tag{5.1}$$

where the integral is over the beam path. Tomographic reconstruction based on Fourier back-projection requires a projected quantity, i.e. a quantity that increases monotonically with an increase in the quantity of interest, as input. A *projected strain*, $J\varepsilon_{111}$, may be obtained by multiplying the average strain by the specimen thickness,

$$J\varepsilon_{111} = \int_s \varepsilon_{111} ds = \overline{\varepsilon_{111}} \cdot \int_s ds \tag{5.2}$$

The appropriate thickness by which to multiply at each pixel in the strain map, i.e. $\int_s ds$, was determined by performing a tomographic reconstruction of the specimen morphology using virtual annular dark-field images obtained from the 4D-SPED data, with and inner radius of 20 pixels and an outer radius of 50 pixels, via the methods described in Section 5.1.4. This morphological tomogram was then segmented (by thresholding) and reprojected to obtain thickness maps. The projected strain maps obtained by performing the multiplication described by Equation 5.2, following alignment of the column averaged strain maps, were then used as input to a SIRT reconstruction. The steps involved in this single component strain tomography workflow are summarized in Figure 5.6.

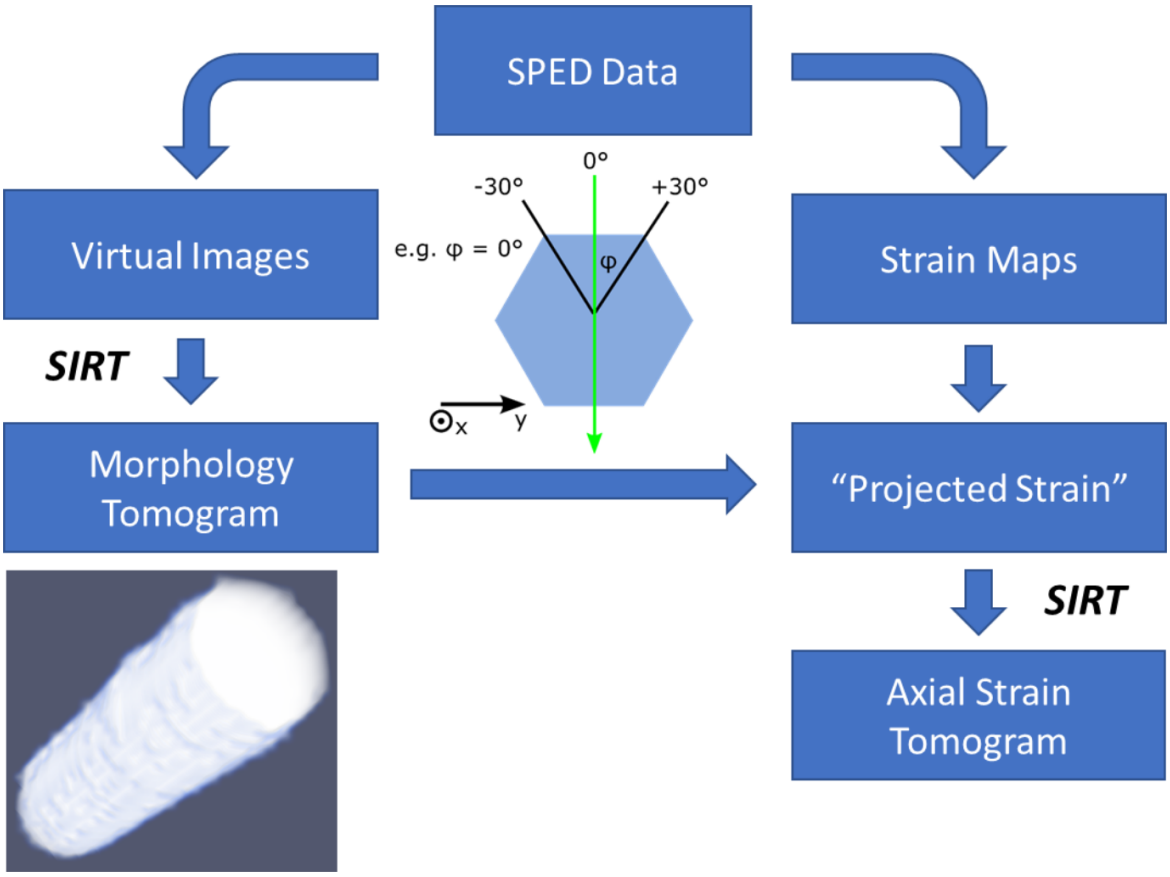

Fig. 5.6 **Steps involved in single component strain tomography**. Virtual images and strain maps are obtained from the SPED data acquired at each tilt in a range $\pm 30°$ from a $[1\bar{1}0]$ zone axis and 6-fold symmetry is imposed to yield a more complete dataset for demonstration. A tomographic reconstruction is performed using the nanowire morphology to obtain the local thickness and convert the strain maps into projected strain maps.

5.3.3 Proof-of-principle Strain Tomogram

The three-dimensional axial strain distribution reconstructed following the steps described above is shown in Figure 5.7, both as a volume reconstruction and as orthosections through the centre of the nanowire on $(11\bar{2})$, $(1\bar{1}0)$ and (111) planes respectively. The hexagonal morphology can be discerned but is suppressed by the spatial resolution. Close inspection of the orthosections reveals that the strain in the antimony doped insert is larger near to the surfaces as compared with the centre of the nanowire. This increase in values near to the surfaces is not seen in regions away from the insert suggesting that it is a true effect and not an artefact of the reconstruction. This observation indicates that the projected (111) interplanar spacing is larger near to the surfaces than at the centre of the nanowire. Further the lower strain region has a dog bone shape near the centre of the nanowire.

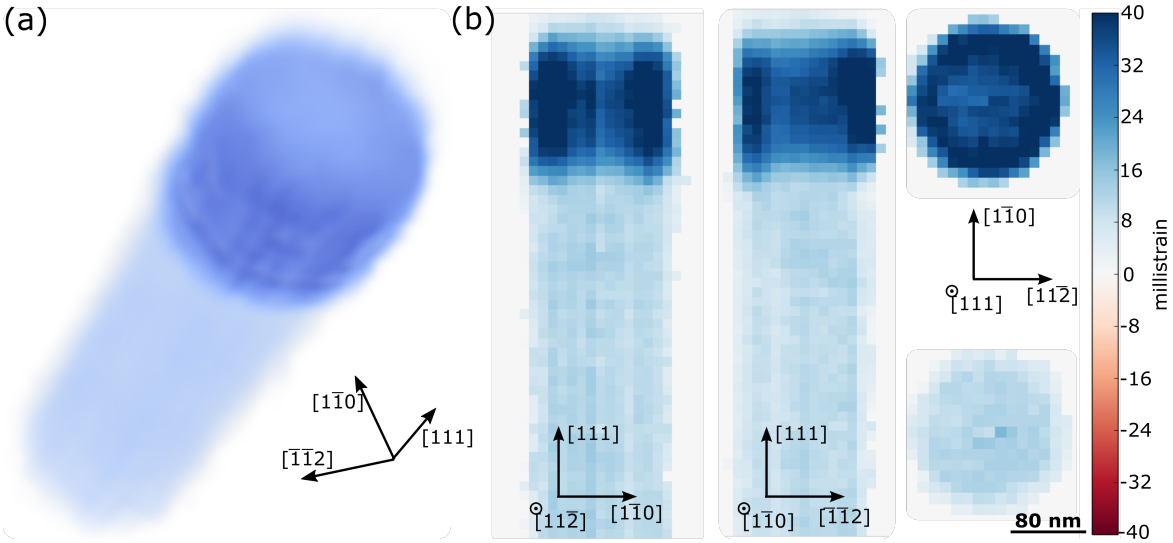

Fig. 5.7 **Axial strain tomogram**. (a) Strain tomogram of the axial strain component. (b) Ortho-slices through the reconstruction showing variations in the strain between the centre (lighter blue) and surface (darker blue) of the nanowire.

To interpret the strain distribution revealed by tomographic reconstruction it is necessary to recall that what has been mapped as strain is the change in the projected lattice compared to pure GaAs. The lattice expansion observed within the $GaAs_{1-x}Sb_x$ insert is therefore the result of both the composition change and epitaxial strain between the insert and the adjoining nanowire. Since we do not know the composition precisely these two contributions cannot be decoupled and it is not possible to be sure whether the expanded outer region is in tension or the inner region is in compression with respect to unstrained bulk $GaAs_{1-x}Sb_x$ of the correct composition. In either case the strain distribution would be somewhat counterintuitive but may be consistent with recent finite element modelling [20], as shown in Figure 5.8. These simulations were performed for GaN nanowires in the wurtzite polymorph with the [0001] axis parallel to the long axis of the nanowire. However, the results were anticipated to also be valid for zinc blende structured nanowires with the long axis parallel to a $\langle 111 \rangle$ crystallographic direction [20], as is the case here. The simulations predict a similar axial strain distribution with the strain in the insert (relative to the unstrained bulk structure) becoming compressive for inserts with a length comparable to the diameter of the nanowire. When the length of the insert is slightly longer than the nanowire diameter, as is the case here, the compressive strain region has a dog bone shape similar to the experimental observation.

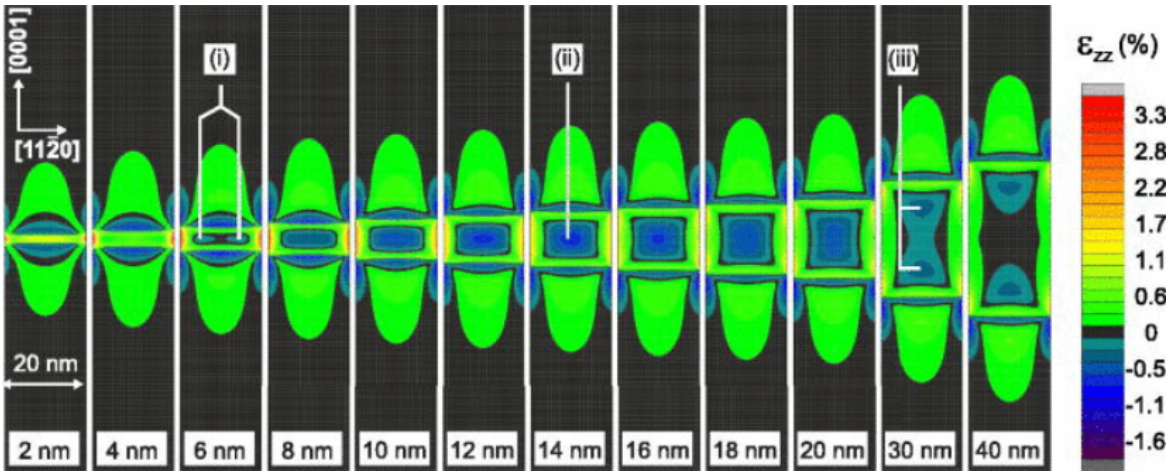

Fig. 5.8 **Finite element modelling of axial heterostructured nanowires**. ε_{0001} for slices through GaN nanowires containing $In_{0.3}Ga_{0.7}N$ inserts with lengths from 2 to 40 nm. As the length of the insert increases the strain decreases and eventually turns negative in a toroidal region (i) that expands until the axial strain reaches a minimum of about $\sim -0.8\%$ in the centre of the insert (ii). A further increase in length results in complete elastic relaxation in the middle of the insert (iii). Reproduced from [20].

5.4 Towards Tensor Tomography

Tensor tomography based on S(P)ED data will require a reconstruction framework and a practical data acquisition scheme as was highlighted above in performing proof-of-principle strain tomography. Recent mathematical work [269] has shown that tomographic reconstruction of a rank two symmetric tensor field (e.g. a strain field) is possible from diffraction data if the diffraction experiment can be related to the transverse ray transform, J,

$$\mathbf{J}f(x,\xi) = \int_{\infty}^{\infty} P_{\xi} f(x, s\xi) ds \tag{5.3}$$

where ξ is a unit vector in the direction of the illumination and

$$P_{\xi} = \left(\mathbf{I} - \frac{1}{|\xi|^2}\xi\xi^T\right) f \left(\mathbf{I} - \frac{1}{|\xi|^2}\xi\xi^T\right) \tag{5.4}$$

is the projection of the tensor field, represented as matrices, onto the plane perpendicular to ξ, with $\mathbf{I}$ the identity matrix. If the experiment can be related to this transverse ray transform then it has been shown that the strain tensor field could be reconstructed from complete data acquired with tilt series about six axes [269] or tilt series performed about three orthogonal axes [270] using a filtered back-projection reconstruction algorithm. The questions to address then are (1) can the S(P)ED experiment be related to the transverse ray transform, and (2) what kind of data acquisition scheme is feasible.

It seems intuitive that it should be possible to relate electron diffraction from a strained single crystal to the transverse ray transform, at least approximately, because the geometry of electron diffraction means that reciprocal lattice vectors approximately perpendicular incident beam direction are measured (see Chapter 2) and a change in the interplanar spacing through the specimen produces a shift in the diffraction spot position as expected. Indeed, these were precisely the features of the diffraction pattern used to perform two-dimensional strain mapping in Section 5.2. However, in addition to the rescaling of the diffraction pattern geometry, the application of a deformation to the crystal potential introduces a phase term and an amplitude scaling[2], which means that linearizing the problem, i.e. assuming that the measured diffraction pattern is the sum of the diffraction patterns from voxels along the beam path, is an approximation that requires validation. This is essentially saying that care is required to think about the implication of the excitation error being different for each voxel along the beam path. Indeed this effect was essentially what was used to obtain VDF image contrast in Section 5.2. Further potential non-linearity should be expected owing to the dynamical nature of electron diffraction. It may be imagined that PED patterns would be more appropriate in integrating through the excitation error and reducing dynamical effects, but this introduces an insensitivity to distortions that move the diffraction condition out of the plane perpendicular to the electron incidence direction and therefore this too requires care. An additional consideration is that the electron diffraction pattern is clearly sensitive to all 9 components of the displacement gradient tensor, i.e. 3 rotation components in addition to the 6 symmetric strain tensor components. The mathematical formalisms recently presented [269, 270] therefore need to be reconsidered for the more general case, although it seems [286] a reconstruction will still be formally possible in this case. Overall, it is highly likely that the experiment is reasonably well approximated by the transverse ray transform but this requires formal verification.

Assuming that the validity of representing electron diffraction as a transverse ray transform is sufficient for useful reconstruction, it is necessary to consider the data acquisition that may be performed. Performing three tilt series about orthogonal axes would provide sufficient data for general reconstruction [270] in the symmetric second rank tensor case but whilst dual-axis electron tomography about two orthogonal axes is feasible [287] tilt about a third orthogonal axis would be very challenging given the geometry of electron microscopy specimens. Whilst it has been shown that two-axis data is insufficient for general reconstruction of a symmetric second rank tensor field it is possible to reconstruct the special

[2]If u is the crystal potential and it is deformed $u(x) \mapsto u(Ax+b)$ by an affine transform A and a translation b, the Fourier transform gives $FT[u(Ax+b)](z) = \frac{\exp(ib\cdot A^{-T}z)}{|A|} FT[u](A^{-T}z)$, which is equal to the scattered wave amplitude in the kinematical approximation (see Chapter 2).

case (the potential case) where the tensor field is of the form of the linear strain tensor [270]. This is because some of the terms are related in this special case by what is physically referred to as strain compatibility. This must also be validated for the 9 component reconstruction case and it seems likely that the small strain limit will again provide simplification. In any case there will be missing data as is typical in electron tomography [277, 19] and it may prove useful, as it has in other analytical tomographies [169], to recast the reconstruction problem as a model fitting problem. It may also be possible to tilt to specific orientations containing maximal information [288] in order to reduce the data required.

5.5 Summary

S(P)ED has recently emerged as a leading candidate for nanoscale strain mapping [163] and the work presented in this chapter continues in this vein. A novel method for two-dimensional strain mapping based on optimization of the image transform has been demonstrated, which has the methodological advantage of recasting the strain mapping problem as a model fitting problem, which may prove useful for future tomographic developments. The two-dimensional strain maps obtained from an axially heterostructured GaAs nanowire suggest that GaAs may adopt the wurtzite phase after the growth of a $GaAs_{1-x}Sb_x$ insert as a result of improved epitaxy. Virtual dark-field imaging also provided interesting qualitative insights into the nanowire strain state but is rarely reported in literature studies. The prospect of forming diffraction contrast images using diffuse scattering, which here highlighted regions where crystallinity is disrupted, is particularly compelling.

Tomographic reconstruction of the normal strain component along the nanowire axis was performed as a proof-of-principle. The results suggest higher strain at the surfaces compared to the interior, which may be consistent with recent theoretical results [20], and illustrate that probing the three-dimensional strain distribution is likely to provide useful insight. This study served primarily to highlight challenges that must be addressed in order to achieve quantitative tensor tomography in future, both in terms of theoretical understanding and experimental design. Initial considerations suggesting a route that may be followed towards this end have been set out.

Chapter 6

Inter-phase Relationships in Alloys

Engineering alloys are typically multi-phase polycrystalline materials containing numerous crystals with different crystal structures and compositions. These microstructural features are tailored on ever smaller scales [289] and, in this context STEM has become a valuable tool, enabling characterisation of microstructural elements on the nanoscale. Here, the emphasis is on nanoscale crystallographic insights obtained using SPED based orientation mapping to reveal inter-phase crystallographic relationships. The application of unsupervised machine learning algorithms to multi-dimensional electron microscopy data, to obtain phase specific characterisation in terms of both crystallography and composition, is also explored.

6.1 Inter-phase Orientation Relationships

Crystal orientations [74, 290] and the relationships between neighbouring crystals [76, 291] are important for understanding macroscopic materials properties [76, 75, 292, 293] and microstructural transformation pathways [294–297]. SPED data can be used to obtain phase and orientation maps (e.g. via pattern matching, see Chapter 4), which must be further analysed to obtain physical insight. Numerous software packages facilitate this analysis such as the open-source MTEX matlab toolbox [298] used here. Here, approaches based on 3-vector, or neo-Eulerian [299], representations of crystal (mis)orientations are developed to reveal inter-phase crystallographic relationships[1]. The premise of this approach is that a preferred crystallographic orientation relationship will result in numerous misorientation vectors near to a particular point within the symmetry reduced region of the misorientation space. To use this idea to assess inter-phase orientation relationships it is necessary to carefully define the symmetry reduced region of the misorientation space.

[1] This work was part of a collaboration primarily with Robert Krakow and was reported in [300].

6.1.1 Representations of Orientations & Misorientations

Orientations and misorientations are described as rotations in 3D space, which can be represented in numerous ways [301, 74, 290, 73, 302]. Most common in crystallographic texture analysis is the Euler angle representation, which describes the rotation as three successive rotations about independent coordinate axes through angles ϕ_1, Φ, ϕ_2, in the Bunge (ZXZ) convention [74, 290]. This is convenient for series expansion of orientation distribution functions [74] but does not convey efficient computation or intuitive plotting[2].

Rotations may be described by special orthogonal matrices *SO(3)*, which are useful for transforming tensor quantities but are not the most computationally efficient representations nor are they convenient for representing orientation distributions. More computationally efficient, is the quaternion representation [73], which is a four-parameter description of a rotation reflecting the mathematically natural description of rotations in 4D. Quaternions are useful because of an interpretation as forming a four-dimensional algebra with efficient computations. The unit quaternions have a two-to-one relationship with $SO(3)$ and define points on the 3-sphere, $\mathbb{S}^3$, in four-dimensional Euclidean space. The unit quaternion $\mathbf{q} = (q_0, q_1, q_2, q_3)$ can also be related to the axis of rotation, described by a unit vector, ξ via $\mathbf{q}_i = \sin\frac{\omega}{2}\,\xi_i$ for i=1,2,3 and the angle of rotation ω via $q_0 = \cos\frac{\omega}{2}$.

Rotations may also be represented by the axis and angle of rotation. (Mis)orientation distributions can be expanded in these terms [307, 308] and the representation is intuitive. A series of so-called neo-Eulerian mappings have been defined, based on this notion, as 3D vectors formed by scaling a unit vector, ξ, parallel to the axis of rotation by a function of the rotation angle, ω, about that axis, $f(\omega)$. The choice of the scaling function, $f(\omega)$, conveys particular properties on the resulting vector space. Frank [299, 309] made five suggestions:

Axis-Angle, $\mathbf{v} = \omega\xi$: Simple and the angular units ease direct interpretation.

Rodrigues-Frank, $\mathbf{r} = \tan\frac{\omega}{2}\xi$: Rectilinear - rotation about an axis is a straight line through any point. Some domains are unbounded as the scaling function tends to infinity.

Conformal, $\mathbf{c} = 2\tan\frac{\omega}{4}\xi$: Equal angle projection of $\mathbb{S}^3$ onto Euclidean space. The configuration in any small region of the map is geometrically similar to that which it would have transferred to any other point in the map.

Homochoric , $\mathbf{z} = \{\frac{3}{4}(\omega - \sin\omega)\}^{1/3}\xi$: Equal volume projection of $\mathbb{S}^3$ onto Euclidean space. The metric tensor determinant is preserved and a random distribution of orientations will have equal probabilities of being found within equal volume elements [299].

[2]The primary issue with plotting Euler angles are: non-singularity of orientations, especially the identity, distorted volume and no direct reference with specimen axes [303–306].

Quaternion Vector, $\mathbf{q} = \sin\frac{\omega}{2}\xi$: Enclosed within a sphere of unit radius and easily related to the quaternion representation, described above.

The neo-Eulerian mappings each offer certain advantages. In particular, the rectilinearity of the Rodrigues-Frank representation has made it popular although the unbounded nature of fundamental zones containing rotations of 180° is a practical issue for low symmetry systems. The homochoric representation is attractive for visualization owing to the equal distribution of randomly distributed points [80]. Here, the axis-angle parametrization is used because it is simple to interpret and can be used in low symmetry systems. The analysis principles developed in the following sections apply equally well to all neo-Eulerian mapping and all are available in the MTEX toolbox [298].

6.1.2 Fundamental Zones & Crystal Symmetry

Crystal symmetry implies that some (mis)orientations are physically indistinguishable. However, equivalent (mis)orientations will be represented by different points in the 3D vector space when expressed as neo-Eulerian vectors. It is only necessary to use a region of the vector space containing each physically distinct (mis)orientation precisely once. Such a region is known as a *fundamental zone* [299, 76, 310] or an *asymmetric domain* [311]. In this section, a consistent definition for the fundamental zone is set out and fundamental zones are tabulated for all crystal symmetries.

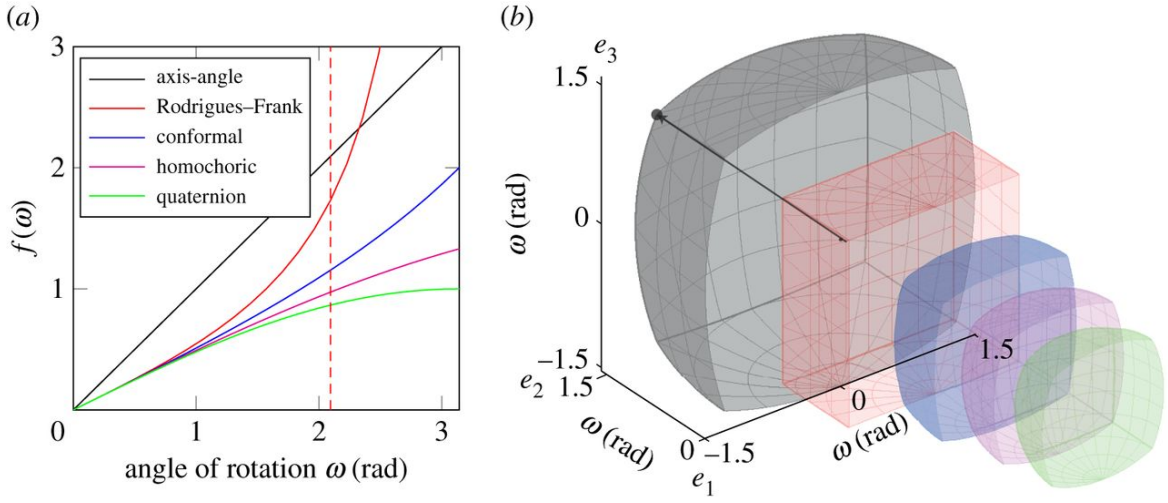

Fig. 6.1 **Neo-Eulerian mappings**. (a) The scaling function for five mappings. (b) Sectioned fundamental zone for 222 symmetry in each of the five neo-Eulerian mappings, illustrating differences in geometry qualitatively. The maximum angle is $2\pi/3$ radians in the [111] direction (indicated by the black arrow).

Fundamental zones have previously been specified by a number of authors based on Rodrigues-Frank parameters [76, 311, 310]. Here, the calculation was instead achieved following a construction based on quaternion geometry and Voronoi tessellation, as described in Krakow *et al.* [300]. The fundamental zone may then be transformed into any of the neo-Eulerian representations. These representations differ geometrically, due to the different scaling functions used in each case. The scaling functions, $f(\omega)$, shown in Figure 6.1a, are all approximately linear up to $\sim$1 radian and then diverge. The bounding surfaces of the fundamental zone are curved in all cases except Rodrigues-Frank, see Figure 6.1b, reflecting the aforementioned rectilinearity.

The particular fundamental zone obtained depends on the alignment of axes and the order in which symmetry operators are combined for misorientations. Standard conventions were set out in Krakow et al [300], where the authors suggested taking the highest symmetry system as the reference system and aligning crystallographic axes to orthonormal reference axes following,

$$\mathbf{e_1} = \mathbf{a}/a, \mathbf{e_2} = \mathbf{z} \times \mathbf{x}, \mathbf{e_3} = \mathbf{c}^*/c^* \tag{6.1}$$

where $\mathbf{e}_1$, $\mathbf{e}_2$, $\mathbf{e}_3$ are orthonormal basis vectors of the crystal reference frame h and **a,b,c** are crystallographic basis vectors.

Symmetry Equivalence of (Mis)orientations

Calculation of the fundamental zone is based on selecting, from symmetry equivalent points, the point closest to the origin (smallest angle of rotation) and rejecting more remote points. When multiple equivalent points have the same distance to the origin a constraint is placed on the direction of the axis of rotation. To express this mathematically, it is noted that crystal coordinates are subject to symmetry described by the group of symmetry operators, s, comprising the crystallographic point group S. A symmetry operation applied to the crystal coordinates produces a physically identical configuration and therefore the crystal coordinates h can be identified with a set sh $(s \in S)$ of symmetrically equivalent crystal coordinates[3]. Considering Equation 2.1 yields the following expression for symmetrically equivalent orientations.

$$\boldsymbol{g}_i = \boldsymbol{g}_i s, s \in S \tag{6.2}$$

[3]Some authors [303] have suggested applying symmetry to the specimen coordinate system but this can be confusing with respect to misorientations and is avoided in this work.

Misorientations are subject to the symmetry operations of crystallographic point groups, S_1 and S_2, associated with the crystal coordinate systems, h_1 and h_2, which are related by the misorientation, $\boldsymbol{m}_{12}$. Considering the effect of symmetry on each crystal coordinate system, as described above, and using Equation 2.3 the following expression for symmetrically equivalent misorientations is obtained.

$$\boldsymbol{m}_{12} = s_2 \boldsymbol{m}_{12} s_1, s_1 \in S_1, s_2 \in S_2 \tag{6.3}$$

Unique selection of a misorientation (referred to as the *disorientation)* to represent all symmetrically equivalent misorientations[4] requires a constraint on both the angle of rotation and axis of rotation because several symmetrically equivalent misorientations may have the same rotational angle[5]. Here, the misorientation with the smallest angle of rotation (known as the disorientation angle) and an axis of rotation within the inverse pole figure (IPF) sector corresponding to the point group of common symmetries, $S_C = S_1 \cap S_2$, is chosen.

Relating Symmetry to Fundamental Zones

Construction of the fundamental zone may be understood by considering that the symmetry operators map the reference (mis)orientation or identity, which is at the origin of the 3D vector space, to a set of *identity equivalent points* throughout the vector space following Equations 6.2 & 6.3. The fundamental zone then comprises the set of points that are closer to the identity at the origin than any of the other identity equivalent points. Indeed this is precisely the notion used by Morawiec [311] and in this work to compute the fundamental zone. This is similar to the construction of the Brillouin Zone in reciprocal space and helps to rationalize the observed fundamental zone geometries.

Fundamental zones for orientations involve only one set of symmetry operators according to Equation 6.2. This is also equivalent to the formation of a misorientation fundamental zone when $S_2 = 1$. A two-fold symmetry axis produces an identity equivalent point at a position 180° from the origin along the symmetry axis. Points up to 90° from the origin along this axis are clearly closer to the identity at the origin than to the identity equivalent point and therefore the boundary of the fundamental zone is at 90° along this axis. This idea extends easily to other rotational symmetry operators with triads, tetrads and hexads each producing identity equivalent points at 120°, 90° and 60° along the respective symmetry

[4] If the crystallographic point groups S_1, S_2 comprise N_1 and N_2 symmetry elements, then each misorientation generally has $N_1 \times N_2$ symmetry equivalents.

[5] Specifically, if we denote $S_C = S_1 \cap S_2$ the group of common symmetries of S_1 and S_2. Then for any misorientation m with rotational angle $\omega(m)$ and rotational axis $\xi(m)$ the symmetrically equivalent misorientations sms^{-1}, $s \in S_c$ have the same rotational angle $\omega(sms^{-1}) = \omega(m)$ but different rotational axis $\xi(sms^{-1}) = s\xi(m)$.

axis. Visualizing the curvature of the bounding surfaces of the fundamental zone is more difficult and depends on the particular representation chosen. The principle is to construct the surface corresponding to rotation about axes orthogonal to each symmetry axis and passing through the easily defined bounding point on that symmetry axis. The inner envelope of these surfaces will then define the fundamental zone.

Considering, as an example, the *222* point group, the diad operators constrain the domain to $\pm 90^\circ$ along the coordinate axes producing a convex cube as shown in Figure 6.2b. For the *622* point group the hexad operator constrains the domain to $\pm 30^\circ$ along $\boldsymbol{e}_3$ and the diad operators constrain the domain to $\pm 90^\circ$ along each of the corresponding axes, as shown in Figure 6.2d. It is therefore reasonably intuitive to deduce the qualitative shape of the fundamental zone for orientations.

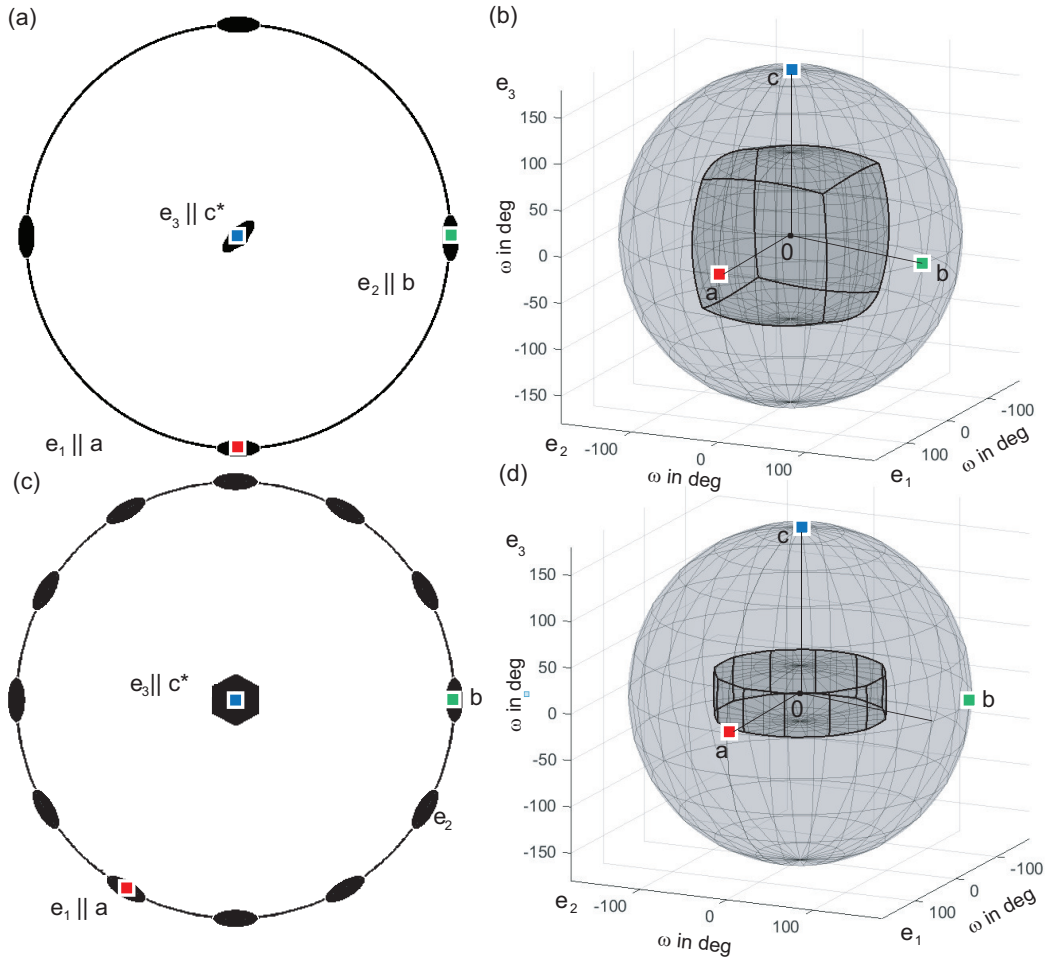

Fig. 6.2 **Symmetry elements and fundamental zones for orientations.** Symmetry and *fundamental zones* in axis-angle space for: (a,b) crystals with point group *222* (c,d) crystals with point group *622*.

Fundamental zones for misorientations are formed in different ways depending on whether the symmetry groups contain common elements [311]. When the symmetry groups do not contain common elements, all symmetry equivalent misorientations have a unique misorientation angle and the fundamental zone is constructed by selecting the misorientation closest to the origin. This is the case for the *432 - 3* fundamental zone shown in Figure 6.3a,b. If the symmetry groups do contain common elements then some symmetry equivalent misorientations will have the same angle of rotation and the restriction on the misorientation axis discussed above is required. This is the case for the *622 - 222* fundamental zone shown in Figure 6.3c,d. All symmetrically equivalent misorientations with the same misorientation angle lie within the higher symmetry *622* fundamental zone. Each diad from the *222* point group then effectively excludes half of the space. However, a pair of diads implies the third and therefore the fundamental zone is 1/4 the original domain rather than 1/8. The particular segments defining the fundamental zone correspond to the defined IPF segment.

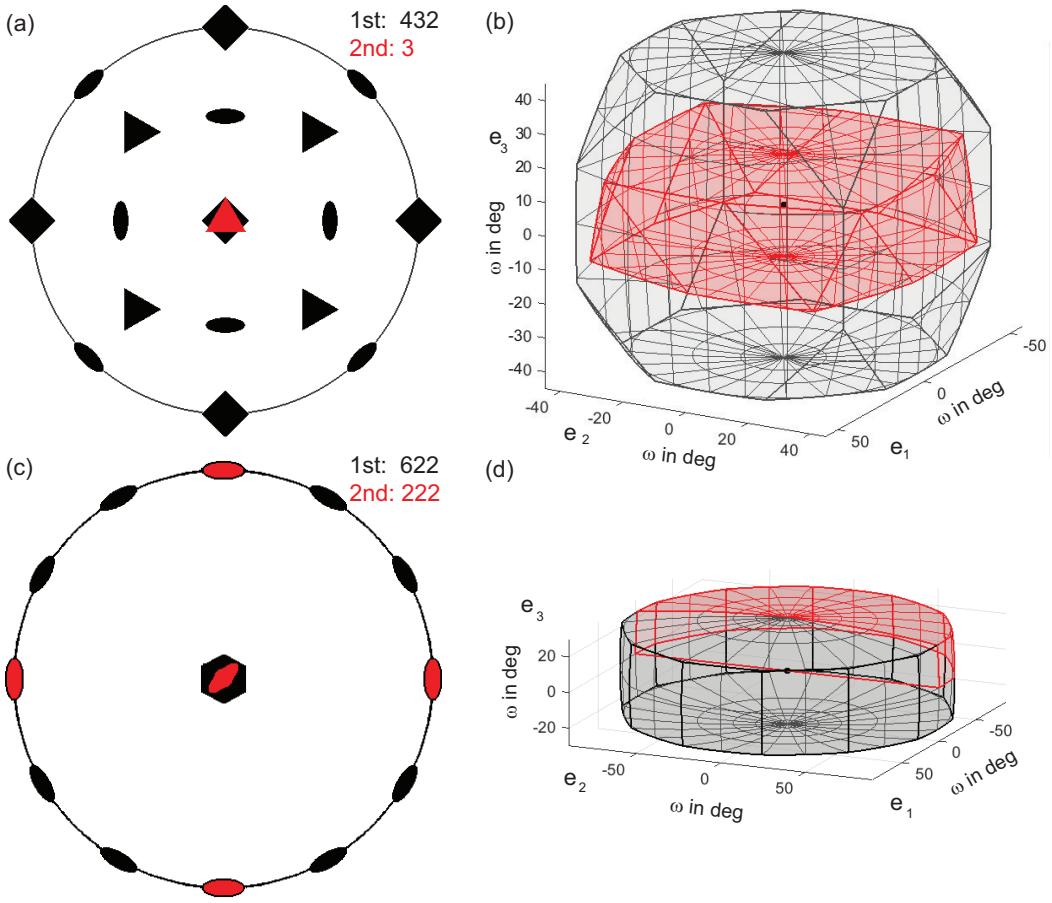

Fig. 6.3 **Symmetry elements and fundamental zones for misorientations.** Symmetry and *fundamental zones* in axis-angle space for: (a,b) crystals with point group (PG) *432* and combination of PGs *432-3* (c,d) crystals with PG *622* and combination of *622-222*.

The segmentation seen in Figure 6.3d leads to a notion of *domain geometries* where the fundamental zone is either (i) one of the domain geometries (as in Figure 6.2 or Figure 6.3b) or (ii) a segment of it, produced by cutting with planes often parallel to $\mathbf{e}_1$, $\mathbf{e}_2$ or $\mathbf{e}_3$, as in Figure 6.3d. This notion makes it tractable to discuss the appropriate fundamental zones for all crystal combinations.

Fundamental Zones for all Crystals

Crystals possess point group symmetry described by one of the 32 crystallographic point groups. 11 of these point groups are *proper point groups* and only contain symmetry operations that are proper rotations. The remaining crystallographic point groups contain improper symmetry operations that involve inversion. Treatment of improper operations has varied between authors. Here, we adopt the convention in which the crystals may only be related by a proper rotation operation and therefore only the proper point groups must be considered. Fundamental zones for all proper point group combinations were computed and it was found that 15 distinct *domain geometries* occur, as shown in Figure 6.4, which we label a-o in order of increasing maximum angle of rotation. The correspondence between fundamental zones for misorientations and these domain geometries is given in Table 6.1.

Table 6.1 **Fundamental zones for all combinations of proper point groups.** Expressed as sections of the domain geometries shown in Figure 6.4. The self-symmetry combinations do not include so-called grain exchange symmetry, which is an additional effective symmetry arising when the two crystals cannot be distinguished [28] and would halve the domain space.

	432	23	622	6	32	3	422	4	222	2	1
1	c	d	f	k	h	m	g	l	i	n	o
2	c/2	d/2	f/2	f	f	h	g/2	g	i/2	n/2	
222	c/4	d/4	f/4	f/2	f/2	f	g/4	g/2	i/4		
4	c/4	c/2	e/2	j/2	e	j	g/4	l/4			
422	c/8	c/4	e/4	e/2	e/2	e	g/8				
3	a	b	f/3	k/3	h/3	m/3					
32	a/2	b/2	f/6	f/3	h/6						
6	a/2	b/2	f/6	k/6							
622	a/4	b/4	f/12								
23	c/12	d/12									
432	c/24										

Of the 15 domain geometries, 11 (all excluding a, b, e, and j) are the fundamental zones for orientations and, equivalently, misorientations with $S_2 = 1$. The effect of rotational symmetry operators in truncating the orientation space perpendicular to the axis of rotation can be seen in each case. This is particularly clear for the lenticular fundamental zones o,

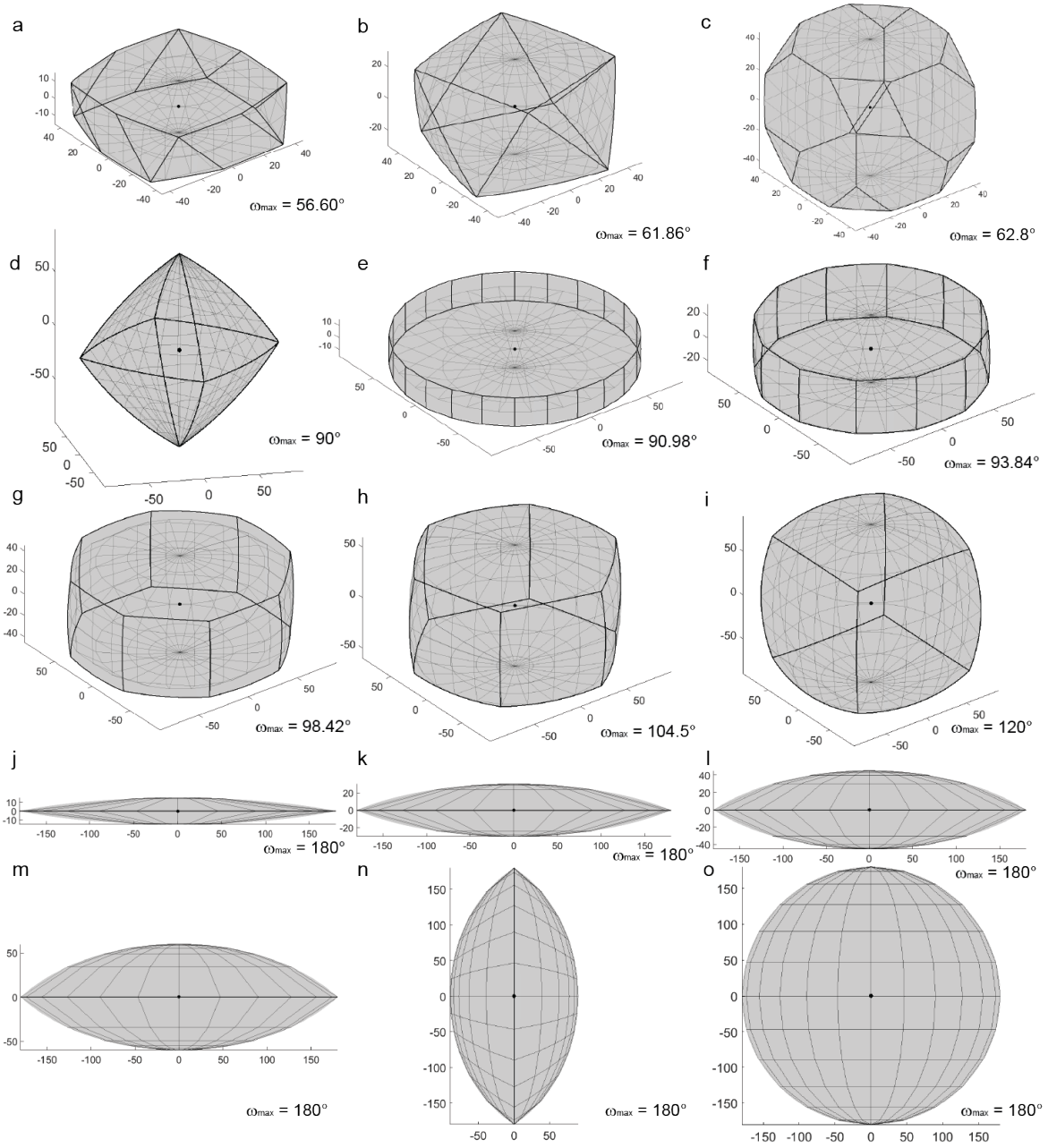

Fig. 6.4 **Domain geometries in axis-angle space.** Combinations of point group symmetries leading to fundamental zones that are one of these domain geometries or a section of it are provided in Table 6.1. The origin is marked with a point.

n, m, l and k, which are formed with the application of: no symmetry, a diad axis, a triad axis, a tetrad axis, and a hexad axis parallel to the short axis of the fundamental zone. The maximum misorientation angle (from the centre) along the axis parallel to this symmetry axis is then limited to 180°, 90°, 60°, 45°, and 30° respectively. Conventional crystallographic settings, with the monoclinic diad parallel to e_2 result in domain n being truncated along the e_2 axis whereas others are truncated along e_3.

Fundamental zones for misorientations combining proper point groups without common symmetry elements define new domain geometries centred around the origin, as described above. These are the domain geometries a, b, e and j in Figure 6.4. In all other cases, the fundamental zone is a segment of one of these 15 domain geometries with a volume indicated by the associated fraction in Table 6.1. The fundamental zones calculated in this work agree with those reported for some proper point group combinations by various authors [311–314].

An additional point applies to grain boundary misorientations where the two crystals are of the same phase, i.e., $S_1 = S_2$. In this case, it is not possible to distinguish misorientation $\boldsymbol{m}$ between grain A and grain B from the inverse misorientation $\boldsymbol{m}^{-1}$ between grain B and grain A. This effectively introduces an additional symmetry, known as *grain exchange symmetry* [315] which halves the fundamental zone.

Boundaries of the Fundamental Zone

The fundamental zone contains each symmetrically equivalent misorientation once. In the interior of the fundamental zone the vector space behaves approximately like the ordinary three-dimensional Euclidean space. In particular, misorientations clustering randomly around a fixed orientation relationship appear as one cloud. However, when plotting the fundamental zone as a bounded domain in 3D space it is important to consider a misorientation lying on the boundary and the appearance when a cluster of misorientations crosses the boundary.

A misorientation on the boundary of the fundamental zone is equivalent to another misorientation elsewhere on the boundary [299]. A cluster crossing the boundary will therefore reappear at a symmetry equivalent point, similar to crossing the boundary of a Brillouin zone in reciprocal space. However, the topology of the space is more complicated for orientations and rotations are also involved. The most common situation is that a cluster reappears just at the opposite face but rotated about the face centre, as shown in Figure 6.5a for the *432-3* fundamental zone. A cluster crossing the fundamental zone boundary at a corner typically reappears at a different corner, as shown in Figure 6.5b. At some edges (and corners in other fundamental zones) the cluster may re-enter at an immediately adjacent point, as shown in Figure 6.5c. Finally, less intuitive splitting can occur including: re-entry through a nearby face and splitting into more than two clusters, as shown in Figure 6.5d.

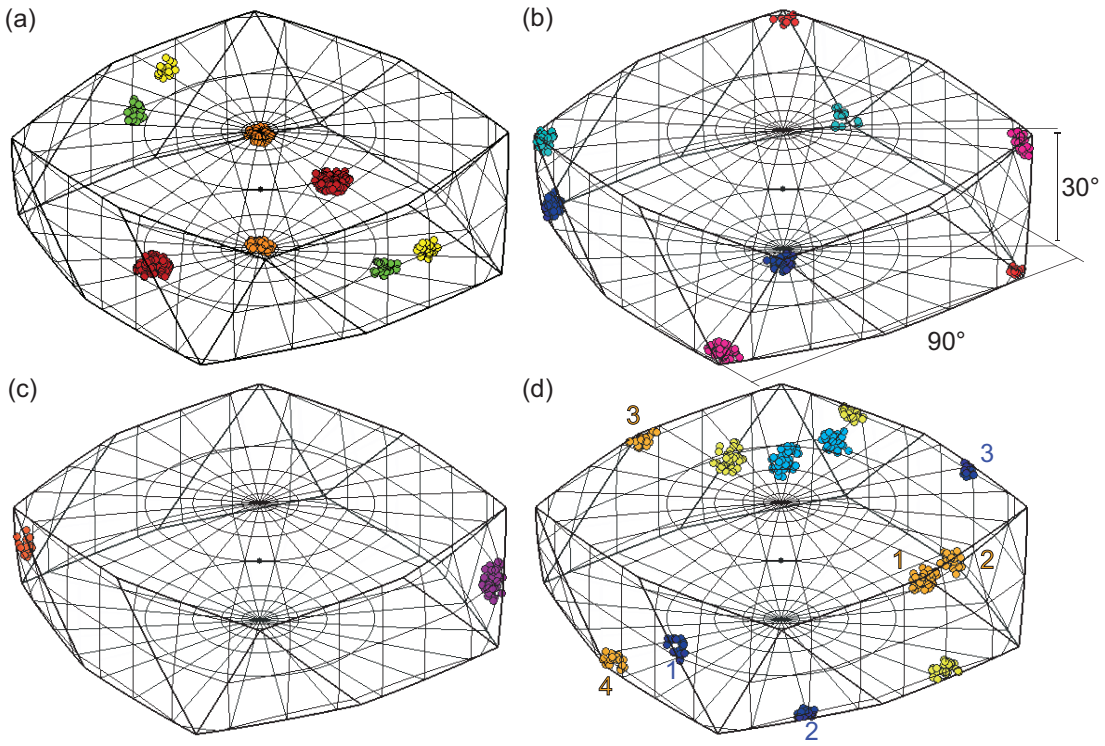

Fig. 6.5 **Misorientation clusters at ($m\bar{3}m$)-($\bar{3}$) fundamental zone boundaries.** (a) Clusters may reappear at an opposite boundary face, either directly opposite or opposite and rotated; (b) Clusters at a corner may reappear at another corner; (c) Clusters may not reappear in a different position; (d) Clusters at edges and triple points can split into more than two clusters.

When clusters cross fundamental zone boundaries, visualization may be aided by colouring symmetry related clusters based on misorientation from a given orientation relationship or a cluster centre, as shown in Figure 6.5. It can also be helpful to inspect the symmetrized dataset prior to reducing the data to the fundamental zone as it is the application of symmetry that results in the splitting. Finally, it may be advantageous to move away from 'standard' conventions for the fundamental zone definition to better reflect the data.

Alternative Axis Alignments

Adopting 'standard' conventions for the alignment of coordinate and symmetry axes has the advantage of familiarity with a misorientation space and enables direct comparison between datasets. However, alternative axis alignments may simplify the interpretation of data by reflecting underlying crystallographic symmetry [311]. For example, the cubic-trigonal fundamental zone for misorientations has the trigonal triad axis and the cubic tetrad axis aligned following the standard conventions, as shown in Figure 6.3a,b. Crystallographically, it may make sense to align the triad axes of the trigonal and cubic systems, as illustrated

in Figure 6.6a,b. This alternative alignment leads to a fundamental zone of geometry c/3 whereas the standard alignment leads to geometry a. The alignment of triad axes is particularly advantageous if these symmetry axes are aligned in important crystallographic orientation relationships. In this alternative alignment, misorientations about the triad axis are situated along the e_3 axis rather than at vertices in the standard fundamental zone, as shown in Figure 6.6c,d.

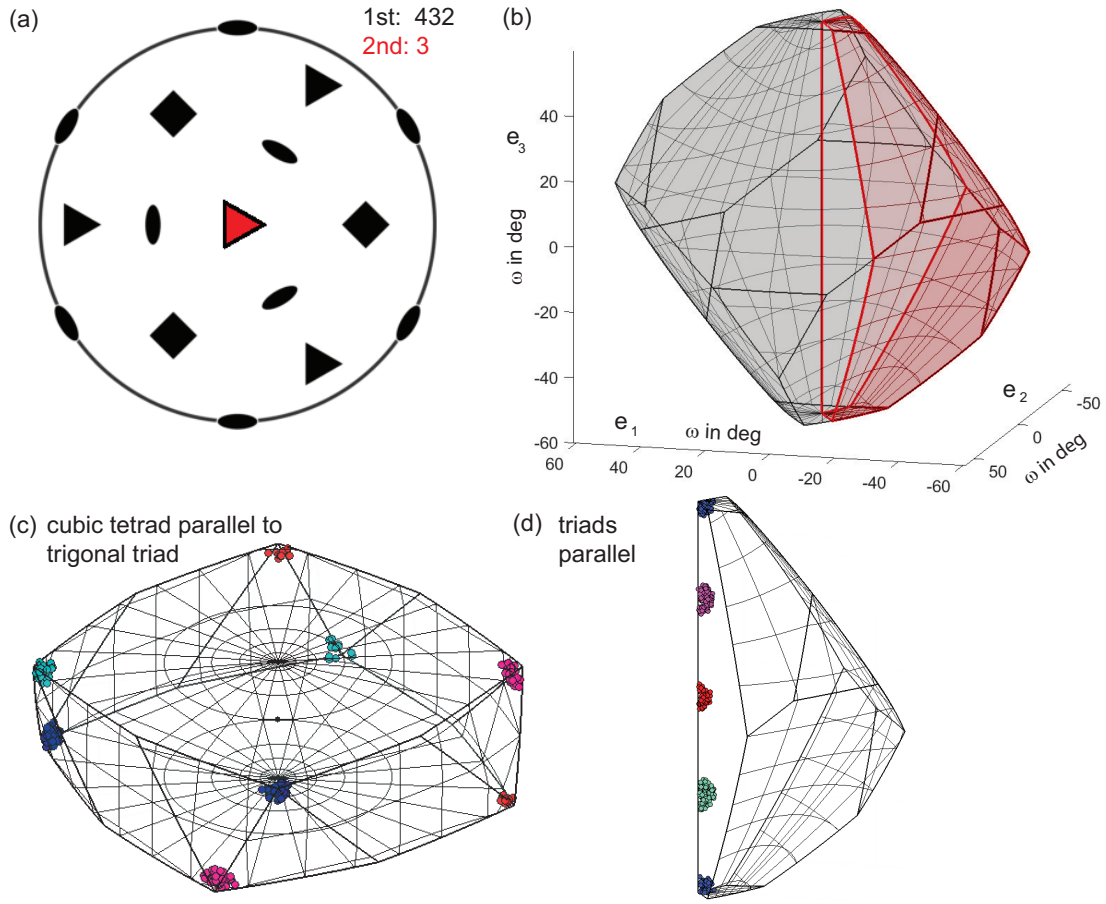

Fig. 6.6 **Symmetry aligned fundamental zones.** (a) Stereographic projection of symmetry elements for cubic ($m\bar{3}m$) and trigonal ($\bar{3}$) point groups with triad axes parallel to e_3. (b) corresponding symmetry reduced *fundamental zones* (c) Clusters at vertices; (d) Clusters along the triad axis (e_3-axis).

6.1.3 Misorientation Distributions & Orientation Relationships

Orientation mapping experiments typically yield numerous misorientation measurements describing a discrete distribution of points in the misorientation space. The existence of preferred crystallographic orientation relationships will result in a higher density of

points, compared to a random distribution, at characteristic positions in the misorientation space. Quantitative assessment of this distribution is typically made using a *misorientation distribution function* (MDF), which is a continuous probability density function describing the likelihood of observing each particular misorientation in the specimen [79]. To obtain a continuous MDF from a distribution of discrete measurements it is necessary to fit an appropriate model function to the data. If the distribution is unimodal then it may be described by a Bingham quarternion distribution (or equivalently the von Mises-Fisher distribution on SO(3)) and more general MDFs are then obtained by series expansion of various possible functions [73]. This could enable a statistically grounded assessment of the significance of an apparent cluster of measured misorientations within the fundamental zone. However, inspection of the discrete distribution may be sufficient to obtain physical insight although this is inherently qualitative. This is the path followed in the case study below primarily because the number of independent boundaries measured is insufficient to determine the MDF across the whole misorientation space.

6.2 Case Study: TCP Phases in ATI718Plus

ATI718Plus (hereafter 718Plus) is a recently developed alloy, produced with a view to replace the current workhorse alloy in the gas turbine industry, Inconel 718. This new alloy offers an operating temperature increase of about 37 K whilst maintaining workability and weldability [316], which is achieved through changes in the alloy composition. Most importantly, the Al:Ti ratio is increased and W is added, leading to a change in the precipitation behaviour within the γ-Ni (Ni/Al, $Fm\bar{3}m$) matrix. In particular, the primary strengthening phase responsible for increased dislocation drag in 718Plus is coherent γ' (Ni_3Al/Ti, $Pm\bar{3}m$), rather than γ'' (Ni_3Nb, $I4/mmm$) in 718 [317]. This is important because γ' is stable to higher temperatures. The grain boundary precipitates are also affected and, in 718Plus, are predominantly η ($Ni_3Nb_{0.5}(Al/Ti)_0.5$, $P6_3/mmc$) rather than δ (Ni_3Nb, $Pmmn$) in 718. The morphology of η-phase precipitates depends on the thermo-mechanical treatment to which the alloy has been subjected. Often it occurs in colonies with a Blackburn orientation relationship $\{111\}_\gamma||\{001\}_\eta$ with respect to one of the adjacent grains [318]. The η phase precipitates then grow in a disc-like morphology on the $\{111\}$ matrix planes [319]. After prolonged annealing, η precipitates can grow significantly in size, spanning entire grains, as well as growing in aspect ratio to form "blocky" precipitates with distinct facets [320]. Since η and γ' compete for the same alloying elements this growth typically results in γ' precipitate free zones [321].

Topologically close-packed (TCP) phases form in most nickel-based superalloys [322, 323] when exposed to high temperature for long periods of time or during solidification and welding [324–326]. Compositionally, TCP phases typically are composed principally of Ni, Cr, Co, Mo, and W. Crystallographically, TCP phases are relatively complex [327–329] but at the simplest level consist of pseudo-hexagonal layers of atoms stacked to form sites with coordination numbers as high as 16, accommodating atoms of very different sizes with packing efficiencies comparable to those of ideal close-packed structures [328]. TCP phase precipitates are potentially detrimental to mechanical performance if they occur in significant volume fractions. This is because they deplete the matrix of solute atoms which otherwise aid solid solution strengthening [329] and they cannot be used as strengthening phases themselves due to low number density[330]. Prior to this work the occurrence of TCP phases in 718Plus had been relatively little studied and those studies that reported TCP phases in 718Plus [331, 324, 326, 332] largely neglected their crystallography. The observation of TCP phases in 718Plus had also mostly been attributed to solidification of the alloy after casting [331] or to welding [324, 326, 332]. Interestingly, no TCP phases were reported in a previous study on long term stability of 718Plus (732°C, 2500 hrs) by Radavich *et al.* [333]. Here, the occurrence of TCP phases in 718Plus was investigated in detail[6]. SPED was applied in combination with analysis in three-dimensional misorientation spaces to reveal inter-phase crystallographic relationships between TCP precipitates and surrounding microstructure. Machine learning techniques were then applied to obtain phase-specific characterisation in terms of both crystallography and composition.

6.2.1 Materials & Methods

718Plus samples were provided by Rolls-Royce Deutschland Ltd. & Co KG. The initial ingot material was triple vacuum melted by Allegheny Technologies Inc. for high cleanliness and forged into billet product. This was followed by subsolvus forging and heat treatment at T=843-871°C for 16 hr, T=954-982°C for 1 hr, 788°C for 8 hr followed by furnace cooling and 704°C for 8 hr. These heat treatments were performed by Otto Fuchs KG. A further annealing at 788°C for 500 hr was performed in house. Samples were extracted from the mid-radius of the heat-treated forgings using electric discharge machining (EDM). Slices of 300-500 μm were cut using a saw and 3 mm diameter discs were produced using EDM. These discs were ground to approximately 200 μm thickness and further thinned by electrolytic twin-jet polishing using a Tenupol and 10 vol.% perchloric acid solution at -5° C.

[6]The work presented here was part of a collaboration with Robert Krakow, who performed: heat treatments, specimen preparation, EDX data acquisition, and conventional TEM characterisation. The complete work was reported in Krakow *et al.* [334].

SPED was performed using a Philips CM300 FEGTEM operated at 300 kV and controlled using a NanoMegas Digistar system. The probe was aligned with a convergence semi-angle of ~ 5 mrad and a precession angle of 9 mrad. Scans were acquired with a step size of 10 or 20 nm depending on the region of interest and the dwell time was 40-60 ms. STEM-EDX mapping was performed using an FEI Tecnai Osiris operated at 200 kV with a step size of 3 nm. The gun lens was adjusted to produce a large probe current of 0.7 nA for increased X-ray generation, which allowed a dwell time of 200-250 ms per pixel.

6.2.2 TCP phase occurrence & identification

Characterisation via bright-field TEM imaging and small angle CBED was used to assess the occurrence of TCP phase precipitates in 718Plus, as reported in full in Krakow *et al.* [334]. This characterisation revealed that TCP precipitates were present in the material even without additional annealing. Small angle CBED patterns, as shown in Figure 6.7, were recorded near major zone axes of eight TCP precipitates and used to identify consistent crystallographic phases [334]. It was found that the data recorded from these TCP particles was consistent with either hexagonal C14 Laves phase ($P6_3/mmc$) or tetragonal sigma (σ) phase ($P4_2/mnm$). The lattice parameters were measured to be $a = 4.9 \pm 0.1$ Å, $c = 7.8 \pm 0.1$ Å and $a = 8.8 \pm 0.1$ Å, $c = 4.5 \pm 0.1$ Åfor C14 Laves and σ phases respectively. The unit

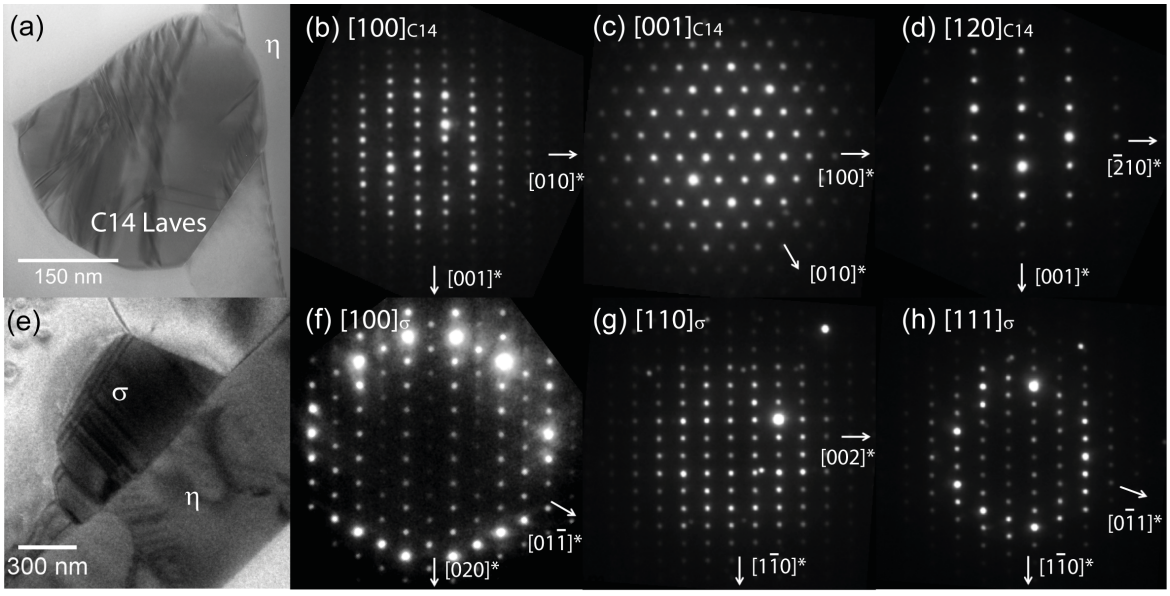

Fig. 6.7 **Conventional TEM of TCP phase particles.** (a) Bright-field TEM image of a representative C14 Laves phase particle. (b-d) Small-angle CBED patterns near major zone axes of the hexagonal C14 Laves phase. (e) Bright-field TEM image of a representative σ phase particle. (b-d) Small-angle CBED patterns near major zone axes of the σ phase.

cells of the η phase and identified TCP phases are shown in Figure 6.8. The particles are typically blocky in morphology and exhibit internal faulting, which is in contrast to other Ni based superalloys in which the TCP particles are plate-like [327]. 80 TCP precipitates were observed and 96% of these occurred at $\gamma-\eta$ phase boundaries, often along particular facets of the η phase precipitates. TCP particles were also observed at some grain boundaries although it remains possible that these formed at $\gamma-\eta$ phase boundaries that were removed during TEM sample preparation. This observation of C14 Laves and σ-phase precipitates primarily at distinct facets of η-phase precipitates directed attention towards the crystallographic relationships between TCP phase precipitates and the surrounding microstructure.

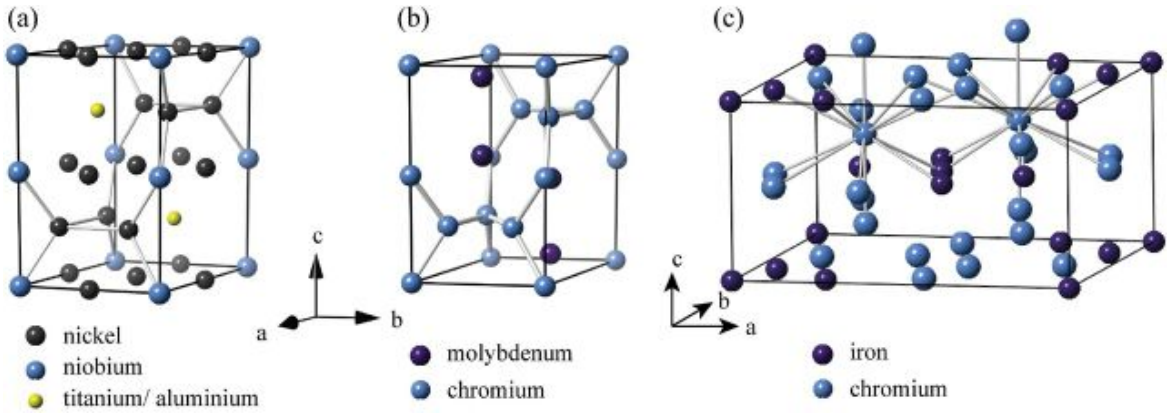

Fig. 6.8 **Unit cells of the phases studied.** (a) η phase, (b) C14 Laves phase, and (c) σ phase.

6.2.3 Crystallographic Orientation Relationships

Phase and orientation maps were obtained by applying the template matching method of Rauch *et al.*, see Chapter 4, to 4D-SPED data acquired from 10 TCP particles. A representative phase map, produced using this approach, from a region containing a σ-phase precipitate is shown in Figure 6.9a. Crystallographic relationships between the phases may be illustrated by plotting pole figures for poles coincident between phases, as shown in Figure 6.9b-d. In this particular example an apparent crystallographic relationship between η and σ can be identified as:

$$[100]_\eta||[110]_\sigma, (001)_\eta||(001)_\sigma \tag{6.4}$$

An apparent crystallographic relationship between the σ-phase and the γ-phase, that has previously been reported in other Ni alloys [], may also be identified as:

$$[011]_\gamma||[140]_\sigma, (111)_\gamma||(001)_\sigma \tag{6.5}$$

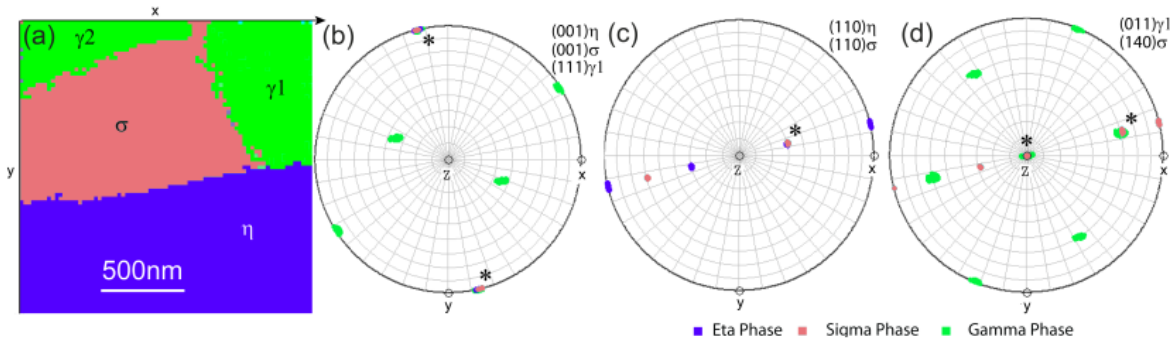

Fig. 6.9 **Phase and orientation mapping of sigma phase particle.** (a) Phase map showing a σ phase precipitate and surrounding microstructure. (b-d) Pole figures showing important crystallographic poles. Note that in the η phase $\{110\}_\eta$ poles are parallel to the $\langle 100\rangle_\eta$ directions. * marks common poles.

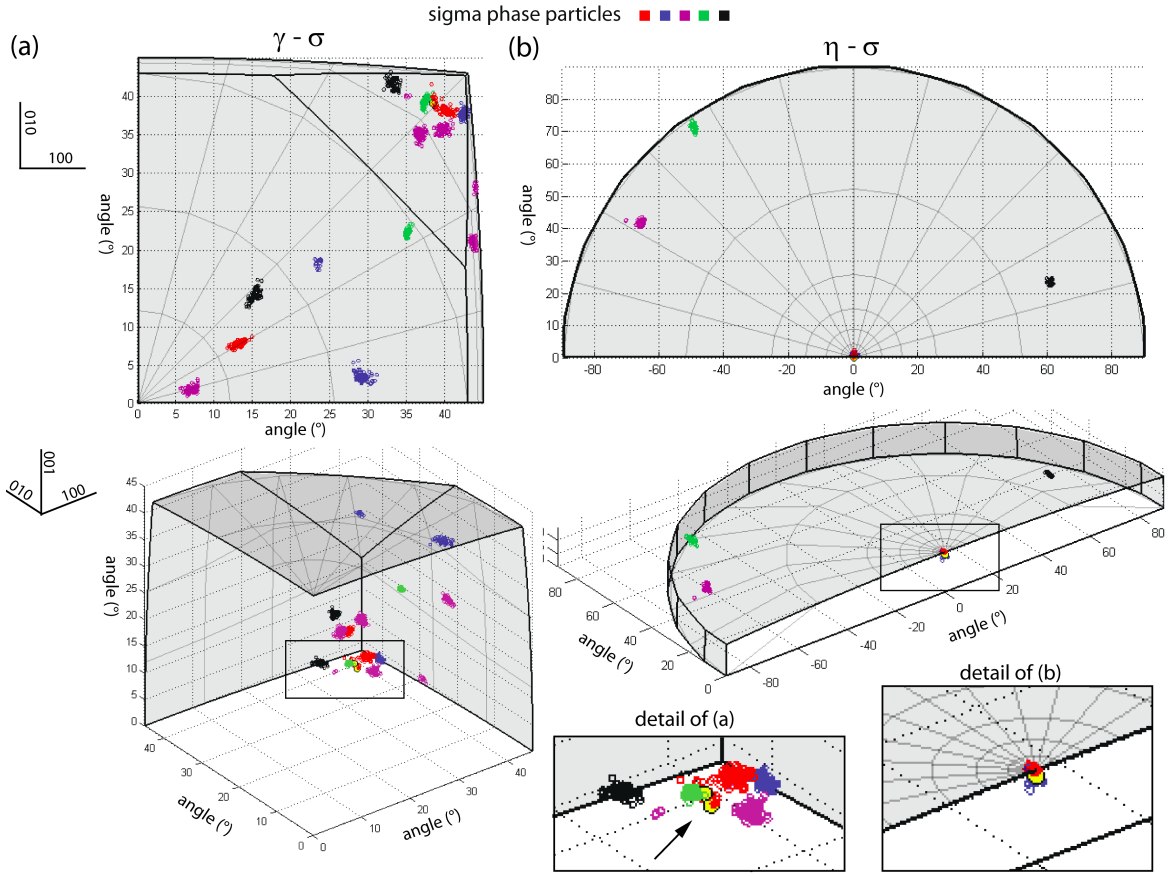

Fig. 6.10 **Sigma phase disorientations in fundamental zone.** (a) γ-σ disorientations. (b) η-σ disorientations.

Whilst this pole figure based analysis is insightful it requires numerous poles for each phase to be plotted until a coincident pair is found and it is not ideal for comparing numerous particles with different orientations since it is referred to the specimen reference frame. Since numerous particles must be assessed in order to make any statement about crystallographic relationships the pole figure approach is not ideal. The misorientation space approach set out above has the advantage that it is in the crystal reference basis so data from particles with different orientations can be plotted in the same figure. Further, the disorientation is a uniquely defined vector quantity so does not require numerous plots to be made. Crystallographic relationships between five σ-phase particles and their surrounding microstructure were compared by plotting the disorientation between phases in the appropriate fundamental zone of axis-angle space, as shown in Figure 6.10. For each phase combination, 50 disorientations were calculated from the orientations associated with 50 randomly selected pixels in each phase. The orientation relationships described above are marked with bounded yellow circles.

It was found that the $\eta - \sigma$ orientation relationship identified in the initial region of interest occurred in two of five instances and in the remaining three cases, the $\eta - \sigma$ relationship did not indicate a strong crystallographic preference. On the other hand, in every region of interest a $\sigma - \gamma$ boundary with disorientations near to the proposed OR was observed. Four regions of interest fulfil the relationship closely and one cluster is situated about 5° away from the relationship.

A phase map and corresponding pole figures from a region containing two C14 Laves phase precipitates are shown in Figure 6.11. In this region the misorientation between the C14 Laves precipitates and the adjacent η-phase precipitate can be well described by relatively low index parallelisms as:

$$[210]_\eta || [631]_{C14}, (\bar{1}21)_\eta || (10\bar{6})_{C14} \tag{6.6}$$

Crystallographic relationships between four C14 Laves phase precipitates and their surrounding microstructure were compared in axis-angle space, as shown in Figure 6.12. In this case, no preferential crystallographic relationship between the C14 Laves phase precipitates and either the η-laths or γ matrix was observed and the misorientation clusters associated with each region of interest are situated across the fundamental zones.

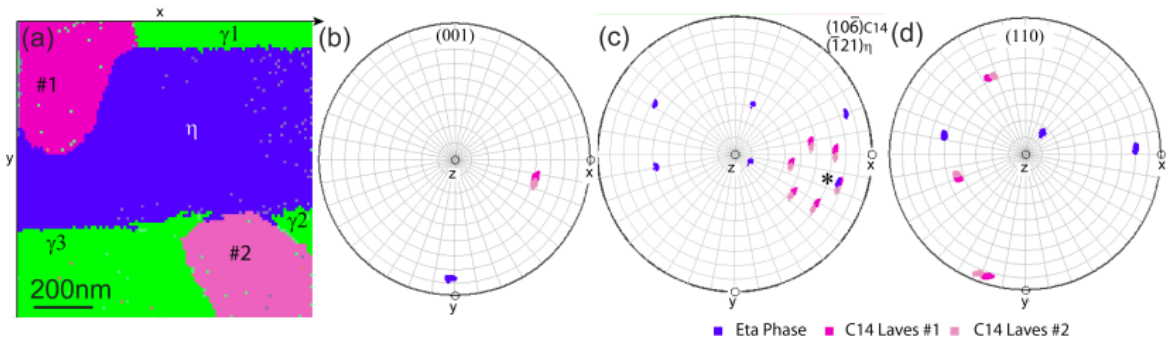

Fig. 6.11 **Phase and orientation mapping of Laves phase particle.** (a) Phase map showing two C14 precipitates and surrounding microstructure (b-d) pole figures showing important crystallographic poles. *indicates common poles.

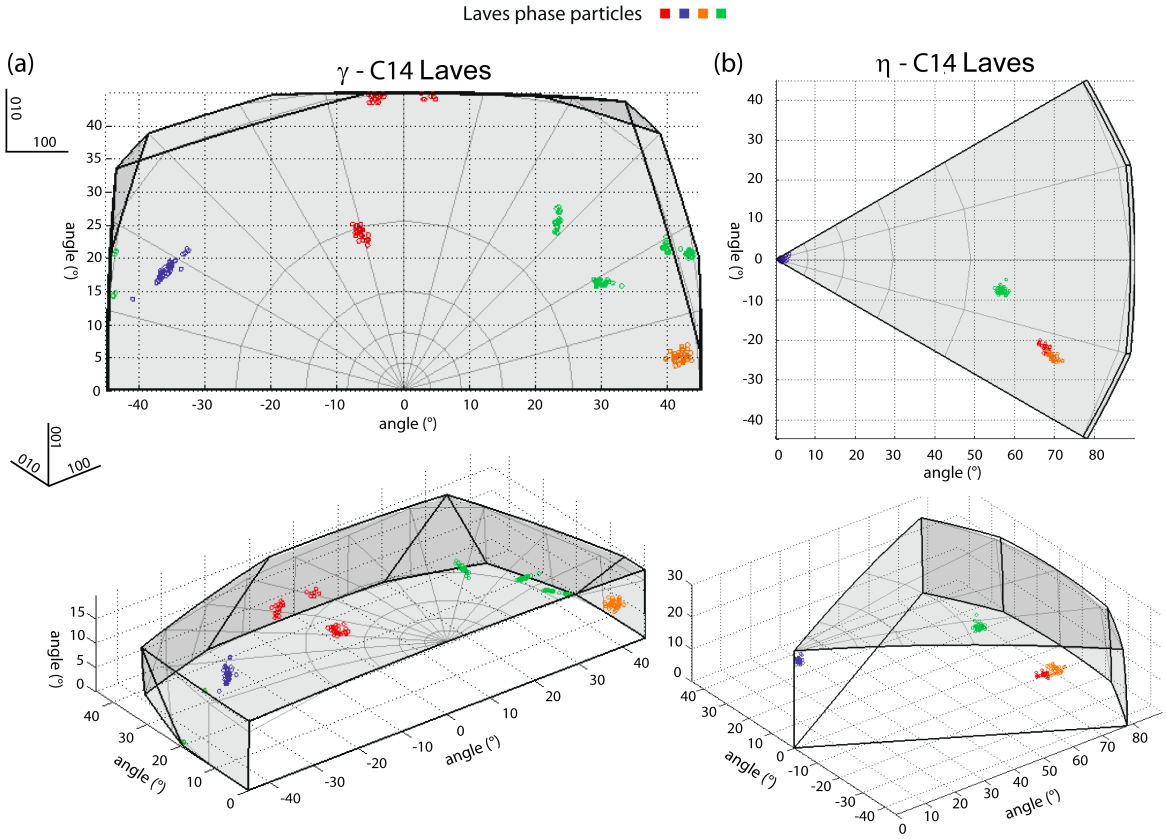

Fig. 6.12 **Laves phase disorientations in fundamental zone.** (a) γ-C14 Laves disorientations. (b) η-C14 Laves disorientations.

.

6.2.4 Learning Phase Specific Signals

Complete characterisation of a multi-phase, polycrystalline microstructure requires specification of the composition, crystallographic structure and crystal orientation at each volume element. Typically the microstructure is such that the composition, crystallography and orientation is similar locally within given crystals i.e. a grain or a precipitate and the number of diffraction patterns acquired in a S(P)ED experiment or spectra in a STEM-EDX experiment is much larger than the number of significantly different microstructural elements. In such cases, unsupervised machine learning methods may be applied to learn unique, phase-specific, signals corresponding to each microstructural element, as discussed in more detail in Chapter 4. Here, the potential of such methods to obtain phase specific signals is explored in application to two regions of interest in the 718Plus alloy containing TCP precipitates. The two regions included one C14 Laves phase particle (ROI1) and one sigma phase particle (ROI2) situated in surrounding microstructure comprising one or two γ grains and an η phase precipitate, as shown in Figure 6.13. The specimen was not aligned to any particular crystallographic orientation.

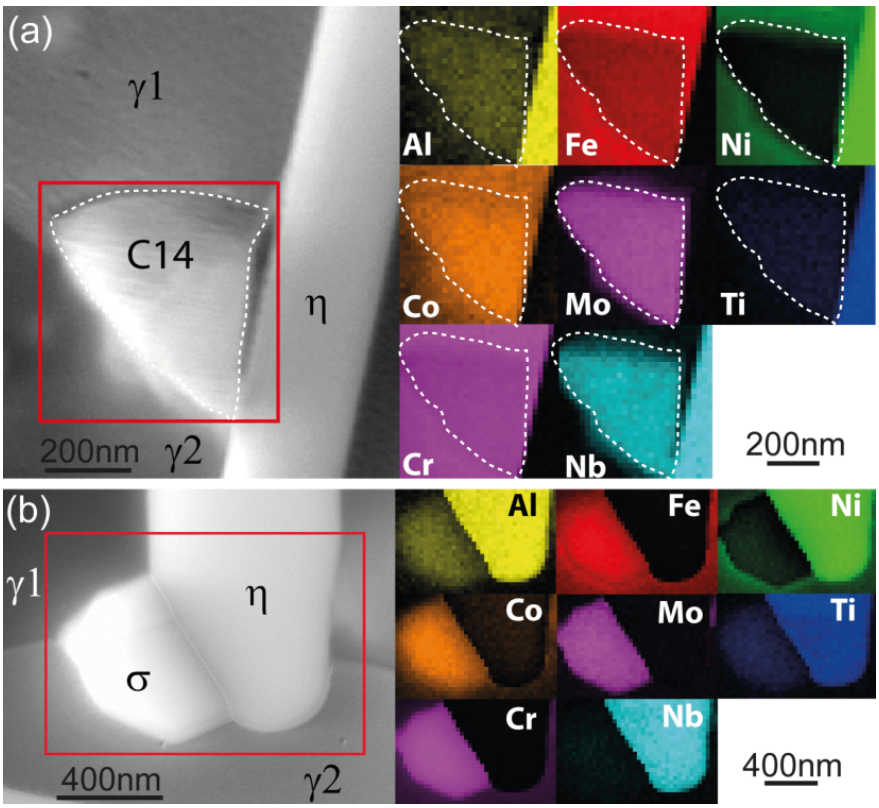

Fig. 6.13 **ADF-STEM images and elemental maps of TCP particles.** EDX spectrum images from two regions of interest to which unsupervised machine learning techniques were applied. (a) C14 Laves phase, and (b) σ phase.

Application of unsupervised learning methods to obtain phase specific signals involved the application of two linear decompositions, which are described in more detail in Chapter 4. Firstly, principal component analysis (PCA) was performed to determine intrinsic dimensionality of the data based on inspection of plots of the fraction of variance explained by each principal component. The aim is to identify a *regime change* from relatively high-variance to relatively low-variance components, indicating a low intrinsic dimensionality when only high-variance components are retained. Secondly non-negative matrix factorization (NMF) was applied to obtain more physical component signals. The results of both of these steps applied to ROI1 and ROI2 are shown in Figures 6.14 & 6.15 respectively. The PCA decomposition of both the EDX and SPED data from ROI1 shows a clear regime change, after 4 components are included in the model (Figure 6.14a,b) enabling the intrinsic dimensionality to be determined (one component corresponds to surrounding vacuum). A regime change is also seen, after 3 components, for PCA decomposition of EDX data from ROI2 (Figure 6.15a). However, there is only a gradual decrease in the variance described by PCA components of the SPED data from this region, without a clear regime change. In this case, the physically significant components to be included could only be determined by inspection of the components and in this case it was found that beyond 4 components the additional components began to represent small orientation variations within microstructural elements most likely due to bending in the thin film specimen. Ultimately, a low intrinsic dimensionality of 3 or 4 component signals could be identified to describe the microstructural elements present in all of the EDX and SPED datasets.

Component signals and corresponding loading maps obtained by NMF, taking the number of components corresponding to the number of microstructural elements as identified by inspection of the raw data, are shown in Figures 6.14 & 6.15. The loading maps reveal microstructural regions with characteristic composition or crystallography and therefore highlight regions with particular composition and crystallography respectively. These loading maps indicate that the corresponding component signals correspond to unique signals associated with the TCP precipitate, η phase precipitate, and γ phase respectively (from top to bottom in Figures 6.14 & 6.15). In ROI1 (Figure 6.14) there is one crystal of each phase and therefore the loading maps associated with SPED and EDX data can be related directly. In ROI2, (Figure 6.14) there are two γ grains with different orientations and therefore two SPED components corresponding to these two grains which have approximately the same composition and are therefore associated with only one EDX component. Taking account of this, the loading maps resulting from decomposition of SPED and EDX data can be seen to be well correlated spatially, both with each other and with the observations from more conventional analyses presented in Figure 6.13.

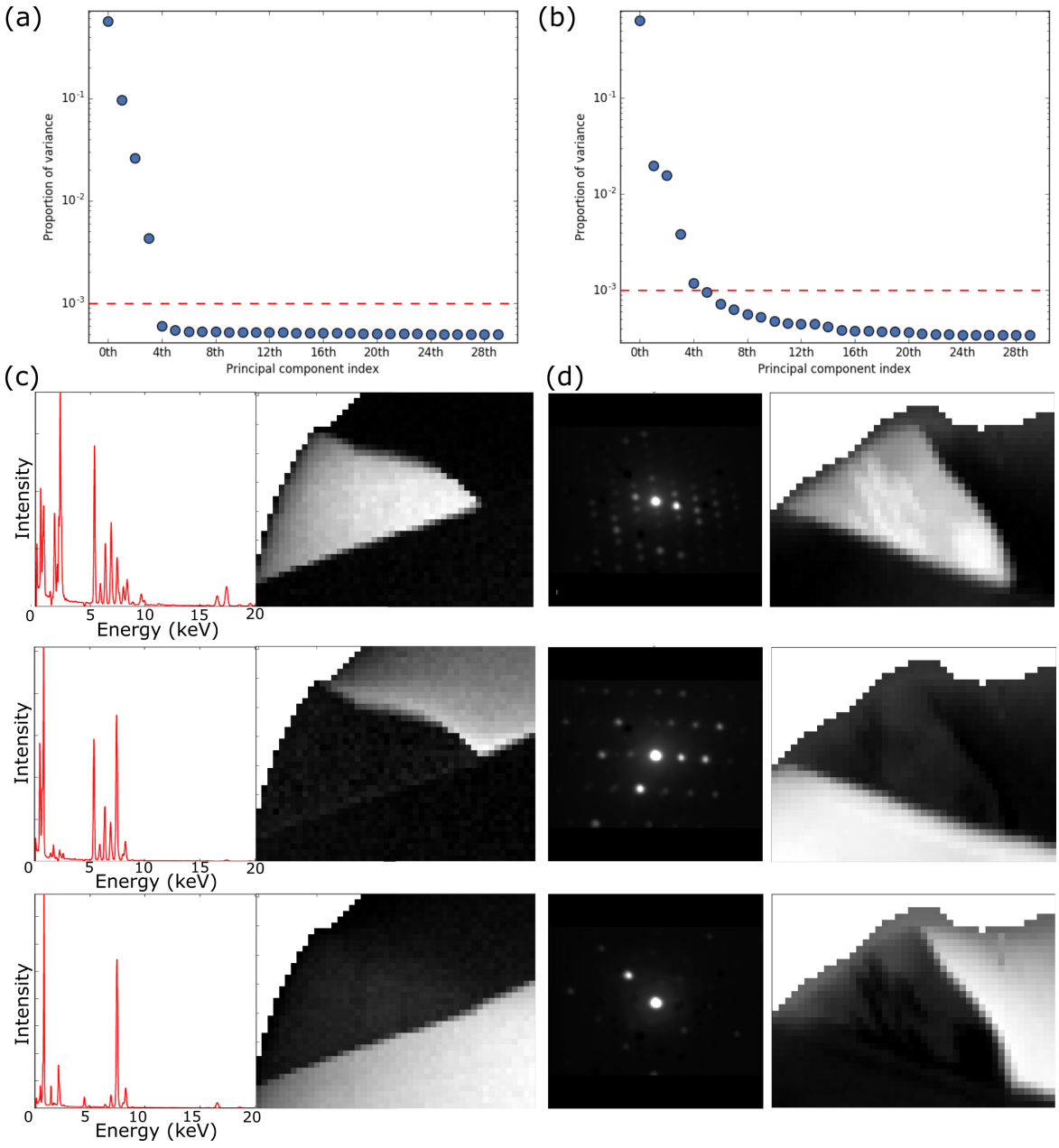

Fig. 6.14 **Unsupervised learning results from ROI1 containing a C14 laves phase particle.** (a,b) PCA scree plots for decomposition of EDX and SPED data respectively. The 10^{-3} level is indicated to highlight different scales. (c,d) Learnt component signals (spectra or diffraction patterns) and corresponding loading maps obtained using NMF.

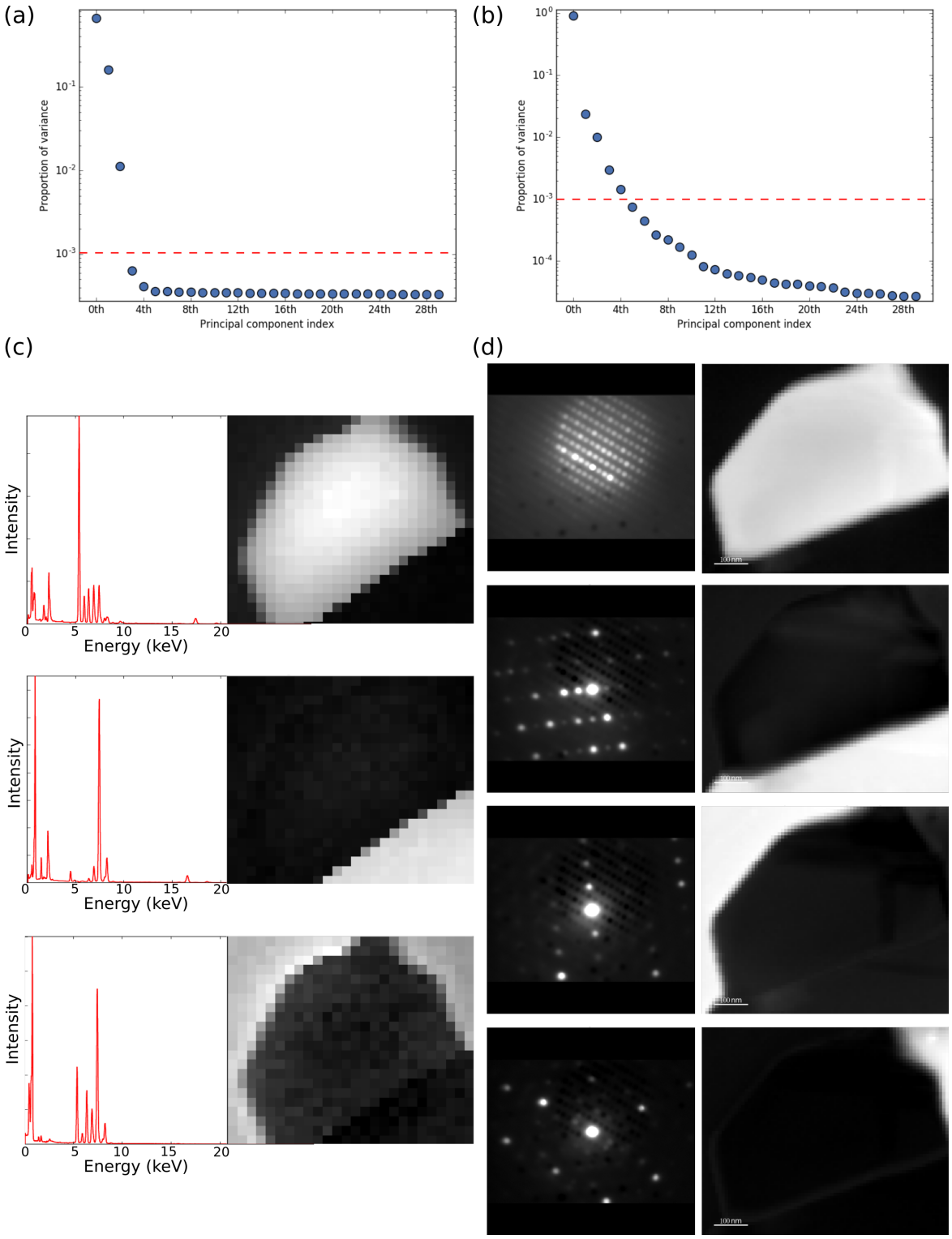

Fig. 6.15 **Unsupervised learning results from ROI2 containing a *sigma* phase particle.** (a,b) PCA scree plots for decomposition of EDX and SPED data respectively. The 10^{-3} level is indicated to highlight different scales. (c,d) Learnt component signals (spectra or diffraction patterns) and corresponding loading maps obtained using NMF.

NMF component signals highlight differences between microstructural elements and resemble physical X-ray spectra and diffraction patterns. However, these component signals contain pseudo-subtractive features where the non-zero background of the experimental data allows the algorithm to apportion signal that is strong in more than one phase to only one or other component signal in an unphysical way. Nevertheless, the learnt component diffraction patterns could be indexed and used to recover the orientation relationship between the phases in reasonable agreement with the more conventional pattern matching analysis. Quantification of the learnt component EDX spectra was not however reliable, most likely due to the presence of mostly the same elements, and therefore X-ray peaks, in all of the phases but with different ratios, which makes pseudo-subtractive effects more significant. Instead the loading maps were used to define masks on the raw data within which the spectra were summed. Quantification of these spatially averaged spectra was was performed via the HyperSpy Python library [231] using the Cliff-Lorimer method [198] with X-ray intensities extracted using a model fitting procedure in which a Gaussian function is fitted to each X-ray line. The compositions obtained following this procedure are reported in Table 6.2 and are comparable to the values reported in the literature for TCP precipitates in alloy 718 to within a few atomic %, which is a reasonable estimate of the experimental error [335–337, 334].

Table 6.2 **Phase compositions of the TCP phases particles.** As determined from a spectrum obtained by summation over pixels within the particle using masks based on loading maps obtained by NMF. = Low energy peak (1.48 keV) - subject to absorption, ** = peak approaching noise limit.

at.%	Al	Ti	Cr	Fe	Co	Nb	Ni	Mo	W
TCP2 (C14)	0.7	0.0**	26.0	11.2	14.9	5.2	29.1	8.7	4.3
TCP3 (σ)	0.6	0.1**	52.2	10.1	11.2	0.3	19.9	4.2	1.6

6.2.5 Discussion & Conclusions

TCP precipitates were observed in 718Plus after significantly shorter annealing times (ca. 30 hr) than previous studies [333]. Of the TCP precipitates studied, approximately half, were C14 Laves phase and half were σ phase although in one instance a C36 Laves phase precipitate was observed. These precipitates often occur at the $\gamma - \eta$ interface on facets of η particles, which may be expected due to chemical segregation associated with these η particles and also suggested that crystallographic relationships with the η phase particles may play a significant role. The composition of the TCP phases observed and the absence of α-Cr, the predominant co-precipitate of δ in 718 [335, 338], suggests that the TCP phases observed may be dominated by the local availability of specific elements. The σ phase, for

example, rejects Nb and Ni more so than the C14 Laves phase. It is therefore more likely for nucleation to occur at η-γ phase boundaries, in line with our observations here showing all TCPs found at the grain boundary were C14 Laves phase.

The orientation relationship between η and σ seems to be a consequence of the $\gamma-\eta$ orientation relationship which has likely been formed during forging and pre-solution treatment and therefore before any σ formation. If a precipitate grows on any of the four equivalent $\{111\}$ planes in γ, then there is a 25% chance that it will also be in an OR with η, which is comparable to the ratio found in this study. In line with the above, in both occurrences of the orientation relationship, the η basal plane facet was the one occupied by σ. This suggests that certain η facets promote certain disorientations, but that the stronger stabilizing effect comes from the γ matrix, which is also intuitive as σ grows into the γ grain. Coherency, or the lack thereof, might also explain why no strong orientation relationship was found between C14 Laves phase precipitates and their surrounding microstructure. The lattice mismatch of ca. 6% is likely too large for epitaxy between C14 Laves and η phase crystallographic planes. The same would apply to C14 Laves and the close-packed γ matrix planes as the mismatch between η and γ is very small.

It is also assumed that stable nuclei will be sensitive to the degree of coherency at the interface, especially σ phase, which has been shown to grow in γ according to a distinct orientation relationship (OR), matching up the close-packed planes. This preference was found for all sites of interest studied. As has been pointed out before by Rae et al. [327] the lattice mismatch has a strong effect on the morphology of TCP precipitates in the γ matrix. They show that the phase forms sheets in the matrix to establish a good match, thicker particles for increased mismatch and conclude that alloys with a good match between and γ are particularly prone to early precipitation. In the light of these considerations, it seems plausible to assume that, in 718Plus, the phase has a greater mismatch with γ as particles have a blocky morphology. This might also explain why the OR is not fulfilled closely, with deviations of about 3°.

6.3 Summary & Prospects

The results presented in this chapter demonstrate that 4D-SPED can be leveraged as a powerful tool for investigating inter-phase relationships in engineering alloys, when combined with advanced data analysis methods including unsupervised machine learning and misorientation analysis in three-dimensional misorientation spaces. The use of three-dimensional misorientation spaces provides an intuitive and visual way to identify and assess crystallographic orientation relationships as demonstrated in the case study presented. This analysis could

equally be applied to orientation mapping data acquired using electron backscatter diffraction data or X-ray mapping techniques. The application of unsupervised learning methods to both SPED and EDX data to learn phase specific signals is an attractive way to reduce very large datasets to the microstructurally essential features. The results shown here suggest that this approach is feasible and already useful in a pragmatic sense, although the development of more specialised algorithms, perhaps incorporating alternative regularisation schemes, to enable physical component signals to be learnt routinely would be of major benefit. In the short term the use of learnt loading maps to mask the original data provides a good compromise. Overall this combination of a new experimental approach to acquire data providing nanoscale crystallographic insight, in SPED, and advanced data processing methods opens the way to many empirical polycrystalline nanostructure studies. The goal of such studies would be to acquire maximum experimental constraint on the relationship between two crystals to enable calculation of the relevant interface structures in complex modern engineering alloys. An example of this idea is presented in the following chapter using polycrystalline graphene as a structurally simple test case.

Chapter 7

Graphene Structure & Topography

Graphene and related two-dimensional materials have attracted intense recent interest driven by extraordinary physical and chemical behaviour [339, 340] and the prospect of disruptive technological change [341]. Many potential applications (e.g. transparent flexible electrodes) require large area graphene films, and chemical vapour deposition (CVD) has emerged as a promising synthesis method to meet this need [342–344]. As is typical of crystalline matter, CVD graphene films contain structural defects (e.g. vacancies, dislocations, and grain boundaries) causing deviation from the idealized picture of a single layer of carbon atoms arranged on a planar hexagonal lattice. The same is true of other two-dimensional (2D) materials, and these defects may be deleterious for performance [345], or may enhance specific properties [346] and tunability through defect control [347]. Characterisation of defect structures is therefore a key element in developing structure-property relationships in graphene and related 2D materials.

Many studies have probed defects in graphene using various techniques such as: Raman spectroscopy, atomic force microscopy, scanning tunneling microscopy, and (S)TEM, which is the focus here. A key feature of 2D materials is that they are free to buckle as membranes in three-dimensional space unless constrained by bonding to a substrate. Indeed, such buckling is a necessity for freestanding two-dimensional crystals [348, 349] and also stabilities defect structures by screening in-plane elastic strain fields [350–352]. Extreme buckling, either intentional, or due to growth or sample transfer, may result in the graphene film being wrinkled, folded or crumpled [353–355]. Few-layer islands may also occur on predominantly monolayer material [356] and these layers may be mis-stacked [357–362]. These features combine to produce diverse topographic landscapes. Films produced by CVD are also typically polycrystalline [89, 363] and therefore contain grain boundaries at the convergence of single-crystalline grains with different lattice orientations. Such grain boundaries have been characterised primarily using electron diffraction and dark-field TEM imaging [364, 365], to

determine misorientation across grain boundaries, and atomic resolution (S)TEM imaging to reveal boundary structures [364, 366]. Finally, point defects such as disclinations and dislocations occur and mediate structural transformations in the graphene film. These point defects and grain boundaries may be described generally as topological defects because they require that the regular connectivity of 6-membered hexagonal rings is broken with the presence of smaller or larger rings, typically 5 or 7 membered (but occasionally 4 or 8 membered). Despite this extensive investigation, there remains a need for quantitative assessment of defect structures on length scales from 10 nm to 1μm. This length scale bridges a key gap between the atomic scale and the device scale and is the scale on which features such as sub-grain orientation variations and various forms of film buckling are expected to occur. There is also a need to develop an efficient quantitative and direct characterisation framework that may be applied to reveal structural features on these length scales in 2D materials in general. Here, 4D-SED is combined with advanced *post-facto* data analysis to characterise the structure and topography of CVD graphene across these length scales. The methods developed define a robust characterisation framework that may be applied to other 2D materials.

7.1 Materials & Methods

7.1.1 Material Condition

CVD graphene was synthesised[1] on 35 mm thick commercial copper (Cu) foils. The Cu substrates were annealed for 30 min in a hot-wall reactor at 1000°C in a H_2 atmosphere (20 sccm at $\sim$ 200 mTorr). The graphene growth started at the same temperature with the injection of 5 sccm of CH_4 at a pressure of $\sim$ 300 mTorr for 30 min. The system was then cooled in vacuum. Samples of CVD graphene were prepared for electron microscopy by transfer to a gold quantifoil TEM grid (1.2/1.3 quantifoil, Agar Scientific). The transfer procedure involved depositing PMMA on the graphene/Cu sample and wet-etching the copper substrate in an aqueous solution of ammonium persulfate (0.1 M). The PMMA/graphene film was then rinsed and transferred to the TEM grid. After drying, the PMMA layer was removed in acetone.

[1] Synthesis and specimen preparation were performed by Ugo Sassi, Domenico De Fazio and Stephen Hodge working under Prof. Andrea Ferrari at the Cambridge Graphene Centre.

7.1.2 SED Acquisition

SED was performed using a Philips CM300 FEGTEM operated at 50 kV with a Nanomegas Digistar system, as described in Chapter 3. The use of an incident electron energy < 60 keV makes knock-on damage, the dominant damage mechanism in graphene, negligible. The diffraction patterns were recorded with 144×144 binned pixels per pattern (2×2 binning), an exposure time of 60 ms and a nominal camera length of 11 cm. The step size in the scan was 10.6 ± 0.2 nm based on calibration performed at the experimental conditions and the convergence semi-angle was $\sim$1.5 mrad. The scan region was 120×120 probe positions, resulting in 4D-SED datasets comprising 14 400 electron diffraction patterns.

7.1.3 Data Analysis

Analysis of the 4D-SED data was performed using methods described in Chapter 4. Prior to detailed analysis a number of pre-processing steps were applied to the raw data. First, an affine transformation corresponding to a stretch in the x-direction by a factor of 1.45 was applied to correct for the off-axis camera geometry. Second, the data was aligned with respect to translation of the direct beam. Third, a background subtraction was applied to correct for a complex structured background arising due to low level light in the microscope room being detected by the optical camera and the inhomogeneous response of the phosphor screen to electrons. To subtract this background efficiently, from all recorded diffraction patterns, the mean diffraction pattern from the region of interest was calculated and a morphological erosion operation applied to remove bright spots corresponding to diffracted beams. This eroded average image was then taken to be the background and subtracted from all recorded diffraction patterns, with values falling below zero being set to zero. The effects of these pre-processing steps on the data are illustrated in Figure 7.1.

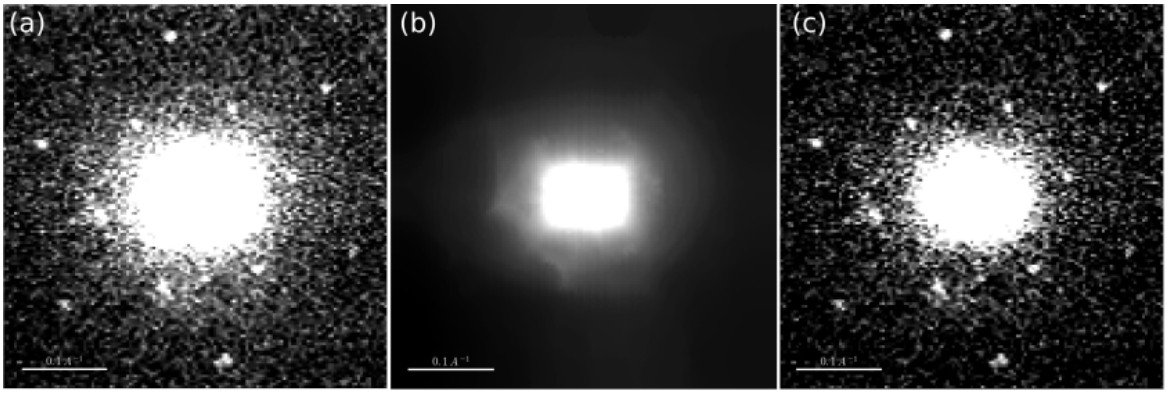

Fig. 7.1 **Pre-processing SED data.** (a) Raw diffraction pattern. (b) Morphologically eroded average diffraction pattern. (c) Background subtracted diffraction pattern.

7.2 Results & Discussion

7.2.1 Imaging & Learning Grain Structure

Polycrystalline graphene films are most simply characterised by identifying grains within which the lattice orientation is similar, often to within a range of $\pm 10^{\circ}$. This is the aim of conventional TEM analysis of polycrystalline graphene films using selected area electron diffraction (SAED) and dark-field imaging[364, 365]. Similar characterisation can be performed using 4D-SED data and determining the grain structure at this coarse level is an important initial step in directing more detailed local analyses of the 4D-SED data within individual grains. Grain structure was assessed initially by considering the spatially averaged diffraction pattern from across four regions of interest and by forming diffraction contrast images with selected diffracted beams, as shown in Figure 7.2 and described in detail below.

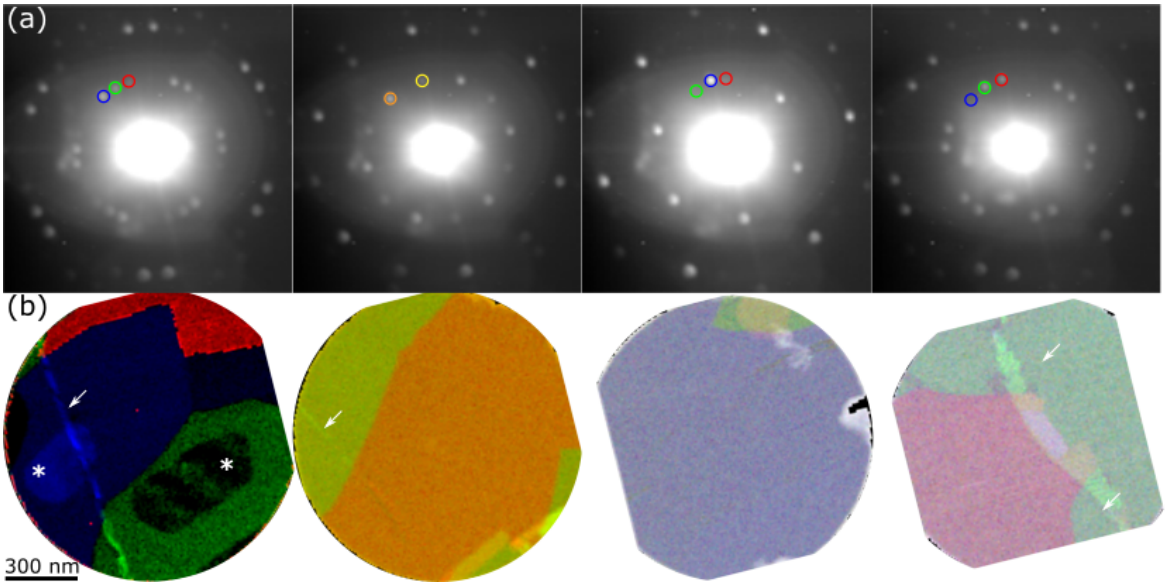

Fig. 7.2 **SED data from CVD graphene.** (a-d) Average diffraction patterns from 4 regions of interest with integration windows used to form virtual dark-field (VDF) images marked. (e-h) Colour composite images formed using VDFs corresponding to the integration windows marked in (a-d). Arrows indicate possible folds in the graphene film and stars indicate possible bilayer islands.

Spatially-averaged diffraction patterns were obtained by summing all diffraction data from each mapped region, as shown in Figure 7.2a. Multiple sets of reflections with hexagonal geometry can be seen indicating the number of grains within each scanned region, which here appears to be 2 or 3 in each case. Diffraction contrast images were formed by plotting the intensity within selected subsets of pixels (disc radius 2px) as a function of probe position

to form *virtual dark-field* (VDF) images [195, 367]. Multiple VDF images were combined as false colour maps to reveal the morphology of the grain structure, as shown in Figure 7.2b. The orientation resolution of these VDF images is set by the size of the integration window used to form the image and here is $\sim \pm 3^{\circ}$, which is approximately a factor of 2 improvement on conventional dark-field images where a physical aperture plays a similar role [364]. The contrast in these VDF images also hints at greater structural complexity and features likely to correspond to folds and bilayer islands were identified, as indicated in Figure 7.2b. Although this simple analysis provides a useful overview of the data, more sophisticated analysis is required to reveal the full structural complexity and to make best use of the wealth of information in the 4D-SED data. Analysis methods are developed in the following to obtain maximum information from this data using the most structurally diverse region mapped (leftmost in Figure 7.2) as an illustrative example.

4D-SED data retains a 2D diffraction pattern at each probe position, oversampling the grain structure and enabling the application of unsupervised machine learning methods to determine significant contributions to the data. Non-negative matrix factorization (NMF) [249] was applied to perform this task by factorizing the data matrix into two non-negative matrices via least squares optimization, as described in Chapter 4, to obtain *component patterns* and their associated *loading* at each position. The number of component patterns must be specified and the statistical variance described by increasingly many principal components obtained by an initial singular value decomposition (SVD), as shown in Figure 7.3a, can guide this choice. The SVD results did not produce a clear regime change between "high-variance" and "low-variance" principal components so NMF decompositions were therefore performed with 6, 10, 20, 30, 40, and 50 components and the results were inspected to identify physical components. Beyond 40 components no additional physical components were obtained and only 10 of these 40 components contained physically interesting signals with respect to structural defects in the graphene film. The other NMF components account for variations in the data due to acquisition artifacts, which play a significant role in this case because the diffraction signal is relatively weak. Fortunately, these additional components could be easily identified as corresponding to artifacts rather than physically interesting signal, as shown for example in Figure 7.3b. Most are either long wavelength sinusoidal contributions expected when noisy smooth background is decomposed (e.g. top right) or fine oscillations (e.g. bottom) likely associated with electrical interference. NMF therefore reduces the data to a relatively small number of component patterns, even accounting for the iterative testing required here.

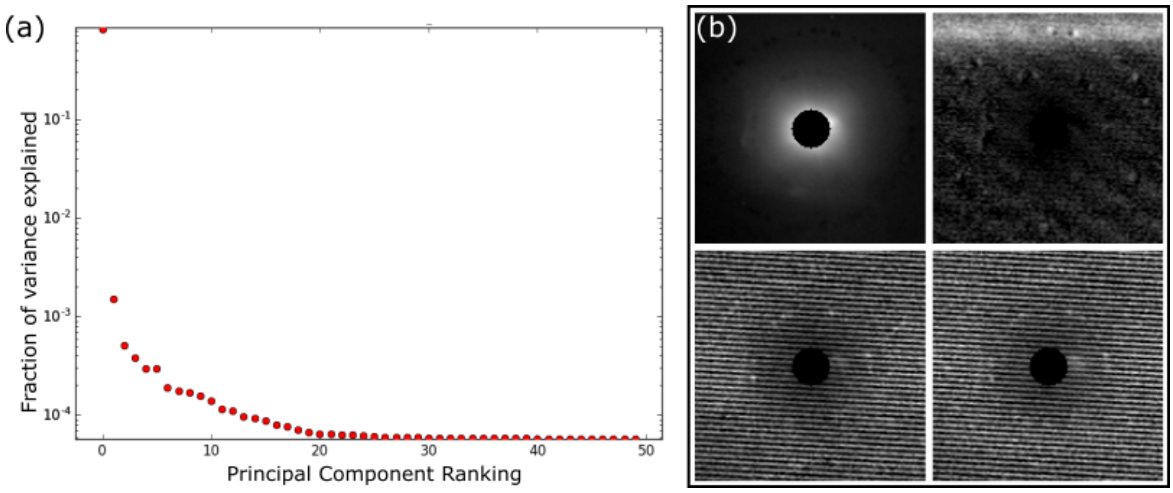

Fig. 7.3 **Singular value decomposition of graphene SED data.** (a) Scree plot for SVD results. (b) The four most significant NMF components that were considered to be physically uninteresting. Corresponding to (top) decomposition of background and (bottom) decomposition of scan noise.

NMF components containing physically interesting information and their spatial loadings are shown in Figure 7.4. Six component patterns (Figure 7.4a-f) correspond to grains with different orientations, identifying six grains rather than the three evident from naively summing the diffraction data, which is an important advantage of automated analysis. The automated machine learning approach, performed *post-facto* therefore reduces the chance of missing significant details compared to conventional TEM methods. In two cases the loading of the component is strong away from the primary grain (* in Figure 7.4d,e), overlapping with the region where component (b) has significant loading. These three components differ in orientation and this result indicates that a second rotated layer is present at the starred locations. Given the morphology of the overlap features, this is most likely due to the graphene film being folded under itself. Three component patterns were obtained with strong second order reflections (Figure 7.4g-i) and are primarily associated with regions identified as potential bilayer islands. Two of these components exhibited spatial undulation in the loading (Figure 7.4g,h). This indicates spatial variation in the diffracted intensities across this region but direct interpretation of the ensemble effect is challenging. Finally, a component pattern with an apparently split reflection near to other loadings was obtained, as shown in Figure 7.4j. Unsupervised machine learning therefore focuses attention on salient structural features providing a roadmap for further data analysis using more detailed and direct methods that may be applied to selected subsets of the 4D-SED data.

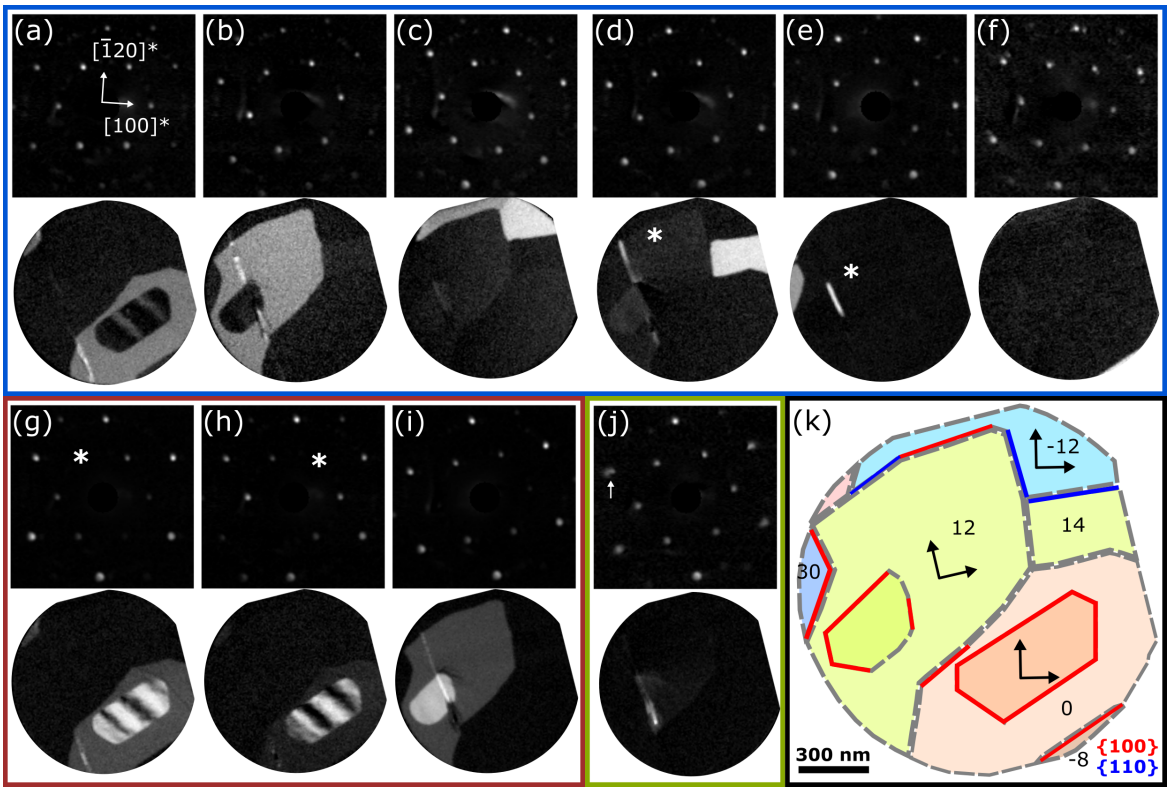

Fig. 7.4 **Component patterns and loading maps obtained by NMF.** (a-f) Six monolayer grains are learnt. Overlap between loading maps (b,d,e) indicates small orientation variations in the grain. (g-i) Learnt bilayer islands. Ripple in loading maps and missing reflections (*) in component patterns (g,h) suggest mis-stacking. (j) Broad second order reflections suggest a fold in the film. (k) Model indicating the layer number, orientation in degrees and facet indexation based on the NMF learning results. Positive rotations are anticlockwise.

Physical insight into the graphene grain structure can be obtained intuitively from the reduced data representation obtained by unsupervised learning, which retains the link between real and reciprocal space. The grains are $\sim 1\mu$m in diameter and typically elongated with aspect ratios $\sim 2-3$, reliable size estimates are however difficult here because the dimensions are similar to the scan size and to the holes in the grid. A lattice orientation can be assigned to each region where the loading of a given component pattern is significant, with respect to anti-clockwise rotation from the selected reference orientation indicated in Figure 7.4a. The grain boundaries and the edges of bilayer islands appear faceted and by identifying facets perpendicular to reciprocal lattice vectors a number of low-index facets can be identified, as shown in Figure 7.4k. Considering the lattice relationships illustrated in Figure 7.5, most facets are $\{100\}$ lattice planes, which are "zig-zag" edges. This is consistent with this termination being lower energy than "armchair" edges. Unsupervised learning of 4D-SED data therefore provides both a roadmap for further analysis and simple physical insight.

7.2.2 Diffracted Intensities: Layer Number & Mis-stacking

Diffracted intensity modulation across bilayer islands were identified by unsupervised machine learning and quantitative analysis of this variation, is developed here. Diffracted intensities are sensitive to the crystal potential projected in the beam direction, which may vary in graphene due to: (1) the local number of layers in the graphene film [349], (2) the angle between the incident beam direction and the local graphene plane normal [349], and (3) displacements between layers in multi-layer regions [357]. The effect on the diffracted intensity was modelled using the kinematical framework, which is sufficient to describe diffraction from graphene since carbon is a weak electron scatterer, i.e. low atomic number, and the material is atomically thin. Two symmetry inequivalent diffracted beams are typically

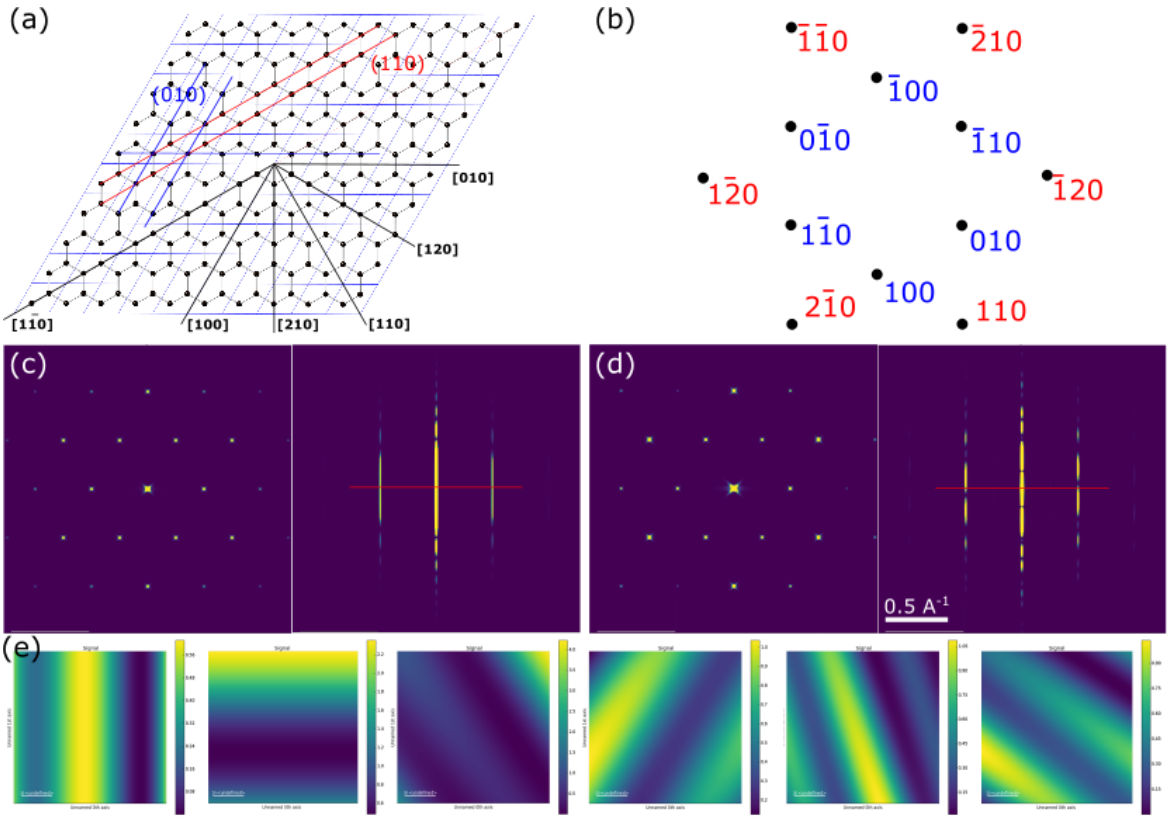

Fig. 7.5 **Simulated diffraction from graphene.** (a) Real space graphene lattice and direction vectors. (b) Indexed diffraction pattern corresponding to a graphene lattice oriented as in (a). (c) Kinematical simulation of scattering intensity from monolayer material in the a*-b* and a*-c* planes respectively. (d) Kinematical simulation of scattering intensity from bilayer material in the a*-b* and a*-c* planes respectively. (e) Bilayer intensity variation of three first order and three second order reflections for displacements (in cartesian coordinates) of one layer away from Bernal stacking.

recorded at normal incidence, and are referred to as first-order $\{100\}$ and second order $\{110\}$ reflections respectively, as shown in Figure 7.5b. Within the kinematical approximation, the intensity of a diffracted beam, I, at normal electron incidence is proportional to the structure factor squared, $|F_{hkl}|^2$, and can be evaluated analytically to obtain $I_{100} = f(s)^2$, $I_{110} = 4f(s)^2$ for monolayer material, and $I_{100} = f(s)^2$, $I_{110} = 16f(s)^2$ for bilayer material; where $f(s)$ is the atomic scattering factor evaluated at the scattering vector magnitude, s. The difference in scattering vector magnitude for first and second order diffracted beams results in intensity ratios, $I_{100}/I_{110} = 1.12, 0.28$ for monolayer and bilayer material respectively [348]. This led Meyer *et al.* [348, 349] to establish that the ratio I_{100}/I_{110} may be used assess the number of layers in a graphene film in cases where it is reasonable to assume: Bernal stacking, normal electron incidence, and near pristine atomic structure[2].

Intensity variation with tilt and inter-layer displacement away from Bernal stacking can also be evaluated in the kinematic framework, here using the full scattering simulation approach described in Chapter 2. The effect of tilt is significantly different for monolayer and bilayer material and is most simply understood by considering the a*-c* plane of the three-dimensional scattered intensity (reciprocal space), as shown in Figure 7.5c,d. The measured diffraction pattern is the intersection of the Ewald sphere, which may be approximated as a plane perpendicular to the incident beam direction, with this three dimensional scattered intensity, as indicated for normal incidence. In the a*-c* plane, strong diffracted intensity is along rods parallel to c* due to the small number of scattering layers perpendicular to that direction. In the monolayer case, the rods of strong intensity are peaked in the c*=0 plane and because the material is so thin the intensity variation is weak for tilts in the range $\pm 10^\circ$. In the bilayer case, interference between electrons scattered from each layer breaks up the rods of strong intensity and, in particular, the symmetry about c*=0 is broken in the first order reflections. In bilayer material at normal incidence, the Ewald sphere intersection is in the tail of an intensity spike and therefore tilt in opposite directions results in an increase or decrease in the scattered intensity for a given reflection. For second order reflections, the intensity spike is symmetric about c*=0 but varies more quickly than for the monolayer, with a minimum reached at $\sim 10^\circ$ tilt. The effect of inter-layer translation is essentially to produce no intensity variation when the translation is perpendicular to the g-vector and an approximately sinusoidal variation when in other directions, as shown in Figure 7.5e. Tilt and inter-layer displacement therefore break the 6-fold symmetry of bilayer diffraction.

Spatially averaged diffraction patterns from monolayer and bilayer regions are shown in Figure 7.6a,b for a tilt series performed over a range of $\pm 15^\circ$ in steps of 5°. This can

[2] Atomic disorder modifies the intensity ratio since I_{110}, which corresponds to higher spatial frequencies, will be more strongly reduced than I_{100}.

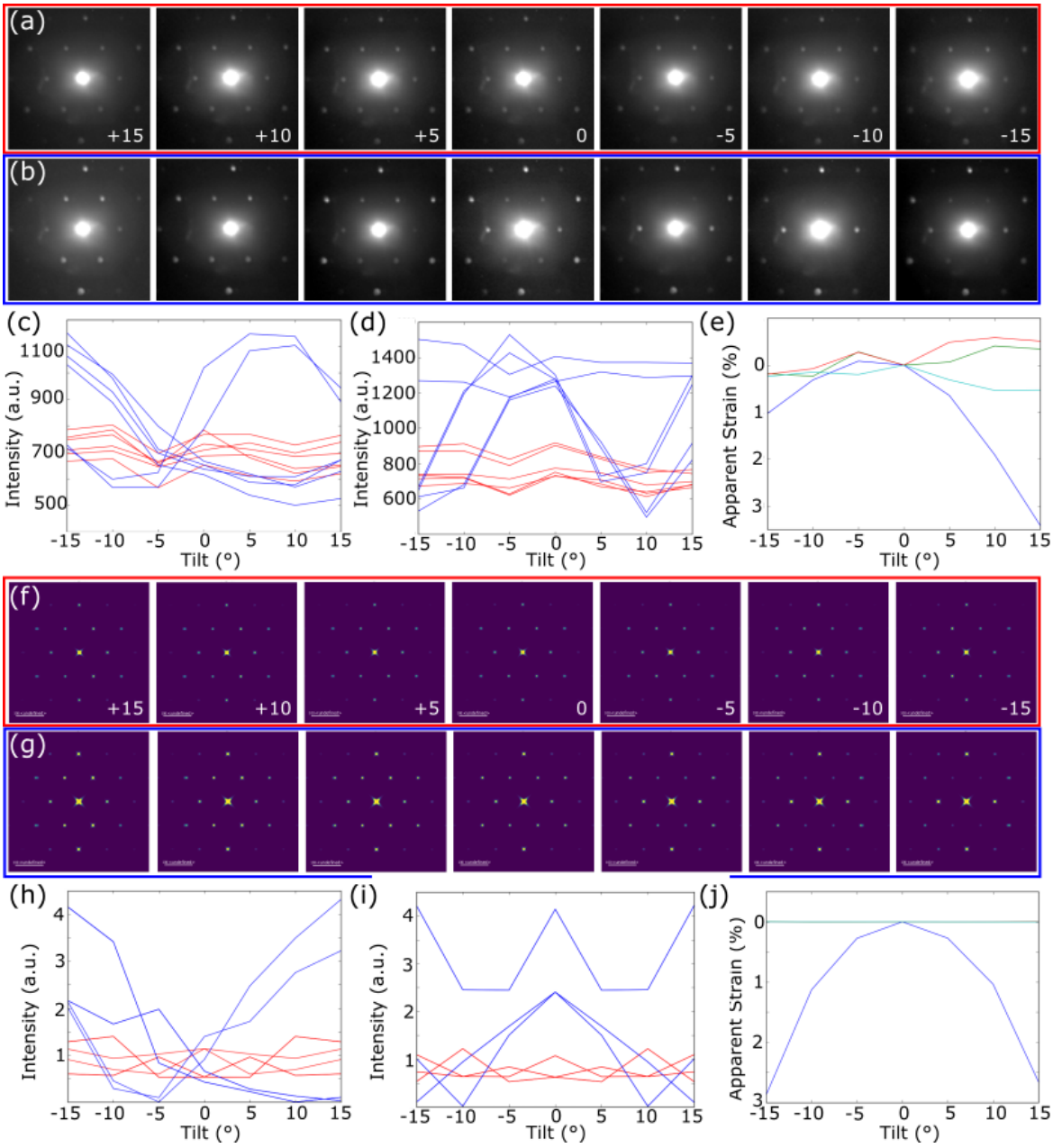

Fig. 7.6 **SED tilt series for monolayer/bilayer identification**. (a) a selected monolayer region and (b) a selected bilayer region recorded through a tilt series over a range of $\pm 15°$. (c,d) Measured I_{10}, I_{11} as a function of tilt for monolayer (red) and bilayer (blue) (e) Apparent "strain" due to change in the diffraction geometry with tilt. (f-j) Simulated equivalents of the aforementioned measured quantities.

be compared with diffraction patterns simulated for the same tilt series, as shown in Figure 7.6c,d. At nominally normal electron incidence the experimental bilayer diffraction pattern does not have 6-fold symmetry, implying either tilt or inter-layer displacement. The intensity ratio metric described above will not apply precisely in such a case although the condition $I_{100} < I_{110}$ should remain for at least some reflection pairs in the bilayer case, as this can be seen and used to differentiate monolayer and bilayer material. A more robust differentiation between monolayer and bilayer material is obtained by considering I_{100} and I_{110} as a function of tilt angle, as shown in Figure 7.6e,f. Minimal variation in the monolayer diffracted intensity was observed over this tilt range whereas significant variations were observed in the bilayer diffracted intensities, verifying the assignment of the number of layers unambiguously. One of the I_{110} values does not vary significantly with tilt indicating that the tilt axis happens to be approximately parallel to this g-vector, which is approximately vertical in the diffraction pattern plane and enabled a comparable simulation to be performed. The spread in intensity between Friedel paired reflections and all monolayer intensities gives an indication of the random error in the experiment and analysis, which can be seen to be on the order $\pm 20\%$. Although this is a significant error it is not surprising given the detector arrangment and will improve with more advanced detectors.

Geometric changes in the diffraction pattern occur as a result of tilt in addition to the intensity variations discussed above. As the Ewald sphere intersection moves along the spike of strong diffracted intensity, due to tilt, the measured scattering vector in projection varies approximately as $1/\cos(\alpha)$ where α is the angle of tilt about an axis perpendicular to the beam direction and the reciprocal lattice vector. Since strong diffracted intensity occurs in long streaks for graphene, due to the very small dimensions of the material, a tilt of the lattice can induce a significant change in the magnitude of the measured diffraction vector as can be seen clearly in the simulated tilt series shown in Figure 7.6c,d. This suggests that apparent strain in the diffraction pattern may be used as a quantitative proxy for local lattice tilt. To validate this approach, the affine image transformation approach, described in Chapter 4, was used to map apparent "strain" as a function of tilt of the graphene film for both theoretical and experimental data, as shown in Figure 7.6. Since the tilt is about an axis parallel to [100] the only component of apparent "strain" should be ε_{210}, which was found to be the case. The comparison between theoretical and experimental apparent "strain" values, particularly the components that should be zero, gives an indication of error in the experimental analysis, which can be estimated as $\pm 0.5\%$ for monolayer material. This is somewhat larger than can ideally be achieved with 4D-SED based strain mapping approaches due to the weak signal in this case but is sufficient to glean useful insight. For bilayer material, the strong variation of intensity with tilt makes this strain mapping approach unreliable in bilayer regions.

Bilayer islands can be assessed in detail following the above understanding of the effects of tilt and interlayer displacement. VDF images (integration disc radius 2px) of the two bilayer islands, formed using all corresponding first and second order reflections, are shown in Figures 7.7 & 7.8. This formation of numerous images from a single dataset is advantageous compared to conventional alternatives, where each image would have to be acquired separately, both in terms of acquisition efficiency and because all images are formed with the specimen having received identical electron dose. Since the VDF images are formed using background subtracted 4D-SED data it should be possible to interpret VDF image contrast quantitatively, as follows. VDF images and a spatially averaged diffraction pattern from the smaller bilayer island are shown in Figure 7.7. The 6-fold symmetry of the spatially averaged diffraction pattern is broken with a first-order reflection being almost absent, as shown in Figure 7.7c, implying either tilt or inter-layer displacement. The variation in diffracted intensities as a function of probe position can be assessed via inspection of the VDF images and plots of diffracted intensity as a function of position along a line across the region, as in Figure 7.7a,b,d,e. There is only a little spatial variation in diffracted intensities across this bilayer island implying that the tilt or inter-layer displacement is approximately

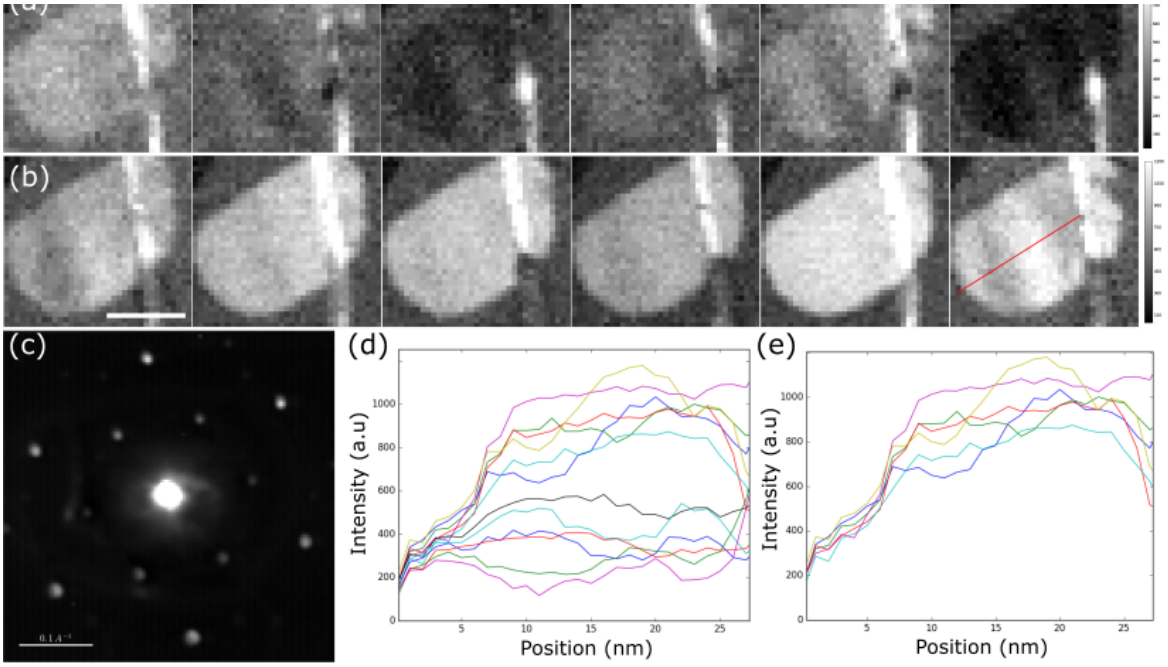

Fig. 7.7 **VDF images of bilayer island.** (a) using first order diffracted beams, and (b) using second order diffracted beams. (c) Spatially averaged diffraction pattern from this region. Line traces (4px width) showing (d) I_{100} and (e) I_{110} as a function of position across the bilayer island.

constant across the island. The intensity of all second order reflections is approximately similar, whereas the intensity of the first order reflections is split to approximately three levels. This intensity splitting suggests that compared to the ideal case one first order reflection becomes stronger, another becomes weaker and the third is relatively little affected. This is not consistent with a tilted bilayer, which would result in two of three first order reflections being affected similarly but is consistent with a fixed offset between layers in a direction parallel to the g-vector where the diffracted intensity is reduced.

VDF images and a spatially averaged diffraction pattern from the larger bilayer island are shown in Figure 7.8. Again the 6-fold symmetry of the diffraction pattern is broken and in this case significant spatial variation in the diffracted intensity is observed for all reflections, resulting in contrast of light/dark fringes in the VDF images. This spatial intensity variation indicates that any tilt or inter-layer displacement must also be changing in space. In the case of inter-layer displacement, a spatial variation in the projected layer sites implies that one or both of the layers is buckled so that the projected inter-atomic vectors in each layer are not identical. Without such buckling only constant offset would be possible. Combined buckling and displacement between layers in bilayer graphene has been previously explained in terms of *dislocations* between the graphene layers [357]. This is appealing because such dislocations would be described fully by a line vector and a Burgers vector, **b**.

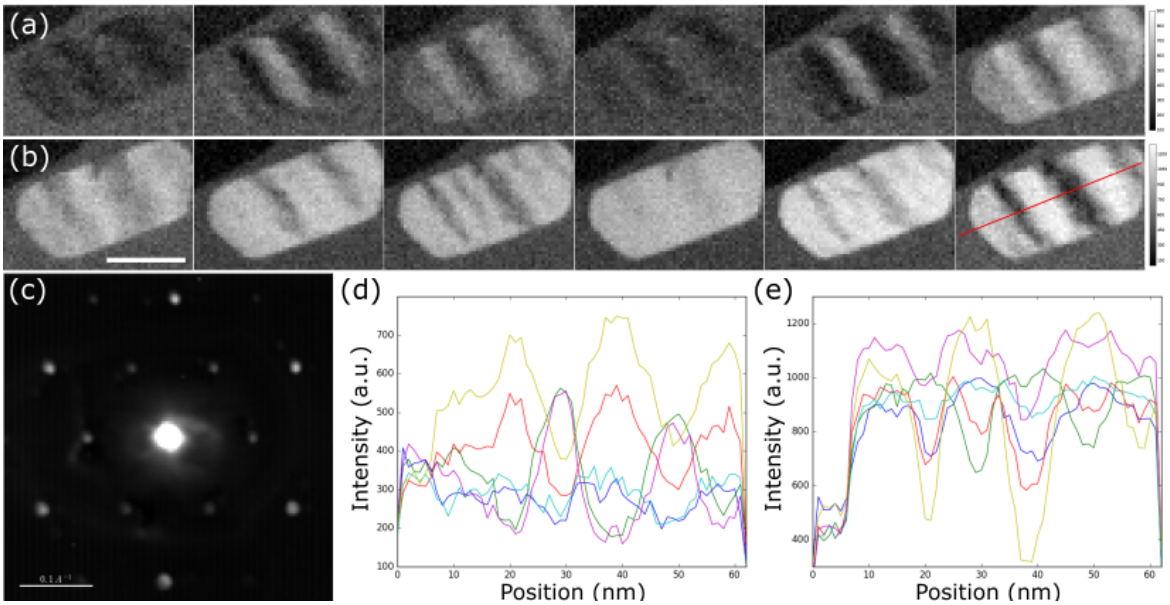

Fig. 7.8 **VDF images of bilayer island showing ripples.** (a) using first order diffracted beams, and (b) using second order diffracted beams. (c) Spatially averaged diffraction pattern from this region. Line traces (4px width) showing (d) I_{100} and (e) I_{110} as a function of position across the bilayer island.

Determination of the Burgers vector has a long history in electron microscopy [15] based on the fact that when a diffraction contrast image is formed with a diffraction vector, **g**, parallel to the Burgers vector, **b**, no contrast is observed associated with the defect. This condition will only be met exactly for perfect edge dislocations and multiple images can be formed to find this condition, which is known as $\mathbf{g} \cdot \mathbf{b}$ analysis. Considering the diffracted intensity variation across the bilayer, using the line traces shown in Figure 7.8d,e, it can be seen that two of the three I_{100} values show significant variation changing by a factor of ~ 2, whereas the third shows minimal variation, although not none. This analysis suggests that the offset between layers may be approximated by an inter-layer dislocation with $b = \langle 110 \rangle$ although this is not perfectly constrained. This is perhaps unsurprising given the relatively small dimensions of the bilayer islands and the absence of restraining material in the inter-layer direction. Indeed the mis-stacking is perhaps better imagined as the combined effect of topographic buckling in both of the graphene layers and the importance of such buckling has been noted in studies of bilayer mis-stacking [357].

Repeated measurement of the region was found to result in the strong diffracted intensity variations in the larger bilayer region disappearing, as shown in Figure 7.9. This indicates that the energy transferred from the electron beam to the specimen during observation is sufficient to *anneal* the mis-stacking and cause the bilayer region to become ideally stacked over time. This can be rationalized by the electron beam inducing a dynamic ripple in the graphene film, like moving a dislocation out from between the layers, which then tends to settle closer to ideal stacking. The fact that the defect can be removed relatively easily further supports the suggestion that these defects are not tightly constrained as in the case of true dislocations surrounded by restraining material. This supports the suggestion that the contrast is predominantly due to inter-layer dislocations and that the lack of a perfect invisibility criterion may, at least in part, be because the ideal structure has been disrupted by dose imparted during alignment prior to the first measurement. Overall this analysis highlights the

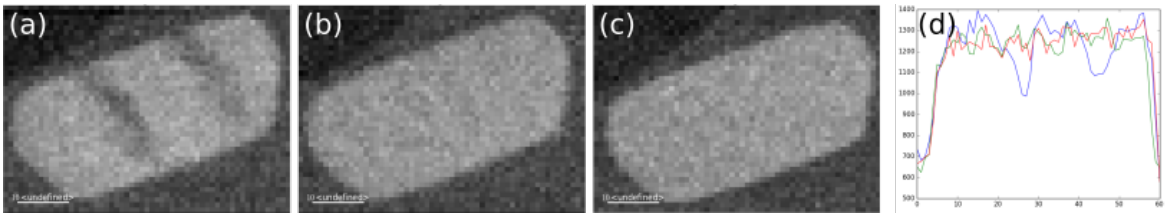

Fig. 7.9 **VDF images of bilayer island through tilt series.** The same g_{100} reflection was used for each image and all first order reflections were identical at the end of the tilt series. The first and last images are both formed with the beam at normal incidence to the graphene film and show that the spatial variation in diffracted intensity seen initially was no longer present at the end of the experiment.

versatility of *post-facto* diffraction contrast imaging using 4D-SED data to forming images with numerous diffraction conditions. The dose consistency of such *post-facto* analysis is also clearly important here because imparting more dose destroys the feature of interest. The results presented demonstrate the feasibility of quantitative diffraction contrast imaging in the 4D-SED scheme.

7.2.3 Quantitative Grain & Topographic Mapping

Quantitative spatially resolved structural insights can be obtained from the 4D-SED using automated analysis. The orientation of the graphene lattice was mapped with respect to rotation about the beam direction, which was assumed to be approximately perpendicular to an idealized hexagonal lattice. This orientation mapping was achieved using the template matching approach implemented in the *pyxem* library, as described in Chapter 4. The angular resolution of this approach is $\sim 0.5 - 1^{\circ}$ which is approximately an order of magnitude better than is possible with dark-field TEM imaging [364, 365], as discussed above, and is similar to previously reported line diffraction profiles [365]. The orientation of the lattice at every position in the scan was plotted as the absolute angle of anti-clockwise rotation away from the reference configuration shown in Figure 7.10. This spatially resolved orientation map reveals both the grain structure and sub-grain orientation variations in a quantitative manner and was analysed using the MTEX Matlab toolbox [298]. Grain boundaries were identified automatically based on applying a threshold to the misorientation between adjacent pixels at a level of 10°, which is a typical value in crystallographic texture analysis. This threshold was selected to avoid an excessive number of spurious grain boundaries being identified around misindexed single pixels and identifies high-angle grain boundaries. Sub-grain orientation variations are therefore implicitly defined as those that are less sharp than this condition and this includes relatively low-angle grain boundaries.

The grain boundary misorientation, θ_m, across each high-angle grain boundary was obtained based on the orientation of pixels on either side of the boundary. This local measurement is in contrast to the relatively coarse grain orientation averaging performed in more traditional analyses [364]. The orientation of the boundary line, θ_l, was then extracted using ImageJ. The specification of θ_m and θ_l fully characterises the crystallographic character of a grain boundary in 2D materials [366] and this can be used to constrain simulations of atomic structure in the boundary[3], which is not directly probed in 4D-SED. The experimentally obtained values of θ_m and θ_l were transformed into corresponding Miller indices describing each interface, using a look up table and a tolerance of $\Delta\tan(\theta) =$

[3]Grain boundary simulations described here were performed by Leonie Woodland working as a summer student under supervision of the author.

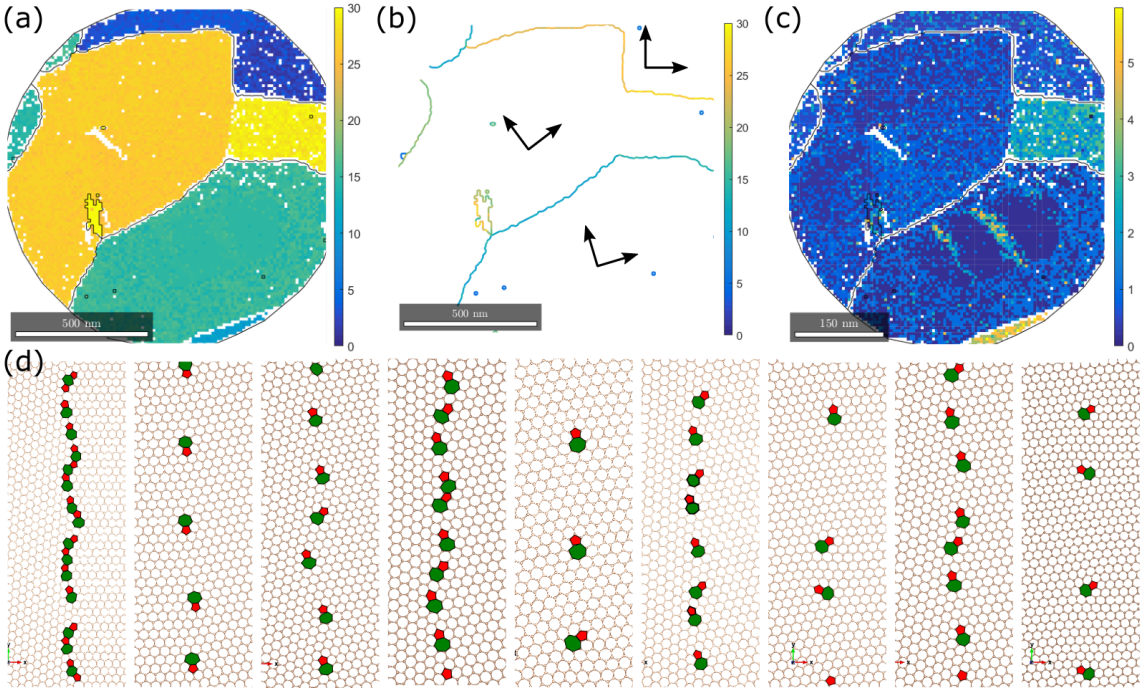

Fig. 7.10 **Grain boundaries modelled based on experimental measurements.** (a) Orientation map in degrees. (b) Grain boundaries determined with a 10° threshold, coloured by misorientation angle across the boundary in degrees. (c) Misorientation with respect to the grain mean at each probe position. (d) Simulated grain boundary structures obtained by centroidal Voronoi tessellation and conjugate gradient energy minimization for measured θ_m and θ_l values. Pentagons and heptagons are highlighted in red and green, respectively.

0.05. These Miller index descriptions were used to generate grain boundary structures via the centroidal Voronoi tessellation (CVT) algorithm described by Ophus *et al.*[366]. The CVT algorithm provides a computationally-attractive method for annealing graphene grain boundaries by treating the carbon atoms as vertices of Voronoi cells, and relaxing the lattice using Lloyd's algorithm. The tessellation tends towards regular hexagons in two dimensions, and, when a perfect tessellation is impossible, form pentagons and heptagons in a manner similar to known topological defects in graphene. The annealed structures were relaxed by conjugate gradient energy minimisation [368, 369] using the ReaxFF C-C bond potential [370–372]. An additional free parameter is the offset along the interface line, which was found to be important for obtaining physical results. To account for this, 50 evenly spaced offsets along the interface line were tested for each Miller index pair and the lowest energy structure taken. Illustrative examples of the grain boundary structures obtained following this procedure are shown in Figure 7.10d. All of these simulated structures comprise numerous pentagonal and heptagonal rings, which are predominantly aggregated as pairs forming $\mathbf{b}_{1,0}$

type dislocations. A similar structure estimate maybe obtained based on a regular array of such dislocations, with the misorientation angle then being given by:

$$\theta_m = 2\arcsin\left(\frac{|b_{1,0}|}{2d_{1,0}}\right) \tag{7.1}$$

where, $d_{1,0}$ is the distance between dislocations. However, this simpler model only properly applies to symmetric tilt grain boundaries, whereas a number of those observed are asymmetric tilt boundaries, which is only captured through the CVT based approach. This workflow therefore provides a route to construct empirically grounded models of grain structure across relatively large regions of graphene film.

Sub-grain orientation variations are visualised by plotting the misorientation with respect to the mean orientation within each grain. It can be seen that the misorientation within a grain can be as high as 3° and such sub-grain orientation variations have not previously been mapped quantitatively in graphene. Such sub-grain orientation variations were present to some degree in all mapped grains and imply the existence of other defect structures such as: small angle grain boundaries, comprising an array of dislocations, or folds, which allow such rotations whilst maintaining a continuous hexagonally coordinated membrane. These two possibilities may be distinguished if the local tilt of the surface normal to an approximated hexagonal lattice at each pixel can also be mapped since folds will imply much

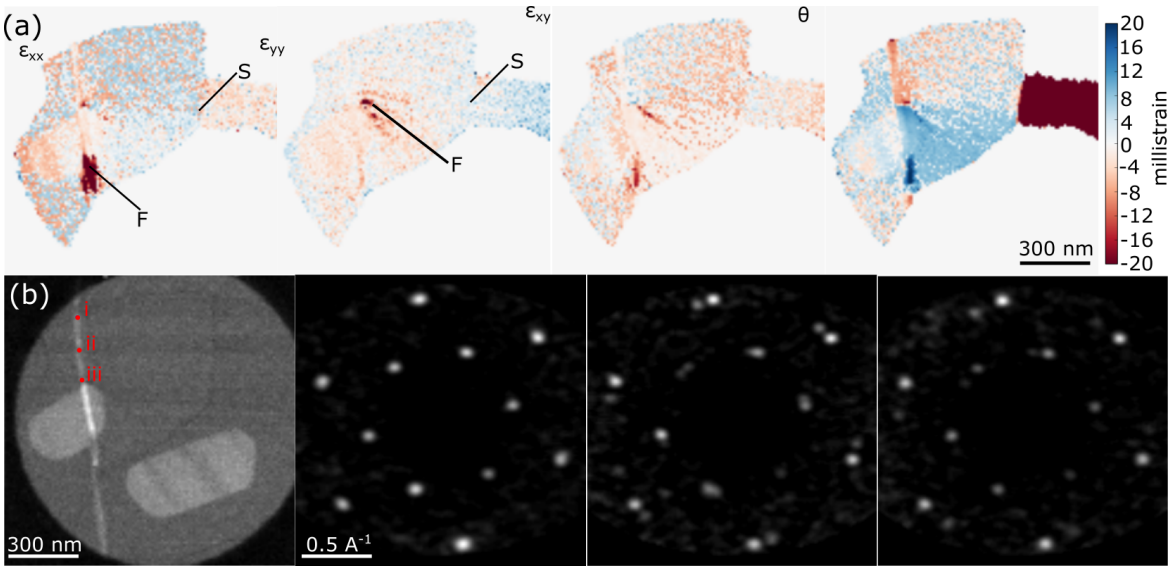

Fig. 7.11 **Maps of apparent "strain" and rotation** (a) Measured "strain" components. Folds (F) and small-angle grain boundaries (S) are indicated. (b) This apparent strain is in fact due to local buckling of the graphene lattice

more significant tilts. "Strain" maps therefore provide a proxy for mapping buckling of the membrane and the apparent "strain" due to buckling should always be compressive.

Apparent "strain" in the 4D-SED data, arising primarily due to lattice tilt, as detailed above, was mapped using the affine image transformation approach to produce strain maps, as shown in Figure 7.11. The measured "strain" is small near to high-angle grain boundaries validating their treatment as two-dimensional grain boundaries. A small-angle grain boundary is also evident with a misorientation of around 30 mrad and no measurable strain in the 4D-SED data. Such small angle grain boundary structures were also simulated using the CVT approach described above. The largest apparent "strains" are $\sim 3\%$ which corresponds to a local tilt of the lattice of $\sim 15^{\circ}$ (see Figure 7.6j) and indicate the presence of a significant buckling in the graphene membrane. Two buckled regions can be identified with a slight rotation of the graphene lattice between them and indicates the membrane is folded to allow this rotation. This is the same fold that was identified initially based on overlap in the results of unsupervised machine learning, as shown in Figure 7.4j. Further confirmation that the film is indeed folded is given by direct inspection of the data, where the splitting of diffracted spots from the upper and lower parts of the fold, as shown in Figure 7.11b. This folding is almost certainly a result of transferring the specimen on to a TEM grid. Such transfer is however involved in most current device production using CVD graphene and such topography may affect performance.

7.3 Summary & Conclusions

Scanning electron diffraction combined with versatile post-facto analysis has been demonstrated to enable rigorous assessment of layer number, grain-structure, mis-stacking and topography of chemical vapour deposited graphene, enabling comprehensive ‘crystal cartography’ at the mesoscale. In addition to highly versatile computational imaging approaches (analogous to conventional TEM but which offer significant adaptability of analysis), application of advanced analytical methods enabled novel, intricate and quantitative mapping of mesoscale structure and topography. Use of unsupervised machine learning to interrogate the rich 4D-SED data sets achieved more objective assessment of variations in the diffraction signal and provided a roadmap for more quantitative analysis. This approach requires very little prior knowledge and revealed some features easily missed in the more conventional approaches, as well as yielding a very efficient representation of the key features in the data. Orientation mapping revealed sub-grain orientation variations, and combining real and reciprocal space information to extract the grain boundary line orientation and the misorientation across the boundary enabled self-consistent models for the grain boundary structures to be

simulated. This provides a framework to construct empirically grounded large area atomic structural models that may be used to simulate key properties (e.g. transport properties or mechanical properties) in the presence of defects on length scales relevant to devices. Finally, the topography of the graphene membrane was mapped quantitatively, revealing the nature of folds and buckling in bilayer islands. The demonstrated methods are readily applicable to other two-dimensional materials, and by providing comprehensive, elucidation of their mesoscale structure and topography should play a significant role in better understanding their processing-structure-property relationships.

Chapter 8

Nanostructure in Polyethylene

Polymers are ubiquitous in modern technology but inherent structural complexity and characterisation challenges have limited detailed nanostructural understanding. Polymer crystals comprise molecular chains packed as identical helices with aligned axes [373–375], but complete crystallization is rare due to slow kinetics exacerbated by long-chains, entanglement, and side-groups [374]. Semi-crystalline structures containing crystals extending $\sim 10-50$ nm along the chain axis, i.e. much less than the chain length, are typical [376, 377], implying the crystals must be *chain-folded lamellae*, with individual molecules folding into single crystals [378, 379], or *fringed micelles*, in which multiple molecules align within one or more crystals [374]. Chain-folded crystals can be inferred when grown from dilute solution and are widely considered significant in melt-grown material where fringing and inter-lamellar linkages are also likely, due to entanglement, which physically couples phases, e.g. leading to a *rigid amorphous fraction* at the amorphous-crystalline interface [374]. Polymers may also form *mesophases* with intermediate degrees of order [380, 381].

Structural characterisation of polymers typically relies on bulk scattering and spectroscopic studies that provide insights into the average structure but require corroboration with local microscopic observations to determine nanostructure [382]. Transmission electron microscopy and diffraction are natural choices for such local measurement but have been limited by beam sensitivity [182, 184, 185] and low contrast [383]. TEM of polymers has thus typically provided only morphological insight [384, 385] when applied to material produced under melt processing conditions. Representative polymer crystallites and important defects have been well characterised but it has rarely been possible to directly measure these features within nanostructure. Recently, scanning diffraction experiments using X-rays [386] and electrons [387, 388] have been suggested to meet this need. Here, scanning electron diffraction (SED) is developed as a direct local probe of polymer nanostructure in application to a fibre spun sample of ultra-high molecular weight polyethylene (UHMWPE).

Polyethylene is the most industrially significant polymer and is the prototypical semi-crystalline polymer, forming crystal structures analogous to the n-alkanes [382, 380]. Polyethylene chains adopt a low-energy all *trans* conformation in a planar zig-zag that may be considered a helix with a 180° rotation between CH_2- units [374]. The stable crystal structure at room temperature and pressure is orthorhombic (Pnam, a=7.39Å, b=4.93Å, c=2.54Å) with the chain axis aligned along the c-axis and the planar zig-zag of the two chains in the unit cell approximately perpendicular to one another [389] (like longer n-alkanes). A monoclinic polymorph (C2/m, a=8.09Å, b=2.54Å, c=4.79Å), with the chain axis aligned along the b-axis and the planar zig-zag of the chains parallel to one another (like shorter n-alkanes), is frequently found in drawn polyethylene [390] as a result of martensitic shear transformation from the orthorhombic phase [391, 392]. Shear transformation of the orthorhombic phase can also lead to deformation twinning in orthorhombic polyethylene on {110} and {310} planes [391, 83]. Growth twins also occur [376]. This polymorphism is related to both the orthorhombic and the monoclinic structures being only slightly distorted from a close-packed hexagonal arrangement, as shown in Figure 8.1.

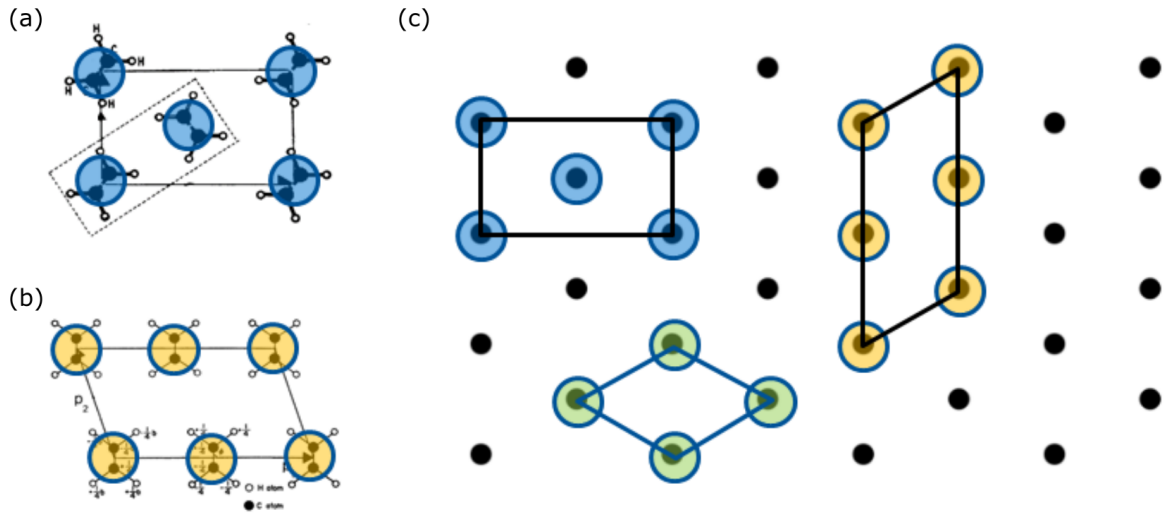

Fig. 8.1 **Crystal phases of polyethylene**. (a) Orthorhombic structure with herringbone chain packing. (b) Monoclinic structure with parallel chain packing. (c) Orthorhombic, monoclinic and hexagonal unit cells on a hexagonal lattice, illustrating pseudo-hexagonality.

Disorder in polyethylene spans a range from idealized crystal structures with all *trans* C-C bonds to randomly coiled molecules [56] containing numerous *gauche* bonds. The fold surface in chain-folded lamellae must also contain *gauche bonds* [393], as does the *con*formationally *dis*ordered (*condis*) hexagonal (a=4.85Å, c=2.39Å) mesophase [394, 395]. Gauche bonds are therefore a fundamental characteristic of disorder in polyethylene and deviation from exact conformational angles is typical. The hexagonal condis phase is stable at

elevated temperature and pressure [394] but has also been reported to form under irradiation [396–398] and in fibre samples [399–401]. Further, the condis phase may play an important role in crystallization from the melt [401–403] and all known extended-chain crystals are believed to have passed through this mesophase [380]. Gauche bonds in the hexagonal mesophase are present in a density corresponding to separation by ca. five trans CH_2 units and spectral signatures have suggested the presence of both -GTG'- 'kink' defects and -GG- 'double-gauche' defects [395], with the former being predominant, these *gauche* bonds are mobile and allow the chains, which inter-penetrate their neighbours at any instant, to occupy average positions of hexagonal symmetry despite lower molecular symmetry [380].

Morphologically, polyethylene macrostructure is typically characterised as lamellar, fibrillar or nodular [377]. Lamellar crystals are known to display a range of features such as splaying, curvature and multilayer structures become significant in 3D morphology [377]. Under shear flow processing conditions the chain alignment behaviour is rather different with molecules tending to be aligned with the flow direction leading to the formation of fibrils [404]. These extended chain fibrils can act as heterogeneous nucleation sites for the nucleation of crystalline lamellae with chain axes aligned with the fibrils. This crystallization sequence can lead to a crystal morphology known as a shish-kebab structure comprising chain extended fibrils and chain folded lamellar crystals [404]. However, direct measurement of the local structure in such polyethylene macrostructures has not generally been possible and here the shish-kebab macrostructure in a fibre-spun UHMWPE sample is investigated by developing 4D-SED as a hybrid diffraction-imaging microscopy technique.

8.1 Materials & Methods

8.1.1 Material Condition

Ultra-high molecular weight linear polyethylene (UHMWPE) was purchased from Mitsui Chemicals (Hizex 240M) and processed under shear-flow conditions [405] to produce thin fibres that were sectioned for SED investigation[1]. The UHMWPE had a weight-average molecular weight $M_w = 2.0 \times 10^6$ amu and heterogeneity index $\frac{M_w}{M_n} = 12$, where M_n is the number-average molecular weight. A polymer solution was prepared in decalin ($C_{10}H_{18}$) at 210 °C using a twin screw extruder with a polymer concentration, c = 10.0 wt% corresponding to a concentration ratio, c/c* = 20, where c* is the overlap concentration. An antioxidant (2,6-ditert- butyl-p-cresol) was also added with a concentration of 1 wt% of the total solution and insoluble impurities were filtered off using a mesh filter (400 lines/inch). Fibres were

[1] UHMWPE samples were prepared by Prof. Hiroshi Jinnai and Dr. Takeshi Higuchi (Tohoku University).

produced by fibre spinning [405] using a spinneret attached to the twin-screw extruder, which was operated at a temperature of 170 °C, with a throughput of 1 g/min and an orifice diameter of 0.8 mm. Extrudates were drawn into fibres with a take-up velocity of 60 m/min whilst being cooled by nitrogen gas at room temperature. This processing has been previously demonstrated to produce material with the shish-kebab macrostructure [405].

Electron transparent thin-film specimens were prepared from the UHMWPE fibres, which were first cut into pieces ~ 2 mm long. One such piece was then cut into thin sections, ~ 70 nm thick, at room temperature using a diamond blade mounted on an ultramicrotome (Ultratome V, LKB Co., Ltd.) so that the sections were oriented with the plane of the specimen containing the *velocity gradient* and *flow* directions. These sections were then mounted on carbon-coated poly(vinyl formal) film on copper grids.

8.1.2 SED Acquisition

SED was performed using a Philips CM300 FEGTEM controlled using a Nanomegas Digistar system[2], as described in Chapter 3. The instrument was operated at 300 kV, with illumination parameters: spot size = 4, C2 aperture = 10 μm and gun lens = 3. The probe current under these conditions was measured to be ~ 5 pA using a Faraday cup situated beneath the column and the specimen was cooled to a temperature of ~ 100 K using a Gatan liquid nitrogen cooling holder. It should be noted that the orthorhombic polyethylene unit cell contracts by $\sim 3\%$ in **a** and $\sim 1\%$ in **b** on cooling from room temperature to ~ 100 K [406], which makes the material more orthorhombic. Electron diffraction patterns were acquired over a 512×512 pixel array of the optical CCD camera, which imaged the diffraction pattern on the phosphor viewing screen of the microscope with a dwell time of 10 ms per probe position. SED data was acquired with a nominal camera length of 40 cm and the reciprocal space pixel size was calibrated to be 0.01 Å^{-1}/pixel based on data acquired from a GaAs specimen under similar conditions. Scans were performed with a spatial resolution of ~ 4.75 nm (regions 1/2) or ~ 9.5 nm (region 3) and the convergence semi-angle was $\sim$1 mrad. Scan regions comprised 160×160 probe positions.

8.1.3 Electron Dose & Beam Damage

Electron dose was estimated by evaluating the average electron fluence through a disc with diameter equal to the full-width half maximum of the theoretical diffraction limited probe for the measured convergence semi-angle. Taking a measured convergence semi-angle of 1 mrad, the diffraction limited probe size is 2.5 nm for 300 keV electrons. Taking a probe current

[2]The data presented here was acquired by Dr. Sung-Jin Kang (University of Cambridge).

of 5 pA, a probe diameter of 2.5 nm, and a dwell time of 10 ms; gives an electron dose of ~ 600 e/Å^2 and is similar to previous reports of SED applied to semi-crystalline polymers [387]. However, this dose is about an order of magnitude greater than the reported critical dose values for polyethylene illuminated with 100 keV electrons [182] at room temperature. It may be reasonable to expect [182] cooling the specimen to 100 K to raise the critical dose by a factor of ~ 4 and the increase in electron energy from 100 keV to 300 keV to raise this by a further factor of ~ 2, perhaps suggesting that significant damage could be avoided.

Empirically, repeated scanning of the specimen showed that the crystallinity had been degraded almost completely following a single SED acquisition. Nevertheless, high-quality electron diffraction data was obtained in the initial scan. This may suggest that the time taken for structural degradation is slower than the 10 ms exposure time at each probe position, or that the integrated signal over that time is dominated by the initial structure. This may be feasible if the important degradation mechanism requires significant molecular motion [407]. It is also noteworthy that neighbouring pixels in the slow scan direction generally diffracted similarly, imply that any immediate damage was highly localized.

8.1.4 Data Analysis

Analysis of the 4D-SED data involved peak finding, vector indexation and *post-facto* imaging using methods described in Chapter 4. Pre-processing of the data included: (1) binning the data from the 512×512 pixels acquired to 256×256 pixels in order to make the analysis of multiple SED datasets more computationally manageable, (2) applying an affine transformation corresponding to a compression in the vertical direction by a factor of 0.69 to correct for the off-axis camera geometry, (3) centring the diffraction patterns in the 256×256 array by cross-correlation with a disc element, and (4) subtracting an average diffraction pattern from a manually selected amorphous region within the scan region from all other patterns, followed by intensity thresholding, to remove background. Peak finding was performed using the difference of Gaussians method (see Chapter 4) with parameters tuned manually.

Indexation of the data presented various challenges: (1) fewer than 3 Bragg reflections were often recorded per pattern, (2) multiple crystals were frequently sampled along the beam path, (3) all polymorphs needed to be considered and appropriate lattice parameters were uncertain, and (4) errors in peak finding and pattern centring were estimated to give an error of ± 0.02 Å^{-1} meaning that considering only vector magnitude was often ambiguous. The first challenge was addressed by considering summed diffraction patterns over bent regions of the specimen to improve the sampling of reciprocal space and the others required much trial and error. Indices were discounted if they were divisible by a common integer if lower index reflections were not present.

8.2 Results & Discussion

8.2.1 Nanostructure Overview

4D-SED data was acquired from three regions of the UHMWPE specimen, as shown in Figure 8.2. Summed diffraction patterns reveal that high-quality electron diffraction data, with structural information to >1 $Å^{-1}$ resolution, was obtained from multiple crystals in each region. Virtual bright-field and annular dark-field images provide limited insight, as is typical of (S)TEM imaging of unstained polymers [383], although some features are suggestive of crystalline nanostructure (arrowed in Figure 8.2).

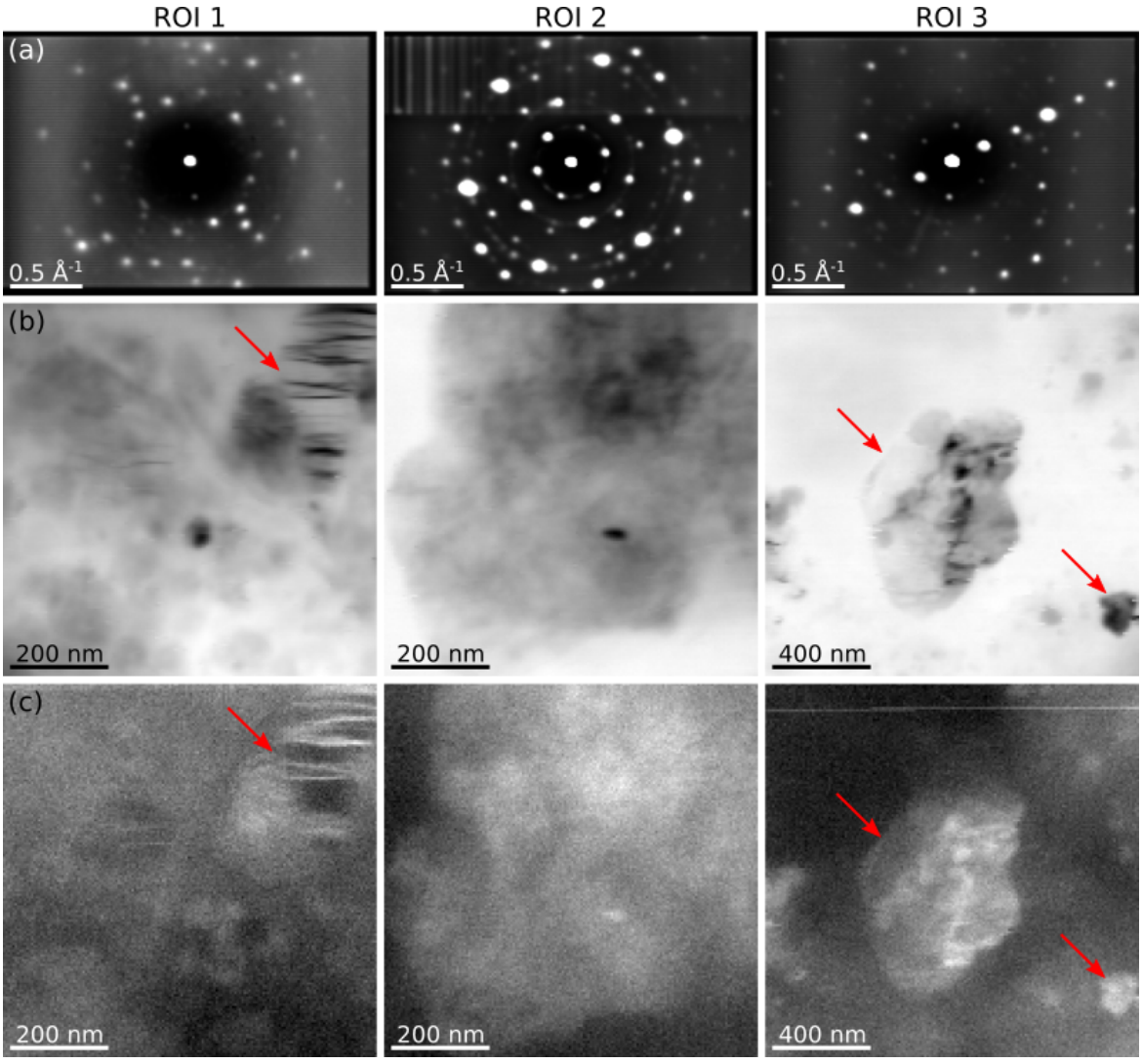

Fig. 8.2 **4D-SED data from polyethylene.** (a) Average diffraction pattern. (b) Virtual bright-field image using disc, radius = 4 pixels ($\sim$ 1 mrad), and (c) using an annular integration window, inner radius = 20 pixels ($\sim$ 5 mrad) and outer radius = 60 pixels ($\sim$ 15 mrad).

Crystals in the polymer nanostructure may be assessed based on the diffraction peaks and corresponding diffraction vectors measured in the 4D-SED data. Inspection of the spatially averaged diffraction patterns, shown in Figure 8.2, suggests that ROI2 & 3 contain only one or two crystals oriented with the electron beam near parallel to the molecular chain axis, which yields a pseudo-hexagonal diffraction pattern in all of the polyethylene crystal structures, whereas ROI1 likely contains more crystals. Measuring the diffraction vectors at each probe position can yield further insight. The distribution of diffraction vector magnitudes provides a structural fingerprint for phase identification, which can be visualized in a histogram, as shown in Figure 8.3a. This one-dimensional scattering profile can be assessed similarly to a powder diffraction pattern, noting that the sampling over different orientations is limited. Peaks in the histogram may be indexed and the first peak at ~ 0.24 Å^{-1} is consistent with either the orthorhombic 110_o or the hexagonal $1\bar{1}00_h$ reflection. No peak corresponding to the 200_o reflection (~ 0.27 Å^{-1}) was observed and neither were equivalent higher order reflections. This suggests that the material in ROI2/3, where the orientation is known by inspection, is in a hexagonal phase, whereas in ROI1 the absence appears to be due to incomplete sampling of orientations and orthorhombic material is present.

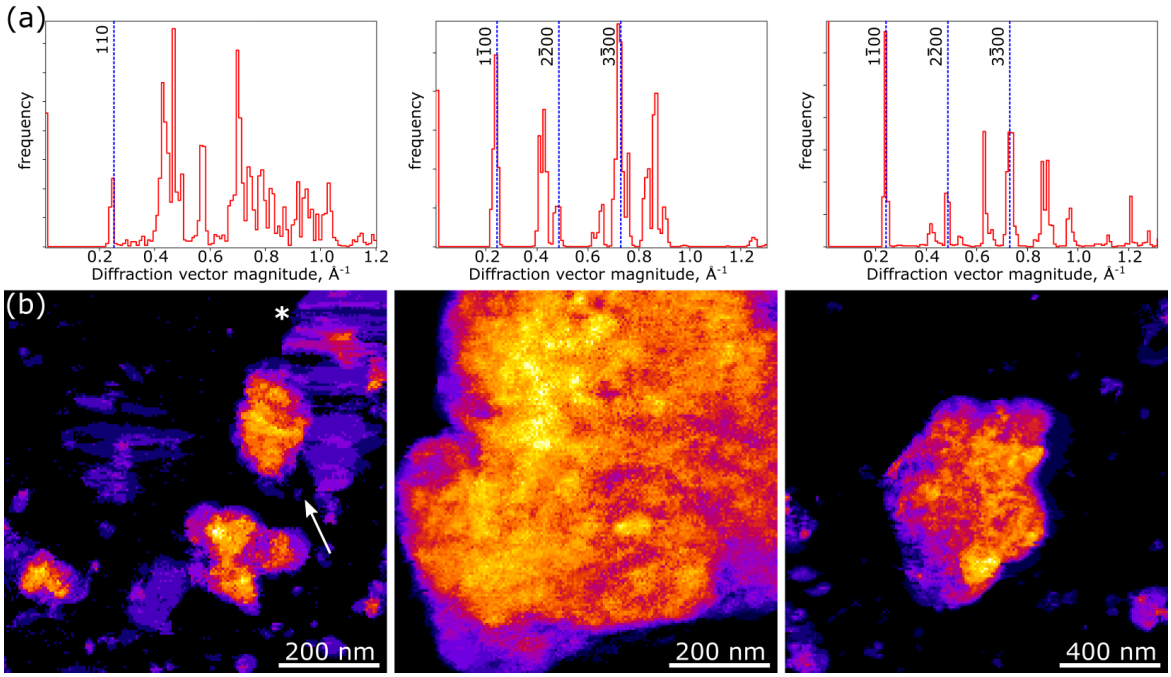

Fig. 8.3 **Polyethylene diffraction vectors**. (a) Histograms of measured diffraction vector magnitudes (bin size is 0.01 Å^{-1}, i.e. the pixel size). (b) Crystallinity maps with intensity equal to the number of peaks recorded from 0 (black) to 20 (white).

Crystalline regions within the semi-crystalline polymer microstructure may be mapped, as shown in Figure 8.3b, by plotting the number of diffraction peaks recorded as a function of probe position. These *crystallinity maps* provide clear contrast without staining, overcoming a key limitation in quantitative microscopy of polymers [383]. The contrast derives not from the diffracted intensity but from the number of peaks found at each probe position so that bright pixels may correspond to single crystals oriented near to major crystallographic zone axes or multiple crystals being sampled. This contrast can be readily segmented by binarizing the image to obtain crystalline area fractions of 37%, 87% and 27% respectively.

Faceting of the crystalline domain mapped in ROI3 could also be explored based on crystallinity map contrast, as shown in Figure 8.4. Edge detection algorithms are readily applied to the binarized crystallinity map and line segments can be extracted, using a Hough transform, and compared[3] with reciprocal lattice vectors in the corresponding diffraction data to index the facets as $\{1\bar{1}00\}$ planes in the hexagonal structure. This is reminiscent of much larger truncated lozenges of orthorhombic polyethylene, produced from dilute solution, in which longer facets are $\{110\}$ type, shorter facets are $\{100\}$ type, and sectorization is common [376]. It is intriguing that some VDF contrast appears to follow internal faceting, similar to sectorization, despite the hexagonal nature of the material. It is also notable that the corners of the lozenge are rounded, perhaps indicating a loss of crystallinity.

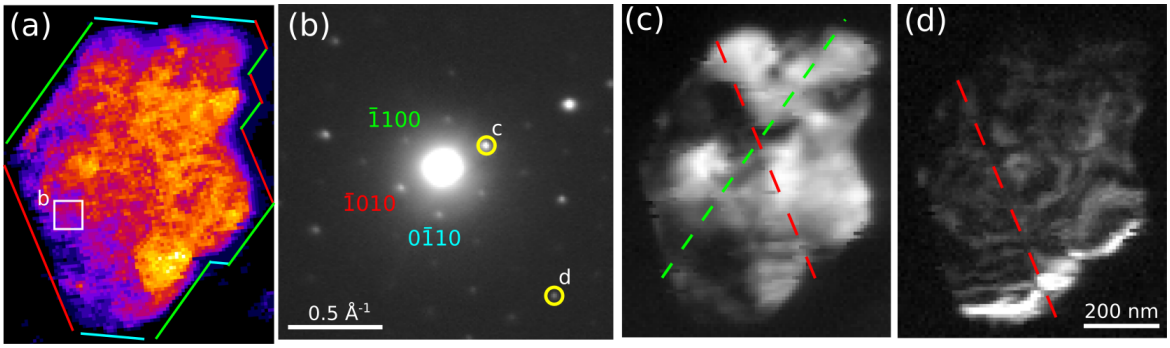

Fig. 8.4 **Crystalline polyethylene lozenge**. (a) Crystallinity map with facets indexed as $\{1\bar{1}00\}$ planes via colours corresponding to (b) the indexation of the average diffraction pattern. (c,d) VDF images formed using the integration windows marked in (b) with dotted lines indicating the trace of $\{1\bar{1}00\}$ planes, which may be associated with steps in contrast.

[3] An anti-clockwise rotation of 5° was applied to the recorded images to account for the rotation between diffraction and imaging planes.

8.2.2 Shish-Kebab Polyethylene

The "shish-kebab" macrostructure of melt-drawn UHMWPE comprises a fibrous and partially crystalline extended chain shish on which chain folded lamellae nucleate and grow into smaller micro-kebabs and larger macro-kebabs [404]. These macrostructural features can be imaged in stained specimens (Figure 8.5a,b) and comparing such an image with the crystallinity map obtained from ROI1 (Figure 8.3) enabled a triangular crystalline region to be identified as a macro-kebab (starred in Figure 8.3). Crystalline regions with non-faceted morphologies were also observed in the crystallinity map. Some of these were small crystalline patches consistent with the chain extended shish structure (arrowed in Figure 8.3) whilst others were not readily related to the shish-kebab model. Here, attention is focused on the structure of the lamellar macro-kebab crystal and the interface with the shish.

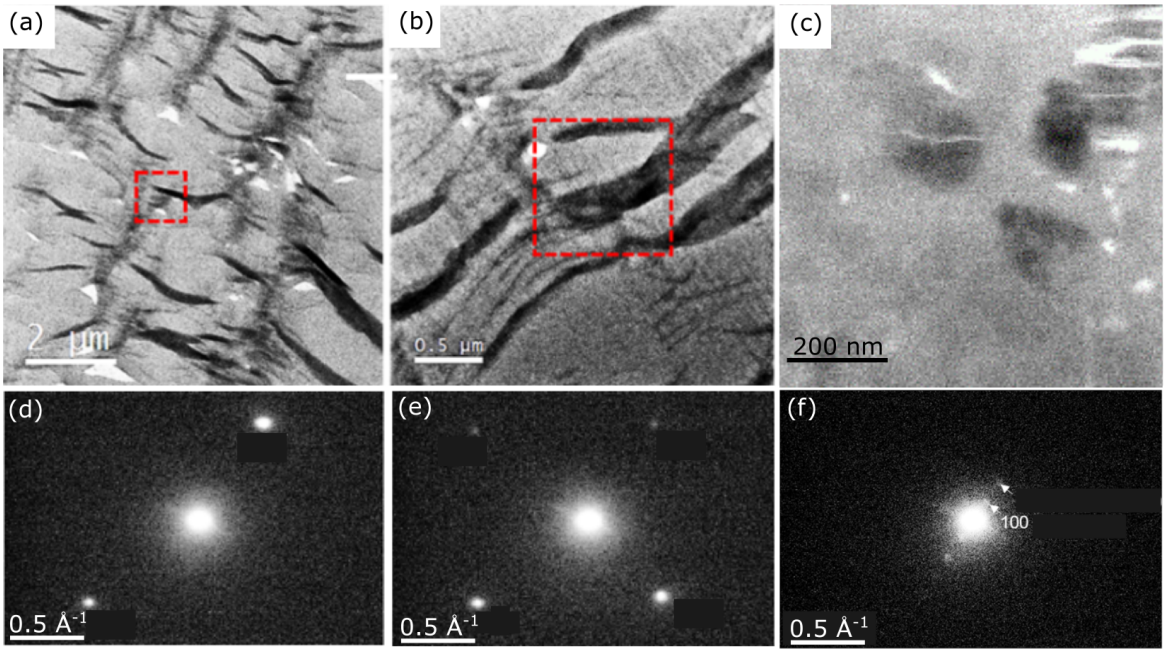

Fig. 8.5 **4D-SED of shish-kebab macrostructure.** (a,b) Conventional TEM images of a RuO_4 stained UHMWPE with shish-kebab macrostructure. Box indicates 4D-SED scan size. (c) Composite VDF image for all reflections associated with the lamella and shish. (d-f) Raw diffraction patterns from (d,e) different positions on the lamella and (f) the shish.

Diffraction patterns from the lamella crystal (Figure 8.5d,e) showed that the diffraction condition varied predominantly along the long axis of the lamella. Individual diffraction patterns typically contained fewer than four reflections and some patterns (e.g. Figure 8.5e) could not be consistently indexed using a single crystal model. A polycrystal model for the lamella was thus required. Diffraction patterns from the crystalline segments of the shish contained two weak reflections (Figure 8.5f), corresponding to an inter-chain spacing

similar to the hexagonal polyethylene structure. Forming a composite VDF image, from VDFs associated with all reflections in the lamella and the shish, reveals the shish-kebab macrostructure - without staining, as shown in Figure 8.5c. The intensity of the diffraction peak associated with the shish is strong in $\sim$ 100 nm segments along a fibril, with a diameter of $\sim$ 50 nm and a total length on the order of micrometres. This suggests that the chain extended shish may contain domains of aligned chains, where the diffraction peak is intense, separated by regions where entanglement may have precluded alignment [404].

Indexation of the diffraction data was achieved[4] based on the magnitude of diffraction vectors and inter-vector angles (see Section 8.1.4) measured in individual diffraction patterns and the summed diffraction pattern from the lamella. Although some individual patterns could not be indexed using one crystal, and therefore a polycrystal model is expected, the summed pattern contains a highly regular arrangement of reflections. This regularity suggests the crystals present may be related by special crystallographic relationships, such as twin relationships [391, 392]. Interestingly, the rows of reflections present in the summed pattern are separated approximately by a common vector of magnitude ~ 2.1 Å^{-1} but this does not correspond to any reciprocal lattice vector of the polyethylene crystal structures. A model was therefore constructed comprising four orthorhombic crystals that yielded diffraction patterns that, when superimposed, matched the summed diffraction pattern from the lamella, as shown in Figure 8.6. The four crystal orientations are approximately related by twinning orientation relationships although the deviation from exact twinning relationships was as much as 5-10°. This deviation may be rationalized based on the soft nature of the material and the highly metastable microstructural state. It should also be noted that the orientation within each crystal varies by a few degrees across it, so the orientation relationship may be more closely met at the interface, although the limited data makes it hard to be quantitative.

VDF images of the region marked in Figure 8.5c are shown in Figure 8.6d. VDF images are bright where a diffraction condition is met and thus reveal how the diffraction condition changes in space. Most VDF images associated with diffraction from the lamella crystal contain bright bands perpendicular to the long axis of the lamella, indicating that the corresponding diffraction condition is met over a short distance along the long axis of the lamella. This may be explained by the lamella being bent about its short axis and/or twisted about its long axis. Some VDF images contain more complex contrast, particularly in the upper part of the lamella, with split bands indicating that the corresponding diffraction condition is met more than once along the long lamella axis. A structural model can therefore be built up using both the diffraction and imaging data.

[4]This indexation was largely due to Dr. Sung-Jin Kang in discussion with the author and Prof. Paul Midgley.

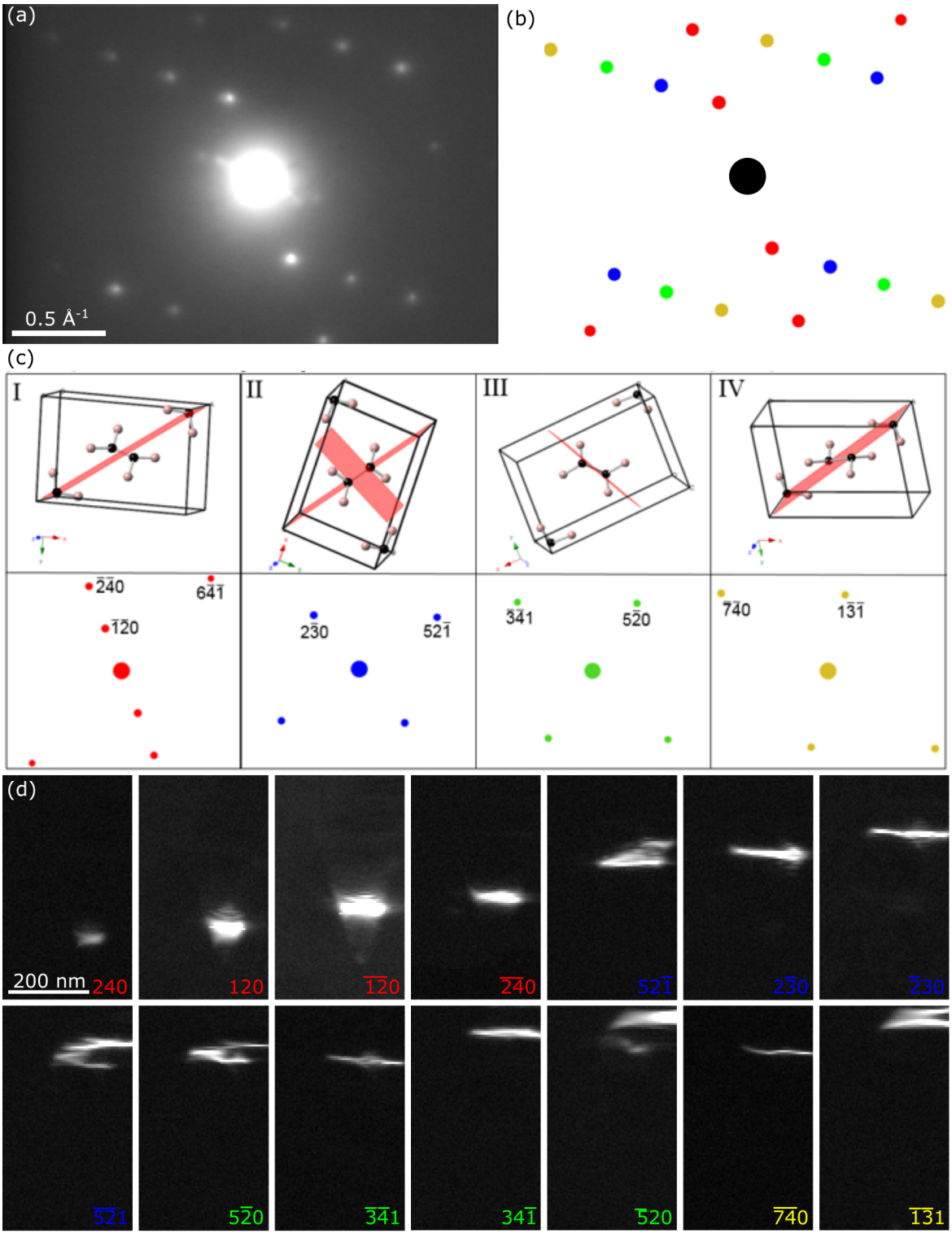

Fig. 8.6 **Hybrid diffraction-imaging of lamella crystal.** (a) Summed diffraction pattern. (b) Indexation of diffraction from lamella crystal. (c) Four orthorhombic crystal orientations included in the model. (d) VDF images associated with each diffracting condition.

A single crystal is located at the tip of the lamella, labelled in red in Figure 8.6. Reflections are excited sequentially along the 120 systematic row, with the $\bar{6}41$ type reflections excited separately at the top and bottom extremes of this region. Since the $[120]^*$ reciprocal lattice vector is approximately aligned with the long axis of the lamella, this indicates that there is only a very small twist about the lamella axis, which primarily affects the excitation of the $\bar{6}41$ reflections, whereas there is significant bending about the short axis of the lamella, which causes the sequential excitation of the 120 systematic row. Considering the distance between maximal excitation of the 240 and $2\bar{4}0$ reflections in both real space and reciprocal space, the curvature of the crystal about the short axis of the lamella is approximated as $\sim 0.6^\circ$ over ~ 250 nm. The VDF images for 120 systematic row reflections contain bright bands with a series of bright fringes either side, which is the rocking curve through the diffracting condition as the crystal is bent into and out of the exact Bragg condition.

Multiple approximately twinned crystals are located in the upper part of the lamella and their location must be considered in order to interpret the VDF image contrast, as shown in Figure 8.7. Twin boundaries in polyethylene are $\{110\}$ or $\{310\}$ planes and, since the c-axis is oriented $\sim 25^\circ$ away from the incident beam direction in the upper part of the lamella, there are regions where overlap between crystals along the beam path is significant. This is consistent with the earlier observation that some individual patterns must be indexed with multiple crystals. In this region the excitation of reflections away from the 120 systematic row changes, suggesting a twist about the long axis of the lamella. This axis

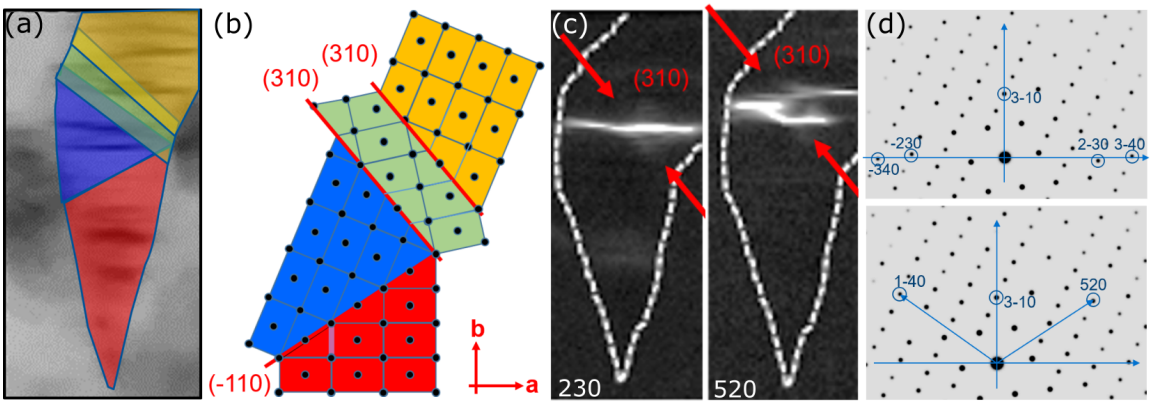

Fig. 8.7 **Twinning in a macro-kebab.** (a) Schematic representation of crystals present. (b) Orthorhombic unit cells in each region, rotated to be viewed along the chain axis, to illustrate twin relationships. (c) VDF images in which the bright band is not split, i.e. $\bar{2}30$ and where it is split, i.e. 520, with the twin boundary indicated. (d) Reciprocal lattice points in the *hk*0 plane showing that reflections giving continuous bands are near perpendicular to $[3\bar{1}0]^*$, whereas those giving split bands are not.

is approximately parallel to the crystallographic b-axis in the (red) crystal at the tip of the lamella. Twisting of polyethylene lamellae about this b-axis is widely reported in spherulites [408] perhaps as a result of unbalanced surface stresses associated with chain folding [409]. In the twinned (blue, green, yellow) crystals present in the upper part of the lamella a $\langle 110 \rangle$ crystallographic direction becomes approximately parallel to the long axis of the lamella. These $\langle 110 \rangle$ directions, like the b-axis direction, are approximately close packed directions in the pseudo-hexagonal close packed orthorhombic polyethylene structure and it appears that the twist continues about this axis. Further, the lamella bends away from the vertical axis of the image in a way that may be consistent with aligning the $\langle 110 \rangle$ directions in the twinned crystals more closely with the b-axis of the initial condition to preserve a common close-packed direction. Most of the VDF images comprise bright bands perpendicular to the long axis of the lamella but those associated with $\overline{5}\overline{2}1$, $\overline{5}\overline{2}0$ and $1\overline{3}\overline{1}$ reflections are split, indicating that the diffraction condition is met more than once. Whilst the short extent along the long axis of the lamella may be explained by twisting about that axis, it is necessary to consider why some bands are split and others are not and why the bands extend across the $\{310\}$ twin boundaries.

Crossing a $\{310\}$ twin boundary, the change in lattice orientation may be described as a rotation of 180° about the $[310]^*$ axis. Diffraction conditions that do not produce split bands are associated with reciprocal lattice vectors (e.g. $[\overline{2}30]^*$ and $[\overline{34}1]^*$) that lie very close to the plane in reciprocal space perpendicular to $[310]^*$ and the twin therefore maps the reciprocal lattice point to a position very close to an equivalent reciprocal lattice point. The twin has very little effect on the locus of Bragg reflection. In real space, these diffraction conditions corresponds to two sets of equivalent atomic planes that are approximately coherent and parallel across the twin boundary. Diffraction conditions that produce split bands are associated with reciprocal lattice vectors (e.g. $[520]^*$) that are not close to the plane perpendicular to $[310]^*$. In this case, the twinning operation does not map an equivalent reciprocal lattice point to a similar location. However, the twin does map a different reciprocal lattice vector of similar magnitude to a nearby point such that it is still integrated to give VDF image contrast but corresponds to a different set of atomic planes. In the case of the $[520]^*$ vector, twinning maps a $[1\overline{4}0]^*$ vector to a similar location, which leads to a 2% difference in magnitude of the measured diffraction vector and a rotation of $\sim 3°$. This geometry is illustrated in Figure 8.7d.

Reflections measured between the tip of the lamella crystal and the shish are shown in Figure 8.8. The magnitude of the diffraction vectors was consistent with the monoclinic structure with three reflections indexed as 210_m reflections one reflection indexed as 200_m. The angle between one of the 210_m reflections and the 120_o systematic row was measured as

23.8° which is close to the 21° angle that would be expected if the material were related by a $T1_1$ type martensitic transformation [392]. Further, the $\sim 90°$ angle between two different 210_m reflections is consistent with monoclinic twinning. VDF images associated with reflections observed between the macro-kebab lamella and the shish reveal small crystalline domains apparently linking the tip of the macro-kebab to the shish. It might be expected that these structures would be micro-kebab lamella crystals but these would be observed along the length of the shish, which is not the case. These small crystalline domains may instead be associated specifically with the nucleation of the macro-kebab lamella and it may therefore be suggested that distorted monoclinic material plays a part in this process.

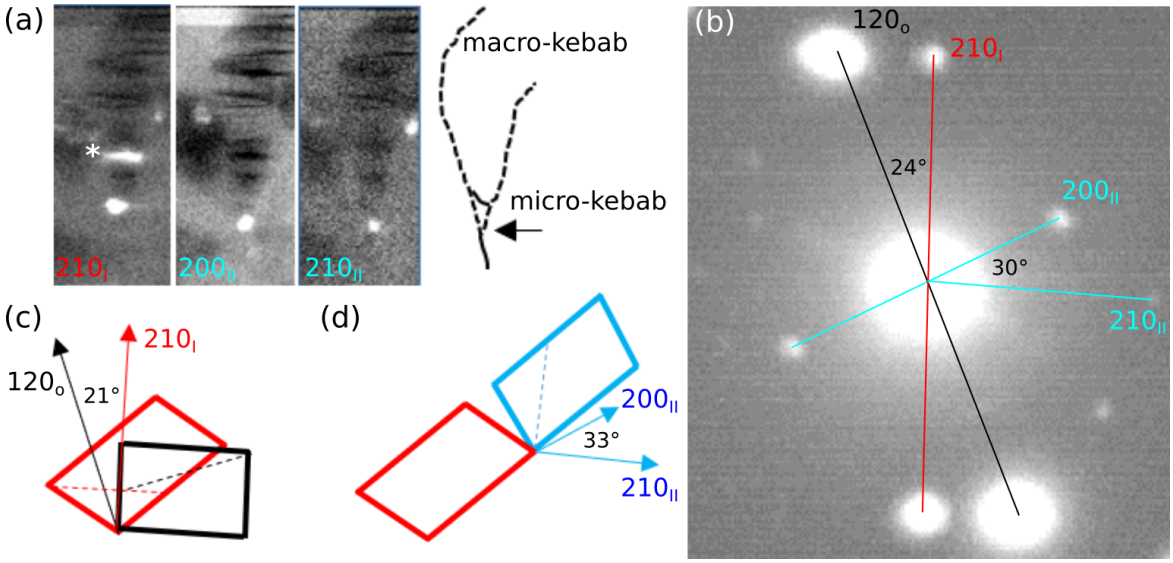

Fig. 8.8 **Structure between lamella and shish.** (a) VDF images associated with reflections marked in (b) a summed diffraction pattern from between the lamella and the shish. The bright band marked (*) is associated with a Kikuchi band associated with the orthorhombic polyethylene crystals passing through the integration window. (c,d) Schematic orientation relationships (c) between monoclinic and orthorhombic polyethylene resulting from type $T1_1$ martensitic transformation and (d) between twinned monoclinic polyethylene crystals.

8.2.3 Condis Phase of Polyethylene

Electron diffraction patterns with strong diffraction to scattering vectors corresponding to a common hexagonal lattice were observed across ROI2, as shown in Figure 8.9. The measured lattice parameter, a = 4.85 ± 0.02 Å is in agreement with the reported hexagonal *condis* phase unit cell [394] but the diffracted intensities in this region typically follow the trend $I_{3\bar{3}00} > I_{1\bar{1}00} > I_{2\bar{2}00}$. In some places, the first and second order reflections were almost entirely absent whilst the third order reflections were strong (e.g. Figure 8.9c). Often $2\bar{1}10$

reflections were not observed and it was not uncommon to observe $I_{4\bar{2}\bar{2}0} > I_{2\bar{1}\bar{1}0}$. Further, the intensity distribution in individual diffraction patterns is typically less than 6-fold symmetric, even when the geometry suggests the diffraction pattern is recorded near to zone axis (i.e. the pattern corresponded to a 2D symmetric lattice). In many regions multiple crystals were sampled along the beam path leading to split reflections, as may be observed in Figure 8.9c,d. These observations suggest that the atoms are arranged, in projection, across positions that approximate a unit cell close to, but not exactly, one third the size of the close-packed hexagonal unit cell. The molecular arrangement breaks the hexagonal symmetry of this hypothetical lattice leading to the reduced symmetry of the diffracted intensities. This symmetry breaking is related to the degree of averaging over conformational disorder along the beam path and would be implicit if the chains were in the all *trans* conformation. Here, the local measurement of diffraction data from volumes in which the averaging over disorder is incomplete makes it possible to reveal local variations in the conformational disorder.

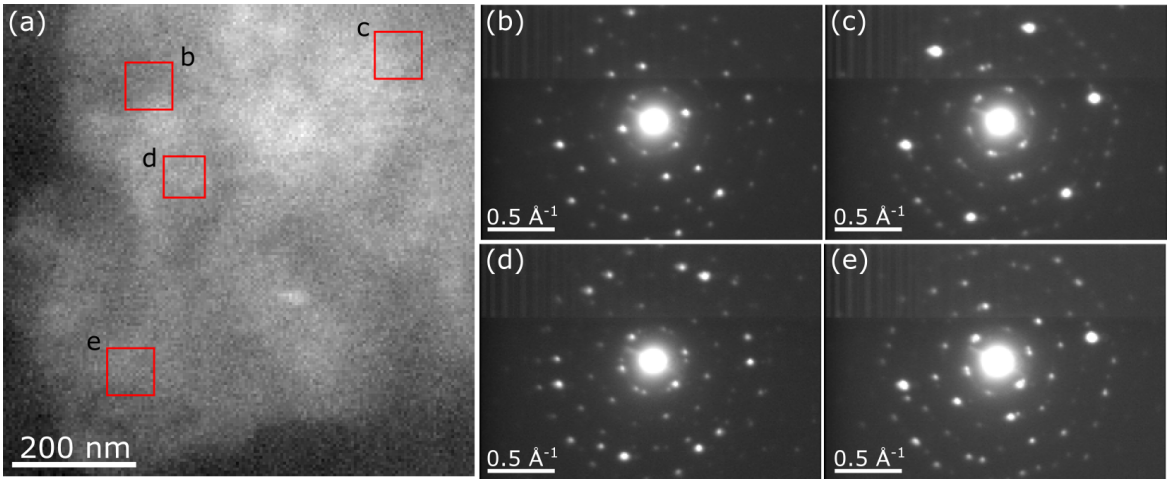

Fig. 8.9 **Diffraction from hexagonal condis phase**. (a) VADF image with integration windows from which (b-e) summed diffraction patterns were obtained.

The simplest model that can explain many of the experimental observations treats the polyethylene chains as cylindrically symmetric in projection and considers their arrangement on an hexagonal projected lattice, as shown in Figure 8.10. Sites indicated in black in Figure 8.10 correspond to the hexagonal lattice sites in the reported mesophase structure and correspond approximately to close packing of the molecular chains. Sites in this projected model can be closer than this because the chains may be offset at different heights. The sites indicated in red in Figure 8.10 correspond to interstices between hexagonally close-packed rods in a single layer and those indicated in blue to the remaining positions that reduce the projected unit cell to one third of the close-packed unit cell size. These blue sites correspond to translations of $\frac{a}{3}\langle 1\bar{1}00\rangle$ from the close-packed sites. If all of these projected sites were

occupied equally then the projected unit cell would be reduced to one third of the close-packed unit cell and $3\bar{3}00$ reflections would be the lowest order observed, as shown in Figure 8.10a. Occupancy of any fraction of the projected sites causes lower order reflections to be observed, as shown in Figure 8.10b-f. If only the red interstitial sites are occupied, as in Figure 8.10b, then $1\bar{1}00$ reflections remain absent whereas if only the blue sites are occupied $I_{3\bar{3}00} > I_{1\bar{1}00}$ as is observed in the experimental data. The intensity distribution depends on the relative occupancy of the sites and the 6-fold lattice symmetry can be broken, e.g. Figure 8.10d. This simple model can therefore reproduce key features of the experimentally observed diffraction patterns. The intensity distribution is also affected by small displacements from the ideal projected sites and by the orientation of asymmetric, i.e. all *trans*, segments of the polyethylene chains, which are not included in this simple model, but have a similar effect on the diffracted intensity distribution to the effects illustrated by this model.

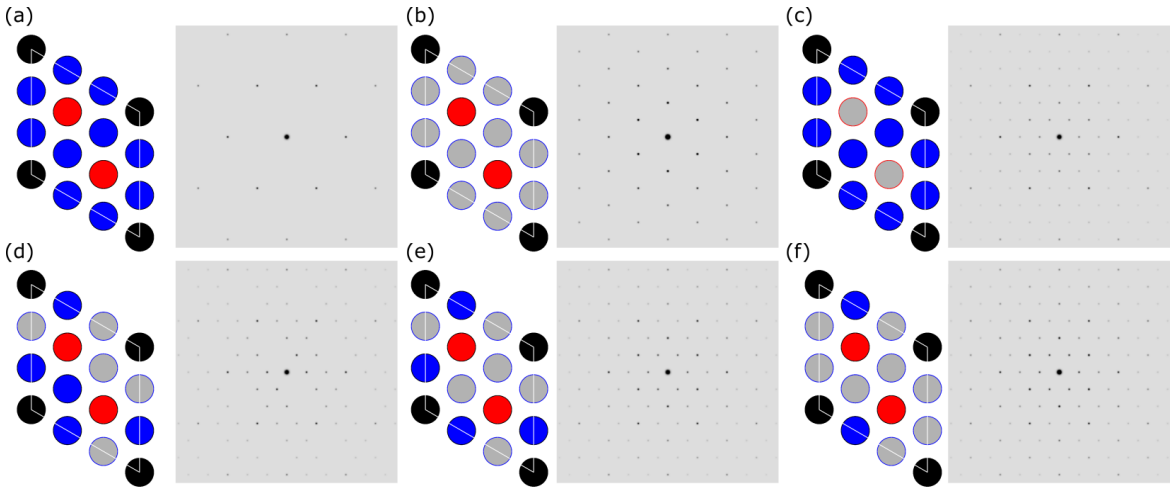

Fig. 8.10 **Condis diffraction model**. Hexagonal close-packed (black) sites, interstitial (red) sites between close-packed rods and intermediate (blue) sites at $\frac{a}{3}\langle 1\bar{1}00\rangle$ from other sites. Grey sites are unoccupied. (a-f) Varying the occupancy of sites changes the relative intensity of first and third order reflections and can break 6-fold symmetry in the diffraction pattern.

Structural insight based on the simple projected site occupancy model requires consideration of how conformationally disordered molecular chains may occupy projected sites. Interstices between hexagonally close-packed rods in a single layer (red sites) may be occupied by stacking multiple layers of rods in an -ABC- stacking sequence (Figure 8.11b) as in the R_{II} rotator phase of the n-alkanes [410–412]. An analogous structure in condis polyethylene could involve stacking of chain folded lamellae although it is unclear why such stacking might arise. Translation by $\frac{a}{3}\langle 1\bar{1}00\rangle$ to move between projected sites may be considered in terms of the -GTG'- *kinks* that are established from spectroscopic studies [395, 381] to be the predominant conformational disorder in the condis phase. Such a kink translates the

chain axis, as shown in Figure 8.11, displacing the projected scattering potential in the plane perpendicular to the chain axis, as required. The translation due to a -GTG'- kink, with the conformational angles strictly fixed to the ideal *trans* or *gauche* conformations, is larger than required but there is significant experimental [413] and theoretical [393, 414, 415] evidence that the conformational angles span a range in practice. It may therefore be reasonable to suggest that -GTG'- kinks, as well as other gauche bonds spanning a range of conformational angles in condis polyethylene, on average, produce translations sufficiently close to $\frac{a}{3}\langle 1\bar{1}00\rangle$ to explain the redistribution of scattering potential across sites in the simple projected site model. The intensity of experimentally measured reflections at a given probe position will thus be related to the local distribution of kinks in the molecular chains.

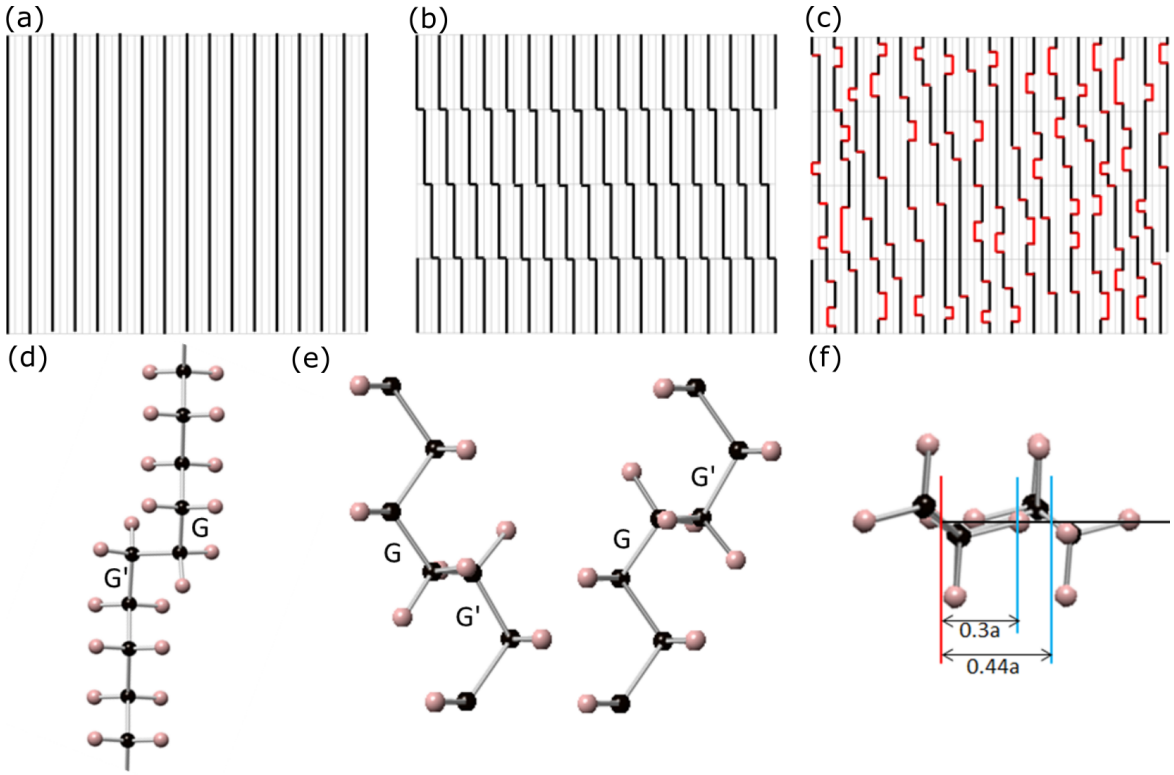

Fig. 8.11 **Conformational disorder and kinks**. Sections through (a) hexagonal close-packed molecular chains, (b) -ABC- interstitially stacked hexagonal close-packed layers, and (c) repeatedly kinked molecular chains. (d-f) Ideal -GTG'- kink defect illustrating associated a 0.44a translation perpendicular to the chain axis. Relaxing the conformational angles to span a range can modify the magnitude of the translation towards 0.3a.

VDF images formed by integrating intensity in a disc of radius 3 pixels positioned around first order reflections are shown in Figure 8.12. Intensity modulation with a pitch of ∼30-40 nm is observed in all of these VDF images with the modulation approximately perpendicular to the corresponding diffraction vector and contrast in images associated with Friedel paired

reflections very similar. This contrast suggests a preponderance of kinks in a direction perpendicular to the diffraction vector in the region where the stripy contrast is observed although it is difficult to construct an atomistic model that would account for the intensity modulation being in the same direction as the kinks. Nevertheless, the fact that different diffraction vectors produce similar contrast in different regions suggests that there may be some domain structure to the kink arrangement with particular kinks tending to be localized together. This suggestion gains support from molecular dynamics simulations [416] that have shown that the energy of similar kinks located near to one another is reduced as compared to the separated kinks, which is intuitive given the disruption to the chain positions.

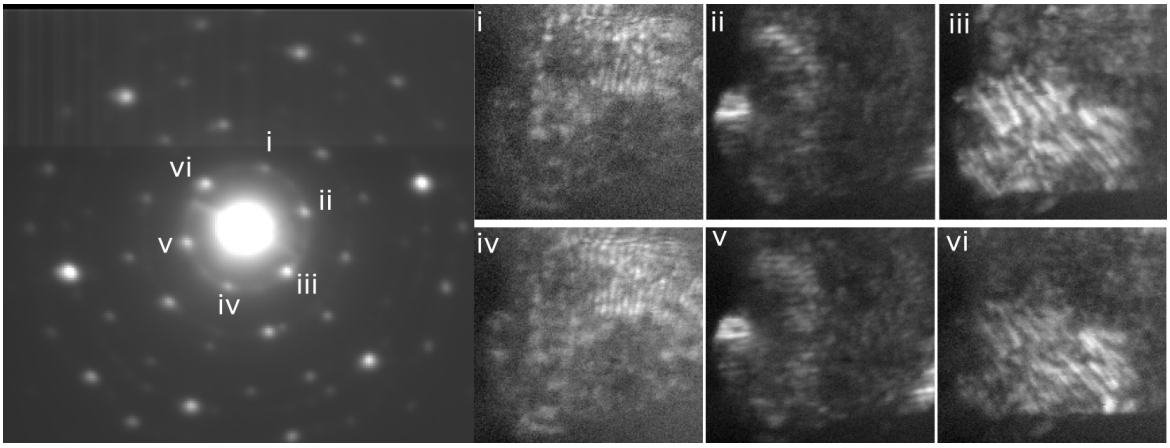

Fig. 8.12 **Virtual dark-field imaging of kink ordering in condis polyethylene**. Summed diffraction pattern from hexagonal condis PE with first-order reflections used to form VDF images (with a 3 pixel radius integration window) i-vi indicated.

VDF images formed by integrating intensity in a disc of radius 3 pixels positioned around second and third order reflections are shown in Figure 8.13. It might be expected that these images would reveal similar contrast to those obtained using first order reflections but with the pitch of the intensity modulated by a factor of 2 or 3 respectively, but this is not the case. In the VDFs associated with second order reflections similar intensity modulations may be discerned but the pitch is similar to first order reflections whereas in the VDFs associated with third order reflections the no such modulation is evident. It seems that the contrast associated with the stronger third order reflection in particular is dominated by other contrast, that may be associated with distortions more akin to strain, whereas the first order reflections are particularly sensitive to kink density.

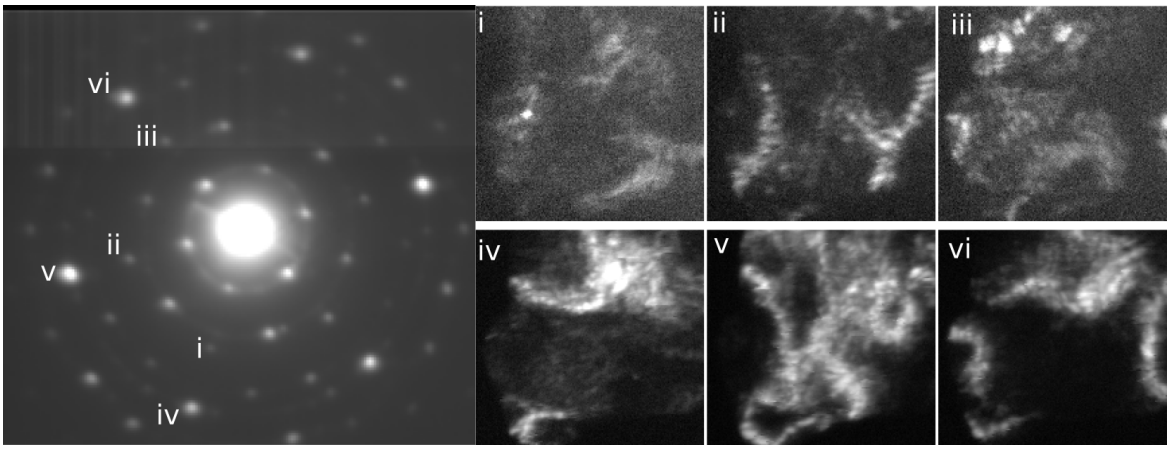

Fig. 8.13 **Virtual dark-field imaging of condis polyethylene**. Summed diffraction pattern from hexagonal condis PE with second and third order reflections used to form VDF images (with a 3 pixel radius integration window) i-vi indicated.

8.3 Summary & Conclusions

Hybrid diffraction-imaging, based on 4D-SED, has been demonstrated here as a powerful probe of polymer nanostructure in application to an melt spun UHMWPE specimen. SED has been shown to enable high-resolution nanostructural data to be obtained from beam sensitive polymer specimens, such as polyethylene, in both real space (5 nm) and reciprocal space (>1 $Å^{-1}$). To obtain this SED data it was necessary to cool the specimen to liquid nitrogen temperatures and to acquire the diffraction data from each probe position within a short time (10 ms). The electron dose imparted during this acquisition ($\sim$ 600 e / $Å^2$) was significantly higher than reported values for the critical dose in polyethylene and the acquisition did cause crystallinity to be destroyed in repeated acquisitions. The fact that high-resolution structural data could nevertheless be obtained suggests that the speed of acquisition may allow the data to be acquired prior to significant atomic rearrangement. Of course many processes associated with beam damage will occur much faster than the millisecond time scale but it is perhaps reasonable that significant molecular motion takes this long [407], especially at cryogenic temperatures. It is anticipated that the recent development of direct electron detectors will enable the dose to be reduced significantly[5] expanding the scope of future studies. It was also demonstrated that interpretable contrast could be obtained in various ways, without staining, by harnessing versatile *post-facto* analysis of the 4D-SED data. Two of the primary factors limiting polymer microscopy [383], beam damage and low contrast, have therefore been overcome using this approach.

[5] A reduction in dose of two-orders of magnitude with respect to the work presented here has in fact been recently achieved by the author, in work not presented in this thesis, using one such detector.

Nanostructural features that have eluded other characterisation techniques have been revealed in this work and placed in local structural context. A macro-kebab lamella of orthorhombic PE was studied and found to be structurally twisted, twinned and, where it meets the shish, transformed. The occurrence of monoclinic PE between the lamella and the shish may provide new insight into the nucleation process. Further, hexagonal condis PE was found to adopt an arrangement in which the chains projected along their axis approximate a unit cell of one third the size of the close-packed unit cell due to conformational disorder producing kinks that translate chains perpendicular to their axis. The diffracted intensities are a measure of averaging over conformational disorder and modulation in first order reflection intensity over space suggests that kinks in the chains may align to some degree in nanoscale domains within the material. 4D-SED therefore provides an unprecedented level of nanostructural characterisation in polymer systems. The methods developed are widely applicable to soft materials in general and provide a platform for a new level of nanostructural understanding in polymers.

Chapter 9

Summary & Prospects

SED microscopy has been developed in a number of ways and the utility of the the technique in materials science has been demonstrated by example through the research presented in this thesis. The overarching achievement of this work has therefore been to establish a framework for characterising nanostructure based on the acquisition and computational analysis of SED microscopy data. This work may be separated into four technique oriented strands where developments have been made and where there are significant prospects for further development towards solving the nanostructure problem set out in Chapter 1.

9.1 Platform for SED Microscopy

SED microscopy requires both experimental and computational methods combined with theoretical understanding in order to acquire, analyse and interpret 4D-SED data. These topics were addressed in Chapters 2, 3 and 4 respectively. Theoretically, SED is typically performed as a coherent STEM experiment with non-overlapping diffraction orders and often a nearly parallel illumination condition. The technique therefore provides a route to utilize the wide range of applications of electron nanodiffraction [417] in a spatially resolved diffraction microscopy approach. Experimentally, a method for aligning a double-conical-rocking electron probe for high-resolution scanning precession electron diffraction was established (Chapter 3) and benefits obtained by using precession in the context of strain mapping and machine learning were discussed (Chapters 4/5). A number of authors have recently published on applications using SPED but exploring the full benefits and limitations of using precession remains an area for more investigation. In particular, a detailed understanding of the implications of using precession on precision and accuracy is required as is true more generally for SED based orientation and strain mapping analyses (Chapter 4). Perhaps the most immediate area for experimental development stems from the use of direct electron

detectors that may enable quantitative use of diffracted intensities that may be used to map local order parameters, for example, if appropriate analysis is also developed.

A robust computational framework for crystallographic microscopy was established through this work in a flexible python code structure named *pyxem* (Chapter 4). This framework is intended to be extensible so that more functionality may be readily added to explore the wider potential of 4D-SED data. Particular areas currently under development include techniques to reveal structure in non-crystalline materials such as fluctuation electron microscopy and scanning pair-distribution function analysis. It would also be of significant benefit to develop the code, which is currently an offline data processing package, in such a way as to provide on-the-fly analysis during experiments. Unsupervised machine learning algorithms were demonstrated to learn significant features within 4D-SED data and the nexus of this idea and the aim of on-the-fly analysis would be true machine learning in which the experiment is automatically adjusted based on data recorded. Considering the ultimate goal of solving the nanostructure problem however the development of robust methodologies that may be applied on a *routine* basis is essential.

9.2 Three-dimensional SED Microscopy

Three-dimensional nanostructure requires three-dimensional characterisation and a particular challenge is to reconstruct continuous changes in the atomic structure resulting from strain and orientation gradients. Steps towards strain tomography based on SED microscopy were reported in Chapter 5 with a proof-of-principle single strain component reconstruction. Further progress towards reconstruction of the full strain tensor from data that is feasible to obtain in the electron microscope requires theoretical and algorithmic developments that are being actively explored. Aside from strain tomography there are a number of other insights that could be obtained from three-dimensional SED microscopy. Grain-wise reconstruction of polycrystalline specimens has been demonstrated using SED data [164, 165] and this provides a route to characterise interfaces in terms of the contact surface as well as the orientation relationship between microstructural elements, developing analysis of inter-phase relationships (e.g. Chapter 6).

9.3 Empirical Bicrystallography

Inter-phase crystallographic relationships may be elucidated using orientation mapping data obtained by SED or any other diffraction mapping technique, most typically EBSD. In Chapter 6, analysis of orientation relationships by visualizing orientation mapping data in

three-dimensional misorientation space was set out. To further rationalize the procedure developed there an automated method for determining the presence and location of clusters in the data [418] should be developed and this could enable quantitative comparison between experimental data and the misorientation distribution function for randomly oriented crystallites. This could be used to provide initial conditions for interface simulations, as demonstrated for the simple two-dimensional case of graphene (Chapter 7), which would be further enhanced by three-dimensional characterisation described above.

9.4 Probing Soft Nanostructure

Investigating nanostructure in polyethylene (Chapter 8) demonstrated that SED microscopy is a versatile hybrid diffraction-imaging technique for probing nanostructure in soft materials. SED microscopy was shown to overcome traditional challenges associated with electron microscopy of soft materials, namely sensitivity to electron irradiation and low contrast. Since comparable local structural measurements have not previously been possible in such systems this area holds particular promise for providing characterisation useful for materials science. A wide-range of important materials also fall in to this category, not only polymers but other organic solids such as pharmaceutical materials.

References

[1] Kochmann, D. M. From atoms to the macroscale: the nonlocal quasi-continuum method. http://www.mm.ethz.ch/research_QC.html Accessed: 2018-08-08.

[2] Furukawa, H., Kim, J., Ockwig, N. W., O'Keeffe, M., and Yaghi, O. M. (2008) Control of Vertex Geometry, Structure Dimensionality, Functionality, and Pore Metrics in the Reticular Synthesis of Crystalline Metal Organic Frameworks and Polyhedra. *Journal of the American Chemical Society,* **130**(35), 11650–11661.

[3] Ayoro, M. I. (2016) International Tables for Crystallography, Vol. A, Wiley-VCH, New York. 6th edition.

[4] Keen, D. A. and Goodwin, A. L. (2015) The crystallography of correlated disorder. *Nature,* **521**, 303–309.

[5] Raabe, D. Multiscale modeling. www.dierk-raabe.com/multiscale-modeling/ Accessed: 2018-08-08.

[6] Kleman, M. and Friedel, J. (2008) Disclinations, dislocations, and continuous defects: A reappraisal. *Reviews of Modern Physics,* **80**, 61–115.

[7] Thomas, J. M., Leary, R. K., Eggeman, A. S., and Midgley, P. A. (2015) The rapidly changing face of electron microscopy. *Chemical Physics Letters,* **631**, 103–113.

[8] APS X-ray Laue Diffraction Microscopy in 3D. https://www.aps.anl.gov/Sectors-33-34/34-ID-E Accessed: 2018-08-08.

[9] Zaefferer, S. (2011) A critical review of orientation microscopy in SEM and TEM. *Crystal Research and Technology,* **46**(6), 607–628.

[10] Pekin, T. C., Gammer, C., Ciston, J., Minor, A. M., and Ophus, C. (2017) Optimizing disk registration algorithms for nanobeam electron diffraction strain mapping. *Ultramicroscopy,* **176**, 170 – 176.

[11] Zuo, J. M. and Spence, J. C. H. (2017) Advanced Transmission Electron Microscopy, Springer, New York. 1st edition.

[12] Fultz, B. and Howe, J. M. (2013) Transmission Electron Microscopy and Diffractometry of Materials, Springer, New York. 4th edition.

[13] Spence, J. C. H. and Zuo, J. M. (1992) Electron Microdiffraction, Springer, New York. 1st edition.

[14] Midgley, P. A. and Eggeman, A. S. (2015) Precession electron diffraction–a topical review. *IUCrJ,* **2**(1), 126–136.

[15] Hirsch, P. B., Howie, A., Nicholson, R. B., Pashley, D. W., and Whelan, M. J. (1993) Electron Microscopy of Thin Crystals, Krieger, London. 2nd edition.

[16] Schematic of a TEM. http://allaboutmicroscopes.blogspot.com/2013/03/ Accessed: 2018-08-08.

[17] Brydson, R. (2011) Aberration-Corrected Analytical Transmission Electron Microscopy, Wiley, New York. 1st edition.

[18] Vincent, R. and Midgley, P. A. (1994) Double conical beam-rocking system for measurement of integrated electron diffraction intensities. *Ultramicroscopy,* **53**(3), 271–282.

[19] Saghi, Z. and Midgley, P. A. (2012) Electron Tomography in the (S)TEM: From Nanoscale Morphological Analysis to 3D Atomic Imaging. *Annual Review of Materials Research,* **42**(1), 59–79.

[20] Krause, T., Hanke, M., Brandt, O., and Trampert, A. (2016) Counterintuitive strain distribution in axial (In,Ga)N/GaN nanowires. *Applied Physics Letters,* **108**(3), 032103.

[21] Blatov, V. A., Shevchenko, A. P., and Proserpio, D. M. (2014) Applied Topological Analysis of Crystal Structures with the Program Package ToposPro. *Crystal Growth & Design,* **14**(7), 3576–3586.

[22] Larson, B. C., Yang, W., Ice, G. E., Budai, J. D., and Tischler, J. Z. (2002) Three-dimensional X-ray structural microscopy with submicrometre resolution. *Nature,* **415**, 887–890.

[23] Ice, G. E. and Pang, J. W. L. (2009) Tutorial on x-ray microLaue diffraction. *Materials Characterization,* **60**, 1191–1201.

[24] Wilkinson, A. J., Britton, T. B., Jiang, J., and Karamched, P. S. (2014) A review of advances and challenges in EBSD strain mapping. *IOP Conference Series: Materials Science and Engineering,* **55**(1), 012020.

[25] Keller, R. R. and Geiss, R. H. (2012) Transmission EBSD from 10 nm domains in a scanning electron microscope. *Journal of Microscopy,* **245**(3), 245–251.

[26] Trimby, P. W. (2012) Orientation mapping of nanostructured materials using transmission Kikuchi diffraction in the scanning electron microscope. *Ultramicroscopy,* **120**, 16–24.

[27] Rouviere, J. L., Béché, A., Martin, Y., Denneulin, T., and Cooper, D. (2013) Improved strain precision with high spatial resolution using nanobeam precession electron diffraction. *Applied Physics Letters,* **103**(24), 241913.

[28] Randle, V. and Engler, O. (2000) Introduction to texture analysis, Gordon and Breach Science Publishers, Philadelphia. 1st edition.

[29] Raabe, D. (2004) Computational Materials Science, Wiley, New York. 1st edition.

[30] Miller, R. E. and Tadmor, E. B. (2009) A unified framework and performance benchmark of fourteen multiscale atomistic/continuum coupling methods. *Modelling and Simulation in Materials Science and Engineering,* **17**(5), 053001.

[31] Billinge, S. J. L. and Levin, I. (2007) The problem with determining atomic structure at the nanoscale. *Science,* **316**(5824), 561–565.

[32] Gleiter, H. (2000) Nanostructured materials: basic concepts and microstructure. *Acta Materialia,* **48**(1), 1 – 29.

[33] Rollett, A., Rohrer, G., and Suter, R. (2015) Understanding materials microstructure and behavior at the mesoscale. *MRS Bulletin,* **40**(11), 951–960.

[34] Atkins, P. and de Paula, J. (2010) Physical Chemistry, Oxford University Press, Oxford. 9th edition.

[35] Kaxiras, E. (2003) Atomic and Electronic Structure of Solids, Cambridge University Press, Cambridge. 1st edition.

[36] Stone, A. (2013) The Theory of Intermolecular Forces, Oxford University Press, Oxford. 2nd edition.

[37] Brown, I. D. (2016) The Chemical Bond in Inorganic Chemistry, Oxford University Press, Oxford. 2nd edition.

[38] Gavezzotti, A. (2010) The lines-of-force landscape of interactions between molecules in crystals; cohesive *versus* tolerant and 'collateral damage' contact. *Acta Crystallographica Section B,* **66**(3), 396–406.

[39] IUCr (1992) Report of the Executive Committee for 1991. *Acta Crystallographica Section A,* **48**(6), 922–946.

[40] Janssen, T. and Janner, A. (2014) Aperiodic crystals and superspace concepts. *Acta Crystallographica Section B,* **70**(4), 617–651.

[41] Grimm, U. (2015) Aperiodic crystals and beyond. *Acta Crystallographica Section B,* **71**(3), 258–274.

[42] Nye, J. F. (2003) Physical Properties of Crystals, Oxford University Press, Oxford. 1 edition.

[43] Egami, T. and Billinge, S. J. L. (2003) Underneath the Bragg Peaks: Structural Analysis of Complex Materials, Pergamon, Oxford. 2nd edition.

[44] Keen, D. A. and McGreevy, R. L. (1990) Structural modelling of glasses using reverse Monte Carlo simulation. *Nature,* **344**, 423–425.

[45] Gereben, O. and Pusztai, L. (1994) Structure of amorphous semiconductors: Reverse Monte Carlo studies on a-C, a-Si, and a-Ge. *Physical Review B,* **50**, 14136–14143.

[46] Sheng, H. W., K, L. W., Alamgir, F. M., Bai, J. M., and E, M. (2006) Atomic packing and short-to-medium-range order in metallic glasses. *Nature,* **439**, 419–425.

[47] Barrat, J.-L., Baschnagel, J., and Lyulin, A. (2010) Molecular dynamics simulations of glassy polymers. *Soft Matter,* **6**, 3430–3446.

[48] Zallen, R. (1985) Models of amorphous solids. *Journal of Non-Crystalline Solids,* **75**(1), 3 – 14.

[49] Zachariasen, W. H. (1932) The Atomic Arrangement in Glass. *Journal of the American Chemical Society,* **54**(10), 3841–3851.

[50] Wooten, F., Winer, K., and Weaire, D. (1985) Computer Generation of Structural Models of Amorphous Si and Ge. *Physical Review Letters,* **54**, 1392–1395.

[51] Bennett, T. D., Goodwin, A. L., Dove, M. T., Keen, D. A., Tucker, M. G., Barney, E. R., Soper, A. K., Bithell, E. G., Tan, J.-C., and Cheetham, A. K. (2010) Structure and Properties of an Amorphous Metal-Organic Framework. *Physical Review Letters,* **104**, 115503.

[52] Keen, D. A. and Bennett, T. D. (2018) Structural investigations of amorphous metal–organic frameworks formed via different routes. *Physical Chemistry Chemical Physics,* **20**, 7857–7861.

[53] Bernal, J. D. (1960) Geometry of the Structure of Monatomic Liquids. *Nature,* **185**, 68–70.

[54] Gaskell, P. H. (1978) A new structural model for transition metal-metalloid glasses. *Nature,* **276**, 484–485.

[55] Miracle, D. B. (2004) A structural model for metallic glasses. *Nature Materials,* **3**, 697–702.

[56] Flory, P. J. (1969) Statistical Mechanics of Chain Molecules, Oxford University Press, Oxford. 1st edition.

[57] Treacy, M., Gibson, J., Fan, L., Paterson, D., and McNulty, I. (2005) Fluctuation microscopy: A probe of medium range order. *Reports on Progress in Physics,* **68**, 2899–2944.

[58] Treacy, M. and Borisenko, K. B. (2012) The Local Structure of Amorphous Silicon. *Science,* **335**, 950–953.

[59] Wunderlich, B. (1997) Metastable mesophases. *Macromolecular Symposia,* **113**(1), 51–65.

[60] Terentjev, E. M. and Weitz, D. A. (2015) The Oxford Handbook of Soft Condensed Matter, Oxford University Press, Oxford. 1st edition.

[61] Delgado-Friedrichs, O., Foster, M. D., O'Keeffe, M., Proserpio, D. M., Treacy, M. M., and Yaghi, O. M. (2005) What do we know about three-periodic nets?. *Journal of Solid State Chemistry,* **178**(8), 2533 – 2554.

[62] Nakamura, T., Hiraoka, Y., Hirata, A., Escolar, E. G., and Nishiura, Y. (2015) Persistent homology and many-body atomic structure for medium-range order in the glass. *Nanotechnology,* **26**(30), 304001.

[63] Hiraoka, Y., Nakamura, T., Hirata, A., Escolar, E. G., Matsue, K., and Nishiura, Y. (2016) Hierarchical structures of amorphous solids characterized by persistent homology. *Proceedings of the National Academy of Sciences,* **113**(26), 7035–7040.

[64] Cheng, Y. and Ma, E. (2011) Atomic-level structure and structure–property relationship in metallic glasses. *Progress in Materials Science,* **56**(4), 379 – 473.

[65] Hirata, A., Guan, P., Fujita, T., Hirotsu, Y., Inoue, A., Yavari, A. R., Sakurai, T., and Chen, M. (2011) Direct observation of local atomic order in a metallic glass. *Nature Materials,* **10**, 28–33.

[66] Yavari, A. R. (2006) Materials Science: A new order for metallic glasses. *Nature,* **439**, 405–406.

[67] Starr, F. W., Sastry, S., Douglas, J. F., and Glotzer, S. C. (Aug, 2002) What Do We Learn from the Local Geometry of Glass-Forming Liquids?. *Physical Review Letters,* **89**, 125501.

[68] Underwood, E. E. (1970) Quantitative Stereology, Addison-Wesley, Boston. 1st edition.

[69] Roters, F., Eisenlohr, P., Hantcherli, L., Tjahjanto, D. D., Bieler, T. R., and Raabe, D. (2009) Overview of constitutive laws, kinematics, homogenization and multiscale methods in crystal plasticity finite-element modeling: Theory, experiments, applications. *Acta Materialia,* **58**, 1152–1211.

[70] Groeber, M. A., Uchic, M. D., Dimiduk, D. M., Bhandari, Y., and Ghosh, S. (2007) A framework for automated 3D microstructure analysis & representation. *Journal of Computer-Aided Materials Design,* **14**(1), 63–74.

[71] Groeber, M., Ghosh, S., Uchic, M. D., and Dimiduk, D. M. (2008) A framework for automated analysis and simulation of 3D polycrystalline microstructures.: Part 1: Statistical characterization. *Acta Materialia,* **56**(6), 1257 – 1273.

[72] Callahan, P., Groeber, M., and Graef, M. D. (2016) Towards a quantitative comparison between experimental and synthetic grain structures. *Acta Materialia,* **111**, 242 – 252.

[73] Morawiec, A. (2004) Orientations and rotations - Computations in crystallographic textures, Springer-Verlag, Berlin, Heidelberg. 1st edition.

[74] Bunge, H.-J. (1982) Texture Analysis in Materials Science (book), Butterworths, Berlin 2nd edition.

[75] Kelly, A. and Knowles, K. M. (2012) Crystallography and Crystal Defects, Wiley, New York. 2nd edition.

[76] Sutton, A. P. and Baluffi, R. (2007) Interfaces in Crystalline Materials, Oxford University Press, Oxford 1st edition.

[77] Schusteritsch, G. and Pickard, C. J. (2014) Predicting interface structures: From $SrTiO_3$ to graphene. *Physical Review B,* **90**(3), 1–7.

[78] Sutton, A. P., Banks, E. P., and Warwick, A. R. (2015) The five-dimensional parameter space of grain boundaries. *Proceedings of the Royal Society A: Mathematical, Physical and Engineering Science,* **471**(2181), 20150442.

[79] Patala, S. and Schuh, C. (2011) The topology of homophase misorientation spaces. *Philosophical Magazine,* **91**(10), 1489–1508.

[80] Patala, S., Mason, J. K., and Schuh, C. A. (2012) Improved representations of misorientation information for grain boundary science and engineering. *Progress in Materials Science,* **57**(8), 1383–1425.

[81] Patala, S. (2017) Approximating coincidence - turning a new page for bicrystallography. *Acta Crystallographica Section A Foundations and Advances,* **73**(2), 85–86.

[82] Bilby, B. A. and Crocker, A. G. (1965) The theory of the crystallography of deformation twinning. *Proceedings of the Royal Society of London A: Mathematical, Physical and Engineering Sciences,* **288**(1413), 240–255.

[83] Bevis, M. and Crocker, A. G. (1968) Twinning shears in lattices. *Proceedings of the Royal Society of London A: Mathematical, Physical and Engineering Sciences,* **304**(1476), 123–134.

[84] Bevis, M. and Crocker, A. G. (1969) Twinning modes in lattices. *Proceedings of the Royal Society of London A: Mathematical, Physical and Engineering Sciences,* **313**(1515), 509–529.

[85] Mermin, N. D. (1979) The topological theory of defects in ordered media. *Reviews of Modern Physics,* **51**, 591–648.

[86] Chisholm, M. F., Kumar, S., and Hazzledine, P. (2005) Dislocations in complex materials. *Science,* **307**(5710), 701–703.

[87] Hull, D. and Bacon, D. J. (2011) Introduction to Dislocations, Butterworth-Heinemann, Oxford. 5th edition.

[88] Thomas, J. M. (1974) Topography and topology in solid state chemistry. *Philosophical Transactions of the Royal Society,* **277**, 251–286.

[89] Yazyev, O. V. and Chen, Y. P. (2014) Polycrystalline graphene and other two-dimensional materials. *Nature Nanotechnology,* **9**(10), 755–767.

[90] Chu, M., Sun, Y., Aghoram, U., and Thompson, S. E. (2009) Strain: A Solution for Higher Carrier Mobility in Nanoscale MOSFETs. *Annual Review of Materials Research,* **39**(1), 203–229.

[91] Das, S., Hofmann, F., and Tarleton, E. (2018) Consistent determination of geometrically necessary dislocation density from simulations and experiments. *International Journal of Plasticity,* **109**, 18 – 42.

[92] Ice, G. E., Budai, J. D., and Pang, J. W. L. (2011) The Race to X-ray Microbeam and Nanobeam Science. *Science,* **334**(6060), 1234–1239.

[93] Midgley, P. A. and Thomas, J. M. (2014) Multi-dimensional electron microscopy. *Angewandte Chemie - International Edition,* **53**(33), 8614–8617.

[94] Ludwig, W., Schmidt, S., Lauridsen, E. M., and Poulsen, H. F. (2008) X-ray diffraction contrast tomography: a novel technique for three-dimensional grain mapping of polycrystals. I. Direct beam case. *Journal of Applied Crystallography,* **41**(2), 302–309.

[95] Johnson, G., King, A., Goncalves-Honnicke, M., Marrow, J., and Ludwig, W. (2008) X-ray diffraction contrast tomography: a novel technique for three-dimensional grain mapping of polycrystals. II. The combined case. *Journal of Applied Crystallography,* **41**, 310–318.

[96] Liu, H. H., Schmidt, S., Poulsen, H. F., Godfrey, A., Liu, Z. Q., Sharon, J. A., and Huang, X. (5, 2011) Three-dimensional orientation mapping in the transmission electron microscope.. *Science,* **332**(6031), 833–4.

[97] Chapman, H. N. and Nugent, K. A. (2010) Coherent lensless X-ray imaging. *Nature Photonics,* **4**, 833–839.

[98] Pfeifer, M. A., Williams, G. J., Vartanyants, I. A., Harder, R., and Robinson, I. K. (2006) Three-dimensional mapping of a deformation field inside a nanocrystal. *Nature,* **442**, 63–66.

[99] Robinson, I. K. and Harder, R. (2009) Coherent X-ray diffraction imaging of strain at the nanoscale. *Nature Materials,* **8**, 291–298.

[100] Newton, M. C., Leake, S. J., Harder, R., and Robinson, I. K. (2010) Three-dimensional imaging of strain in a single ZnO nanorod. *Nature Materials,* **9**, 120–124.

[101] Krivanek, O. L., Chisholm, M. F., Nicolosi, V., Pennycook, T. J., Corbin, G. J., Dellby, N., Murfitt, M. F., Own, C. S., Szilagyi, Z. S., Oxley, M. P., Pantelides, S. T., and Pennycook, S. J. (2010) Atom-by-atom structural and chemical analysis by annular dark-field electron microscopy. *Nature,* **464**, 571–574.

[102] Scott, M. C., Chen, C.-C., Mecklenburg, M., Zhu, C., Xu, R., Ercius, P., Dahmen, U., Regan, B. C., and Miao, J. (2012) Electron tomography at 2.4-angstrom resolution. *Nature,* **483**, 444–447.

[103] Chen, C.-C., Zhu, C., White, E. R., Chiu, C.-Y., Scott, M. C., Regan, B. C., Marks, L. D., Huang, Y., and Miao, J. (2013) Three-dimensional imaging of dislocations in a nanoparticle at atomic resolution. *Nature,* **496**, 74–77.

[104] Xu, R., Chen, C.-C., Wu, L., Scott, M. C., Theis, W., Ophus, C., Bartels, M., Yang, Y., Ramezani-Dakhel, H., Sawaya, M. R., Heinz, H., Marks, L. D., Ercius, P., and Miao, J. (2015) Three-dimensional coordinates of individual atoms in materials revealed by electron tomography. *Nature Materials,* **14**, 1099–1103.

[105] Yang, Y., Chen, C.-C., Scott, M. C., Ophus, C., Xu, R., Pryor, A., Wu, L., Sun, F., Theis, W., Zhou, J., Eisenbach, M., Kent, P. R. C., Sabirianov, R. F., Zeng, H., Ercius, P., and Miao, J. (2017) Deciphering chemical order/disorder and material properties at the single-atom level. *Nature,* **542**, 75–79.

[106] Jacques, S. D. M., Di Michiel, M., Kimber, S. A. J., Yang, X., Cernik, R. J., Beale, A. M., and Billing, S. J. L. (2013) Pair distribution function computed tomography. *Nature Communications,* **4**, 2536.

[107] Mino, L., Borfecchia, E., Segura-Ruiz, J., Giannini, C., Martinez-Criado, G., and Lamberti, C. (2018) Materials characterization by synchrotron x-ray microprobes and nanoprobes. *Reviews of Modern Physics,* **90**, 025007.

[108] Holt, M., Harder, R., Winarski, R., and Rose, V. (2013) Nanoscale Hard X-Ray Microscopy Methods for Materials Studies. *Annual Review of Materials Research,* **43**(1), 183–211.

[109] Stangl, J., Mocuta, C., Diaz, A., Metzger, T. H., and Bauer, G. (2009) X-Ray Diffraction as a Local Probe Tool. *ChemPhysChem,* **10**(17), 2923–2930.

[110] Murray, C. E., Ying, A., Polvino, S. M., Noyan, I. C., Holt, M., and Maser, J. (2011) Nanoscale silicon-on-insulator deformation induced by stressed liner structures. *Journal of Applied Physics,* **109**(8), 083543.

[111] Schwartz, A., Kumar, M., Adams, B., and Field, D. (2009) Electron Backscatter Diffraction in Materials Science, Springer, New York and London. 1st edition.

[112] Humphreys, F. J. (2001) Grain and subgrain characterisation by electron backscatter diffraction. *Journal of Materials Science,* **36**(16), 3833–3854.

[113] Venables, J. A. and Bin-Jaya, R. (1977) Accurate microcrystallography using electron back-scattering patterns. *Philosophical Magazine,* **35**(5), 1317–1332.

[114] Wright, S. I., Wright, S. I., Adams, B. L., and Adams, B. L. (1992) Automatic-Analysis of Electron Backscatter Diffraction Patterns. *Metallurgical Transactions A,* **23**(3), 759–767.

[115] Krieger Lassen, N. C. (1998) Automatic high-precision measurements of the location and width of Kikuchi bands in electron backscatter diffraction patterns. *Journal of Microscopy,* **190**(3), 375–391.

[116] Chen, Y. H., Park, S. U., Wei, D., Newstadt, G., Jackson, M. A., Simmons, J. P., De Graef, M., and Hero, A. O. (2015) A Dictionary Approach to Electron Backscatter Diffraction Indexing. *Microscopy and Microanalysis,* **21**(3), 739–752.

[117] Ram, F. and Graef, M. D. (2018) Phase differentiation by electron backscatter diffraction using the dictionary indexing approach. *Acta Materialia,* **144**, 352 – 364.

[118] Friedrich, T., Bochmann, A., Dinger, J., and Teichert, S. (2018) Application of the pattern matching approach for EBSD calibration and orientation mapping, utilising dynamical EBSP simulations. *Ultramicroscopy,* **184**, 44 – 51.

[119] Nolze, G., Winkelmann, A., and Boyle, A. P. (2016) Pattern matching approach to pseudosymmetry problems in electron backscatter diffraction. *Ultramicroscopy,* **160**, 146 – 154.

[120] Nolze, G., Jürgens, M., Olbricht, J., and Winkelmann, A. (2018) Improving the precision of orientation measurements from technical materials via EBSD pattern matching. *Acta Materialia,* **159**, 408 – 415.

[121] Winkelmann, A., Trager-Cowan, C., Sweeney, F., Day, A. P., and Parbrook, P. (2007) Many-beam dynamical simulation of electron backscatter diffraction patterns. *Ultramicroscopy,* **107**(4-5), 414–421.

[122] Winkelmann, A. and Nolze, G. (2015) Point-group sensitive orientation mapping of non-centrosymmetric crystals. *Applied Physics Letters,* **106**(7), 072101.

[123] Wilkinson, A. J., Meaden, G., and Dingley, D. J. (2006) High-resolution elastic strain measurement from electron backscatter diffraction patterns: New levels of sensitivity. *Ultramicroscopy,* **106**(4-5), 307–313.

[124] Wilkinson, A. J., Meaden, G., and Dingley, D. J. (2006) High resolution mapping of strains and rotations using electron backscatter diffraction. *Materials Science and Technology,* **22**(11), 1271–1278.

[125] Britton, T. B., Jiang, J., Karamched, P. S., and Wilkinson, A. J. (2013) Probing deformation and revealing microstructural mechanisms with cross-correlation-based, high-resolution electron backscatter diffraction. *The Journal of The Minerals, Metals & Materials Society,* **65**(9), 1245–1253.

[126] Britton, T. B. and Wilkinson, A. J. (2011) Measurement of residual elastic strain and lattice rotations with high resolution electron backscatter diffraction. *Ultramicroscopy,* **111**(8), 1395–1404.

[127] Rollett, A., Lee, S., Campman, R., and Rohrer, G. (2007) Three-dimensional characterization of microstructure by electron back-scatter diffraction. *Annual Review of Materials Research,* **37**(1), 627–658.

[128] Morawiec, A. (1999) Automatic orientation determination from Kikuchi patterns. *Journal of Applied Crystallography,* **32**(4), 788–798.

[129] Morawiec, A., Fundenberger, J.-J., Bouzy, E., and Lecomte, J.-S. (2002) A program for determination of crystallite orientations from TEM Kikuchi and CBED diffraction patterns. *Journal of Applied Crystallography,* **35**(2), 287–287.

[130] Fundenberger, J. J., Morawiec, A., Bouzy, E., and Lecomte, J. S. (2003) System for creating orientation maps using TEM. *Materials Chemistry and Physics,* **81**(2-3), 535–537.

[131] Fundenberger, J. J., Morawiec, A., Bouzy, E., and Lecomte, J. S. (2003) Polycrystal orientation maps from TEM. *Ultramicroscopy,* **96**(2), 127–137.

[132] Zaefferer, S. and Schwarzer, R. A. (1994) Automated Measurement of Single Grain Orientations in the TEM. *Zeitschrift fur Metallkunde,* **85**(8), 585–591.

[133] Schwarzer, R. A. and Sukkau, J. (1998) Automated crystal orientation mapping (ACOM) with a computer controlled TEM by interpreting transmission Kikuchi patterns. *Materials Science Forum,* **273-275**, 215–222.

[134] Nellist, P.D., M. B. and Rodenburg, J. (1995) Resolution beyond the 'information limit' in transmission electron microscopy. *Nature,* **374**, 630–632.

[135] Jiang, Y., Han, Y., Deb, P., Gao, H., Xie, S., Purohit, P., Tate, M., Park, J., Gruner, S., Elser, V., and Muller, D. (2018) Electron ptychography of 2D materials to deep sub-angstrom resolution. *Nature,* **559**, 343–349.

[136] Jones, P. M., Rackham, G. M., and Steeds, J. W. (1977) Higher Order Laue Zone Effects in Electron Diffraction and Their Use in Lattice Parameter Determination. *Proceedings of the Royal Society of London A,* **354**, 197–222.

[137] Vincent, R., Preston, A., and King, M. A. (1988) Measurement of strain in silver halide particles by convergent beam electron diffraction. *Ultramicroscopy,* **24**, 409–419.

[138] Kimoto, K., Usami, K., Sakata, H., and Tanaka, M. (1993) Measurement of strain in locally oxidized silicon using convergent-beam electron diffraction. *Japanese Journal of Applied Physics, Part 2: Letters,* **32**, L211–L214.

[139] Toda, A. and Ikarashi, N. (2000) Local lattice strain measurements in semiconductor devices by using convergent-beam electron diffraction. *Journal of Crystal Growth,* **210**, 341–345.

[140] Armigliato, A., Balboni, R., Carnevale, G. P., Pavia, G., Piccolo, D., Frabboni, S., Benedetti, A., and Cullis, A. G. (2003) Application of convergent beam electron diffraction to two-dimensional strain mapping in silicon devices. *Applied Physics Letters,* **82**(13), 2172–2174.

[141] Senez, V., Armigliato, A., De Wolf, I., Carnevale, G., Balboni, R., Frabboni, S., and Benedett, A. (2003) Strain determination in silicon microstructures by combined convergent beam electron diffraction, process simulation, and micro-Raman spectroscopy. *Journal of Applied Physics,* **94**(9), 5574–5583.

[142] Armigliato, A., Balboni, R., and Frabboni, S. (2005) Improving spatial resolution of convergent beam electron diffraction strain mapping in silicon microstructures. *Applied Physics Letters,* **86**(6), 1–3.

[143] Spessot, A., Frabboni, S., Balboni, R., and Armigliato, A. (2007) Method for determination of the displacement field in patterned nanostructures by TEM/CBED analysis of split high-order Laue zone line profiles. *Journal of Microscopy,* **226**(2), 140–155.

[144] Herring, R., Norouzpour, M., Saitoh, K., Tanaka, N., and Tanji, T. (2015) Determination of three-dimensional strain state in crystals using self-interfered split HOLZ lines. *Ultramicroscopy,* **156**, 37–40.

[145] Morawiec, A. (2005) Formal conditions for unambiguous residual strain determination by CBED. *Philosophical Magazine,* **85**(15), 1611–1623.

[146] Kim, K.-H., Payne, D. A., and Zuo, J. M. (2013) Determination of fluctuations in local symmetry and measurement by convergent beam electron diffraction: applications to a relaxor-based ferroelectric crystal after thermal annealing. *Journal of Applied Crystallography,* **46**(5), 1331–1337.

[147] Shao, Y.-T. and Zuo, J.-M. (2017) Nanoscale symmetry fluctuations in ferroelectric barium titanate, $BaTiO_3$. *Acta Crystallographica Section B,* **73**(4), 708–714.

[148] Hÿtch, M. J. and Minor, A. M. (2014) Observing and measuring strain in nanostructures and devices with transmission electron microscopy. *MRS Bulletin,* **39**(02), 138–146.

[149] Zaefferer, S. (2000) New developments of computer-aided crystallographic analysis in transmission electron microscopy. *Journal of Applied Crystallography,* **33**(1), 10–25.

[150] Rauch, E. F. and Veron, M. (2005) Coupled microstructural observations and local texture measurements with an automated crystallographic orientation mapping tool attached to a tem. *Materialwissenschaft und Werkstofftechnik,* **36**(10), 552–556.

[151] Morawiec, A., Bouzy, E., Paul, H., and Fundenberger, J. J. (2014) Orientation precision of TEM-based orientation mapping techniques. *Ultramicroscopy,* **136**, 107–118.

[152] Usuda, K., Numata, T., Irisawa, T., Hirashita, N., and Takagi, S. (2005) Strain characterization in SOI and strained-Si on SGOI MOSFET channel using nano-beam electron diffraction (NBD). *Materials Science and Engineering B: Solid-State Materials for Advanced Technology,* **124-125**, 143–147.

[153] Armigliato, A., Frabboni, S., and Gazzadi, G. C. (2008) Electron diffraction with ten nanometer beam size for strain analysis of nanodevices. *Applied Physics Letters,* **93**(16), 10–13.

[154] Shan, Z., Wiezorek, J. M. K., Knapp, J. A., Follstaedt, D. M., Stach, E. a., and Mao, S. X. (2008) Large lattice strain in individual grains of deformed nanocrystalline Ni. *Applied Physics Letters,* **92**(9), 2006–2009.

[155] Sourty, E., Stanley, J., and Freitag, B. (2009) Using STEM with quasi-parallel illumination and an automated peak-finding routine for strain analysis at the nanometre scale. In *Proceedings of the 16th IEEE International Symposium on the Physical and Failure Analysis of Integrated Circuits* IEEE pp. 479–484.

[156] Uesugi, F., Hokazono, A., and Takeno, S. (2011) Evaluation of two-dimensional strain distribution by STEM/NBD. *Ultramicroscopy,* **111**(8), 995–998.

[157] Baumann, F. H. (2014) High precision two-dimensional strain mapping in semiconductor devices using nanobeam electron diffraction in the transmission electron microscope. *Applied Physics Letters,* **104**(26), 262102.

[158] Clément, L. and Delille, D. Quantitative Strain Measurement in Advanced Devices: A Comparison Between Convergent Beam Electron Diffraction and Nanobeam Diffraction chapter 3, pp. 65–80 Wiley New York. (2013).

[159] Béché, A., Rouvière, J. L., Barnes, J. P., and Cooper, D. (2013) Strain measurement at the nanoscale: Comparison between convergent beam electron diffraction, nanobeam electron diffraction, high resolution imaging and dark field electron holography. *Ultramicroscopy,* **131**, 10–23.

[160] Vigouroux, M. P., Delaye, V., Bernier, N., Cipro, R., Lafond, D., Audoit, G., Baron, T., Rouvière, J. L., Martin, M., Chenevier, B., and Bertin, F. (2014) Strain mapping at the nanoscale using precession electron diffraction in transmission electron microscope with off axis camera. *Applied Physics Letters,* **105**(19), 191906.

[161] Wang, Y. Y., Rouviere, J., Murray, C. E., Bernier, N., and Bruley, J. (2015) Nanoscale strain distributions in embedded SiGe semiconductor devices revealed by precession electron diffraction and dual lens dark field electron holography. *Applied Physics Letters,* **106**(4), 042104.

[162] Cooper, D., Bernier, N., and Rouvière, J.-L. (2015) Combining 2 nm Spatial Resolution and 0.02% Precision for Deformation Mapping of Semiconductor Specimens in a Transmission Electron Microscope by Precession Electron Diffraction. *Nano Letters,* **15**(8), 5289–5294.

[163] Cooper, D., Denneulin, T., Bernier, N., Béché, A., and Rouvière, J.-L. (2016) Strain mapping of semiconductor specimens with nm-scale resolution in a transmission electron microscope. *Micron,* **80**, 145 – 165.

[164] Eggeman, A. S., Krakow, R., and Midgley, P. A. (2015) Scanning precession electron tomography for three-dimensional nanoscale orientation imaging and crystallographic analysis. *Nature Communications,* **6**, 7267.

[165] Meng, Y. and Zuo, J.-M. (2016) Three-dimensional nanostructure determination from a large diffraction data set recorded using scanning electron nanodiffraction. *IUCrJ,* **3**(5), 300–308.

[166] Midgley, P. A. and Dunin-Borkowski, R. E. (2009) Electron tomography and holography in materials science. *Nature Materials,* **8**(4), 271–280.

[167] Midgley, P. A., Weyland, M., Thomas, J. M., and Johnson, B. F. G. (2001) Z-contrast tomography: a technique in three-dimensional nanostructural analysis based on Rutherford scattering. *Chemical Communications,* **1**(10), 907–908.

[168] Leary, R. K. and Midgley, P. A. (2016) Analytical electron tomography. *MRS Bulletin,* **41**(7), 531–536.

[169] Collins, S. M. and Midgley, P. A. (2017) Progress and opportunities in EELS and EDS tomography. *Ultramicroscopy,* **180**, 133 – 141.

[170] Kirkland, E. J. (2010) Advanced Computing in Electron Microscopy, Springer, New York. 2nd edition.

[171] Reimer, L. and Kohl, H. (2008) Transmission Electron Microscopy, Springer, New York. 2nd edition.

[172] De Graef, M. (2003) Introduction to Conventional Transmission Electron Microscopy, Cambridge University Press, Cambridge. 1st edition.

[173] Spence, J. C. H. (2013) High-Resolution Electron Microscopy, Oxford University Press, Oxford. 4th edition.

[174] Cowley, J. M. (1995) Diffraction Physics, North-Holland, New York. 2nd edition.

[175] Pennycook, S. J. and Nellist, P. D. (2011) Scanning Transmission Electron Microscopy, Springer, New York. 1st edition.

[176] Humphreys, C. J. (1979) The scattering of fast electrons by crystals. *Reports on Progress in Physics,* **42**(11), 1825.

[177] Doyle, P. A. and Turner, P. S. (1968) Relativistic Hartree–Fock X-ray and electron scattering factors. *Acta Crystallographica Section A,* **24**(3), 390–397.

[178] Bethe, H. (1928) Theorie der Beugung von Elektronen an Kristallen. *Annalen der Physik,* **392**(17), 55–129.

[179] Cowley, J. M. and Moodie, A. F. (1957) The scattering of electrons by atoms and crystals. I. A new theoretical approach. *Acta Crystallographica,* **10**(10), 609–619.

[180] Midgley, P., Saunders, M., Vincent, R., and Steeds, J. (1995) Energy-filtered convergent-beam diffraction: examples and future prospects. *Ultramicroscopy,* **59**(1), 1 – 13.

[181] Egerton, R. F. (2011) Electron Energy-Loss Spectroscopy in the Electron Microscope, Springer, New York. 1st edition.

[182] Egerton, R. F., Li, P., and Malac, M. (2004) Radiation damage in the TEM and SEM. *Micron,* **35**, 399–409.

[183] Egerton, R. F. and Malac, M. (2004) The Lateral Range and Energy Deposition of Fast Secondary Electrons. *Microscopy and Microanalysis,* **10**(S02), 1382–1383.

[184] Egerton, R. F. (2012) Mechanisms of radiation damage in beam-sensitive specimens, for TEM accelerating voltages between 10 and 300 kV. *Microscopy Research and Technique,* **75**, 1550–1556.

[185] Egerton, R. F. (2013) Control of radiation damage in TEM. *Ultramicroscopy,* **127**, 100–108.

[186] Nellist, P. and Pennycook, S. (1999) Incoherent imaging using dynamically scattered coherent electrons. *Ultramicroscopy,* **78**(1), 111 – 124.

[187] Palatinus, L., Jacob, D., Cuvillier, P., Klementová, M., Sinkler, W., Marks, L. D., and IUCr (2013) Structure refinement from precession electron diffraction data. *Acta Crystallographica Section A Foundations of Crystallography,* **69**(2), 171–188.

[188] Rauch, E. F., Portillo, J., Nicolopoulos, S., Bultreys, D., Rouvimov, S., and Moeck, P. (2010) Automated nanocrystal orientation and phase mapping in the transmission electron microscope on the basis of precession electron diffraction. *Zeitschrift für Kristallographie,* **225**(2-3), 103–109.

[189] Mahr, C., Müller-Caspary, K., Grieb, T., Schowalter, M., Mehrtens, T., Krause, F. F., Zillmann, D., and Rosenauer, A. (2015) Theoretical study of precision and accuracy of strain analysis by nano-beam electron diffraction. *Ultramicroscopy,* **158**, 38 – 48.

[190] Gjønnes, K. (1997) On the integration of electron diffraction intensities in the Vincent-Midgley precession technique. *Ultramicroscopy,* **69**(1), 1 – 11.

[191] White, T., Eggeman, A., and Midgley, P. (2010) Is precession electron diffraction kinematical? Part I: Phase-scrambling multislice simulations. *Ultramicroscopy,* **110**(7), 763 – 770.

[192] Eggeman, A., White, T., and Midgley, P. (2010) Is precession electron diffraction kinematical? Part II: A practical method to determine the optimum precession angle. *Ultramicroscopy,* **110**(7), 771 – 777.

[193] Eggeman, A. S. and Midgley, P. A. (2012) Chapter 1 - Precession Electron Diffraction. In *Advances in Imaging and Electron Physics* Vol. 170, pp. 1–63 Elsevier London.

[194] Palatinus, L., Brázda, P., Boullay, P., Perez, O., Klementová, M., Petit, S., Eigner, V., Zaarour, M., and Mintova, S. (2017) Hydrogen positions in single nanocrystals revealed by electron diffraction. *Science,* **355**(6321), 166–169.

[195] Moeck, P., Rouvimov, S., Rauch, E. F., Véron, M., Kirmse, H., Häusler, I., Neumann, W., Bultreys, D., Maniette, Y., and Nicolopoulos, S. (2011) High spatial resolution semi-automatic crystallite orientation and phase mapping of nanocrystals in transmission electron microscopes. *Crystal Research and Technology,* **46**(6), 589–606.

[196] Viladot, D., Veron, M., Gemmi, M., Peiro, F., Portillo, J., Estrade, S., Mendoza, J., Llorca-Isern, N., and Nicolopoulos, S. Orientation and phase mapping in the transmission electron microscope using precession-assisted diffraction spot recognition: state-of-the-art results. *Journal of Microscopy,* **252**(1), 23–34.

[197] Wang, Z. (1994) Dislocation contrast in high-angle hollow-cone dark-field TEM. *Ultramicroscopy,* **53**(1), 73 – 90.

[198] Williams, D. B. and Carter, C. B. (2009) Transmission Electron Microscopy A Textbook for Materials Science, Springer, New York. 3rd edition.

[199] Own, C., Sinkler, W., and Marks, L. (2007) Prospects for aberration corrected electron precession. *Ultramicroscopy,* **107**(6), 534 – 542.

[200] Own, C. S., Marks, L. D., and Sinkler, W. (2005) Electron precession: A guide for implementation. *Review of Scientific Instruments,* **76**(3), 033703.

[201] Krivanek, O., Nellist, P., Dellby, N., Murfitt, M., and Szilagyi, Z. (2003) Towards sub-0.5Å electron beams. *Ultramicroscopy,* **96**(3), 229 – 237.

[202] Haider, M., Hartel, P., Müller, H., Uhlemann, S., and Zach, J. (2009) Current and future aberration correctors for the improvement of resolution in electron microscopy. *Philosophical Transactions of the Royal Society of London A: Mathematical, Physical and Engineering Sciences,* **367**(1903), 3665–3682.

[203] Haider, M., Uhlemann, S., Schwan, E., Rose, H., Kabius, B., and Urban, K. (1998) Electron microscopy image enhanced. *Nature,* **392**, 768 – 769.

[204] Krivanek, O., Dellby, N., and Lupini, A. (1999) Towards sub-Å electron beams. *Ultramicroscopy,* **78**(1), 1 – 11.

[205] Eggeman, A. S., Illig, S., Troisi, A., Sirringhaus, H., and Midgley, P. A. (2013) Measurement of molecular motion in organic semiconductors by thermal diffuse electron scattering.. *Nature materials,* **12**(11), 1045–9.

[206] Eggeman, A., London, A., and Midgley, P. (2013) Ultrafast electron diffraction pattern simulations using GPU technology. Applications to lattice vibrations. *Ultramicroscopy,* **134**, 44 – 47.

[207] Lin, J. and Cowley, J. (1986) Calibration of the operating parameters for an HB5 stem instrument. *Ultramicroscopy,* **19**(1), 31 – 42.

[208] Cowley, J. (1992) Twenty forms of electron holography. *Ultramicroscopy,* **41**(4), 335 – 348.

[209] Sawada, H., Sannomiya, T., Hosokawa, F., Nakamichi, T., Kaneyama, T., Tomita, T., Kondo, Y., Tanaka, T., Oshima, Y., Tanishiro, Y., and Takayanagi, K. (2008) Measurement method of aberration from Ronchigram by autocorrelation function. *Ultramicroscopy,* **108**(11), 1467 – 1475.

[210] Yi, F., Tiemeijer, P., and Voyles, P. M. (2010) Flexible formation of coherent probes on an aberration-corrected STEM with three condensers. *Journal of Electron Microscopy,* **59**(S1), S15–S21.

[211] Freeman, L. A., Howie, A., and Treacy, M. M. J. (1977) Bright field and hollow cone dark field electron microscopy of palladium catalysts. *Journal of Microscopy,* **111**(2), 165–178.

[212] Koch, C. T. (2011) Aberration-compensated large-angle rocking-beam electron diffraction. *Ultramicroscopy,* **111**(7), 828 – 840.

[213] Beanland, R., Thomas, P. J., Woodward, D. I., Thomas, P. A., and Roemer, R. A. (2013) Digital electron diffraction – seeing the whole picture. *Acta Crystallographica Section A,* **69**(4), 427–434.

[214] Liao, Y. and Marks, L. D. (2012) On the alignment for precession electron diffraction. *Ultramicroscopy,* **117**, 1 – 6.

[215] Barnard, J. S., Johnstone, D. N., and Midgley, P. A. (2017) High-resolution scanning precession electron diffraction: Alignment and spatial resolution. *Ultramicroscopy,* **174**, 79–88.

[216] Berry, M. and Upstill, C. (1980) IV Catastrophe Optics: Morphologies of Caustics and Their Diffraction Patterns. Vol. 18 of Progress in Optics, pp. 257 – 346 Elsevier London.

[217] Erni, R., Rossell, M. D., Kisielowski, C., and Dahmen, U. (2009) Atomic-Resolution Imaging with a Sub-50-pm Electron Probe. *Physical Review Letters,* **102**, 096101.

[218] Horowitz, P. and Hill, W. (2015) The Art of Electronics, Cambridge University Press, Cambridge 3rd edition.

[219] Rauch, E. F. and Duft, A. (7, 2005) Orientation Maps Derived from TEM Diffraction Patterns Collected with an External CCD Camera. In *Textures of Materials - ICOTOM 14* Vol. 495 of Materials Science Forum, pp. 197–202.

[220] McMullan, G., Faruqi, A., and Henderson, R. (2016) Chapter One - Direct Electron Detectors. In Crowther, R., (ed.), *The Resolution Revolution: Recent Advances In cryoEM*, Vol. 579 of Methods in Enzymology, pp. 1 – 17 Academic Press.

[221] Tate, M. W., Purohit, P., Chamberlain, D., Nguyen, K. X., Hovden, R., Chang, C. S., Deb, P., Turgut, E., Heron, J. T., Schlom, D. G., and et al. (2016) High Dynamic Range Pixel Array Detector for Scanning Transmission Electron Microscopy. *Microscopy and Microanalysis,* **22**(1), 237–249.

[222] Zuo, J. M. (2000) Electron detection characteristics of a slow-scan CCD camera, imaging plates and film, and electron image restoration. *Microscopy Research and Technique,* **49**(3), 245–268.

[223] Zou, X., Hovmoller, S., and Oleynikov, P. (2011) Electron Crystallography: Electron Microscopy and Electron Diffraction, Oxford University Press, Oxford. 1st edition.

[224] Liao, Y. and Marks, L. D. (2013) Reduction of electron channeling in EDS using precession. *Ultramicroscopy,* **126**, 19 – 22.

[225] Estradé, S., Portillo, J., Yedra, L., Rebled, J. M., and Peiró, F. (2012) EELS signal enhancement by means of beam precession in the TEM. *Ultramicroscopy,* **116**, 135 – 137.

[226] Johnstone, D. N., Crout, P. A., Martineau, B., Høgås, S., Laulainen, J., Collins, S., Smeets, S., Morzy, J., Doherty, T., Prestat, E., Ostasevicius, T., Bergh, T., and Ånes, H. pyxem/pyxem: pyXem 0.7.1. https://doi.org/10.5281/zenodo.2650296 (2019).

[227] Beck, K. (2003) Test Driven Development: By Example, Addison-Wesley, Boston. 1st edition.

[228] Oliphant, T. E. (2007) Python for Scientific Computing. *Computing in Science & Engineering,* **9**(3), 10–20.

[229] Millman, K. J. and Aivazis, M. (2011) Python for Scientists and Engineers. *Computing in Science & Engineering,* **13**(2), 9–12.

[230] Stewart, J. M. (2014) Python for scientists, Cambridge University Press, Cambridge 1st edition.

[231] de la Pena, F., Ostasevicius, T., Tonaas Fauske, V., Burdet, P., Jokubauskas, P., Nord, M., Sarahan, M., Prestat, E., Johnstone, D. N., Taillon, J., Jan Caron, J., Furnival, T., MacArthur, K. E., Eljarrat, A., Mazzucco, S., Migunov, V., Aarholt, T., Walls, M., Winkler, F., Donval, G., Martineau, B., Garmannslund, A., Zagonel, L.-F., and Iyengar, I. (2017) Electron Microscopy (Big and Small) Data Analysis With the Open Source Software Package HyperSpy. *Microscopy and Microanalysis,* **23**(S1), 214–215.

[232] Juhás, P., Farrow, C. L., Yang, X., Knox, K. R., and Billinge, S. J. L. (2015) Complex modeling: a strategy and software program for combining multiple information sources to solve ill posed structure and nanostructure inverse problems. *Acta Crystallographica Section A,* **71**(6), 562–568.

[233] Pedregosa, F., Grisel, O., Weiss, R., Passos, A., and Brucher, M. (2011) Scikit-learn : machine learning in Python. *Journal of Machine Learning Research,* **12**, 2825–2830.

[234] van der Walt, S., Schönberger, J. L., Nunez-Iglesias, J., Boulogne, F., Warner, J. D., Yager, N., Gouillart, E., and Yu, T. (2014) scikit-image: image processing in Python. *PeerJ,* **2**, e453.

[235] Oliphant, T. E. (2015) Guide to NumPy, CreateSpace Independent Publishing Platform, USA, Online 2nd edition.

[236] Jones, E., Oliphant, T., and Peterson, P. SciPy: Open source scientific tools for Python. http://www.scipy.org/" (2001) Accessed: 2018-08-08.

[237] Hunter, J. D. (2007) Matplotlib: A 2D Graphics Environment. *Computing in Science & Engineering,* **9**(3), 90–95.

[238] Ostaševičius, T., Peña, F., and Midgley, P. (2016) SAMFire - a smart adaptive fitting algorithm for multi-dimensional microscopy. *Proceedings of the European Microscopy Congress,* pp. 95–96.

[239] Munshi, A. M., Dheeraj, D. L., Fauske, V. T., Kim, D. C., Huh, J., Reinertsen, J. F., Ahtapodov, L., Lee, K. D., Heidari, B., van Helvoort, A. T. J., Fimland, B. O., and Weman, H. (feb, 2014) Position-Controlled Uniform GaAs Nanowires on Silicon using Nanoimprint Lithography. *Nano Letters,* **14**(2), 960–966.

[240] White, T. A. Structure solution using precession electron diffraction and diffraction tomography PhD thesis University of Cambridge (2009).

[241] Murphy, K. P. (2012) Machine Learning: A Probabilistic Perspective, MIT Press, Boston. 1st edition.

[242] Belianinov, A., Vasudevan, R., Strelcov, E., Steed, C., Yang, S. M., Tselev, A., Jesse, S., Biegalski, M., Shipman, G., Symons, C., Borisevich, A., Archibald, R., and Kalinin, S. (2015) Big data and deep data in scanning and electron microscopies: deriving functionality from multidimensional data sets. *Advanced Structural and Chemical Imaging,* **1**(1), 6.

[243] Kalinin, S. V., Sumpter, B. G., and Archibald, R. K. (2015) Big-deep-smart data in imaging for guiding materials design. *Nature Materials,* **14**, 973–980.

[244] de la Peña, F., Berger, M.-H., Hochepied, J.-F., Dynys, F., Stephan, O., and Walls, M. (2011) Mapping titanium and tin oxide phases using EELS: an application of independent component analysis.. *Ultramicroscopy,* **111**(2), 169–76.

[245] Rossouw, D., Burdet, P., de la Peña, F., Ducati, C., Knappett, B. R., Wheatley, A. E. H., and Midgley, P. A. (2015) Multicomponent Signal Unmixing from Nanoheterostructures: Overcoming the Traditional Challenges of Nanoscale X-ray Analysis via Machine Learning. *Nano Letters,* **15**(4), 2716–2720.

[246] Rencher, A. and Christensen, W. (2002) Methods of Multivariate Analysis, Wiley, New York. 3rd edition.

[247] Hyvärinen, A. and Oja, E. (2000) Independent component analysis: Algorithms and applications. *Neural Networks,* **13**(4-5), 411–430.

[248] Lee, D. D. and Seung, H. S. (1999) Learning the parts of objects by non-negative matrix factorization. *Nature,* **401**(6755), 788–791.

[249] Hoyer, P. O. (2004) Non-negative Matrix Factorization with Sparseness Constraints. *Journal of Machine Learning Research,* **5**, 1457–1469.

[250] Hyvärinen, A., Karhunen, J., and Oja, E. (2001) Independent Component Analysis, Wiley, New York. 1st edition.

[251] Martineau, B. H., Johnstone, D. N., van Helvoort, A. T. J., Midgley, P. A., and Eggeman, A. S. (2019) Unsupervised machine learning applied to scanning precession electron diffraction data. *Advanced Structural and Chemical Imaging,* **5**(1), 3.

[252] Kannan, R., Ievlev, A. V., Laanait, N., Ziatdinov, M. A., Vasudevan, R. K., Jesse, S., and Kalinin, S. V. (2018) Deep data analysis via physically constrained linear unmixing: universal framework, domain examples, and a community-wide platform. *Advanced Structural and Chemical Imaging,* **4**(1), 6.

[253] Eggeman, A. S., White, T. A., and Midgley, P. A. (2010) Is precession electron diffraction kinematical? Part II. A practical method to determine the optimum precession angle.. *Ultramicroscopy,* **110**(7), 771–777.

[254] Kobler, A. and Kübel, C. (2016) Challenges in quantitative crystallographic characterization of 3D thin films by ACOM-TEM. *Ultramicroscopy,* **173**, 84–94.

[255] Rouvière, J. and Sarigiannidou, E. (2005) Theoretical discussions on the geometrical phase analysis. *Ultramicroscopy,* **106**(1), 1 – 17.

[256] Ozdol, V. B., Gammer, C., Jin, X. G., Ercius, P., Ophus, C., Ciston, J., and Minor, A. M. (2015) Strain mapping at nanometer resolution using advanced nano-beam electron diffraction. *Applied Physics Letters,* **106**(25), 253107.

[257] Thompson, S. E., Armstrong, M., Auth, C., Alavi, M., Buehler, M., Chau, R., Cea, S., Ghani, T., Glass, G., Hoffman, T., Jan, C. ., Kenyon, C., Klaus, J., Kuhn, K., Ma, Z., Mcintyre, B., Mistry, K., Murthy, A., Obradovic, B., Nagisetty, R., Nguyen, P., Sivakumar, S., Shaheed, R., Shifren, L., Tufts, B., Tyagi, S., Bohr, M., and El-Mansy, Y. (2004) A 90-nm logic technology featuring strained-silicon. *IEEE Transactions on Electron Devices,* **51**(11), 1790–1797.

[258] Brunetti, G., Settefrati, A., Hazotte, A., Denis, S., Fundenberger, J.-J., Tidu, A., and Bouzy, E. (2012) Determination of gamma-gamma' lattice misfit in a single-crystal nickel-based superalloy using convergent beam electron diffraction aided by finite element calculations. *Micron,* **43**(2), 396 – 406.

[259] Gibson, J. and Treacy, M. (1984) The effect of elastic relaxation on the local structure of lattice-modulated thin films. *Ultramicroscopy,* **14**(4), 345 – 349.

[260] Gibson, J. M., Hull, R., Bean, J. C., and Treacy, M. M. J. (1985) Elastic relaxation in transmission electron microscopy of strained-layer superlattices. *Applied Physics Letters,* **46**(7), 649–651.

[261] Hull, R. (1993) Finite element analysis of stress relaxation in thin foil plan-view transmission electron microscopy specimens. *Applied Physics Letters,* **63**(16), 2291–2293.

[262] Clément, L., Pantel, R., Kwakman, L. F. T., and Rouvière, J. L. (2004) Strain measurements by convergent-beam electron diffraction: The importance of stress relaxation in lamella preparations. *Applied Physics Letters,* **85**(4), 651–653.

[263] Hÿtch, M., Houdellier, F., Hüe, F., and Snoeck, E. (2011) Dark-field electron holography for the measurement of geometric phase. *Ultramicroscopy,* **111**(8), 1328 – 1337.

[264] Hÿtch, M. J. and Plamann, T. (5, 2001) Imaging conditions for reliable measurement of displacement and strain in high-resolution electron microscopy. *Ultramicroscopy,* **87**(4), 199–212.

[265] Hÿtch, M., Putaux, J.-L., and Penisson, J.-M. (2003) Measurement of the displacement field of dislocations to 0.03 A by electron microscopy. *Nature,* **423**, 270–273.

[266] Galindo, P. L., Kret, S., Sanchez, A. M., Laval, J.-Y., Yáñez, A., Pizarro, J., Guerrero, E., Ben, T., and Molina, S. I. (2007) The Peak Pairs algorithm for strain mapping from HRTEM images. *Ultramicroscopy,* **107**(12), 1186 – 1193.

[267] Korsunsky, A. M., Vorster, W. J., Zhang, S. Y., Dini, D., Latham, D., Golshan, M., Liu, J., Kyriakoglou, Y., and Walsh, M. J. (2006) The principle of strain reconstruction tomography: Determination of quench strain distribution from diffraction measurements. *Acta Materialia,* **54**(8), 2101 – 2108.

[268] Korsunsky, A. M., Baimpas, N., Song, X., Belnoue, J., Hofmann, F., Abbey, B., Xie, M., Andrieux, J., Buslaps, T., and Neo, T. K. (2011) Strain tomography of polycrystalline zirconia dental prostheses by synchrotron X-ray diffraction. *Acta Materialia,* **59**(6), 2501 – 2513.

[269] Lionheart, W. R. B. and Withers, P. J. (2015) Diffraction tomography of strain. *Inverse Problems,* **31**(4), 045005.

[270] Desai, N. M. and Lionheart, W. R. B. (2016) An explicit reconstruction algorithm for the transverse ray transform of a second rank tensor field from three axis data. *Inverse Problems,* **32**(11), 115009.

[271] Kauko, H., Fimland, B. O., Grieb, T., Munshi, A. M., Müller, K., Rosenauer, A., and van Helvoort, A. T. J. (2014) Near-surface depletion of antimony during the growth of GaAsSb and GaAs/GaAsSb nanowires. *Journal of Applied Physics,* **116**(14), 144303.

[272] Pryor, C. E. and Pistol, M.-E. (2005) Band-edge diagrams for strained III–V semiconductor quantum wells, wires, and dots. *Physical Review B,* **72**, 205311.

[273] Signorello, G., Karg, S., Björk, M. T., Gotsmann, B., and Riel, H. (2013) Tuning the Light Emission from GaAs Nanowires over 290 meV with Uniaxial Strain. *Nano Letters,* **13**(3), 917–924.

[274] Spirkoska, D., Arbiol, J., Gustafsson, A., Conesa-Boj, S., Glas, F., Zardo, I., Heigoldt, M., Gass, M. H., Bleloch, A. L., Estrade, S., Kaniber, M., Rossler, J., Peiro, F., Morante, J. R., Abstreiter, G., Samuelson, L., and Fontcuberta i Morral, A. (2009) Structural and optical properties of high quality zinc-blende/wurtzite GaAs nanowire heterostructures. *Physical Review B,* **80**, 245325.

[275] Larsson, M. W., Wagner, J. B., Wallin, M., Håkansson, P., Fröberg, L. E., Samuelson, L., and Wallenberg, L. R. (2006) Strain mapping in free-standing heterostructured wurtzite InAs/InP nanowires. *Nanotechnology,* **18**(1), 015504.

[276] de la Mata, M., Magén, C., Caroff, P., and Arbiol, J. (2014) Atomic Scale Strain Relaxation in Axial Semiconductor III–V Nanowire Heterostructures. *Nano Letters,* **14**(11), 6614–6620.

[277] Weyland, M. and Midgley, P. A. (2004) Electron tomography. *Materials Today,* **7**(12), 32 – 40.

[278] Frank, J. (1992) Electron Tomography, Plenum, New York and London. 1st edition.

[279] Gordon, R., Bender, R., and Herman, G. T. (1970) Algebraic Reconstruction Techniques (ART) for three-dimensional electron microscopy and X-ray photography. *Journal of Theoretical Biology,* **29**(3), 471 – 481.

[280] Gilbert, P. (1972) Iterative methods for the three-dimensional reconstruction of an object from projections. *Journal of Theoretical Biology,* **36**(1), 105 – 117.

[281] Leary, R., Saghi, Z., Midgley, P. A., and Holland, D. J. (2013) Compressed sensing electron tomography. *Ultramicroscopy,* **131**, 70 – 91.

[282] Venkatakrishnan, S. V., Drummy, L. F., Jackson, M. A., Graef, M. D., Simmons, J., and Bouman, C. A. (2013) A Model Based Iterative Reconstruction Algorithm For High Angle Annular Dark Field-Scanning Transmission Electron Microscope (HAADF-STEM) Tomography. *IEEE Transactions on Image Processing,* **22**(11), 4532–4544.

[283] Gürsoy, D., De Carlo, F., Xiao, X., and Jacobsen, C. TomoPy: a framework for the analysis of synchrotron tomographic data. *Journal of Synchrotron Radiation,* **21**(5), 1188–1193.

[284] Straumanis, M. E. and Kim, C. D. (1965) Solid solubility in system GaSb-GaAs. *Journal of the Electrochemical Society,* **112**, 112–113.

[285] Köhl, M., Schroth, P., Minkevich, A. A., Hornung, J.-W., Dimakis, E., Somaschini, C., Geelhaar, L., Aschenbrenner, T., Lazarev, S., Grigoriev, D., Pietsch, U., and Baumbach, T. (2015) Polytypism in GaAs nanowires: determination of the interplanar spacing of wurtzite GaAs by X-ray diffraction. *Journal of Synchrotron Radiation,* **22**(1), 67–75.

[286] Sharafutdinov, V. (1994) Integral Geometry of Tensor Fields, De Gruyter, Berlin, Boston. 1st edition.

[287] Tong, J., Arslan, I., and Midgley, P. (2006) A novel dual-axis iterative algorithm for electron tomography. *Journal of Structural Biology,* **153**(1), 55 – 63.

[288] Collins, S. M., Leary, R. K., Midgley, P. A., Tovey, R., Benning, M., Schönlieb, C.-B., Rez, P., and Treacy, M. M. J. (2017) Entropic Comparison of Atomic-Resolution Electron Tomography of Crystals and Amorphous Materials. *Physical Review Letters,* **119**, 166101.

[289] Whang, S. H. (2011) Nanostructured metals and alloys: processing, microstructure, mechanical properties and applications, Woodhead Publishing, Oxford. 1st edition.

[290] Kocks, U., Tome, C., and Wenk, H.-R. (1998) Texture and Anisotropy - Preferred Orientations in Polycrystals and their Effect on Materials Properties, Cambridge University Press, Cambridge. 1st edition.

[291] Pond, R. and Vlachavas, D. S. (1983) Bicrystallography. *Proceedings of the Royal Society A,* **A 386**, 95–143.

[292] Hielscher, R., Mainprice, D., and Schaeben, H. (2010) Material Behavior: Texture and Anisotropy. In Freeden, W., Nashed, M. Z., and Sonar, T., (eds.), *Handbook of Geomathematics*, pp. 973–1003 Springer Berlin Heidelberg Berlin, Heidelberg.

[293] Lojkowski, W. and Fecht, H. J. (2000) Structure of intercrystalline interfaces. *Progress in Materials Science,* **45**(5), 339–568.

[294] Zhang, W. Z. and Weatherly, G. C. (2005) On the crystallography of precipitation. *Progress in Materials Science,* **50**(2), 181–292.

[295] Zhang, M. X. and Kelly, P. M. (2009) Crystallographic features of phase transformations in solids. *Progress in Materials Science,* **54**(8), 1101–1170.

[296] Christian, J. W. (1994) Crystallographic theories, interface structures, and transformation mechanisms. *Metallurgical and Materials Transactions A,* **25**(9), 1821–1839.

[297] Dahmen, U. (1982) Orientation relationships in precipitation systems. *Acta Metallurgica,* **30**(1), 63–73.

[298] Bachmann, F., Hielscher, R., and Schaeben, H. (2, 2010) Texture analysis with MTEX - free and open source software toolbox. *Solid State Phenomena,* **160**, 63–68.

[299] Frank, F. C. (1988) Orientation mapping. *Metallurgical Transactions A,* **19**(3), 403–408.

[300] Krakow, R., Bennett, R. J., Johnstone, D. N., Vukmanovic, Z., Solano-Alvarez, W., Lainé, S. J., Einsle, J. F., Midgley, P. A., Rae, C. M., and Hielscher, R. (2017) On three-dimensional misorientation spaces. *Proceedings of the Royal Society A,* **473**(2206), 20170274.

[301] Stuelpnagel, J. (1964) On the parametrization of the three-dimensional rotation group. *SIAM Review,* **6**(4), 422–430.

[302] Rowenhorst, D., Rollett, A. D., Rohrer, G. S., Groeber, M., Jackson, M., Konijnenberg, P. J., and De Graef, M. (2015) Consistent representations of and conversions between 3D rotations. *Modelling and Simulation in Materials Science and Engineering,* **23**(8), 083501.

[303] Neumann, P. (1991) Representation of orientations of symmetrical objects by Rodrigues vectors. *Textures and Microstructures,* **14-18**, 53–58.

[304] Randle, V. and Day, A. (1993) Use of Rodrigues-Frank space for representation of microtexture and grain boundary parameters. *Materials Science and Technology,* **9**(12), 1069–1078.

[305] Zhao, J. and Adams, B. L. (1988) Comments on an asymmetric domain for intercrystalline misorientation in cubic materials in the space of Euler angles. *Acta Crystallographica Section A,* **44**(1), 326–336.

[306] Grimmer, H. (1989) Comments on an asymmetric domain for intercrystalline misorientation in cubic materials in the space of Euler angles. *Acta Crystallographica Section A,* **45**(1), FC1–FC2.

[307] Mason, J. K. and Schuh, C. A. (2008) Hyperspherical harmonics for the representation of crystallographic texture. *Acta Materialia,* **56**(20), 6141–6155.

[308] Mason, J. K. (2009) The relationship of the hyperspherical harmonics to SO(3), SO(4) and orientation distribution functions. *Acta Crystallographica Section A: Foundations of Crystallography,* **65**(4), 259–266.

[309] Frank, F. C. (1992) The conformal neo-eulerian orientation map. *Philosophical Magazine A,* **65**(5), 1141–1149.

[310] Callahan, P. G., Echlin, M., Pollock, T. M., Singh, S., and De Graef, M. (2017) Three-dimensional texture visualization approaches: theoretical analysis and examples. *Journal of Applied Crystallography,* **50**(2), 1–11.

[311] Morawiec, A. (1997) Distributions of misorientation angles and misorientation axes for crystallites with different symmetries. *Acta Crystallographica Section A Foundations of Crystallography,* **53**(3), 273–285.

[312] Heinz, A. and Neumann, P. (1991) Representation of orientation and disorientation data for cubic, hexagonal, tetragonal and orthorhombic crystals. *Acta Crystallographica Section A,* **47**(6), 780–789.

[313] He, Y. and Jonas, J. J. (2007) Representation of orientation relationships in Rodrigues-Frank space for any two classes of lattice. *Journal of Applied Crystallography,* **40**, 559–569.

[314] He, Y. and Jonas, J. J. (2008) Maximum disorientation angles between crystals of any point groups and their corresponding rotation axes. *Journal of Applied Crystallography,* **41**(4), 803–807.

[315] Patala, S. and Schuh, C. A. (2010) Topology of homophase grain boundaries in two-dimensional crystals: the role of grain exchange symmetry. *Computers, Materials & Continua,* **17**(1), 1–18.

[316] Jeniski, R. A. and Kennedy, R. L. (2006) Nickel-base superalloy designed for aerospace. *Advanced Materials and Processes,* **164**(12), 19–22.

[317] Cao, W.-D. and Kennedy, R. L. (2004) Role of chemistry in 718-type alloys – Allvac ® 718Plus ™ alloy development. In *Superalloys 2004 (Tenth International Symposium)* TMS.

[318] Pickering, E., Mathur, H., Bhowmik, A., Messé, O., Barnard, J., Hardy, M. C., Krakow, R., Löhnert, K., Stone, H., and Rae, C. M. (4, 2012) Grain-boundary precipitation in Allvac 718Plus. *Acta Materialia,* **60**(6-7), 2757–2769.

[319] Messé, O., Barnard, J., Pickering, E., Midgley, P. A., and Rae, C. M. (4, 2014) On the precipitation of delta phase in Allvac ® 718Plus. *Philosophical Magazine,* **94**(10), 1132–1152.

[320] Casanova, A., Martín-Piris, N., Hardy, M., and Rae, C. M. (8, 2014) Evolution of secondary phases in alloy ATI 718Plus ® during processing. *MATEC Web of Conferences,* **14**, 09003.

[321] Löhnert, K. and Pyczak, F. (2010) Microstructure evolution in the nickel base superalloy Allvac®718PlusTM. TMS pp. 877–891.

[322] Wilson, A. S. (2016) Formation and effect of topologically close-packed phases in nickel-base superalloys. *Materials Science and Technology,* **0836**(May), 1–11.

[323] Tin, S. and Pollock, T. M. (2003) Phase instabilities and carbon additions in single-crystal nickel-base superalloys. *Materials Science and Engineering A,* **348**(1-2), 111–121.

[324] Vishwakarma, K., Richards, N., and Chaturvedi, M. (5, 2008) Microstructural analysis of fusion and heat affected zones in electron beam welded Allvac® 718PLUS™ superalloy. *Materials Science and Engineering: A,* **480**(1-2), 517–528.

[325] Vishwakarma, K., Richards, N., and Chaturvedi, M. (2005) HAZ microfissuring in EB welded Allvac 718Plus alloy. TMS pp. 637–648.

[326] Vishwakarma, K., Ojo, O. A., Wanjara, P., and Chaturvedi, M. (2010) Linear friction welding of Allvac® 718Plus superalloy. TMS pp. 413–426.

[327] Rae, C. M. and Reed, R. C. (11, 2001) The precipitation of topologically close-packed phases in rhenium-containing superalloys. *Acta Materialia,* **49**(19), 4113–4125.

[328] Rae, C. M., Karunaratne, M. S. A., Small, C. J., Broomfield, R. W., Jones, C. N., and Reed, R. C. (2000) Topologically close packed phases in an experimental rhenium-containing single crystal superalloy. In *Superalloys 2000* TMS pp. 767–776.

[329] Seiser, B., Drautz, R., and Pettifor, D. G. (2011) TCP phase predictions in Ni-based superalloys: Structure maps revisited. *Acta Materialia,* **59**(2), 749–763.

[330] Burke, M. G. and Miller, M. K. (1991) Precipitation in alloy 718: a combined AEM and APFIM investigation. In *Superalloys 718, 625, 706 and Derivatives 1991* TMS pp. 337–350.

[331] Cao, W.-D. (2005) Solidification and solid state phase transformation of Allvac ® 718PLUS ™ alloy. TMS pp. 165–177.

[332] Idowu, O. A., Ojo, O. A., and Chaturvedi, M. (2007) Effect of heat input on heat affected zone cracking in laser welded ATI Allvac 718Plus superalloy. *Materials Science and Engineering: A,* **455**, 389–397.

[333] Radavich, J. F. and Carneiro, T. (2005) A microstructural study of alloy 718PlusTM. In *Superalloys 718, 625, 706 and Derivatives 2005* TMS pp. 329–340.

[334] Krakow, R., Johnstone, D., Eggeman, A., Hünert, D., Hardy, M., Rae, C., and Midgley, P. (2017) On the crystallography and composition of topologically close-packed phases in ATI 718Plus ®. *Acta Materialia,* **130**, 271–280.

[335] Wlodek, S. T. and Field, R. D. (1994) The effects of long time exposure on alloy 718. In *Superalloys 718, 625, 706 and Derivatives* TMS pp. 659–670.

[336] Sijbrandij, S., Miller, M., Horton, J., and Cao, W.-D. (1998) Atom probe analysis of nickel-based superalloy IN-718 with boron and phosphorus additions. *Materials Science and Engineering: A,* **250**(1), 115–119.

[337] Burke, M. G. and Miller, M. (2011) Grain boundary intermetallic phases in alloy 718. In *MRS Proceedings* Vol. 186, pp. 215–218.

[338] Brooks, J. and Bridges, P. (1988) Metallurgical stability of Inconel alloy 718. In *Superalloys 1988 (Sixth International Symposium)* TMS pp. 33–42.

[339] Novoselov, K. S., Geim, A. K., Morozov, S. V., Jiang, D., Katsnelson, M. I., Grigorieva, I. V., Dubonos, S. V., and Firsov, A. A. (2005) Two-dimensional gas of massless Dirac fermions in graphene. *Nature,* **438**(7065), 197–200.

[340] Wang, Q. H., Kalantar-Zadeh, K., Kis, A., Coleman, J. N., and Strano, M. S. (2012) Electronics and optoelectronics of two-dimensional transition metal dichalcogenides. *Nature Nanotechnology,* **7**, 699–712.

[341] Ferrari, A. C., Bonaccorso, F., Fal'ko, V., Novoselov, K. S., Roche, S., Bøggild, P., Borini, S., Koppens, F. H. L., Palermo, V., Pugno, N., Garrido, J. A., Sordan, R., Bianco, A., Ballerini, L., Prato, M., Lidorikis, E., Kivioja, J., Marinelli, C., Ryhänen, T., Morpurgo, A., Coleman, J. N., Nicolosi, V., Colombo, L., Fert, A., Garcia-Hernandez, M., Bachtold, A., Schneider, G. F., Guinea, F., Dekker, C., Barbone, M., Sun, Z., Galiotis, C., Grigorenko, A. N., Konstantatos, G., Kis, A., Katsnelson, M., Vandersypen, L., Loiseau, A., Morandi, V., Neumaier, D., Treossi, E., Pellegrini, V., Polini, M., Tredicucci, A., Williams, G. M., Hee Hong, B., Ahn, J.-H., Min Kim, J., Zirath, H., van Wees, B. J., van der Zant, H., Occhipinti, L., Di Matteo, A., Kinloch, I. A., Seyller, T., Quesnel, E., Feng, X., Teo, K., Rupesinghe, N., Hakonen, P., Neil, S. R. T., Tannock, Q., Löfwander, T., and Kinaret, J. (2014) Science and technology roadmap for graphene, related two-dimensional crystals, and hybrid systems. *Nanoscale,* **7**(11), 4598–4810.

[342] Li, X., Cai, W., An, J., Kim, S., Nah, J., Yang, D., Piner, R., Velamakanni, A., Jung, I., Tutuc, E., Banerjee, S. K., Colombo, L., and Ruoff, R. S. (2009) Large-area synthesis of high-quality and uniform graphene films on copper foils.. *Science,* **324**(5932), 1312–1314.

[343] Bae, S., Kim, H., Lee, Y., Xu, X., Park, J.-S., Zheng, Y., Balakrishnan, J., Lei, T., Ri Kim, H., Song, Y. I., Kim, Y.-J., Kim, K. S., Özyilmaz, B., Ahn, J.-H., Hong, B. H., and Iijima, S. (2010) Roll-to-roll production of 30-inch graphene films for transparent electrodes. *Nature Nanotechnology,* **5**(8), 574–578.

[344] Hofmann, S., Braeuninger-Weimer, P., and Weatherup, R. S. (2015) CVD-enabled graphene manufacture and technology. *Journal of Physical Chemistry Letters,* **6**(14), 2714–2721.

[345] Yu, Q., Jauregui, L. A., Wu, W., Colby, R., Tian, J., Su, Z., Cao, H., Liu, Z., Pandey, D., Wei, D., Chung, T. F., Peng, P., Guisinger, N. P., Stach, E. A., Bao, J., Pei, S. S., and Chen, Y. P. (2011) Control and characterization of individual grains and grain boundaries in graphene grown by chemical vapour deposition. *Nat Mater,* **10**(6), 443–449.

[346] Lee, G.-H., Cooper, R. C., An, S. J., Lee, S., van der Zande, A., Petrone, N., Hammerberg, A. G., Lee, C., Crawford, B., Oliver, W., Kysar, J. W., and Hone, J. (2013) High-Strength Chemical-Vapor-Deposited Graphene and Grain Boundaries. *Science,* **340**(6136), 1073–1076.

[347] Tsen, A. W., Brown, L., Levendorf, M. P., Ghahari, F., Huang, P. Y., Havener, R. W., Ruiz-Vargas, C. S., Muller, D. A., Kim, P., and Park, J. (2012) Tailoring Electrical Transport Across Grain Boundaries in Polycrystalline Graphene. *Science,* **336**(6085), 1143–1146.

[348] Meyer, J. C., Geim, A. K., Katsnelson, M. I., Novoselov, K. S., Booth, T. J., and Roth, S. (2007) The structure of suspended graphene sheets. *Nature,* **446**, 60–63.

[349] Meyer, J. C., Geim, A. K., Katsnelson, M. I., Novoselov, K. S., Obergfell, D., Roth, S., Girit, C., and Zettl, A. (2007) On the roughness of single- and bi-layer graphene membranes. *Solid State Communications,* **143**(1-2), 101–109.

[350] Yazyev, O. V. and Louie, S. G. (2010) Topological defects in graphene: Dislocations and grain boundaries Oleg. *Physical Review B - Condensed Matter and Materials Physics,* **812**, 195420.

[351] Zhang, T., Li, X., and Gao, H. (2014) Defects controlled wrinkling and topological design in graphene. *Journal of the Mechanics and Physics of Solids,* **67**(1), 2–13.

[352] Warner, J. H., Fan, Y., Robertson, A. W., He, K., Yoon, E., and Lee, G. D. (2013) Rippling graphene at the nanoscale through dislocation addition. *Nano Letters,* **13**(10), 4937–4944.

[353] Kim, K., Lee, Z., Malone, B. D., Chan, K. T., Alemán, B., Regan, W., Gannett, W., Crommie, M. F., Cohen, M. L., and Zettl, A. (2011) Multiply folded graphene. *Physical Review B,* **83**(24), 1–8.

[354] Deng, S. and Berry, V. (2016) Wrinkled, rippled and crumpled graphene: an overview of formation mechanism, electronic properties, and applications. *Materials Today,* **19**(4), 197 – 212.

[355] Ortolani, L., Cadelano, E., Veronese, G. P., Degli Esposti Boschi, C., Snoeck, E., Colombo, L., and Morandi, V. (2012) Folded graphene membranes: Mapping curvature at the nanoscale. *Nano Letters,* **12**(10), 5207–5212.

[356] Ping, J. and Fuhrer, M. S. (2012) Layer number and stacking sequence imaging by transmission electron microscopy. *Nano Letters,* **12**, 4635–4641.

[357] Butz, B., Dolle, C., Niekiel, F., Weber, K., Waldmann, D., Weber, H. B., Meyer, B., and Spiecker, E. (2014) Dislocations in bilayer graphene.. *Nature,* **505**(7484), 533–7.

[358] Alden, J. S., Tsen, A. W., Huang, P. Y., Hovden, R., Brown, L., Park, J., Muller, D. a., and McEuen, P. L. (2013) Strain solitons and topological defects in bilayer graphene.. *Proceedings of the National Academy of Sciences of the United States of America,* **110**(28), 11256–60.

[359] Brown, L., Hovden, R., Huang, P., Wojcik, M., Muller, D. A., and Park, J. (2012) Twinning and twisting of tri-and bilayer graphene. *Nano letters,* **12**(3), 1609–1615.

[360] Lin, J., Fang, W., Zhou, W., Lupini, A. R., Idrobo, J. C., Kong, J., Pennycook, S. J., and Pantelides, S. T. (2013) AC/AB stacking boundaries in bilayer graphene. *Nano Letters,* **13**(7), 3262–3268.

[361] Yuk, J. M., Jeong, H. Y., Kim, N. Y., Park, H. J., Kim, G., Shin, H. S., Ruoff, R. S., Lee, J. Y., and Lee, Z. (2014) Superstructural defects and superlattice domains in stacked graphene. *Carbon,* **80**(1), 755–761.

[362] Na, M. Y., Lee, S.-M., Kim, D. H., and Chang, H. J. (2015) Dark-field Transmission Electron Microscopy Imaging Technique to Visualize the Local Structure of Two-dimensional Material, Graphene. *Applied Microscopy,* **45**(1), 23–31.

[363] Ovid'ko, I. (2012) Review on grain boundaries in graphene. Curved poly- and nanocrystalline graphene structures as new carbon allotropes. *Review of Advanced Materials Science,* **30**, 201–224.

[364] Huang, P. Y., Ruiz-Vargas, C. S., van der Zande, A. M., Whitney, W. S., Levendorf, M. P., Kevek, J. W., Garg, S., Alden, J. S., Hustedt, C. J., Zhu, Y., Park, J., McEuen, P. L., and Muller, D. a. (2011) Grains and grain boundaries in single-layer graphene atomic patchwork quilts.. *Nature,* **469**(7330), 389–92.

[365] Kim, K., Lee, Z., Regan, W., Kisielowski, C., Crommie, M. F., and Zettl, A. (2011) Grain boundary mapping in polycrystalline graphene. *ACS Nano,* **5**(3), 2142–2146.

[366] Ophus, C., Shekhawat, A., Rasool, H., and Zettl, A. (2015) Large-scale experimental and theoretical study of graphene grain boundary structures. *Physical Review B,* **92**(20), 205402.

[367] Gammer, C., Burak Ozdol, V., Liebscher, C. H., and Minor, A. M. (2015) Diffraction contrast imaging using virtual apertures. *Ultramicroscopy,* **155**, 1–10.

[368] Plimpton, S. (1995) Fast Parallel Algorithms for Short-Range Molecular Dynamics. *Journal of Computational Physics,* **117**(1), 1–19.

[369] Aktulga, H., Fogarty, J., Pandit, S., and Grama, A. (2012) Parallel reactive molecular dynamics: Numerical methods and algorithmic techniques. *Parallel Computing,* **38**(4), 245 – 259.

[370] Goverapet Srinivasan, S. and Van Duin, A. C. T. (2011) Molecular-dynamics-based study of the collisions of hyperthermal atomic oxygen with graphene using the ReaxFF reactive force field. *Journal of Physical Chemistry A,* **115**(46), 13269–13280.

[371] Srinivasan, D., Lawless, L. U., and Ott, E. A. (2012) Experimental determination of TTT diagram for ally 718PLUS®. In *Superalloys 2012: 12th International Symposium on Superalloys* TMS pp. 759–768.

[372] Goverapet Srinivasan, S., Van Duin, A. C. T., and Ganesh, P. (2015) Development of a ReaxFF potential for carbon condensed phases and its application to the thermal fragmentation of a large fullerene. *Journal of Physical Chemistry A,* **119**(4), 571–580.

[373] Strobl, G. R. (1996) The Physics of Polymers: Concepts for Understanding their Structures and Behavior, Springer-Verlag, Berlin, Heidelberg. 3rd edition.

[374] Wunderlich, B. (1973) Macromolecular Physics: Volume 1 , Academic Press, New York and London. 1st edition.

[375] Kitaigorodsky, A. I. (1973) Molecular Crystals and Molecules, Academic Press, New York and London 1st edition.

[376] Bassett, D. C. (1981) Principles of Polymer Morphology, Cambridge University Press, Cambridge. 1st edition.

[377] Phillips, P. J. (1990) Polymer crystals. *Reports on Progress in Physics,* **53**(5), 549.

[378] Keller, A. (1957) A note on single crystals in polymers: evidence for a folded chain configuration. *Philosophical Magazine,* **2**, 1171–1175.

[379] Keller, A. (1968) Polymer crystals. *Reports on Progress in Physics,* **31**(2), 623–704.

[380] Androsch, R., Di Lorenzo, M. L., Schick, C., and Wunderlich, B. (2010) Mesophases in polyethylene, polypropylene, and poly(1-butene). *Polymer,* **51**, 4639–4662.

[381] Ungar, G. (1986) From plastic-crystal paraffins to liquid-crystal polyethylene: continuity of the mesophase in hydrocarbons. *Macromolecules,* **19**(5), 1317–1324.

[382] Strobl, G. R. (2006) Crystallization and melting of bulk polymers: New observations, conclusions and a thermodynamic scheme. *Progress in Polymer Science,* **31**, 398–442.

[383] Drummy, L. F. and Kubel, C. (2010) Polymer Microscopy: Current Challenges. *Polymer Reviews,* **50**, 231–234.

[384] Libera, M. R. and Egerton, R. F. (2010) Advances in the Transmission Electron Microscopy of Polymers. *Polymer Reviews,* **50**, 321–339.

[385] Holland, V. F. (1964) Dislocations in Polyethylene Single Crystals. *Journal of Applied Physics,* **35**(11), 3235–3241.

[386] Gutt, C., Grodd, L., Mikayelyan, E., Pietsch, U., Kline, R. J., and Grigorian, S. (2014) Local Orientational Structure of a P3HT pi–pi Conjugated Network Investigated by X-ray Nanodiffraction. *The Journal of Physical Chemistry Letters,* **5**(13), 2335–2339.

[387] Panova, O., Chen, X. C., Bustillo, K. C., Ophus, C., Bhatt, M. P., Balsara, N., and Minor, A. M. (2016) Orientation mapping of semicrystalline polymers using scanning electron nanobeam diffraction. *Micron,* **88**, 30–36.

[388] Kang, S.-J., Johnstone, D., Jinnai, H., Higuchi, T., Murase, H., and Midgley, P. (2016) SAMFire - a smart adaptive fitting algorithm for multi-dimensional microscopy. *Proceedings of the European Microscopy Congress 2016,* pp. 692–693.

[389] Bunn, C. W. (1939) The crystal structure of long-chain normal paraffin hydrocarbons. The “shape” of the <CH2 group. *Trans. Faraday Soc.,* **35**, 482–491.

[390] Seto, T., Hara, T., and Tanaka, K. (1968) Phase Transformation and Deformation Processes in Oriented Polyethylene. *Japanese Journal of Applied Physics,* **7**(1), 31–42.

[391] Frank, F. C., Keller, A., and O’Connor, A. (1958) Deformation processes in polyethylene interpreted in terms of crystal plasticity. *Philosophical Magazine,* **3**(25), 64–74.

[392] Bevis, M. J. and Allan, P. S. (1974) Stress-induced martensitic transformations and twinning in organic molecular crystals. In Roberts, M. W. and Thomas, J. M., (eds.), *Surface and Defect Properties of Solids: Volume 3*, Vol. 3, pp. 93–131 The Royal Society of Chemistry London.

[393] Petraccone, V., Allegra, G., and Corradini, P. (1972) Calculation of minimum potential energy of folds and kinks in polyethylene crystals. *Journal of Polymer Science Part C: Polymer Symposia,* **38**(1), 419–427.

[394] Bassett, D. C., Block, S., and Piermarini, G. J. (1974) A high-pressure phase of polyethylene and chain-extended growth. *Journal of Applied Physics,* **45**(10), 4146–4150.

[395] Tashiro, K., Sasaki, S., and Kobayashi, M. (1996) Structural Investigation of Orthorhombic to Hexagonal Phase Transition in Polyethylene Crystal: The Experimental Confirmation of the Conformationally Disordered Structure by X ray Diffraction and Infrared Raman Spectroscopic Measurements. *Macromolecules,* **29**(23), 7460–7469.

[396] Ungar, G., Grubb, D., and Keller, A. (1980) Effect of radiation on the crystals of polyethylene and paraffins: 3. Irradiation in the electron microscope. *Polymer,* **21**(11), 1284 – 1291.

[397] Ungar, G. and Keller, A. (1980) Effect of radiation on the crystals of polyethylene and paraffins: 1. Formation of the hexagonal lattice and the destruction of crystallinity in polyethylene. *Polymer,* **21**(11), 1273 – 1277.

[398] Ungar, G. (1981) Radiation effects in polyethylene and n-alkanes. *Journal of Materials Science,* **16**, 2635–2656.

[399] Tsubakihara, S., Nakamura, A., and Yasuniwa, M. (1996) Melting and Crystallization of Ultra-High Molecular Weight Polyethylene with Appearance of Hexagonal Phase I. Melting Processes of Fibers under Constrained State. *Polymer Journal,* **28**, 489–495.

[400] Tsubakihara, S. and Yasuniwa, M. (1996) Melting and Crystallization of Ultra-High Molecular Weight Polyethylene with Appearance of Hexagonal Phase II. Strain-Induced Crystallization of Thermal-Contracted Sample. *Polymer Journal,* **28**, 563–567.

[401] Kato, S., Tanaka, H., Yamanobe, T., and Uehara, H. (2015) In Situ Analysis of Melt-Drawing Behavior of Ultrahigh Molecular Weight Polyethylene Films with Different Molecular Weights: Roles of Entanglements on Oriented Crystallization. *The Journal of Physical Chemistry B,* **119**(15), 5062–5070.

[402] Rastogi, S., Hikosaka, M., Kawabata, H., and Keller, A. (1991) Role of mobile phases in the crystallization of polyethylene. Part 1. Metastability and lateral growth. *Macromolecules,* **24**(24), 6384–6391.

[403] Sirota, E. B. (2007) Polymer Crystallization: Metastable Mesophases and Morphology. *Macromolecules,* **40**(4), 1043–1048.

[404] Somani, R. H., Yang, L., Zhu, L., and Hsiao, B. S. (2005) Flow-induced shish-kebab precursor structures in entangled polymer melts. *Polymer,* **46**(20), 8587 – 8623.

[405] Hashimoto, T., Murase, H., and Ohta, Y. (2009) Shear-Induced Phase Separation of Entangled Polymer Solutions : Formation of Optically Anisotropic Strings as Precursor Structures of Shish-Kebab. *Macromolecular Symposium,* **279**, 88–95.

[406] Davis, G. T., Eby, R. K., and Colson, J. P. (1970) Thermal Expansion of Polyethylene Unit Cell: Effect of Lamella Thickness. *Journal of Applied Physics,* **41**(11), 4316–4326.

[407] Grubb, D. T. (1974) Radiation damage and electron microsocpy of organic polymers. *Journal of Materials Science,* **9**, 1715–1736.

[408] Keith, H. D. and Padden, F. J. (1996) Banding in Polyethylene and Other Spherulites. *Macromolecules,* **29**(24), 7776–7786.

[409] Lotz, B. and Cheng, S. Z. (2005) A critical assessment of unbalanced surface stresses as the mechanical origin of twisting and scrolling of polymer crystals. *Polymer,* **46**(3), 577 – 610.

[410] Sirota, E. B., King Jr., H. E., Singer, D. M., and Shao, H. H. (1996) Rotator phases of the normal alkanes : An x - ray scattering study. *The Journal of Chemical Physics,* **98**(7), 5809–5824.

[411] Sirota, E. B. and Singer, D. M. (1994) Phase transitions among the rotator phases of the normal alkanes. *The Journal of Chemical Physics,* **101**(12), 10873–10882.

[412] Ungar, G. and Masic, N. (1985) Order in the Rotator Phase of n-Alkanes. *Journal of Physical Chemistry,* **89**, 1036–1042.

[413] Snyder, R. G. (1967) Vibrational Study of the Chain Conformation of the Liquid n-Paraffins and Molten Polyethylene. *The Journal of Chemical Physics,* **47**, 1316–1048.

[414] Reneker, D. and Mazur, J. (1983) Dispirations, disclinations, dislocations, and chain twist in polyethylene crystals. *Polymer,* **24**(11), 1387 – 1400.

[415] Reneker, D. H. and Mazur, J. (1988) Small defects in crystalline polyethylene. *Polymer,* **29**(1), 3 – 13.

[416] Scherr, H., Hägele, P. C., and Grossmann, H. P. (1974) Atomistic calculations of kink defects in the polyethylene crystal by means of semiempirical potentials. *Colloid and Polymer Science,* **252**(10), 871–879.

[417] Cowley, J. (2004) Applications of electron nanodiffraction. *Micron,* **35**(5), 345 – 360.

[418] Krakow, R., Bennett, R. J., Johnstone, D. N., Midgley, P. A., Hielsher, R., and Rae, C. M. F. (2017) Inter-phase Relationships Revealed in 3-Dimensional Orientation Spaces. *Microscopy and Microanalysis,* **23**(S1), 202–203.

Appendix A

List of Publications

Johnstone, D. N., Crout, P. A., Martineau, B., Høgås, S., Laulainen, J., Collins, S., Smeets, S., Morzy, J., Doherty, T., Prestat, E., Ostasevicius, T., Bergh, T., and Ånes, H. pyxem/pyxem: pyXem 0.7.1. https://doi.org/10.5281/zenodo.2650296 (2019).

Martineau, B. H., Johnstone, D. N., van Helvoort, A. T. J., Midgley, P. A., and Eggeman, A. S. (2019) Unsupervised machine learning applied to scanning precession electron diffraction data. *Advanced Structural and Chemical Imaging,* **5**(1), 3.

Sunde, J. K., Johnstone, D. N., Wenner, S., van Helvoort, A. T., Midgley, P. A., and Holmestad, R. (2019) Crystallographic relationships of T-/S-phase aggregates in an Al–Cu–Mg–Ag alloy. *Acta Materialia,* **166**, 587 – 596.

Li, S., Limbach, R., Longley, L., Shirzadi, A. A., Walmsley, J. C., Johnstone, D. N., Midgley, P. A., Wondraczek, L., and Bennett, T. D. (2019) Mechanical Properties and Processing Techniques of Bulk Metal–Organic Framework Glasses. *Journal of the American Chemical Society,* **141**(2), 1027–1034.

Hou, J., Ashling, C. W., Collins, S. M., Krajnc, A., Zhou, C., Longley, L., Johnstone, D., Chater, P. A., Li, S., Coudert, F.-X., Keen, D. A., Midgley, P. A., Mali, G., Chen, V., and Bennett, T. Metal-Organic Framework Crystal-Glass Composites. https://doi.org/10.26434/chemrxiv.7093862.v1 (2018).

Weiss, B. P., Fu, R. R., Einsle, J. F., Glenn, D. R., Kehayias, P., Bell, E. A., Gelb, J., Araujo, J. F. D. F., Lima, E. A., Borlina, C. S., Boehnke, P., Johnstone, D. N., Harrison, T. M., Harrison, R. J., and Walsworth, R. L. (2018) Secondary magnetic inclusions in detrital zircons from the Jack Hills, Wester Australia, and implications for the origin of the geodynamo. *Geology,* **46**(5), 427–430.

Krakow, R., Johnstone, D., Eggeman, A., Hünert, D., Hardy, M., Rae, C., and Midgley, P. (2017) On the crystallography and composition of topologically close-packed phases in ATI 718Plus ®. *Acta Materialia,* **130**, 271–280.

Krakow, R., Bennett, R. J., Johnstone, D. N., Vukmanovic, Z., Solano-Alvarez, W., Lainé, S. J., Einsle, J. F., Midgley, P. A., Rae, C. M., and Hielscher, R. (2017) On three-dimensional misorientation spaces. *Proceedings of the Royal Society A,* **473**(2206), 20170274.

Barnard, J. S., Johnstone, D. N., and Midgley, P. A. (2017) High-resolution scanning precession electron diffraction: Alignment and spatial resolution. *Ultramicroscopy,* **174**, 79–88.

Karagiannidis, P. G., Hodge, S. A., Lombardi, L., Tomarchio, F., Decorde, N., Milana, S., Goykhman, I., Su, Y., Mesite, S. V., Johnstone, D. N., Leary, R. K., Midgley, P. A., Pugno, N. M., Torrisi, F., and Ferrari, A. C. (2017) Microfluidization of Graphite and Formulation of Graphene-Based Conductive Inks. *ACS Nano,* **11**(3), 2742–2755.